Forschungsbericht 2023-23

Investigations into Rapid Aeroelastic Stability Estimation in Turbomachines for Preliminary Design

Michael Blocher

Deutsches Zentrum für Luft- und Raumfahrt
Institut für Aeroelastik
Göttingen

DLR Deutsches Zentrum für Luft- und Raumfahrt

Forschungsbericht 2023-23

Investigations into Rapid Aeroelastic Stability Estimation in Turbomachines for Preliminary Design

Michael Blocher

Deutsches Zentrum für Luft- und Raumfahrt
Institut für Aeroelastik
Göttingen

165 Seiten
78 Bilder
7 Tabellen
199 Literaturstellen

Deutsches Zentrum für Luft- und Raumfahrt

Herausgeber:

Deutsches Zentrum
für Luft- und Raumfahrt e. V.
Wissenschaftliche Information
Linder Höhe
D-51147 Köln

ISSN 1434-8454
ISRN DLR-FB-2023-23
Erscheinungsjahr 2023

DOI: 10.57676/6j5p-7112

Schlagworte: Aeroelastik, Turbomaschine, Vorauslegung, Flattern, aeroelastische Stabilität
(Veröffentlicht auf Englisch)

Michael BLOCHER
DLR, Institut für Aeroelastik, Göttingen

Untersuchungen zur schnellen Abschätzung der aeroelastischen Stabilität von Turbomaschinen in der Vorauslegung
Technische Universität Berlin

Zusammenfassung:

Turbomaschinen sind ein unerlässlicher Teil der heutigen Energieversorgung und des Transportwesens. Ihre Zuverlässigkeit trägt dazu bei Gewinn zu maximieren und Kosten zu minimieren. Außerdem müssen Treibstoffverbrauchs- und Abgasanforderungen berücksichtigt werden um ökologischen Gesichtspunkten Rechnung zu tragen. Um alle diese Kriterien erfüllen zu können, wird die Geometrie moderner Turbomaschinenrotoren und -statoren zunehmend mit automatisierten Optimierungswerkzeugen festgelegt. Zum aktuellen Zeitpunkt beinhalten diese Vorauslegungswerkzeuge Kriterien zur Beurteilung der aerodynamischen Effizienz und der strukturellen Festigkeit der Bauteile. Im Gegensatz dazu wird die aeroelastische Stabilität von Turbomaschinenstufen traditionellerweise sehr spät im Auslegungsprozess, also nach dem Ende des automatisierten Entwurfsprozesses, berücksichtigt. Diese Vorgehensweise verursacht sehr hohe Kosten wenn Neuauslegungen aufgrund aeroelastischer Probleme nötig werden.

Um die Berechnung der aeroelastischen Stabilität in einen automatischen Vorauslegungsprozess zu integrieren, müssen Methoden verfügbar sein um die Flatterneigung einer gegebenen Geometrie zu beurteilen. Es existieren verschiedene aeroelastische Verfahren mit variierendem numerischen Aufwand und unterschiedlicher Genauigkeit mit deren Hilfe die aeroelastische Stabilität einer gegebenen Geometrie beurteilt werden kann. Um eine Methode zu finden die aeroelastische Stabilität mit nach Industriemaßstäben vertretbarem numerischen Aufwand abzuschätzen, wurde die Entwicklung der Rechnerleistung und der numerischen aeroelastischen Methoden untersucht. Es wird die Möglichkeit betrachtet, wissenschaftliche Methoden welche vor ~ 20 - 25 Jahren genutzt wurden um die aeroelastische Stabilität abzuschätzen, heute als Vorauslegungswerkzeuge zu nutzen.

Um die Machbarkeit und Genauigkeit dieser Hypothese zu verifizieren, wurden drei traditionelle Methoden der aeroelastischen Stabilitätsbeurteilung untersucht, welche die bezahlbare Bandbreite des numerischen Aufwands abdecken:

- Als Vergleichsmethode, welche dem Vorgehen am DLR vor ~ 7 Jahren entspricht, wurde die Möglichkeit untersucht, die Energiemethode in Verbindung mit einem 3D zeitlinearisierten RANS-Löser zu nutzen. Verschiedene Möglichkeiten, den numerischen Aufwand dieser Methode zu reduzieren, wurden beurteilt.

- Um das absolute Minimum an möglichem numerischem Aufwand auszuloten, welcher nötig ist um eine aeroelastische Aussage treffen zu können, wurde die Belastbarkeit einer Ein-Gleichungs-Auslegungsregel (reduzierte Kreisfrequenz im aerodynamischen Auslegungspunkt) untersucht, welche Mitte des 20. Jahrhunderts genutzt wurde.

- Abschließend wurde die Möglichkeit untersucht, eine einfachere instationäre aerodynamische Methode (instationäre Potentialströmung) in Verbindung mit der Energiemethode zu nutzen. Dazu wurde ein Vortex Lattice Verfahren um diverse Turbomaschinenfunktionen erweitert, um in der Lage zu sein das Potential eines solchen Lösers für schnelle und zuverlässige oder korrigierbare aerodynamische Ergebnisse bei harmonisch schwingenden Schaufeln abzuschätzen.

Aus den Ergebnissen folgt, dass der vielversprechendste Ansatz für eine schnelle aeroelastische Stabilitätsbeurteilung im Vorauslegungsprozess die Nutzung eines 3D zeitlinearisierten RANS-Lösers in Kombination mit geeigneten Methoden zur Reduktion des numerischen Aufwands ist. Wenn eine geeignete Methode zur Auswahl der zu berechnenden Fälle genutzt wird, könnte dieser Ansatz ab sofort im Vorauslegungsprozess von Turbomaschinenstufen genutzt werden.

Keywords: aeroelasticity, turbomachinery, preliminary design, flutter, aeroelastic stability

Michael BLOCHER
German Aerospace Center (DLR), Institute of Aeroelasticity, Göttingen

Investigations into Rapid Aeroelastic Stability Estimation in Turbomachines for Preliminary Design
Technical University Berlin

Abstract:

Turbomachines are a vital part of today's energy and transportation industry. They need to perform reliably in order to maximize profit and minimize costs. Fuel efficiency and exhaust gas property demands need to be considered in order to meet ecological concerns. To meet all these criteria, rotor and stator row geometries of modern turbomachines are more and more often designed with automated optimization tools. To date, these preliminary design tools include aerodynamic efficiency and structural durability considerations. However, the aeroelastic stability of turbomachinery stages is traditionally treated very late in the design process after the end of the automated preliminary design cycle. This practice causes very large costs if a redesign is necessary due to aeroelastic problems.

To include aeroelastic stability considerations into an automated preliminary design tool chain, methods need to be available to assess the flutter susceptibility of a given geometry configuration. There exists a wide range of possible aeroelastic procedures with varying numerical effort and different degrees of accuracy to judge the aeroelastic stability of a given geometry. In order to find a method to estimate the aeroelastic stability with affordable numerical effort for industrial purposes yet with sufficient accuracy, the development of computational performance and numerical aeroelastic methods over the past years is reviewed. It is proposed that scientific methods for aeroelastic stability estimation from ~ 20 - 25 years ago might be suitable to be used as preliminary design tools, today.

To investigate the feasibility and accuracy of this proposed approach, three traditional methods for aeroelastic stability assessment covering the affordable range of numerical complexity were considered:

- As a baseline approach which resembles the used approach at DLR ~ 7 years ago, the possibility of automating and using the energy method in combination with a 3D time-linear RANS solver was investigated. Various approaches of reducing the numerical cost of this approach were evaluated.

- To gauge the absolute minimum of numerical effort possible to generate an aeroelastic assessment, the validity of a one-equation design rule (reduced angular frequency at aerodynamic design point) used in the middle of the 20^{th} century was investigated.

- Finally, the possibility of using a simpler unsteady aerodynamic method (unsteady potential flow) in combination with the energy method was investigated. To do so, a vortex lattice method was equipped with turbomachinery features to judge its potential to deliver fast and reliable or correctable unsteady aerodynamic results with harmonically deforming blades.

It was concluded that the most promising approach to rapid aeroelastic stability analysis in preliminary design was the use of a 3D time-linear RANS solver in combination with suitable reduction techniques. If the computed cases are selected with a suitable algorithm, this approach might be used in preliminary design of turbomachinery stages, starting today.

Acknowledgements

There are many people who deserve thanks after the conclusion of a PhD thesis: family, friends, colleagues, mentors, advisors, and many more.

But there is one who deserves more thanks than all the rest combined:

Danke, Stephanie!

Ohne Deine Unterstützung hätte ich das nicht geschafft!

Contents

List of Figures

List of Tables

Nomenclature

Latin Symbols

A	Area
$\mathcal{A}$	Aerodynamic forces
$\lceil \boldsymbol{C}^{()} \rfloor$	Aerodynamic influence coefficient matrix
$\mathbb{C}$	The entity of complex numbers
$[\boldsymbol{d}]$	Discrete damping matrix
d	Damping
e	Mathematical constant e, base of the natural logarithm
$\mathcal{E}$	Elastic forces
$\vec{f}$	Force vector
$\vec{\boldsymbol{F}}$	Generalized external / aerodynamic force vector
$\vec{\boldsymbol{f}}$	Discrete force vector
f	Frequency
Im	Imaginary part of a complex number
I	Inertia forces
j	Imaginary unit
$\lceil \boldsymbol{K} \rfloor$	Generalized stiffness matrix
$[\boldsymbol{k}]$	Discrete stiffness matrix
K	Generalized stiffness
k	Stiffness
L_c	Characteristic length
$\lceil \boldsymbol{M} \rfloor$	Generalized mass matrix
$[\boldsymbol{m}]$	Discrete mass matrix
M	Generalized mass
m	Mass
$\vec{\boldsymbol{n}}$	Normal vector outward of the body
n	Nodal diameter number
P	Number of degrees of freedom of the structure
p	Pressure
$\vec{\boldsymbol{q}}$	Vector of the generalized coordinates
q	Generalized coordinate
Re	Real part of a complex number
$\vec{\boldsymbol{r}}$	Distance vector
S	Surface of a volume of fluid flow
Sr	Strouhal number
t	Time
$\vec{\boldsymbol{v}}$	Fluid velocity vector
v_∞	Fluid flow velocity in undisturbed flow
$\vec{\boldsymbol{w}}$	Discrete displacement vector
$\vec{x}$	Displacement vector
x	1^{st} direction in a Cartesian coordinate system
y	2^{nd} direction in a Cartesian coordinate system
z	3^{rd} direction in a Cartesian coordinate system

Greek Symbols

δ	Damping constant
η	Isentropic efficiency
Λ	Global aerodynamic damping (log. dec.)
μ	Doublet strength per unit area
∇	Nabla operator
$[\mathbf{\Phi}]$	Matrix of the eigenmode shape vectors (modal matrix)
Φ	Velocity potential
ϕ	Velocity perturbation potential
$\vec{\boldsymbol{\phi}}$	Eigenmode shape vector
π	Mathematical constant π
σ	Source strength per unit area
σ_n	Inter-blade phase angle (IBPA)
ω	Angular frequency ($\omega = 2\pi f$)
ω_{red}	Reduced frequency

Subscripts and Indices

$_\infty$	Properties in undisturbed flow
$_B$	Properties of a body immersed in a flow
$_P$	Properties of a point in potential flow or on a surface in potential flow
$_W$	Properties of a wake behind a body immersed in a flow
$_J$	Counter for the panels on a body surface
$_K$	Counter for the panels on a body surface
$_L$	Counter for the panels on a wake surface
$_l$	Property on the lower side of a wake
$_r$	Eigenmode number
$_u$	Property on the upper side of a wake

Superscripts

^{H}	Conjugate transpose of a matrix
^{T}	Transpose of a matrix

Abbreviations

ACARE	Advisory Council for Aviation Research and Innovation in Europe
ADP	Aerodynamic Design Point
AGARD	Advisory Group for Aerospace Research and Development of the North Atlantic Treaty Organization (NATO)
C	Programming language
CFC	Carbon Fiber Composite
CFD	Computational fluid dynamics
CFRP	Carbon Fiber Reinforced Polymer
CRISP	Counter Rotating Integrated Shrouded Propfan
DLM	Doublet Lattice Method
DNS	Direct Numerical Simulation
EPFL	École Polytéchnique Fédérale de Lausanne
EU	European Union
FE	Finite element
FORTRAN	Programming language
HCF	High cycle fatigue
IBPA	Inter-blade phase angle

LCO	Limit cycle oscillations
LES	Large Eddy Simulation
MAC	Modal Assurance Criterion
MTU	MTU Aero Engines AG (originally "Motoren- und Turbinen-Union")
NASA	National Aeronautics and Space Administration
ND	Nodal diameter
POD	Proper orthogonal decomposition
RANS	Reynolds-averaged Navier-Stokes
RHS	Right hand side of an equation
ROM	Reduced order model
RPM	Revolutions Per Minute
TRACE	Turbomachinery Research Aerodynamic Computational Environment

Symbols

$\lvert \ \rvert$	Magnitude of a vector
$[\ ]$	Matrix
$\lceil \ \rfloor$	Diagonal matrix
$\{\ \}$	Domain of an equation
$\vec{\ }$	Vector
$\hat{\ }$	Maximum amplitude of a harmonic oscillation or magnitude of a complex value
$\dot{\ }$	First derivative in time
$\ddot{\ }$	Second derivative in time

1. Introduction

Turbomachines are a core component of today's transportation and energy generation. Even though the change to renewable energy is taking place, there will be a need for efficient and reliable gas turbines in the near and even more distant future. When designing new turbomachines, there are many factors which require attention. The required power output, the desired weight, reliability and cost of operation are just a few of the many topics which need to be addressed. The aeroelastic stability of all components in all operating points is a key factor for the reliable operation of a gas turbine.

Traditionally, the aeroelastic stability of a newly designed part is assured at the very end of the design cycle. This leads to undesirable redesign loops and additional development costs if aeroelastic instabilities are discovered. The late treatment of aeroelastic stability in the design process is due to the considerable computational effort necessary for its evaluation. This prohibits an inclusion of aeroelastic considerations into earlier design phases which might include automated design loops where many possible shapes are considered.

This thesis explores possible approaches which can be used to include preliminary aeroelastic tests for flutter stability into early design phases. It contains a summary of fast aerodynamic methods for aeroelastic stability estimation and their potential use in a preliminary design phase.

The structure of the thesis is summarized here briefly:

- *This chapter introduces the challenges faced by turbomachine engineers, the term aeroelasticity and its implications in general and for the special case of turbomachines and will point out the necessity for fast aeroelastic methods.*

- *Chapter 2 will give a short introduction to structural mechanics of turbomachine parts, aerodynamics in turbomachines and then combine these two to treat aeroelasticity in turbomachines.*

- *Then, an overview over possible rapid methods to treat flutter in earlier design phases is given in chapter 3. The considerations and deductions leading to the investigation of three possible approaches to assess the aeroelastic stability are given. The theory for these faster and less numerically expensive methods and the extensions implemented for the investigation of preliminary turbomachinery designs are presented.*

- *In chapter 4, the results of the numerical tests and validations are presented together with the test cases used.*

- *In the last chapter 5, a summary and conclusion is drawn as to the usefulness of the different solution strategies to address the problem introduced in chapter 1.5.*

This chapter will give a short motivation for the increasing importance of aeroelastic problems in turbomachines (chapter 1.1). Then a short introduction to aeroelasticity in general is given in chapter 1.2. The importance of aeroelasticity in turbomachines is reinforced in chapter 1.3, and the nature of aeroelastic problems in turbomachines is differentiated into three main categories. Then, a general overview of published approaches to aeroelasticity in turbomachinery design in general is given in chapter 1.4. In the last section of this chapter (1.5), the main problem of this thesis will be introduced and a solution hypothesis will be stated.

1.1. Motivation

The global economy depends heavily on air traffic. On the one hand, there are people that need to travel long distances for business or pleasure. On the other hand, some goods need to be transported over long distances fast. As a consequence, global air traffic is at an all-time high and experts even expect an increase in air travel and air transport in the future [88].

At the same time, the limitation of earths fossil fuels is well established [118] and long term consequences like climate change due to carbon dioxide emissions receive increasing attention in the public opinion.

This conflict of objectives of people wanting to travel far and fast together with the desire for fast air cargo and being faced with growing ecological impacts, led to the formulation of ACARE's Flightpath 2050. ACARE is the "Advisory Council for Aviation Research and Innovation in Europe" and was founded to support the "Directorate-General for Research and Innovation" and the "Directorate-General for Mobility and Transport" of the European Union (EU) and especially their "High Level Group on Aviation Research".

ACARE's Flightpath 2050 [82] formulates goals for the research in the EU in order to maintain and extend a technological advantage of European stakeholders while reducing the impact of air traffic on the environment. To quote the most ambitious goal: "In 2050, technologies and procedures available allow a 75% reduction in CO_2 emissions per passenger kilometer to support the Air Transport Action Group (ATAG) target, and a 90% reduction in nitrogen oxide (NOx) emissions. The perceived noise emission of flying aircraft is reduced by 65%. This is relative to the capabilities of typical new aircraft in 2000."

Additionally to this, it is in the airline companies' best interest to demand more economical engines from the manufacturers, since fuel costs amount to a substantial portion of the overall operational costs (between 16% and 35% according to Sainarayan & Combes [149]).

To reach these goals and to meet the demands of airline companies, the fuel efficiency of aeroengines needs to be improved constantly. There are two main strategies which are being pursued to achieve this: (i) the bypass mass flow is increased (more air is accelerated by the fan, but not ingested by the core gas turbine) and (ii) the mass of the core engine is reduced without diminishing the power output.

A higher bypass ratio often leads to larger fan diameters with longer blades. Mass reduction often means reduction of compressor stages and usage of lighter materials. Less stages while maintaining the global properties of the gas turbine results in a higher compression ratio for each stage. To summarize, the trend in aeroengine development is towards longer, lighter blades which are subjected to a higher aerodynamic load. This in turn, can lead to dynamic aeroelasticity problems which may cause long term durability issues or catastrophic short term blade loss events.

The investigation of the aeroelastic properties of each component is therefore a vital part of the design process of every new aeroengine.

1.2. Introduction to Aeroelasticity

Aeroelasticity is the science of the interaction of elastic bodies and aerodynamic loads. In 1946, Collar [38] published a paper containing an elegant sketch to explain the problem of aeroelasticity. Collar's triangle of forces visualizes the three physical effects that give rise to "dynamic aeroelasticity" if they are present at the same time.

In figure 1.1, the field of dynamic aeroelasticity is defined via the aerodynamic forces $\mathcal{A}$, the inertia forces I and the elastic forces $\mathcal{E}$. Elastic ($\mathcal{E}$) and inertia forces I occurring at the same time give rise to structural vibrations. Classical flight mechanics is concerned with just aerodynamic ($\mathcal{A}$) and inertia forces I. Static aeroelastic effects (steady state deformation of structures due to aerodynamic loads) is an interaction of aerodynamic ($\mathcal{A}$) and elastic forces $\mathcal{E}$. Once a structure is subject to all three forces, dynamic aeroelastic effects occur.

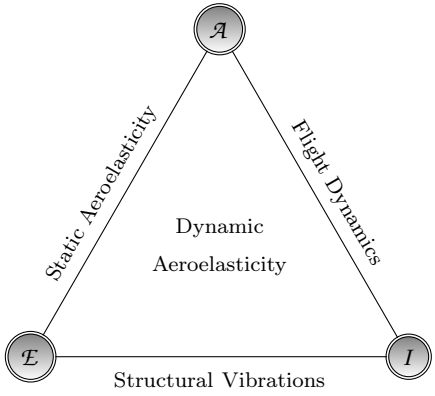

Figure 1.1.: Collar's triangle of forces (adapted from Collar [38]).

It has been observed that the interaction of these three forces can lead to severe structural failures. The most prominent and widely known example is the destruction of the Tacoma Narrows Bridge in 1940. Also airplane wing failure due to dynamic aeroelasticity was observed and investigated by German and allied scientists during World War II. In the post-WW II era, aeroelastic problems were observed in highly loaded military jet engines and known vibration cases of steam turbines that occurred already prior to the war were attributed to aeroelastic causes (Sisto [160]).

For a general introduction to the topic of aeroelasticity the books by Försching [51], Fung [60], Bisplinghoff et al. [18] or Dowell et al. [48] have proven useful.

1.3. Aeroelasticity in Turbomachines

Since the invention of turbomachines, the development goal of turbomachine engineers has been to increase the energy turnover in the machine while reducing the overall mass of the engine at the same time. An increase of energy turnover can be realized by increasing the size of the machine (more stages, bigger diameter) or by increasing the blade loading. The mass of the engine can be reduced by increasing the blade loading and thereby reducing the number of stages, by lighter design or the use of new (lighter) materials. Consequently, ever lighter and more flexible blades are subject to ever increasing aerodynamic loads.

As stated by many researchers (Förstching [52] and Grieb [67] among others), this increase in aerodynamic loading and reduction of structural stability leads to flow states in a turbomachine which have all the attributes of dynamic aeroelasticity. Similar to all other aeroelastic problems in civil or aircraft engineering, the occurring vibration leads either to a deformation amplitude beyond the material's strain resistance (resulting in instant failure) or to a recurring vibration with a defined amplitude (limit cycle oscillation, LCO) which in turn leads to failure due to high cycle fatigue (HCF).

Engineers generally divide the topic of aeroelasticity in turbomachines into two different phenomena with an optional third classification:

1.3.1. Aeroelastic Instability / Flutter

The self-induced vibration of a coupled structural and aerodynamic system is the aeroelastic stability problem. It is also known as flutter. The driving mechanism is an interaction between the blade's vibration and the unsteady pressure load on the blade's surface due to this vibration. An oscillating blade induces periodic pressure fluctuations with the same

base frequency on the vibrating blade's surface and its neighbors' surfaces. Due to these motion induced pressure fluctuations, the blade is experiencing an alternating force on its surface. Depending on the local distribution and the phase relation between vibration and pressure fluctuation, the original vibration is being damped or excited. The former case results in an exponentially decreasing vibration amplitude. In the latter case, the unsteady blade loads lead to a higher vibration amplitude. This in turn leads to higher unsteady pressure loads. The result is an exponentially increasing vibration amplitude leading to instant material failure. This is called flutter or aeroelastic instability. For less severe cases, nonlinear effects lead to an equilibrium of cause and effect for the unsteady flow response and the resulting blade vibration giving rise to an LCO.

1.3.2. Forced Response

Forced response is caused by alternating aerodynamic loads that do not originate from the vibration of the investigated blade row itself. These alternating aerodynamic loads may be wakes or potential fields from neighboring blade rows. Also struts and obstructions in the inflow channel, a non-axial inflow or boundary layer ingestion are possible excitation mechanisms. The resulting vibration of the turbomachinery structure due to these alternating aerodynamic loads is called forced response.

Generally, forced response often cannot be avoided, but does not lead to instant catastrophic failure, in most cases. Instead, it results in vibrations with a limited amplitude which in turn can lead to HCF.

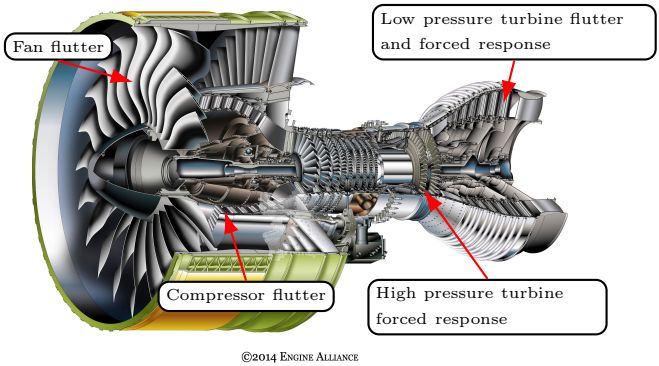

Figure 1.2.: Schematic of a jet engine with highlighted areas in which aeroelastic phenomena mainly occur (original schematic of the jet engine from the web page of Pratt & Whitney [143]).

1.3.3. Flow Instability Induced Vibrations / Acoustic Resonance

Some researchers identify a third phenomenon of aerodynamic excitation of structures in turbomachines, e.g. Clark et al. [37] call this "non-synchronous vibrations", Marshall & Imregun [114] refer to this as "acoustic resonance". Since the publication of Marshall & Imregun, the use of the term "acoustic resonance" has changed. Nowadays, "acoustic resonance" is only used for phenomena where acoustic (pressure wave propagation) effects have an impact on the aeroelastic stability (flutter).

The identified third phenomenon is somewhat different: In highly loaded turbomachine stages additional flow instabilities occur which are not externally induced (no forced response) and independent of a structural deformation (no flutter). These flow instabilities

can lead to structural deformations and machine damage like flutter and forced response. Mostly, the distinction between flow instabilities in (partly) attached flow (vortex shedding, unsteady flow separation and reattachment → non-synchronous vibrations) and flow instabilities in fully separated flow (separated flow vibrations) is made.

1.3.4. Aeroelastically Affected Turbomachinery Parts and Operating Conditions

It has been observed that not all blade rows of turbomachines are equally susceptible to aeroelastic effects. Figure 1.2 indicates components of gas turbines which have experienced aeroelastic problems in the past. Slender fan and compressor blades are mainly subject to flutter problems. Turbine blades are mainly excited by the wakes of neighboring blade rows (forced response). But flutter may also occur in the low pressure turbine and additional aeroelastic phenomena like non-synchronous vibrations and separated flow vibrations may occur seemingly at random.

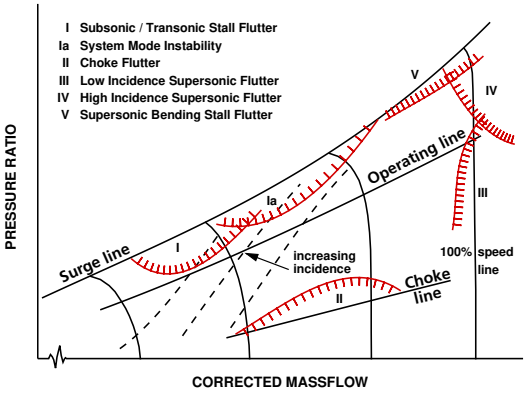

Figure 1.3.: Aeroelastic stability boundaries in a compressor map (according to Fottner [54]).

Additionally to the observation that long and slender blades are endangered to experience aeroelastic phenomena more often than shorter more sturdy ones, it was observed that aeroelastic problems mostly do not arise on the operating line of a turbomachine but rather when the machine is used at an off design operating point (e.g. Fottner [54]). Figure 1.3 highlights operating conditions at which aeroelastic instabilities were observed in the past and indicates that flutter problems mainly occur at the upper limit of the operating speed and near surge and choke boundaries during part load operation.

1.4. State of the Art

Figure 1.2 shows the schematic of a two-spool turbofan engine. The design of such a complex machine requires countless considerations and calculations and is commonly performed by separating the engine into components which are designed by different engineering teams and sometimes even different companies. A general introduction to aeroengine design is given in Bräunling [27].

The topic of this thesis is located in the area of aeroelastic design of compressors and turbines with a focus on fans and compressors. There are unsteady effects of pressure and structural interaction in the combustion chamber, as well, which receive attention in the literature, but they are omitted, here.

Traditionally, aerodynamic and structural design of compressor or turbine stages was done separately with a clear focus on aerodynamic efficiency and potential adjustments to consider structural integrity (see. e.g. Bräunling [26] or Grieb [68]). One key aspect of this process was the so-called "stacking" method (Bräunling [26], Crouse [45]). This means that blade profiles for a specific channel section were either chosen from a database or designed specifically for their properties at certain design flow conditions (current radius, expected flow angle, desired pressure build-up or release, etc.). The chosen blade profiles were then stacked above one another and blended into a single blade. In recent years, with more and more computational power available and more and more reliable structural and aerodynamic numerical codes, the design approach changes towards an integrated optimization approach considering aerodynamic efficiency and structural integrity at the same time. Jones Jr. [89] presented a multidisciplinary design algorithm as early as 2002 and used it to theoretically improve the efficiency of NASA Rotor 67 (Strazisar et al. [167]). Since then, this approach has been widely used and is becoming the industrial standard for designing new turbomachine rotors and stators (Turner et al. [175], Aulich & Siller [7], Goerke et al. [64]). Lately, even manufacturing variations are being considered in this process (Kamenik et al. [91]). Also, the scope of the optimizations broadens more and more to include more geometric features. E.g. Hergt et al. [80] optimized a tandem compressor design or Obaida et al. [131] included the hub contour. Also, the used methods in optimization algorithms include more and more features to predict for example the influence of friction dampers (Hüls et al. [86]) or make use of large eddy simulations for cooling design in turbines (Zhang & He [198]).

Even with all these advancements in numerical fluid dynamics and structural mechanics methods, the aeroelastic proof of new compressor or turbine designs is still mostly done separately from the multi-objective design algorithms.

A very well respected overview of aeroelastic methods is given in Bartels & Sayma [9]. It covers airframes as well as turbomachines and is hence not as committed to turbomachines as the article published by Marshall & Imregun [114]. This widely accepted review of aeroelastic methods in turbomachines is still applicable today. Marshall & Imregun divided the methods of aeroelastic stability prediction in turbomachines into three approaches:

- Classical methods
  Fluid and structure are treated completely separated from each other.
- Partially integrated methods
  Fluid-structure-interaction is implemented on a data exchange base (fluid and structure are treated separately, but data like surface pressure or surface deformation is exchanged at certain points so the processes can influence each other).
- Fully integrated methods
  Fluid and structure are treated by the same solution method in the same equation system.

This separation of aeroelastic methods still holds today with the majority of research efforts being dedicated to partially integrated methods and classical methods being used extensively in the industry.

1.4.1. Classical Methods

Marshall & Imregun [114] list a number of "classical approaches" all of which have in common that the aerodynamic response to a surface deformation is employed to determine the aeroelastic stability of the structure. In the last 25 years, these methods have been used extensively with a clear focus on improving the aerodynamic methods used to predict the aerodynamic response to a blade deformation in turbomachinery.

- Arnone et al. [4] present the research into blade flutter with a 3D time-linearized Navier-Stokes solver and the energy method compared to a simpler stability estimation method.

- Srivastava et al. [165] recount a stator row failure due to aeroelastic instability which was subsequently investigated with the energy method and Duke University's in-house solver.

- The 3D time-linearized Navier-Stokes solver of Volvo Aero at KTH is used in Mayorca et al. [117] to compute the aerodynamic response to given surface deformations.

- Vedeneev et al. [181] published an account of 3D unsteady RANS energy method computations with a commercial solver and the comparison to experimental results.

- Peeren & Vogeler [134] give an example for the use of DLR's in-house solver TRACE being used for flutter redesign with the energy method. Further examples of DLR TRACE being used for aeroelastic stability assessment are published in Leichtfuss et al. [106], Kersken et al. [96] Heners et al. [77], Ashcroft et al. [6] or Frey et al. [58].

- Rendu et al. [146] present one of the newest investigations with a nonlinear unsteady 3D RANS solver from Imperial College London. They substantiate the insight that aeroelastic phenomena in turbomachines are highly three dimensional and cannot be treated with 2D approximations. Vahdati et al. [178] give an overview of the research conducted at Imperial College concerning fan aeroelasticity not limited to classical methods.

This recount is by far not complete but highlights contributions from major research players in the field (University of Florence, Duke University, gas turbine research in Russia, DLR and Imperial College, respectively).

1.4.2. Partially Integrated Methods

As already stated, there are substantial research efforts dedicated to understand the influence of flow and structure on each other. Just a few are listed here.

- Gnesin et al. [63] published unsteady 3D Euler simulations coupled to a modal structural model of an aeroelastic standard configuration as early as 2000.

- Corral & Gallardo [40] present an approach which they call fully coupled but which is partially integrated by the definition of Marshall & Imregun [114]. They present a 2D case of an unsteady RANS finite volume solver connected to a two degree of freedom structural model.

- Im et al. [87] present a 3D unsteady RANS solution coupled with a 5 degree of freedom modal structural approach to investigate the aeroelastic behavior of NASA rotor 67.

- Placzek & Dugeai [137] couple a 3D unsteady RANS solver to a modal model containing all inter-blade phase angles of one eigenmode shape to determine the aerodynamic damping for all IBPAs in one computational run.

- Antona et al. [3] derive the time-linearized 3D RANS solution for a range of eigenmode shapes and couple aerodynamics and structural mechanics in generalized coordinates in the frequency domain.

- Dhopade et al. [47] present a partially integrated method implemented in a commercial code for unsteady RANS and Finite Element representation of the structure. Only IBPA 0° is computed and presented.

- In more recent years, Miller & McNamara [125] presented a 2D unsteady RANS investigation of different coupling approaches for panel flutter.
- Also, Berthold et al. [17] investigated a 3D harmonic balance RANS solver coupled with a modal model of a turbine's deformation with friction contacts.
- Schuff & Chenaux [154] presented a 2D unsteady RANS solution for a compressor cascade coupled to a two degree of freedom model for the blades.
- Suzuki et al. [169] showed a 3D unsteady RANS investigation coupled to a modal model of the structures deformation.
- Finally, Schuff & Chenaux [155] presented an adaption of the p-k method for turbomachines which combines the results of multiple frequency domain 3D time-linearized and harmonic balance RANS solutions with prescribed mesh deformation with the results of numerical modal analysis to determine the rotor stability in the frequency domain.

As already noted by Marshall & Imregun [114], the directly coupled methods are mostly in two dimensions. Since then, computational power has increased significantly and nowadays it is possible to use modal methods to treat fully three dimensional cases. It was observed that the literature makes a difference between "fully coupled" methods which mean "partially integrated" in the terminology of Marshall & Imregun [114] and a multitude of terms for the "fully integrated methods" which are so scarce that there seems to be no clear term for them, as of yet (sometimes, the term "monolithic" is used, but even this term is sometimes used for only "partially integrated" methods).

1.4.3. Fully Integrated Methods

Marshall & Imregun [114] already noted that the simultaneous solution of fluid and structural equations in one equation system is not trivial since most structural problems are formulated as finite element methods and most fluid dynamic problems are treated with the finite volume method. The solution approach to these two is fundamentally different and prohibits their implementation into the same equation system. There exist finite element methods for fluid dynamic problems and finite volume methods for structural problems but they are not widely used and consequently there are not many scientists with access and knowledge for a successful implementation. Marshall & Imregun [114] only cite three sources, only one of which has a turbomachinery relation (Bendiksen [16]).

This impression has not changed in the past 25 years. The extension of fully integrated methods to turbomachinery applications seems to be no primary concern and only cases far off topic (e.g. Wu & Cai [196] with an application to blood flow) are discussed in the literature.

1.4.4. Increased Scope of Aeroelastic Considerations

While the aeroelastic considerations for turbomachines in the past were mainly treated as single stage phenomena, the perspective of aeroelasticity in turbomachines widens constantly.

The trend for aeroelastic computations is towards more and more realistic boundary conditions and to include more and more flow phenomena. E.g. Rządkowski et al. [148] presented a 3D Euler computation of a 7.5 stage compressor with a modal coupling approach. Rahmati et al. [145] and [144] investigated the influence of adjacent blade rows on aeroelastic stability. Naung et al. [129] report on the fluid-structure coupled computation of a complete wind turbine with generator housing and tower for aeroelastic effects. The effect of channel length and nozzles on fan stability is investigated by Zhang et al. [199].

1.4.5. Experimental Efforts

Between 2008 and 2013 efforts were undertaken by a large number of partners to establish a data base of flutter test cases to validate numerical tools in the EU project FUTURE. The summary report by Fransson [55] contains a detailed report of the test cases designed and investigated as well as a list of publications detailing the different findings further. Already during the project it became clear that the experimental data generated was vital to validating the numerical models used by the different project partners, since the numerical results of the different participants (all major players in the field of turbomachinery design using their respective trusted codes) differed greatly (Vogt & Fransson [185]).

Since then, there have been numerous additional experimental efforts to investigate aeroelastic phenomena in turbomachines. Holzinger et al. [85] and [84] document the continued use of one of the compressors of the FUTURE project for aeroelastic experiments. In Seeley et al. [158] the setup of a turbine flutter experiment in a linear turbine cascade is recounted. This experiment delivered global aerodynamic damping values, but did not result in unsteady pressure measurements on the blades' surface. Malzacher et al. [112] conducted experiments in a low-speed cascade on the effect of aerodynamic mistuning (angle-of-attack variations) on the aeroelastic stability. The interaction of blade rows (forced response) and its influence on the stability of compressor blades was investigated experimentally by Terstegen et al. [173]. Watanabe et al. [189] present a study in which they use high speed pressure sensitive paint to measure the unsteady pressure on the complete surface of an oscillating blade in a linear cascade. Phan & He [136] investigated the influence of tip clearance on the aeroelastic stability with an influence coefficient method in a low-speed cascade. Meinzer & Seume [121] published results on the measurement of aerodynamic damping in a turbine blisk.

Still, it can be deduced from the published experimental results that comprehensive measurements of real world examples are exceedingly expensive and very scarce. On the other hand, linear cascades which provide less expensive results suffer from limitations which are acknowledged by all authors. Nonetheless, all experiments provide valuable validation data for the available numerical tools for aeroelasticity.

1.5. The Knowledge Gap of Rapid Aeroelastic Stability Methods for Turbomachines

As can be seen from the examples given in chapter 1.4, even the minimum necessary proof for aeroelastic stability is numerically expensive. Therefore, the aeroelastic analysis of a turbomachine stage is traditionally performed very late in the design process. If redesign becomes necessary due to aeroelastic considerations, this increases the global cost of the design effort substantially. One of the main goals of researchers in the field of aeroelasticity in turbomachines has therefore always been to find methods to judge the aeroelastic risks of a certain design as early in the design process as possible.

As introduced in chapter 1.3, aeroelasticity in turbomachines is generally divided into aeroelastic stability problems (flutter), aerodynamic forcing problems (forced response) and flow instability problems.

- Flow instability induced vibrations are very difficult to predict even with the most sophisticated numerical models available today (efforts to do so have been made by Lu et al. [109], [110] or Espinal et al. [49], both of them using nonlinear unsteady 3D RANS full annulus computations). Also, they do not occur frequently. This prohibits their treatment in preliminary design for turbomachines.

- Flow conditions vulnerable to forced response can be identified via a Campbell diagram (first introduced by Campbell [28], nicely explained by Schmitt [153] and mentioned as standard approach in Marshall & Imregun [114]). Campbell investigated the failure of steam turbine rotors and struggled with stability problems

and excessive rotor vibration. Still, his approach of depicting eigenfrequencies over rotation speed to identify critical operating regions with mechanical or aerodynamic excitation is still widely used 100 years after it was first presented. Since a structural model is generated already in very early design stages for structural integrity calculations, the Campbell diagram can be obtained with insignificant additional cost. Using this diagram, rotation rates and flow states vulnerable to forced response can already be identified in early design stages and appropriate measures can be taken.

Consequently, forced response is already being treated successfully in preliminary design of turbomachines. Flow instability problems on the other hand are not understood well enough and do not occur frequently enough to be considered in preliminary design at the present time. These two aeroelastic phenomena will consequently be ignored for the rest of this thesis.

However, aeroelastic stability (flutter) is reasonably well understood and numerical methods exist which allow its treatment in the final design stages. To avoid redesign due to aeroelastic instability, methods need to be found to estimate and predict flutter already in early design stages.

When Marshall & Imregun [114] wrote their review of aeroelastic methods for turbomachines in 1996, they presented several "standard" methods to predict flutter in turbines or compressors. Since then computational power has increased significantly. Moore's Law (formulated in 1975 by Moore [127]) states that a doubling of microprocessor complexity is to be expected every two years. Surprisingly, this forecast stayed accurate until now (Roser & Ritchie [147]) and even though the limit of scaling down microprocessors seems almost reached, chip manufacturers are working on strategies to further increase computer performance (Waldrop [188]). With recent advancements in quantum computer technology [56], further exponential numerical performance increases seem possible.

To exemplify the computational advances made during the last 25 years, a simple calculation can help: $2^{12} = 4096$. This basically means that a computation which would have needed the time and money of 1 CPU hour in 1996 will require the time and money equivalent of 1 CPU second in 2021 (today).

This tremendous increase in computing power and reduction of cost has led to research into rapid aeroelastic methods for preliminary design use. E.g. Goulos & Pachidis [66] present a method to compute the aeroelastic properties of helicopter rotors for multidisciplinary design use. They use three different simplified aerodynamics models to approximate the unsteady aerodynamics and concentrate on the real-time deformation of the helicopter blade. Mallik et al. [111] use indicial functions derived from 2D steady Navier-Stokes computations to determine the aeroelastic stability of large-aspect aircraft wings.

No similar work in the recent past for turbomachinery blades has been identified. So there is a necessity to research rapid aeroelastic methods for preliminary design in turbomachines. Pope [138] makes an estimation on the development of the application of computational methods over time. He states, based on works by previous authors, that the factor of computational cost between 'repetitive' (standard computations in a design process), 'application' (research computations) and 'large scale research' is roughly $1{:}10^3{:}10^6$. Together with the implications of Moore's Law ($10^3 \approx 1024 = 2^{10}$, doubling every two years $\Rightarrow$ computational power increases by a factor of 1000 every 20 years), Pope then concluded that a transition from 'large scale research' to 'application' or from 'application' to 'repetitive' occurs every 20 years. The methods for turbomachinery aeroelastic stability assessment presented in Marshall & Imregun [114] undoubtedly had solid theoretical foundations and led to sufficiently stable designs. However, the focus of research has since shifted towards more elaborate and accurate representations of the structure and flow in turbomachines. The purpose of this thesis is therefore:

- Review and revisit methods for turbomachinery aeroelastic stability estimation used 25 or more years ago and identify promising methods which might be used with acceptable numerical effort and cost in preliminary design today or in the future.

- Test one or more of the identified promising methods for their validity in present day fan or compressor design and compare them to trusted present day aeroelastic stability estimation methods.
- Evaluate the potential of the proposed approach(es) to deliver sufficiently accurate results for preliminary design purposes and establish a road map on how to best apply this knowledge for future design of turbomachinery fans, compressors or turbines.

2. Aeroelasticity in Turbomachines

In chapter 1, a short introduction to the topic of aeroelasticity in turbomachines and the motivation for finding fast methods to estimate flutter susceptibility of a certain blade design was given. In this chapter, the theoretical background for the prediction of flutter in turbomachines will be given. The following chapters will introduce reduced methods for the aerodynamics part of flutter prediction and their exploration.

This chapter is divided into three sections. Chapter 2.1 introduces aerodynamics with a special focus on aerodynamic phenomena important for turbomachines and aeroelasticity in turbomachines. Then, the treatment of structural dynamics in turbomachines is elaborated in chapter 2.2. Chapter 2.3 will then combine these two and give a foundation for aeroelastic stability analysis in fans, compressors or turbines.

2.1. Aerodynamics of Turbomachines

The basic equations of fluid dynamics for general Newtonian fluid flow are the Navier-Stokes equations. They consist of the continuity equation, the momentum conservation equation and the energy conservation equation. Depending on the degree of approximation used to solve these equations, different approaches to fluid dynamics can be identified. Common to all these methods is the possibility to use them in two or three dimensions.

There exist three Navier-Stokes equations for four unknowns (density, velocity, pressure and internal energy). This closure problem can be remedied by introducing "equations of state" relating pressure, density & temperature and internal energy, density & temperature. Then, there exist five equations for five unknowns which make a solution theoretically possible. However, until now, no analytical solution has been found to the full set of Navier-Stokes equations.

Even though, the focus of this thesis are turbomachines, the basic fluid dynamic equations are the same for external aircraft flow or the flow through an engine. Computational fluid dynamics codes for turbomachines most often contain modules which allow for the reduction of the computational domain via cyclic symmetry and the treatment of centrifugal forces on the fluid. Hence, the theory is the same and there will be no special focus on turbomachinery fluid dynamic solvers.

2.1.1. Direct Numerical Simulation (DNS)

The British meteorologist Richardson hypothesized that energy is dissipated in a fluid flow by vortices which break up into smaller vortices until the energy of their fluid motion is dissipated by the viscosity of the fluid. Based on this hypothesis, the Russian mathematician Kolmogorov derived relationships for the smallest scales in turbulent flow (smallest existing vortices in a flow) depending on the kinematic viscosity of the fluid and the dissipation of turbulent kinetic energy (Pope [141]). There exist "smallest scales" for length and time which define the resolution necessary in space and time to resolve the smallest turbulence scales. If a fluid flow is discretized in space and time in a manner that can resolve these smallest scales (sufficiently fine grid, sufficiently small time stepping procedure), it is possible to numerically find fluid flow properties which satisfy the Navier-Stokes equations to the desired accuracy. This is called direct numerical simulation. An introduction to DNS for incompressible flows can be found in Pope [139]. He also states that turbulence is by nature three-dimensional and chaotic, which is the reason that he states that a two-dimensional DNS is possible but not sensible.

Until very recently, the direct numerical solution of the Navier-Stokes equations was so expensive that only very limited problems for academic purposes could be solved. Since $\sim$2010, researchers of the University of Southampton have started to publish data on the implementation and successful use of a direct numerical solver for turbomachinery application (Sandberg et al. [150], [151], Michelassi et al. [124], [123] and Wheeler et al. [191]).

2.1.2. Large Eddy Simulation (LES)

Trapped between the need for time accurate turbulence data for large scale flows and the unavailability of sufficient computing resources, it was again a meteorologist who proposed the foundations of the so-called large eddy simulation (LES) (Smagorinsky [162]).

Pope [140] explains LES in the following way: The Navier-Stokes equations are subjected to a filter operation which suppresses the smallest scale motions (where the energy is dissipated, and which require the highest numerical effort). The remaining flow equations, together with an appropriate sub-grid scale model (to dissipate the energy) represent the flow motion containing the larger vortices contained in the fluid motion. Pope states that a high quality LES is supposed to resolve 80% of the contained energy of the turbulence.

LES are by design always unsteady and three dimensional if realistic solutions are required. Due to the applied small scale filtering, the discretization in space and time does not need to be as fine as for DNS, resulting in lower computational requirements for speed and memory. Still, at the moment (2021) the use of LES for turbomachinery applications requires access to substantial resources, putting it in the region of research applications, but not everyday design use. As with DNS, the use of two-dimensional approaches is possible but not advisable due to the nature of turbulence.

Tyacke & Tucker [176] propose that the number of LES investigations performed in turbomachinery scales with the available computing power. Their hypothesis is that there are many phenomena in turbomachines which cannot be resolved by flow averaged methods (see the following section) and that there is a need for turbulence resolution to understand these phenomena and increase the efficiency of gas turbines further. And indeed, the number of published uses for LES in turbomachines has steadily increased over the past years. E.g. Medic et al. [119] ran comparison simulations to transition experiments conducted in the 1950s by NASA and concluded that transition in turbines can be predicted better with LES than with less computationally expensive methods. The same conclusion was drawn by Memory et al. [122] in the same year, who also compared LES computations to turbine airfoil experiments. Scillitoe et al. [157] reported purely numerical experiments with an LES approach to quantify the influence of the freestream turbulence on a 3D corner separation. Still, the computational load of LES is so high that Fiore & Biolchini [50] investigated methods to reduce the needed computational domain and store the results more effectively.

2.1.3. Reynolds-averaged Navier-Stokes Simulations (RANS)

Most often, the Navier-Stokes equations are separated into mean flow properties and fluctuating flow properties. Since fluctuating flow properties are irrelevant for many applications, they are reduced from the equations leading to the Reynolds-Averaged Navier-Stokes equations.

Together with the equations of state and a suitable turbulence model to model the dissipation of kinetic energy, it is possible to numerically solve the RANS equations for a flow volume which is discretized much more coarsely in space and time than for LES or DNS because it is not necessary to resolve turbulence. This treatment of the Navier-Stokes equations for steady state or unsteady fluid flow is elaborated extensively in the literature on computational fluid dynamics (e.g Versteeg & Malalasekera [183] for general CFD and e.g. Pope [142] for turbulence modeling).

Since the requirements for space and time resolution of the fluid flow of interest are a lot less demanding than for LES or DNS, the solution of the RANS equations in steady or unsteady form is the most often used strategy to investigate turbomachinery flows at the moment.

For flows with a large dimension normal to the main flow direction (e.g. large wing spans for aircraft applications), two-dimensional reductions often produce comparable results at a fraction of the cost.

The big advantage of the RANS equations is also one of their major drawbacks. Since unsteady turbulence phenomena which do not contribute to a change of the mean flow properties are not resolved, their effect cannot be quantified. E.g. Hergt et al. [81] investigated the flow in a transonic compressor cascade experimentally and numerically and concluded that unsteady RANS computations sometimes are unable to resolve flow fluctuations accurately enough for reliable investigations of turbomachinery flow (see also Tyacke & Tucker [176]).

The need for better resolution of numerical solutions for fluid flow in time and space together with the prohibitively high price of LES or DNS led to the development of hybrid forms of CFD which try to combine RANS with LES to resolve at least large scale turbulence.

Detached Eddy Simulation (DES)

Detached eddy simulation was first proposed by Spalart et al. [163] for airplane wings. Its key feature is a treatment of the flow according to LES or RANS depending on discretization size and wall distance. Like this, the advantages of RANS are exploited close to the walls, where LES resolution grids would cause a very high computational load. LES on the other hand, is used in regions far from the walls to capture vortex motion.

An especially interesting case of a DES application was reported by Yamada et al. [197], who performed a full annulus multi-stage DES computation of the first half of an industrial gas turbine compressor to investigate the onset of stall. Sun et al. [168] reported DES investigations on the flutter stability of a last stage turbine blade.

2.1.4. Euler / Inviscid Navier Stokes Simulation

Another important simplification besides the Reynolds-averaging is the assumption of inviscid flow. Additionally assuming an adiabatic fluid leads to the Euler equations, basically a subset of the Navier-Stokes equations with zero viscosity and zero thermal conductivity.

Like the Navier-Stokes equations, the Euler equations can be discretized and solved numerically. Due to the smaller number of terms which need to be computed, Euler solvers are less numerically demanding than full Navier-Stokes (RANS, LES, DNS) solvers. This also led to their earlier implementation and use. Especially for steady state airplane external flows, fluid viscosity often does not impact the flow very much and very realistic results can be obtained.

See e.g. Lowe & Zingg [108] for an application of Euler equations to aircraft design for flutter. There are a number of additional sources which could be cited, but mostly their focus is on the aerodynamic or aeroelastic effects and the Euler solver is merely used as a tried and trusted tool (see Cao [29], van Rooij et al. [180], Voss [186] or Marques et al. [113]). It needs to be noted that all these publications are aircraft applications. Sometimes even two-dimensional Euler computations are accurate enough and are still published in the literature. For turbomachines, fluid viscosity and heat transfer are important effects so that Euler solvers introduce errors which in most cases cannot be neglected.

2.1.5. Potential Flow Methods

For an inviscid and irrotational flow a physical quantity exists whose derivative in the coordinate directions is the velocity $\vec{v}$ of the flow. This quantity is called the velocity

potential Φ of the flow (see e.g. Katz & Plotkin [93]).

$$\nabla\Phi = \vec{\boldsymbol{v}} \tag{2.1}$$

If the additional assumption of incompressibility is made, the continuity equation reduces to:

$$\begin{aligned} \frac{\partial \cancel{\rho}}{\partial t} + \frac{\partial \rho \vec{\boldsymbol{v}}_x}{\partial x} + \frac{\partial \rho \vec{\boldsymbol{v}}_y}{\partial y} + \frac{\partial \rho \vec{\boldsymbol{v}}_z}{\partial z} &= 0 \\ \Rightarrow \frac{\partial \vec{\boldsymbol{v}}_x}{\partial x} + \frac{\partial \vec{\boldsymbol{v}}_y}{\partial y} + \frac{\partial \vec{\boldsymbol{v}}_z}{\partial z} &= 0 \\ \Rightarrow \nabla^2\Phi &= 0 \end{aligned} \tag{2.2}$$

The continuity equation is then the only governing equation for the flow properties. This reduces the numerical effort substantially since this problem can be reduced to a boundary value problem where only the properties on the control volume boundaries need to be found and all other properties in the control volume itself only depend on these.

Real fluid flow, especially in turbomachines, is never irrotational, inviscid and incompressible but for aircraft aerodynamics, these assumptions still often lead to surprisingly accurate results for design purposes. This is one of the reasons, potential flow aerodynamics are still applied in aircraft design, even today (see Voss [186]). That said, potential flow solutions were used for turbomachinery applications with reasonable success while no methods were available to predict the flow more accurately. Marshall & Imregun [114] list a number of them in their review on turbomachinery aeroelasticity, which implies that they were still in use at the end of the last century.

There exist various correction methods to treat viscosity or even to reintroduce compressibility into the solution to correct the results for more realistic flow conditions (see chapter 15 in Katz & Plotkin [93]). As with Euler and RANS methods, two-dimensional formulations are used with success for problems of a mainly two-dimensional nature.

2.1.6. Treatment of Time-Dependent Flow

A large number of real-world aerodynamic problems are not classical "aircraft wing in level flight"-problems. For airplanes, wind gusts introduce time-variable flow conditions. Helicopter blades experience different flow due to the angle-of-attack change over the circumference, tilt of the rotor and the flight direction in general. Wind turbines experience the potential field of the tower and turbomachinery blades experience neighboring blade row influence or non-uniform inflow effects.

Often, these unsteady aerodynamic effects have direct consequences for the structural integrity of the objects suffering from them. The quantification of unsteady effects is therefore vital for many engineering purposes.

For aerodynamic methods there exist different approaches to treat the time-dependency of flow properties. To describe the problem in mathematical terms, steady state problems assume that all terms of the type $\frac{\partial}{\partial t}$ in an equation are nonexistent ($\frac{\partial}{\partial t} = 0$). The solution of an unsteady problem acknowledges that the term(s) $\frac{\partial}{\partial t}$ are not zero, especially (but not only) if there are time-dependent boundary conditions influencing the flow equations. Three methods to model the influence of the time-dependent terms in the aerodynamic equations will be presented with no claim for completeness.

One attribute that all these methods share is their dependency on an initial solution. This means that the time dependent solution "develops" from (assumed) starting values which have to be supplied at the start of the computation.

2.1.6.1. Non-linear Unsteady Methods

Non-linear unsteady methods compute the value of the term(s) $\frac{\partial}{\partial t}$ from the values of the flow variables. Explicit methods use the values of the flow variables at the old time step. Implicit methods compute them from the resulting values of the flow variables at the new time step, resulting in a more complicated solution. The best results are mostly achieved by using a combination of the values of the flow variables at the old time step **and** the new time step.

With a suitable discretization in time and the knowledge of the time-derivative of the flow properties, the values at a later point in time can be computed based on the values at the present time step. As already mentioned, the result will always depend on the initial values of the solution.

For unsteady RANS approaches, most often a steady state solution is taken as starting solution and the unsteady values develop as a result of the boundary conditions. Theoretically, robust and accurate solvers could iterate to an accurate solution given enough time steps no matter what initial values are supplied. In reality, virtually all known nonlinear unsteady Euler or RANS solvers are dependent on reasonable initial values to be able to perform at all or to obtain accurate results.

2.1.6.2. Harmonic Balance Methods

Hall et al. [74] presented the "harmonic balance method" for turbomachines as it is currently used by many aerodynamic solvers. They propose that many aerodynamic phenomena in turbomachines are periodic in time and consequently can be Fourier-transformed into the frequency domain, resulting in very distinct Fourier coefficient peaks at integer multiples of the periodicity frequency.

Hall et al. then assume, that resolving a comparatively low number of harmonics of the periodic frequency is often sufficient to represent the unsteady flow to an engineering degree of accuracy. Together with a pseudo-time stepping algorithm, it is possible to obtain the unsteady fluid flow solution in the frequency domain and capture even higher harmonic effects. Since periodicity in time is assumed implicitly and only a few harmonics are retained, these methods can result in substantially faster computational times than nonlinear unsteady methods.

This method cannot resolve transient effects, but as Hall et al. state, most engineering problems in turbomachines are concerned with time-periodic and not transient effects which can be represented sufficiently well by very few low order terms of a Fourier decomposition. Therefore, this method is often considered a very good trade-off between computational expense and accurate results.

Like the nonlinear unsteady methods, the harmonic balance results should theoretically be independent of the initial values supplied, but in reality most often a reasonable steady state initialization ensures numerical stability and convergence to reliable unsteady results.

2.1.6.3. Time-Linearized Methods

Time-linearized methods take the assumption of time-periodic flow presented in the previous section one step further. For time-linearized methods, the unsteadiness of the flow is assumed to be sinusoidal with the perturbation frequency. Sticking with the Fourier analogy, only the first harmonic of the time-periodic frequency is retained.

Based on this, the unsteady terms $\frac{\partial}{\partial t}$ are approximated to be of the form $\xi \cdot e^{j\omega t}$ where ξ is a synonym for any variable in the flow. Then, the unsteady flow equations are decomposed into a steady state and an unsteady harmonic part. The unsteady part has the additional advantage to be a linear equation system albeit with complex terms which can be solved very efficiently numerically. The steady state part is solved independently with steady state methods and its results are used to solve the unsteady part with the harmonic disturbance boundary conditions.

This approach has been used extensively for Euler and Navier-Stokes solvers in 2D and 3D. Kersken et al. [96] present the implementation of this approach into a the 3D RANS solver used for turbomachinery applications at DLR.

2.1.7. Flow Phenomena in Turbomachinery Aerodynamics Affecting Aeroelasticity

The flow inside a turbomachine spinning at very high revolution speeds is by nature highly unsteady and volatile. This chapter aims at giving a short introduction to flow phenomena which have been observed to be important for aeroelastic effects and which are being researched in order to improve efficiency and safe operation of turbomachines. Often, the introduced aerodynamic effects are ambiguous and may lead to flutter, forced response or non-synchronous vibrations depending on the structure or flow case where they occur. Additionally, the boundaries between these effects are not always easy to draw.

None of the subsequent effects is the focus of this thesis; they are merely mentioned for completeness' sake.

Potential Fields and Wakes of Struts and Neighboring Blade Rows

The most prominent reason for forced response are potential fields and wakes of neighboring blade rows or struts in turbomachines. They lead to a time-periodic flow with the blade passing frequency. See for example Blocher & Gómez Fernández [20] and Gómez Fernández & Blocher [65].

Non-uniform In- or Outflow

Some jet engines are fitted with an S-shaped inlet duct leading to nonuniform flow over the circumference of the compressor stages. The same phenomenon occurs if an engine with a straight circular inlet or outlet duct experiences non-axial in- or outflow due to cross winds or maneuvers. In both cases, a time-periodic flow with the revolution frequency occurs. For research on this topic see e.g. Lee et al. [104] or Zhang et al. [199].

Combustion Instabilities

Fuel combustion is a highly volatile and unsteady process leading to pressure surges affecting the high pressure turbine and its guide vanes. This phenomenon is observed during operation. However, numerical models of combustion instabilities resulting in pressure surges affecting the high pressure turbine are to the author's knowledge not operational, yet.

Shock Motion in Transonic Flow

One of the most widely acknowledged phenomena leading to aerodynamic excitation is the motion of a transonic shock due to minute geometry or flow changes. For a fictitious example of a 2D blade with torsional degree of freedom it is immediately obvious that the back and forth traveling of a shock can lead to an excitation of the blade's motion. In-depth investigations can be found in the literature, e.g. in Srivastava & Keith [164].

Vortex Shedding

Bodies in moderately fast flow shed a von Kármán vortex street. If the flow velocity increases, the body starts to shed turbulent vortices. Depending on the Reynolds number of the flow, this also happens in blade rows of turbomachines, leading to a periodic excitation of the blades (Kielb et al. [100], Clark & Gorrell [36], Daku & Vad [46]). These vortices oscillate either with a natural frequency like von Kármán vortex streets (NSV) or with a frequency induced by upstream or downstream blade rows (forced response).

Corner Effects

In the corners between hub and blade or shroud and blade of a turbomachinery blade row, vortices or separation bubbles form due to the flow direction changes induced by the blades. Like the aforementioned shed vortices they are not stationary but oscillate and may introduce periodic loading on the blade's surface (see e.g. Yamada et al. [197]).

Tip Leakage Flow

The shed vortices and corner vortices described in the two previous sections can be influenced considerably by the flow through the gap between rotor blades and casing / casing treatment. The effects of tip clearance flow on aeroelastic stability can therefore not be neglected. Investigations into this topic can be found e.g. in Krug et al. [102], Möller et al. [126] and Brandstetter et al. [24].

Cavity Flow

Even though leakage flows are undesired and costly, there are gaps and cavities in turbomachines which cannot be avoided. The flow through these cavities and its influence on aeroelastic stability has been acknowledged for a long time. Due to the increased numerical load and the often tedious mesh generation process, this phenomenon stays an area with a need of research efforts (see e.g. Corral et al. [41]).

Rotating Instabilities

Close to the upper operating boundaries of a compressor in the compressor map (see figure 1.3), the pressure buildup over the blade row is so high that the flow begins to stall (no fluid transport through the passage any more). This happens typically in very few defined passages first and evolves into a rotating pattern over the circumference of the rotor (rotating stall). With even further increase in pressure ratio, this may even lead to fluid blowback through the passage, called surge.

These phenomena may lead to an aerodynamic excitation, as well, and are investigated in the community. E.g. Ulbricht [177] investigated rotating instabilities in an annular cascade, Chenaux [35] / Chenaux et al. [34] investigated the stability of blades at reversed flow conditions occurring during surge.

Acoustic Effects

Turbomachines contain many smooth metallic surfaces which are ideal sound wave reflectors. Unfavorable conditions may lead to standing waves forming inside of a turbomachinery stage leading to a periodic excitation of the structure. If this occurs close to a natural eigenfrequency of the blades or vanes, flutter might occur. See e.g. Owczarek [132] for an overview of historic and recent work on this subject.

2.2. Structural Mechanics of Turbomachines

The classical equation of motion describes the motion behavior of an arbitrary body with mass m, damping d and stiffness k which is subjected to an external force $\vec{f}(t)$.

$$m\ddot{\vec{x}}(t) + d\dot{\vec{x}}(t) + k\vec{x}(t) = \vec{f}(t) \tag{2.3}$$

The motion is then the resulting displacement vector $\vec{x}$ and its derivatives in time giving velocity and acceleration. The principle of superposition states that the solution of the equation of motion is the sum of the homogeneous part and the particular part of the solution:

$$\vec{x}(t) = \vec{x}_{homogeneous}(t) + \vec{x}_{particular}(t) \tag{2.4}$$

The homogeneous part of the solution is the solution of the equation of motion without external forces:

$$m\ddot{\vec{x}}(t) + d\dot{\vec{x}}(t) + k\vec{x}(t) = 0 \tag{2.5}$$

2.2.1. Theoretical Solution to the Homogeneous Equation of Motion

Mathematical textbooks give the solution to a second order homogeneous differential equation with constant coefficients like equation (2.3).

$$x(t) = \left(C_1 e^{j\omega t} + C_2 e^{-j\omega t}\right) e^{-\delta t} \qquad \text{where} \quad \{C_1, C_2 \in \mathbb{C}\} \tag{2.6}$$

In this solution the damping constant δ is defined as

$$\delta = \frac{d}{2m}$$

The natural frequency ω_0 of the undamped system is defined as

$$\omega_0 = \sqrt{\frac{k}{m}}$$

ω_0 then is used to derive the natural frequency ω of the damped system:

$$\omega = \sqrt{\omega_0^2 - \delta^2}$$

Depending on the magnitude of δ, the resulting motion of the body due to an initial displacement is either strongly damped (slowly returning to its zero state), a decaying harmonic oscillation around its zero state, a constant harmonic oscillation around its zero state or a harmonic oscillation around its zero state with increasing amplitude.

This last case, where the damping constant is negative and leads to a harmonic oscillation with increasing amplitude is called instability. The solution to the homogeneous equation of motion is therefore also called a stability problem.

The same derivation could be done for the particular problem depending on the nature of the forcing function (see May [116] for harmonic forcing). This is called a forcing problem.

2.2.2. Solution of the Discretized Homogeneous Equation of Motion

Based on equation (2.3) and relying on the formulations of Crawley [44], Kemme [95] or any finite element software theory manual (e.g. MSC Software [128]) the discretized equation of motion for a structure can be given as:

$$\left[\boldsymbol{m}\right]\ddot{\vec{\boldsymbol{w}}}\left(t\right)+\left[\boldsymbol{d}\right]\dot{\vec{\boldsymbol{w}}}\left(t\right)+\left[\boldsymbol{k}\right]\vec{\boldsymbol{w}}\left(t\right)=\vec{\boldsymbol{f}}\left(t\right) \tag{2.7}$$

In equation (2.7), $\left[\boldsymbol{m}\right]$ is the discrete mass matrix of the structure, $\left[\boldsymbol{d}\right]$ is the discrete damping matrix and $\left[\boldsymbol{k}\right]$ is the discrete stiffness matrix. The vectors $\vec{\boldsymbol{f}}\left(t\right)$ and $\vec{\boldsymbol{w}}\left(t\right)$ are the discrete external force and discrete displacement vectors, respectively. Equation (2.7) represents the general relation between externally acting forces and the deformation of a structure in discretized form.

Like the solution of the general equation of motion, the discretized equation of motion has a homogeneous and a particular part. As introduced in chapter 2.2.1, the homogeneous (RHS = 0 → no external forces) discretized equation of motion of a structure is:

$$\left[\boldsymbol{m}\right]\ddot{\vec{\boldsymbol{w}}}\left(t\right)+\left[\boldsymbol{d}\right]\dot{\vec{\boldsymbol{w}}}\left(t\right)+\left[\boldsymbol{k}\right]\vec{\boldsymbol{w}}\left(t\right)=0 \tag{2.8}$$

Likewise, according to the approach of chapter 2.2.1, the first step is the derivation of the eigenfrequencies of the undamped system:

$$\left[\boldsymbol{m}\right]\ddot{\vec{\boldsymbol{w}}}\left(t\right)+\left[\boldsymbol{k}\right]\vec{\boldsymbol{w}}\left(t\right)=0 \tag{2.9}$$

To solve equation (2.9), harmonic vibration is assumed:

$$\vec{\boldsymbol{w}}\left(t\right)=\hat{\vec{\boldsymbol{w}}}\cdot\mathrm{e}^{j\omega t} \tag{2.10}$$

Equation (2.10) gives the deformation for each point of the discretized model over time. $\hat{\vec{\boldsymbol{w}}}$ is the maximum amplitude of the harmonic oscillation of the structure and ω is the angular frequency. Since the second derivative of an exponential function is the squared factor of the exponent times the original function, the acceleration of each point of the discretized model can be expressed as:

$$\ddot{\vec{\boldsymbol{w}}}\left(t\right)=-\omega^{2}\hat{\vec{\boldsymbol{w}}}\cdot\mathrm{e}^{j\omega t} \tag{2.11}$$

If equation (2.10) and its second derivative in time are inserted into equation (2.9), the structural eigenvalue problem is defined.

$$\left(\left[\boldsymbol{k}\right]-\omega^{2}\left[\boldsymbol{m}\right]\right)\hat{\vec{\boldsymbol{w}}}=0 \tag{2.12}$$

The solutions of this eigenvalue problem are the angular eigenfrequencies ω_r and the eigenmode shape vectors $\hat{\vec{\boldsymbol{\phi}}}_r$. The subscript r denotes a counter for the eigenmodes running from 1 to the number of degrees of freedom of the system P. Now, the displacement vector of the structure can be written as a superposition of these eigenmode shapes in generalized coordinates $\vec{\boldsymbol{q}}_{(r)}\left(t\right)$:

$$\vec{\boldsymbol{w}}\left(t\right)=\left[\boldsymbol{\Phi}\right]_{(r)}\vec{\boldsymbol{q}}_{(r)}\left(t\right)\qquad\text{where}\quad\left\{r=1,\,2,\,...,\,P\right\} \tag{2.13}$$

In equation (2.13), the modal matrix $\left[\boldsymbol{\Phi}\right]_{(r)}$ denotes a matrix consisting of all the eigenmode shapes and $\vec{\boldsymbol{q}}_{(r)}\left(t\right)$ denotes the vector of the generalized coordinates. The "generalized" coordinate is a scalar contribution factor for each eigenmode shape, describing how large the contribution of one mode shape is to the overall deformation. This terminology is used extensively and is based on the assumption of linear structural systems which says that a system is linear if its deformations due to two separate load cases can be combined to yield the deformation due to those two loads combined.

$$\left[\boldsymbol{\Phi}\right]_{(r)} = \left[\vec{\phi}_1\,,\,\vec{\phi}_2\,,\,...,\,\vec{\phi}_P\right] \qquad \text{and} \qquad \vec{\boldsymbol{q}}_{(r)}\left(t\right) = \begin{pmatrix} q_1\left(t\right) \\ q_2\left(t\right) \\ \vdots \\ q_P\left(t\right) \end{pmatrix}$$

In this system, all eigenmode shape vectors comply with the orthogonality relation:

$$\left[\boldsymbol{\Phi}\right]_{(r)}^{T}\left[\boldsymbol{m}\right]\left[\boldsymbol{\Phi}\right]_{(r)} = \lceil \boldsymbol{M} \rfloor_{(r)} = \begin{bmatrix} M_1 & & & & \\ & M_2 & & & \\ & & \ddots & & \\ & & & & M_P \end{bmatrix} \tag{2.14}$$

$$\left[\boldsymbol{\Phi}\right]_{(r)}^{T}\left[\boldsymbol{k}\right]\left[\boldsymbol{\Phi}\right]_{(r)} = \left\lceil \left(\boldsymbol{M}\boldsymbol{\omega}^{\boldsymbol{2}}\right) \right\rfloor_{(r)} = \lceil \boldsymbol{K} \rfloor_{(r)} = \begin{bmatrix} K_1 & & & & \\ & K_2 & & & \\ & & \ddots & & \\ & & & & K_P \end{bmatrix} \tag{2.15}$$

The elements of $\lceil \boldsymbol{M} \rfloor_{(r)}$ represent the generalized masses and the elements of $\lceil \boldsymbol{K} \rfloor_{(r)}$ represent the generalized stiffnesses for all eigenmodes r.

The scale of the solution of the undamped discretized equation of motion (2.9) is ambiguous:

$$\begin{aligned} &\left(\left[\boldsymbol{k}\right] - \omega_r^2\left[\boldsymbol{m}\right]\right) \cdot \hat{\vec{\boldsymbol{\phi}}}_r \cdot \mathrm{e}^{j\omega_r t} = 0 \\ \Rightarrow\ &\left(\left[\boldsymbol{k}\right] - \omega_r^2\left[\boldsymbol{m}\right]\right) \cdot x \cdot \hat{\vec{\boldsymbol{\phi}}}_r \cdot \mathrm{e}^{j\omega_r t} = x \cdot 0 \qquad \text{where} \quad \{x \in \mathbb{C}\} \end{aligned} \tag{2.16}$$

Equation (2.16) shows that eigenmodes can be scaled with any number still returning a solution to the homogeneous equation of motion. To still be able to compare different eigensolutions, it is customary to scale the eigenmode shapes so that either the generalized mass of the eigenmode shape is 1, or the generalized stiffness. This results in either $\lceil \boldsymbol{M} \rfloor_{(r)} = \lceil \boldsymbol{1} \rfloor$ or $\lceil \boldsymbol{K} \rfloor_{(r)} = \lceil \boldsymbol{1} \rfloor$.

2.2.3. Crucial Aspects of Structural Dynamics of Turbomachines

Structural damping, the solution of the particular part of the equation of motion, the concept of generalized external forces and the change of the stiffness properties due to external influences for real turbomachinery rotors are important aspects of structural dynamics. Therefore, they are introduced in a brief manner, here.

2.2.3.1. Structural Damping

When simplifying equation (2.8) to equation (2.9) by omitting the damping part for real structures, an error is introduced into the solution. However, if the material damping and other structural damping (friction) is explicitly known, it can be modeled with modern finite element solvers. Depending on the formulation of the material or friction damping model, this will influence the eigenfrequencies and eigenmode shapes of the eigensolution.

The introduction of material damping into a finite element equation system is a field of ongoing research. Depending on the type of material (metal, carbon / glass fiber, plastic, wood) and the different material connections (bolting, welding, gluing, form fitting), different damping models might be employed.

For the research carried out for this thesis, material damping was always considered to be zero. This introduces errors into the results, but is justifiable for three reasons: For

one, the material damping of metallic materials is very small and the material damping of carbon fiber (while considerably larger than that of metal) was observed to be small compared to other influencing factors (blade shape). The second reason is the ongoing trend in turbomachines towards integral parts (blisks) without friction contacts and explicit dampers, which is expected to continue in the future. This is mainly due to the fact that friction dampers and snubbers increase the weight of the gas turbine, so they are omitted whenever possible. Thirdly, small amounts of material damping will not influence the overall eigenmode shapes and eigenfrequencies much.

For preliminary design methods where many other uncertainties exist, a minute frequency and shape uncertainty will not invalidate the overall result, and consequently the omission of structural damping is permissible.

2.2.3.2. Particular Solution and Generalized Forces

The reason behind the solution of the homogeneous part of the discretized equation of motion is almost exclusively to determine the solution of the particular part of the equation of motion with a certain forcing function. Again, using the orthogonality relation, it is possible to determine the influence of a given forcing on the different eigensolutions.

If equation (2.7) (without structural damping) is pre-multiplied with the transpose of the modal matrix, it can then be rewritten as:

$$\begin{aligned}
&\left[\boldsymbol{\Phi}\right]_{(r)}^{T}\left[\boldsymbol{m}\right]\ddot{\vec{\boldsymbol{w}}}\left(t\right)+\left[\boldsymbol{\Phi}\right]_{(r)}^{T}\left[\boldsymbol{k}\right]\vec{\boldsymbol{w}}\left(t\right)=\left[\boldsymbol{\Phi}\right]_{(r)}^{T}\vec{\boldsymbol{f}}\left(t\right)\\
\Rightarrow&\left[\boldsymbol{\Phi}\right]_{(r)}^{T}\left[\boldsymbol{m}\right]\left[\boldsymbol{\Phi}\right]_{(r)}\ddot{\vec{\boldsymbol{q}}}_{(r)}\left(t\right)+\left[\boldsymbol{\Phi}\right]_{(r)}^{T}\left[\boldsymbol{k}\right]\left[\boldsymbol{\Phi}\right]_{(r)}\vec{\boldsymbol{q}}_{(r)}\left(t\right)=\left[\boldsymbol{\Phi}\right]_{(r)}^{T}\vec{\boldsymbol{f}}\left(t\right)\\
\Rightarrow&\lceil\boldsymbol{M}\rfloor_{(r)}\ddot{\vec{\boldsymbol{q}}}_{(r)}\left(t\right)+\lceil\boldsymbol{K}\rfloor_{(r)}\vec{\boldsymbol{q}}_{(r)}\left(t\right)=\left[\boldsymbol{\Phi}\right]_{(r)}^{T}\vec{\boldsymbol{f}}\left(t\right)\qquad\text{where}\quad\left\{r=1,\,2,\,...,\,P\right\}
\end{aligned}\tag{2.17}$$

Since both $\lceil\boldsymbol{M}\rfloor_{(r)}$ and $\lceil\boldsymbol{K}\rfloor_{(r)}$ are matrices with their only entries on the diagonal (orthogonality relation), the result is a set of P (number of degrees of freedom of the system) independent equations.

The right hand side of equation (2.17) alone is called the generalized external force vector:

$$\vec{\boldsymbol{F}}_{(r)}\left(t\right)=\left[\boldsymbol{\Phi}\right]_{(r)}^{T}\vec{\boldsymbol{f}}\left(t\right)\qquad\text{where}\quad\left\{r=1,\,2,\,...,\,P\right\}\tag{2.18}$$

Since $\vec{\boldsymbol{F}}_{(r)}\left(t\right)$ in equation (2.18) is a vector of single values, one for each separate eigenmode shape $\vec{\boldsymbol{\phi}}_r$ and eigenfrequency ω_r, this generalized force vector can easily be used to determine the damping or excitation impact of a given external force $\vec{\boldsymbol{f}}(t)$ on the respective eigenmode shape $\vec{\boldsymbol{\phi}}_r$.

2.2.3.3. Influences on the Stiffness of the Structure

The discretized homogeneous equation of motion (2.8) can be solved with any finite element program capable of numerical modal analysis. It is important to note that the stiffness $\left[\boldsymbol{k}\right]$ is dependent on the inertial load (rotation of a rotor) and the blade surface aerodynamic loading (or any other external load). Both inertia and aerodynamics lead to a deformation which might bend, twist or untwist the blade. The stiffness has to be treated therefore as (see Kemme [95]):

$$\left[\boldsymbol{k}\right]=\left[\boldsymbol{k}\right]_{linear}+\left[\boldsymbol{k}\right]_{inertial}+\left[\boldsymbol{k}\right]_{geometric}\tag{2.19}$$

For most numerical modal analyses it is therefore imperative to perform a loads analysis first and retain its impact on the stiffness before starting the eigenmode analysis.

2.2.4. Symmetry Considerations

Turbomachinery blade rows are in general cyclically symmetrical (see figure 2.1). Real structures are never perfectly symmetrical due to manufacturing tolerances, wear or material imperfections. This phenomenon is called mistuning in turbomachinery and a separation between structural and aerodynamic mistuning is made. Structural mistuning is due to the impact of the geometric and material differences between sectors on the eigenbehavior of the turbomachinery stage. Aerodynamic mistuning is concerned with the flow differences between different passages due to differences of the blades' geometries. See for example Malzacher et al. [112] for an experimental investigation into aerodynamic mistuning.

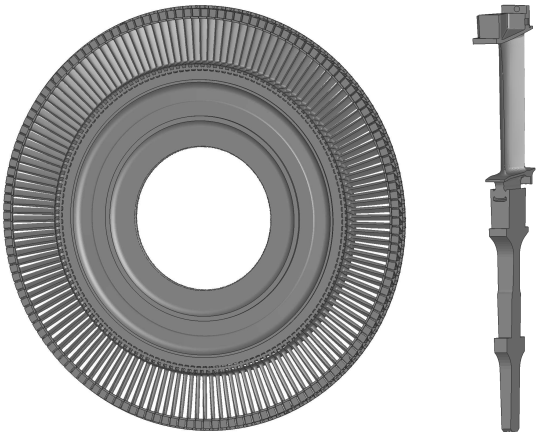

Figure 2.1.: Full turbine bladed disk with 146 blades and one cyclically symmetrical sector of it.

There are two main conflicting research results concerning mistuning in general acknowledged in the community. On the one hand, it is agreed upon that mistuning has a stabilizing effect on cases with flutter problems (first published by Kaza & Kielb [94], more recently by Corral et al. [39] or Gross & Krack [70]). On the other hand, mistuning has been observed to increase the LCO amplitudes of individual blades of forced response cases considerably which is undesirable. Even though it has been proven that this can be avoided and even be used to decrease the maximum forced response amplitude (see e.g. Hohl & Wallaschek [83] and Willeke et al. [194]), this is not used by engine manufacturers, yet. This is due to the increase in complexity this would introduce into the blade selection process which is already tedious due to balancing considerations or the manufacturing tolerances required for machining an intentionally mistuned blisk.

Consequently, for preliminary design almost exclusively perfectly tuned systems or alternating mistuning patterns are assumed. This leads to simplifications in the numerical analysis and introduces the theoretical background for the observed traveling waves.

2.2.4.1. From a Complete Rotor to a Sector

If one assumes the finite element model of each rotor sector to be identical, the mass and stiffness matrices will be block-diagonally similar:

$$
[\boldsymbol{m}]_{rotor} = \begin{bmatrix}
[\boldsymbol{m}]_1 & [\boldsymbol{m}]_{1;2} & [\boldsymbol{0}] & \cdots & [\boldsymbol{0}] & [\boldsymbol{m}]_{1;N} \\
[\boldsymbol{m}]_{2;1} & [\boldsymbol{m}]_2 & [\boldsymbol{m}]_{2;3} & [\boldsymbol{0}] & \cdots & [\boldsymbol{0}] \\
[\boldsymbol{0}] & [\boldsymbol{m}]_{3;2} & [\boldsymbol{m}]_3 & [\boldsymbol{m}]_{3;4} & [\boldsymbol{0}] & \cdots \; [\boldsymbol{0}] \\
\vdots & & \ddots & \ddots & & \vdots \\
[\boldsymbol{0}] & \cdots & [\boldsymbol{0}] & [\boldsymbol{m}]_{(N-1);(N-2)} & [\boldsymbol{m}]_{(N-1)} & [\boldsymbol{m}]_{(N-1);N} \\
[\boldsymbol{m}]_{N;1} & [\boldsymbol{0}] & \cdots & [\boldsymbol{0}] & [\boldsymbol{m}]_{N;(N-1)} & [\boldsymbol{m}]_N
\end{bmatrix}
$$

$$
[\boldsymbol{k}]_{rotor} = \begin{bmatrix}
[\boldsymbol{k}]_1 & [\boldsymbol{k}]_{1;2} & [\boldsymbol{0}] & \cdots & [\boldsymbol{0}] & [\boldsymbol{k}]_{1;N} \\
[\boldsymbol{k}]_{2;1} & [\boldsymbol{k}]_2 & [\boldsymbol{k}]_{2;3} & [\boldsymbol{0}] & \cdots & [\boldsymbol{0}] \\
[\boldsymbol{0}] & [\boldsymbol{k}]_{3;2} & [\boldsymbol{k}]_3 & [\boldsymbol{k}]_{3;4} & [\boldsymbol{0}] & \cdots \; [\boldsymbol{0}] \\
\vdots & & \ddots & \ddots & & \vdots \\
[\boldsymbol{0}] & \cdots & [\boldsymbol{0}] & [\boldsymbol{k}]_{(N-1);(N-2)} & [\boldsymbol{k}]_{(N-1)} & [\boldsymbol{k}]_{(N-1);N} \\
[\boldsymbol{k}]_{N;1} & [\boldsymbol{0}] & \cdots & [\boldsymbol{0}] & [\boldsymbol{k}]_{N;(N-1)} & [\boldsymbol{k}]_N
\end{bmatrix}
$$

with N = number of symmetrical sectors (2.20)

In equation 2.20, the submatrices $[\boldsymbol{m}]_x$ and $[\boldsymbol{k}]_x$ with one subscript denote the influence of the sector on itself and the submatrices $[\boldsymbol{m}]_{x;y}$ and $[\boldsymbol{k}]_{x;y}$ denote the influence of the adjacent sectors on each sector. For identical sector models, all submatrices $[\boldsymbol{m}]_x$ are identical. The same applies for $[\boldsymbol{k}]_x$, $[\boldsymbol{m}]_{x;y}$ and $[\boldsymbol{k}]_{x;y}$, respectively.

Together with the knowledge that the deformation at the cyclic boundary needs to be equal or have a certain cyclic relation dependent on the number of sectors, the problem can be reduced to one treating only one sector of the rotor. Since the size of the matrices $[\boldsymbol{m}]$ and $[\boldsymbol{k}]$ scales squarely with the number of contained elements, the solution effort drops by a factor of $\frac{1}{N^2}$. For the example turbine rotor in figure 2.1 with 146 blades, this would result in a problem $\frac{1}{146^2} = 0.000046913 = 5 \cdot 10^{-5}$ times smaller than the full rotor. Although an FE solution is comparatively cheap with current computational resources, this is substantial. Even for fans with comparatively low blade numbers (e.g. $N = 10, \rightarrow \frac{1}{10^2} = 0.01 = 1 \cdot 10^{-2}$) the savings are obvious with mesh generation only slightly more expensive since the symmetry surface needs to be meshed identically.

To determine all eigensolutions, all possible boundary conditions at the symmetry surfaces need to be considered. The phase shift of the node's deformations at the sector symmetry boundaries can be determined to be:

$$
\sigma_n = n \cdot \frac{2\pi}{N} \qquad \text{with} \quad \left\{ n \mid -\frac{N}{2} < n \leq \frac{N}{2} \right\}_{\mathbb{N}} \tag{2.21}
$$

This phase shift of the harmonic oscillation between neighboring blades is called the inter-blade phase angle σ_n (IBPA). For all $(\sigma_n \neq 0.0) \wedge (\sigma_n \neq \pi)$ the solutions of positive and negative σ_n are combined into one complex linear equation system and result in the simultaneous solution of $\vec{\boldsymbol{\phi}}_{\sigma_n}$ and $\vec{\boldsymbol{\phi}}_{\sigma_{-n}}$. These complex equation systems in turn have not only P solutions, but $2 \cdot P$, with each eigenvalue returning two eigenmode shapes (one for n and one for $-n$). Consequently, $\frac{N+1}{2}$ (for odd N) or $\frac{N+2}{2}$ (for even N) finite element solutions need to be computed to determine the behavior of the complete turbomachinery stage.

In figures 2.2a and 2.2b, the first eigenmode shapes resulting from a computation with finite element cyclic symmetry boundary condition $\sigma_1 = \frac{2\pi}{10}$ and $\sigma_{-1} = -\frac{2\pi}{10}$ are visualized. The straight line with zero deformation in the eigenmode shape plot shows immediately why the number n is called the "nodal diameter".

Depending on necessity and use case, the modal equation of motion (equation (2.17)) can be re-expanded from single sector to full annulus form.

2.2.4.2. Traveling Wave Formulation

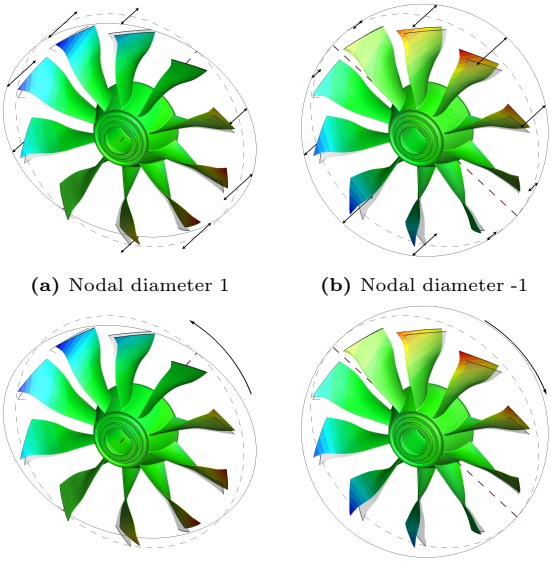

(a) Nodal diameter 1 **(b)** Nodal diameter -1

(c) Traveling wave 1 **(d)** Traveling wave -1

Figure 2.2.: Nodal diameter ± 1 and traveling wave ± 1 eigenmode shapes of the first blade bending eigenmode shape family of a 10 blade blisk.

In chapter 2.2.4.1, the concept of cyclic symmetry and its impact on the eigensolution was introduced. One consequence of the cyclic symmetry was the occurrence of double eigenvalues with two eigenmode shapes $\vec{\tilde{\boldsymbol{\phi}}}_{\sigma_n}$ and $\vec{\tilde{\boldsymbol{\phi}}}_{\sigma_{-n}}$ with the same eigenfrequency ω_n. For these eigenmode shapes, it is possible to show:

$$\begin{aligned} &\left(\left[\boldsymbol{k}\right] - \omega_n^2 \left[\boldsymbol{m}\right]\right) \cdot \vec{\tilde{\boldsymbol{\phi}}}_{\sigma_n} \cdot \mathrm{e}^{j\omega_n t} = 0 \\ &\left(\left[\boldsymbol{k}\right] - \omega_n^2 \left[\boldsymbol{m}\right]\right) \cdot \vec{\tilde{\boldsymbol{\phi}}}_{\sigma_{-n}} \cdot \mathrm{e}^{j\omega_n t} = 0 \\ \Rightarrow &\left(\left[\boldsymbol{k}\right] - \omega_n^2 \left[\boldsymbol{m}\right]\right) \left(x \cdot \vec{\tilde{\boldsymbol{\phi}}}_{\sigma_n} + y \cdot \vec{\tilde{\boldsymbol{\phi}}}_{\sigma_{-n}}\right) \cdot \mathrm{e}^{j\omega_n t} = 0 \qquad \text{where} \quad \{x, y \in \mathbb{C}\} \end{aligned} \tag{2.22}$$

This means that any combination of eigenmode shapes with the same eigenfrequency ω is also a solution to the eigenvalue problem. To exactly reproduce the boundary conditions σ_n imposed during the cyclic symmetry eigenvalue analysis, one can postulate:

$$\begin{aligned} \vec{\tilde{\boldsymbol{\psi}}}_{\sigma_n} &= \frac{1}{\sqrt{2}} \left(\vec{\tilde{\boldsymbol{\phi}}}_{\sigma_n} + j\vec{\tilde{\boldsymbol{\phi}}}_{\sigma_{-n}}\right) \\ \vec{\tilde{\boldsymbol{\psi}}}_{\sigma_{-n}} &= \frac{1}{\sqrt{2}} \left(\vec{\tilde{\boldsymbol{\phi}}}_{\sigma_n} - j\vec{\tilde{\boldsymbol{\phi}}}_{\sigma_{-n}}\right) \end{aligned} \tag{2.23}$$

The result will be eigenmode shapes which do not oscillate about their nodal diameter, but where the maximum oscillation seemingly travels about the symmetry axis of the rotor. The traveling wave eigenmode shape $\vec{\psi}_{\sigma_n}$ will look identical to the eye, but travel around the rotor in the opposite direction as $\vec{\psi}_{\sigma_{-n}}$. This is why the numbers designating the eigenmode shapes n, $-n$ for both $\vec{\phi}$ and $\vec{\psi}$ are the same number (namely the number of visible nodal diameters).

Figure 2.2 illustrates the relation between nodal diameter mode shapes and traveling wave mode shapes for $n = 1$ for an example blisk rotor with 10 blades. The two top figures 2.2a and 2.2b show the purely real eigenmode shapes with nodal diameters. The nodal diameters are indicated by dashed brown lines. The arrows above the blades indicate the maximum deformation of each blade. The related traveling wave mode shapes are illustrated in the two bottom figures 2.2c and 2.2d. For them, the sine wave above the blades indicates a deformation pattern traveling around the circumference of the rotor in the direction indicated by the arrows. For the definition of positive and negative IBPA σ_n and traveling wave number see chapter A.1 in the appendix. This is handled differently in the community and the conventions at DLR are presented. Also in the appendix, figure A.3 illustrates the rest of the possible nodal diameters and traveling waves of the first blade bending eigenmode shape family for a 10 blade example rotor.

If it is postulated that the eigenmode shapes for traveling waves with nodal diameter $n = 0$ and (for cases with even blade number) $n = \frac{N}{2}$ remain unchanged: $\vec{\psi}_0 = \vec{\phi}_0$ and $\vec{\psi}_{\frac{N}{2}} = \vec{\phi}_{\frac{N}{2}}$, the matrices for generalized mass and stiffness for the traveling wave modes can be created:

$$\left[\boldsymbol{\Psi}\right]_{(r)}^{H}\left[\boldsymbol{m}\right]\left[\boldsymbol{\Psi}\right]_{(r)} = \lceil \boldsymbol{M}_{\boldsymbol{\Psi}} \rfloor_{(r)} = \begin{bmatrix} M_{\psi_1} & & & \\ & M_{\psi_2} & & \\ & & \ddots & \\ & & & M_{\psi_P} \end{bmatrix}_i \tag{2.24}$$

$$\left[\boldsymbol{\Psi}\right]_{(r)}^{H}\left[\boldsymbol{k}\right]\left[\boldsymbol{\Psi}\right]_{(r)} = \left\lceil \left(\boldsymbol{M}_{\boldsymbol{\Psi}}\boldsymbol{\omega}^{\boldsymbol{2}}\right)_{(r)} \right\rfloor = \lceil \boldsymbol{K}_{\boldsymbol{\Psi}} \rfloor_{(r)} = \begin{bmatrix} K_{\psi_1} & & & \\ & K_{\psi_2} & & \\ & & \ddots & \\ & & & K_{\psi_P} \end{bmatrix}_i \tag{2.25}$$

The superscript ^{H} denotes the conjugate transpose (transpose with negative imaginary part) of a complex vector or matrix.

Based on this, the generalized equation of motion without structural damping (equation (2.17)) can be rewritten in traveling wave coordinates:

$$\begin{aligned} &\lceil \boldsymbol{M}_{\boldsymbol{\Psi}} \rfloor_{(r)} \ddot{\vec{\boldsymbol{q}}}_{\Psi\ (r)}(t) + \lceil \boldsymbol{K}_{\boldsymbol{\Psi}} \rfloor_{(r)}\, \vec{\boldsymbol{q}}_{\Psi\ (r)}(t) = \left[\boldsymbol{\Psi}\right]_{(r)}^{H} \vec{\boldsymbol{f}}(t) \\ &\qquad \text{with} \quad \{r = 1,\ 2,\ ...,\ P\} \end{aligned} \tag{2.26}$$

In equation (2.26), $\vec{\boldsymbol{q}}_{\Psi}$ are the generalized coordinates in traveling wave form.
The following assumptions are implicitly made:

- The eigenmode shapes $\vec{\phi}_r$ are all normalized in the same way.
- The mass and stiffness matrices are symmetrical.
- The traveling wave eigenmode shapes are created according to equation (2.23).

Based on these assumptions it is possible to show (insert equation (2.23) into one line of equation (2.24)):

$$\begin{aligned} M_{\psi\ \sigma_n} &= \vec{\boldsymbol{\psi}}_{\sigma_n}^{H} \cdot [\boldsymbol{m}] \cdot \vec{\boldsymbol{\psi}}_{\sigma_n} \\ &= \frac{1}{\sqrt{2}} \left(\vec{\boldsymbol{\phi}}_{\sigma_n} + j\vec{\boldsymbol{\phi}}_{\sigma_{-n}} \right)^{H} \cdot [\boldsymbol{m}] \cdot \frac{1}{\sqrt{2}} \left(\vec{\boldsymbol{\phi}}_{\sigma_n} + j\vec{\boldsymbol{\phi}}_{\sigma_{-n}} \right) \\ &= 0.5 \cdot \left(M_{\phi\ \sigma_n} + M_{\phi\ \sigma_{-n}} \right) \\ &= M_{\phi\ \sigma_n} \end{aligned} \tag{2.27}$$

The same proof holds for all $M_{\psi\ \sigma_{-n}}$ and all generalized stiffnesses and leads to the very convenient result that the generalized mass and generalized stiffness matrices for nodal diameter mode shapes and traveling wave mode shapes are essentially the same (if the three assumptions above are followed and the places of the generalized masses and stiffnesses of given σ_n and σ_{-n} in the matrices $\lceil \boldsymbol{M} \rfloor$ and $\lceil \boldsymbol{K} \rfloor$ do not change during the conversion from nodal diameters to traveling waves).

$$\lceil \boldsymbol{M}_{\boldsymbol{\Psi}} \rfloor_{(r)} = \lceil \boldsymbol{M} \rfloor_{(r)} \qquad \text{and} \qquad \lceil \boldsymbol{K}_{\boldsymbol{\Psi}} \rfloor_{(r)} = \lceil \boldsymbol{K} \rfloor_{(r)} \tag{2.28}$$

2.3. Interaction of Fluid and Structure in Turbomachines

In chapter 2.2, the equation of motion was introduced and subsequently simplified and discretized to analyze the structure of a turbomachinery part without external influences or connection to a fluid. If one considers the fluid flow and the structural parts of a turbomachinery stage not separately from each other but combined, the equation of motion can be rewritten to contain the properties of structure **and** fluid.

This leads to the "aeroelastic" equation of motion:

$$\left(m_{st}+m_{fl}\right)\ddot{\vec{x}}\left(t\right)+\left(d_{st}+d_{fl}\right)\dot{\vec{x}}\left(t\right)+\left(k_{st}+k_{fl}\right)\vec{x}\left(t\right)=\vec{f}_{st}\left(t\right)+\vec{f}_{fl}\left(t\right) \tag{2.29}$$

The different terms in equation (2.29) are:

m_{st} = mass of the structure
m_{fl} = mass of the fluid interacting with the structure
d_{st} = material and friction damping of the structure
d_{fl} = fluid damping
k_{st} = stiffness of the structure
k_{fl} = stiffness of the fluid interacting with the structure
$\vec{f}_{st}\left(t\right)$ = external structural forces (inertia, vibrations...)
$\vec{f}_{fl}\left(t\right)$ = external aerodynamic forces (wakes, potential fields, gusts...)

2.3.1. Simplifications for Turbomachinery Aeroelasticity

Starting from the left, there are terms in the aeroelastic equation of motion (2.29), which can be omitted for special cases. Doing so leads to a form which can be solved numerically with the introduction of a minimal error.

For traditional turbomachinery components the structural mass is much higher than the mass of the fluid interacting with it. Schuff & Chenaux [155] have shown that this assumption reaches its limits for modern fan blades, but for a fast stability estimation in a preliminary design process it is still deemed applicable.

$$m_{fl}\approx 0$$

In chapter 2.2.3.1, the reasons for assuming negligible structural damping for turbomachinery parts were introduced. These reasons apply to the aeroelastic equation of motion, as well.

$$d_{st}\approx 0$$

The stiffness of a fluid is considered very small in comparison to the structural stiffness.

$$k_{st}\gg k_{fl}\approx 0$$

For airplane wings, research is being carried out concerning the intentional introduction of external structural forces (control surface deflection) to mitigate aeroelastic problems. This kind of influence would be very difficult to accomplish for turbomachinery blades. Additionally, external vibrations introduced unintentionally into turbomachines are to be avoided at all cost to preserve bearing life. Therefore, no external structural forces are assumed.

$$\vec{f}_{st}\left(t\right)\approx 0$$

This reduces equation (2.29) to the following form:

$$m_{st}\ddot{\vec{x}}\left(t\right)+d_{fl}\dot{\vec{x}}\left(t\right)+k_{st}\vec{x}\left(t\right)=\vec{f}_{fl}\left(t\right) \tag{2.30}$$

This is the general reduced aeroelastic equation of motion. It is used to determine the aeroelastic stability of a turbomachinery part.

Comparison to the Purely Structural Equation of Motion

In chapter 2.2.1, a distinction was made between the homogeneous solution of a differential equation ($RHS = 0$) and the particular solution. The solution of the homogeneous part of the differential equation was termed a "stability" problem. The solution of the particular problem is a "forcing" problem.

From equation (2.30), one can now easily see why there is a distinction made between "flutter" and "forced response" (see chapter 1.3) in aeroelastic analysis.

Flutter is the problem arising if the solution of the homogeneous part of the aeroelastic equation of motion without external forces predicts a self-excited exponentially growing vibration (stability problem with $d_{fluid} < 0$, a.k.a. aerodynamic excitation).

Forced Response is the problem arising if there are periodically occurring external aerodynamic forces which necessitate the solution of the particular part of the aeroelastic equation of motion (forcing problem with $\vec{f}_{fl}(t) \neq 0$).

In principle, this is the distinction Crawley [44] makes between disturbance forces (forced response) and motion dependent aerodynamic forces (flutter).

In chapter 1.3, a third category of aeroelastic phenomena (flow instability induced vibrations) was mentioned. The two possible approaches to the solution of the aeroelastic equation of motion (2.30) leave no third option which explains, why there is no clear position in the community about flow induced vibrations. Some argue, these phenomena belong to the aeroelastic stability problem, some are of the opinion that these phenomena are separate and merit their own term.

2.3.2. The Aeroelastic Stability Equation

In chapter 1.5, it was stated that aerodynamic forcing is already being treated successfully in preliminary design via Campbell diagram analysis. The main focus of this thesis is therefore the homogeneous part of the aeroelastic equation of motion (2.30):

$$m_{st}\ddot{\vec{x}}(t) + d_{fl}\dot{\vec{x}}(t) + k_{st}\vec{x}(t) = 0 \tag{2.31}$$

This immediately leads to the conclusion that the problem can be rewritten as:

$$m_{st}\ddot{\vec{x}}(t) + k_{st}\vec{x}(t) = -d_{fl}\dot{\vec{x}}(t) \tag{2.32}$$

Shifting the focus, the integral problem of fluid and structure can be re-separated. The fluid is only able to dampen the structure by acting via pressure on the surface. Hence, the aeroelastic stability problem can be rewritten as a structural forcing problem with the forcing on the blade surface being dependent on the blade motion itself:

$$m_{st}\ddot{\vec{x}}(t) + k_{st}\vec{x}(t) = \vec{f}_{fl}\left(\dot{\vec{x}}, t\right) \tag{2.33}$$

This differential equation is considered the most general description of the flutter problem in turbomachinery. To solve it, it needs to be discretized for the appropriate geometry and additional simplifications might be introduced in the process.

2.3.3. Advantage of the Traveling Wave Formulation for Turbomachinery Aeroelasticity

In chapter 2.2.4.2, the traveling wave formulation for cyclically symmetrical structures was introduced. The main reason for this was the theoretical background on cyclic symmetry boundary conditions.

In 1956, Lane [103] published his discovery that flutter in turbomachines occurs in "traveling" wave patterns, as well. He observed that neighboring blades oscillated with a certain

phase shift and as a result the deformation looked like a wave racing around the rotor. Since then, this discovery has been corroborated.

The consequence of this discovery for turbomachinery aeroelasticity is obvious:

- The discretized equation of motion in traveling wave form (equation 2.26) has to be used when trying to solve the reduced aeroelastic equation of motion 2.33.
- The IBPA σ_n has to be introduced into the aerodynamic equations, as well.

Consequently, cyclic symmetry boundary conditions might be introduced into the aerodynamic equations used to determine the aerodynamic force on the blade surface $\vec{f}_{fl}\left(\dot{\vec{x}}, t\right)$. This can be used to reduce the numerical effort of the aerodynamic computations.

2.3.4. Determination of the Generalized Aerodynamic Forces

In chapter 2.2.4.2, the discretized equation of motion of a structure in traveling wave coordinates was introduced as:

$$\begin{aligned} &\lceil \boldsymbol{M}_{\boldsymbol{\Psi}} \rfloor_{(r)} \ddot{\vec{\boldsymbol{q}}}_{\Psi\ (r)}(t) + \lceil \boldsymbol{K}_{\boldsymbol{\Psi}} \rfloor_{(r)}\, \vec{\boldsymbol{q}}_{\Psi\ (r)}(t) = \left[\boldsymbol{\Psi}\right]^{H}_{(r)} \vec{\boldsymbol{f}}(t) \\ &\text{with} \quad \{r = 1,\, 2,\, ...,\, P\} \end{aligned} \tag{2.26}$$

On the right hand side of equation (2.26), the generalized external forces in traveling wave form are given. To compute the generalized aerodynamic forces, the eigenmode shapes are multiplied with the forces acting on the blade surface. Assuming that the aerodynamic forces are harmonic with a given angular frequency ω, the generalized external aerodynamic forces are oscillating with that frequency, as well:

$$\left[\boldsymbol{\Psi}\right]^{H}_{(r)} \vec{\boldsymbol{f}}(t) = \vec{\boldsymbol{F}}_{\Psi}(t) = \hat{\vec{\boldsymbol{F}}}_{\boldsymbol{\Psi}} \cdot \mathrm{e}^{j\omega t} = \begin{bmatrix} \frac{\hat{F}_1}{\hat{q}_1} & & & \\ & \frac{\hat{F}_2}{\hat{q}_2} & & \\ & & \ddots & \\ & & & \frac{\hat{F}_P}{\hat{q}_P} \end{bmatrix} \cdot \tilde{\vec{\boldsymbol{q}}}_{\Psi\ (r)} \cdot \mathrm{e}^{j\omega t} = \left\lceil \boldsymbol{C}_{\boldsymbol{\Psi}\ (\boldsymbol{r})} \right\rfloor \cdot \tilde{\vec{\boldsymbol{q}}}_{\Psi\ (r)} \cdot \mathrm{e}^{j\omega t} \tag{2.34}$$

The generalized aerodynamic force can also be represented by generalized aerodynamic coefficients multiplied by the generalized coordinates $\tilde{\vec{\boldsymbol{q}}}_{\Psi\ (r)}$. In equation (2.34), the aerodynamic influence coefficient matrix $\left\lceil \boldsymbol{C}_{\boldsymbol{\Psi}\ (\boldsymbol{r})} \right\rfloor$ contains the generalized aerodynamic forces $\hat{F}_r$ for each eigenmode shape normalized by the size of the eigenmode shape at which they were calculated $\hat{q}_r$. Note that $\left\lceil \boldsymbol{C}_{\boldsymbol{\Psi}\ (\boldsymbol{r})} \right\rfloor$ is not non-dimensionalized by the blade area and the dynamic pressure. This would be the standard approach (see Kemme [95] and May [116]), but bloats the following equations unnecessarily. Both Kemme and May compute the generalized aerodynamic force diagonal elements of $\left\lceil \boldsymbol{C}_{\boldsymbol{\Psi}\ (\boldsymbol{r})} \right\rfloor$ as:

$$\hat{F}_r = -\oint_A \tilde{\vec{\boldsymbol{\psi}}}_r^{H} \left(\hat{p}_{\vec{\boldsymbol{\psi}}_r} \cdot \vec{\boldsymbol{n}} + p \cdot \hat{\vec{\boldsymbol{n}}}_{\vec{\boldsymbol{\psi}}_r} \right) dA \tag{2.35}$$

Here, the generalized aerodynamic force is dependent on the traveling wave mode shape $\vec{\boldsymbol{\psi}}_r$. Therefore, it is calculated as integral value over the surface area of the blade of the traveling mode shape multiplied with the normal pressure on the surface. Since both the pressure on the surface and the normal vector are dependent on the blade deformation vector $\vec{\boldsymbol{\psi}}_r$, both the alternating normal pressure due to the pressure fluctuation $\hat{p}_{\vec{\boldsymbol{\psi}}_r} \cdot \vec{\boldsymbol{n}}$ and the additional part of the alternating normal pressure due to the change in normal direction $p \cdot \hat{\vec{\boldsymbol{n}}}_{\vec{\boldsymbol{\psi}}_r}$ need to be accounted for.

2.3.5. Generalized Flutter Stability Equation and Energy Method

In preliminary design, no detailed investigation of the aeroelastic properties of a design is desired. The only information required is generally if the eigenfrequencies and their respective eigenmode shapes are stable in the design operating range of the turbomachine, or not. Hence, the global aeroelastic stability equation will be introduced and immediately simplified to determine the aeroelastic stability for the most common critical cases.

If equation (2.35) is introduced into equation (2.26), the flutter stability equations in generalized traveling wave coordinates are found:

$$\begin{aligned} &\left\lceil \boldsymbol{M}_{\boldsymbol{\Psi}\ (\boldsymbol{r})} \right\rfloor \ddot{\vec{\boldsymbol{q}}}_{\Psi\ (r)}(t) + \left\lceil \boldsymbol{K}_{\boldsymbol{\Psi}\ (\boldsymbol{r})} \right\rfloor \vec{\boldsymbol{q}}_{\Psi\ (r)}(t) = \left\lceil \boldsymbol{C}_{\boldsymbol{\Psi}\ (\boldsymbol{r})} \right\rfloor \hat{\vec{\boldsymbol{q}}}_{\Psi\ (r)} \cdot \mathrm{e}^{j\omega t} \\ &\qquad \text{with} \quad \{r = 1,\, 2,\, ...,\, P\} \end{aligned} \tag{2.36}$$

With the assumption of harmonic vibration, the time dependency in equation (2.36) can be eliminated:

$$\vec{\boldsymbol{q}}_{\Psi\ (r)}(t) = \hat{\vec{\boldsymbol{q}}}_{\Psi\ (r)} \cdot \mathrm{e}^{j\omega t} \tag{2.37}$$

$$\begin{aligned} \Rightarrow \left(-\omega^2 \left\lceil \boldsymbol{M}_{\boldsymbol{\Psi}\ (\boldsymbol{r})} \right\rfloor + \left\lceil \boldsymbol{K}_{\boldsymbol{\Psi}\ (\boldsymbol{r})} \right\rfloor - \left\lceil \boldsymbol{C}_{\boldsymbol{\Psi}\ (\boldsymbol{r})} \right\rfloor\right) \cdot \hat{\vec{\boldsymbol{q}}}_{\Psi\ (r)} = 0 \\ \text{with} \quad \{r = 1,\, 2,\, ...,\, P\} \end{aligned} \tag{2.38}$$

In chapter 2.2.1, the theoretical solution to such an equation system was given in equation (2.6). This approach has to be used if the damping introduced by $\left\lceil \boldsymbol{C}_{\boldsymbol{\Psi}\ (\boldsymbol{r})} \right\rfloor$ is significant and leads to eigenfrequencies and eigenmode shapes which are different from the original undamped eigenfrequencies and eigenmode shapes. Schuff & Chenaux [155] have shown that this is becoming more and more necessary for modern rotor designs.

However, for a first flutter susceptibility evaluation in a preliminary design study, one might still consider the system lightly damped, with no impact on the original eigendeformation and eigenfrequencies. Then, flutter is a vibration in exactly one undamped structural eigenmode shape and the "energy method" can be used. Carta [32] first used the energy transferred between blade and fluid as a measure for the aeroelastic stability of a flow case. He concluded that the work done by the fluid on the blade over one oscillation cycle is a good indicator whether a flow case is aeroelastically stable or not.

The energy transferred between blade and fluid over one cycle can be calculated as:

$$W_{cycle} = \int_0^{\omega} \dot{\vec{\boldsymbol{x}}}(t) \cdot \vec{\boldsymbol{f}}(t)\, dt \tag{2.39}$$

Here, $\dot{\vec{\boldsymbol{x}}}$ is the blade surface velocity and $\vec{\boldsymbol{f}}$ is the force on the blade. The product of those two is integrated over time and over the blade surface.

If the motion of the blade is considered to be in exactly one eigenmode shape $\vec{\boldsymbol{\psi}}$ with factor $\hat{q}$, the velocity of the blade can be written as:

$$\dot{\vec{\boldsymbol{x}}}(t) = \vec{\boldsymbol{\psi}}\ \hat{q}\ j\omega\ \mathrm{e}^{j\omega t} \tag{2.40}$$

Assuming the fluid responds with a harmonic pressure fluctuation in the same frequency, the pressure on the blade surface can be written as:

$$\vec{\boldsymbol{f}}(t) \approx \mathrm{Re}\left(-\oint_A \left(\hat{p}\vec{\boldsymbol{n}} + p\hat{\vec{\boldsymbol{n}}}\right) \mathrm{e}^{j\omega t}\ dA \right) \tag{2.41}$$

In equation (2.41), $\hat{p}$ denotes the complex Fourier coefficient of the fluctuating pressure and p denotes the steady state surface pressure. Likewise, $\hat{\vec{n}}$ is the complex Fourier coefficient of the surface normal vector and $\vec{n}$ is the steady state surface normal vector.

If a linear dependency between blade deformation and unsteady pressure fluctuation on the blade surface is assumed, the aerodynamic work per cycle can be given as:

$$\hat{W}_c = j\pi \left\|\hat{q}\right\|^2 \oint_A \tilde{\hat{\psi}}^H \left(\hat{p}\vec{n} + p\hat{\vec{n}}\right) dA \tag{2.42}$$

Note the close relationship of equations (2.42) and (2.35). Equation (2.42) represents the aerodynamic work done by the fluid on the structure in complex form. The real part of the aerodynamic work represents the energy transfer from the fluid to the structure. If this energy transfer is positive, the magnitude of the vibration will rise (aerodynamic excitation), if the energy transfer is negative the magnitude of the vibration will decrease (aerodynamic damping). The imaginary part of the aerodynamic work per cycle is the amount of work done by the fluid in one part of the oscillation cycle and received again in another part of the oscillation cycle without any net effect. This can be regarded as an indicator for the aerodynamic stiffness of the fluid.

2.3.6. Summary of the Aeroelastic Stability Approach for Preliminary Design and Solution Algorithm

In the past chapters, the theoretical background of the energy method for flutter stability estimation in turbomachines was presented. First, the general aeroelastic equation of motion 2.29 was simplified from

$$\left(m_{st} + m_{fl}\right)\ddot{\vec{x}}\left(t\right) + \left(d_{st} + d_{fl}\right)\dot{\vec{x}}\left(t\right) + \left(k_{st} + k_{fl}\right)\vec{x}\left(t\right) = \vec{f}_{st}\left(t\right) + \vec{f}_{fl}\left(t\right) \tag{2.29}$$

to

$$m_{st}\ddot{\vec{x}}\left(t\right) + d_{fl}\dot{\vec{x}}\left(t\right) + k_{st}\vec{x}\left(t\right) = 0 \tag{2.31}$$

by omitting small or irrelevant terms.

Then, the problem was reduced to a purely structural problem with aerodynamic forces on the structure's surfaces, and an analogy to the undamped discretized structural equation of motion in traveling wave coordinates (2.26) was drawn.

$$\begin{aligned} &\lceil \boldsymbol{M}_{\Psi} \rfloor_{(r)} \ddot{\vec{q}}_{\Psi\ (r)}\left(t\right) + \lceil \boldsymbol{K}_{\Psi} \rfloor_{(r)} \vec{q}_{\Psi\ (r)}\left(t\right) = \left[\boldsymbol{\Psi}\right]^H_{(r)} \vec{\boldsymbol{f}}(t) \\ &\qquad \text{with} \quad \{r = 1,\, 2,\, ...,\, P\} \end{aligned} \tag{2.26}$$

Equation (2.26) was then expanded and reformulated into another stability problem by transforming the aerodynamic forces on the blade surface into deformation dependent aerodynamic influence coefficients (equation (2.38)).

Then, the energy method was introduced, postulating that the most likely flutter case is a single eigendeformation vibration with virtually no aerodynamic damping. This leaves the aerodynamic work over one oscillation cycle integrated over the structure's surface as a measure for the aeroelastic stability:

$$\hat{W}_c = j\pi \left\|\hat{q}\right\|^2 \oint_A \tilde{\hat{\psi}}^H \left(\hat{p}\vec{n} + p\hat{\vec{n}}\right) dA \tag{2.42}$$

To determine the aerodynamic or "flutter" stability of a turbomachine part, the aerodynamic work of relevant eigenmode shapes at relevant operating conditions needs to be

found. The determination of "relevant" will be reviewed in chapter 4. The possible aerodynamic approaches to determine the unsteady aerodynamic pressure on the structure's surface will be investigated in chapter 3.

Still, having reduced the fully coupled aerodynamic and structural equations of a turbomachinery stage by introducing simplifying assumptions, a solution strategy for the aeroelastic stability of a turbomachinery part can now be applied:

1. Create a structural model of the turbomachinery part.
   a) Determine if symmetry considerations reduce the problem.
2. Determine the operating point at which the stability analysis is to be performed.
   a) Expand the structural model with inertial and aerodynamic blade surface load.
3. Perform a modal analysis solving equation (2.9).
   a) Transform the eigenmode shapes to traveling wave coordinates.
   b) Determine the eigenmode shapes and eigenfrequencies of interest (reduce the population of $\left\lceil \boldsymbol{M}_{\boldsymbol{\Psi}}^{(r)} \right\rfloor$ and $\left\lceil \boldsymbol{K}_{\boldsymbol{\Psi}}^{(r)} \right\rfloor$ in equation (2.26).
4. Determine the aerodynamic response to a forced motion with each remaining eigenmode shape at each eigenfrequency.
5. Determine the likelihood of mode shape coupling or frequency impact of the aerodynamic response.
6. Determine the aerodynamic damping / excitation either via the energy method or via the solution of equation (2.38) (see Schuff & Chenaux [155] for an approach).

When applying the energy method, the two main concerns are numerical modal analysis and aerodynamic response to a deformation of a surface. The numerical modal analysis will not be covered here, since it is a well understood problem with ample solution software (at the Institute of Aeroelasticity the commercial Software MSC Nastran is used). However, the determination of an aerodynamic response to a blade deformation is the main problem and will be covered in the following chapters.

3. Fast Aerodynamic Methods for Rapid Assessment of Aeroelasticity in Preliminary Design

In chapter 1.5, the necessity for aeroelastic stability analyses already during early design stages was stated. It was proposed that methods used successfully 25 years in the past to ascertain aeroelastic stability of turbomachinery stages are tools usable for aeroelastic estimations in preliminary design, today. In chapter 2, aerodynamic and structural methods used in turbomachines were introduced and combined to treat aeroelasticity. The energy method was proposed as possible solution strategy for aeroelastic stability problems (flutter). Even though the energy method may no longer be sufficient for the final proof of aeroelastic stability of a turbomachinery stage, it is still deemed a viable tool for preliminary design estimations.

In this chapter, the described aeroelastic methods by Marshall & Imregun *[114] are highlighted (chapter 3.1). Then, the available aerodynamic methods to estimate the aerodynamic response to a surface deformation are reviewed and a selection of possible aerodynamic approaches is made (chapter 3.2). Important aspects of the selected approaches are presented in chapter 3.3-3.5.*

In the following chapter 4, the selected methods for rapid aerodynamics for aeroelastic stability methods are tested and explored for use cases from DLR projects. Then, in chapter 5, the results are summarized and conclusions regarding the suitability of the proposed methods for rapid aeroelastic analysis in preliminary design are drawn.

3.1. Available Aeroelastic Approaches for Rapid Assessment of Aeroelasticity in Preliminary Design

In chapter 1.5, the proposition of Pope [138] was cited that methods from 'research' applications are "cycled down" to 'repetitive' applications every 20 years. The much cited article by Marshall & Imregun [114] gives an overview of the state of the art in turbomachinery aeroelasticity 25 years ago. Based on this article, the state of the art back then is being reviewed. The different aeroelastic methods are listed and their basic approach is highlighted. Still, the used method for this thesis is the energy method due to its ease of use and experienced reliability in the past. It will be shown that almost all methods rely on unsteady aerodynamic computations which are then evaluated to determine the stability of a turbomachinery stage. Consequently, the aerodynamic methods mentioned by Marshall & Imregun and more recent ones are evaluated for promising avenues which might be pursued as basis for aeroelastic computations.

The scientific development of aerodynamic methods for turbomachines has made a large progress in the past 25 years. When Marshall & Imregun wrote their article, 2D methods were predominantly used. Also, mostly potential flow and Euler solutions were the norm. By now, the use of 3D RANS solvers has replaced these solvers in almost all areas of research and development. The reason for this always increasing complexity is that the use of these more complex (and therefore realistic) methods leads to new discoveries and often improves the current understanding of the flow. Additionally, the results most often represent experimental results better with less assumptions and manual "tuning". E.g. Grüber & Carstens [71] showed that viscosity is very important when computing the aerodynamic damping. Also, it has become common knowledge that 3D effects have a large

impact on aerodynamics and aeroelasticity in turbomachines where the flow is dominated by 3D effects and not largely two-dimensional like for airplane wings (see e.g. Rendu et al. [146], Weaver et al. [190] or Vogt [184]).

In the following chapters, the aeroelastic methods by Marshall & Imregun plus two newer ones are listed (chapters 3.1.2-3.1.8) and their possible fitness for preliminary design is discussed. Then, available unsteady aerodynamic methods to support these aeroelastic methods are categorized to identify promising areas (chapter 3.2.1) of research and subsequently a selection is made.

3.1.1. Methods Dismissed by Marshall and Imregun as Inaccurate

Over time, as new findings are made and boundaries of current methods are tested, unsuitable methods are identified and their use is discontinued. At the time of writing, Marshall & Imregun [114] dismissed various aeroelastic methods as "of little use for the prediction of flutter and other aeroelastic effects, especially for transonic flow speeds where the effects are highly nonlinear, and the flow is no more incompressible". These methods are listed here shortly but no attempt for theoretical explanation is made.

Linearized cascade theories: The basis for the linearized cascade theories is the pressure wave equation in two dimensions (Whitehead [192]). Since the flow effects in turbomachine stages are three-dimensional and transonic effects interact with the waves, there are unquantifiable uncertainties for this method.

Singularity methods: Marshall & Imregun only cite the article by Brase & Eversman [25] as an example for the use of this method, which is mainly concerned by the derivation of this method and has an aircraft wing example use case. The aerodynamics are computed with the doublet lattice method which is unsuitable for turbomachines (see chapter 3.5). There are examples for turbomachinery applications (e.g. Carstens [30]), but it is stated clearly that the examples are for subsonic flow only.

Vortex techniques: The vortex technique describes the unsteadiness of the flow as vortices moving with the flow. Although dismissed by Marshall & Imregun, research in this area is continued (Lee & Feng [105]) and the results are used for forced response estimations.

Frequency-domain panel methods: The basis for frequency domain panel methods is the Fourier expansion in time of the potential flow as for the harmonic balance techniques for Euler or RANS solvers. In chapter 2.1.5, the basis for the potential flow theory was given as inviscid and irrotational flow. Often, the additional assumption of incompressibility is made. Together with further assumptions made (e.g. flat plate for the doublet lattice method), methods are found which may perform sufficiently for airplane wings but were considered unsuitable for turbomachines by Marshall & Imregun.

3.1.2. Actuator Disk Theory

Adamczyk [1] derives a formula for the "normalized damping parameter" of a turbomachinery stage solely depending on the steady state inlet properties, the geometry of the blades and the frequency of oscillation. His derivations are based on two dimensional potential theory and use a blade passage section at 85% channel height as a reference. Even viscosity and blade stall can be included via quasi-steady loss coefficients. However, these coefficients are based on experiments and would have to be recalibrated for each new geometry. Since this is much too expensive, some values from the literature are often reused without adaptation.

While being very efficient and straight forward, there are a few concerns. The mentioned loss coefficients are one. Also, Adamczyk assumes a pure rigid body motion as a flutter

mode shape, only small inter-blade phase angles are permitted and blade rotation is not considered. Therefore, this theory can only be used for the first flexural mode and not for torsional modes.

Nevertheless, there have been very many successful attempts at using actuator disk theory for aeroelastic stability prediction and as a consequence new actuator disk theory approaches are developed, even today (Bontempo & Manna [23]). Also, it is the only listed aeroelastic approach which does not need unsteady aerodynamic computations.

Being independent of an unsteady aerodynamic model is a clear advantage for a method for preliminary design. When researching possible approaches for preliminary design in turbomachines, the actuator disk theory was considered a possibility. However, since there was no obvious extension of the theory to three dimensions and large parameter spaces for blade shape and blade deformations are expected in preliminary design (for which updated loss coefficients would be necessary), the actuator disk theory was dismissed as an option for this research effort.

3.1.3. Indicial Method

According to Marshall & Imregun [114], the indicial method is a method based on transonic small disturbance theory or linearized potential equations. The response of a flow to a step-change is computed first, and then the response of the fluid flow to other motions (namely the deformation of the blade in its eigenmode shape) is computed via a convolution integral. While the aerodynamic part of this approach was based on simple aerodynamic methods when Marshall & Imregun wrote their review, this approach is still used today (Mallik et al. [111]) with the support of 2D RANS aerodynamics.

Marshall & Imregun only cite airplane wing applications and a preliminary investigation only produced airplane wing applications still today. Most researches reference a paper by Leishman [107] as basis, but indicial functions were presented as a means for aeroelasticity as early as 1938 (Garrick [61]).

The indicial method was not considered as an option for rapid aeroelasticity in preliminary turbomachinery design due to the unknown and unpredictable influence of the cyclic nature of a turbomachinery stage. The definition of a step-change for a turbomachinery stage with multiple blades is by no means obvious and depending on the nature of the step-change definition, the result might be influenced.

3.1.4. Aeroelastic Eigensolution Method

The aeroelastic eigensolution method used in the 1990's was basically the direct solution of equation (2.31) in discretized form. To do so, the structural system was often approximated via a system of very few degrees of freedom (mostly pitch, plunge and torsion in 2D) and the aerodynamic damping due to the motion in the various degrees of freedom was derived by aerodynamic formulae based on various degrees of approximation (mostly 2D potential flow or 2D Euler). Then, an approximation of a full rotor with all its blades (approximated in 2D) could be computed even considering mistuning (Kaza & Kielb [94]) by superposing the solutions.

One more recent application of this method is by Korte & Peitsch [101], who compare a coupled or uncoupled aeroelastic eigensolution approach in 3D with a state-space approach and the energy method for a turbine stage with intentional mistuning.

In chapter 2.3, the derivation of the aeroelastic eigensolution method was highlighted. Korte & Peitsch investigated the impact of the mode shape interaction in their article and Schuff & Chenaux [155] stress that mode coupling might occur in modern fan blade designs. However, due to the availability of the simplified version of the eigensolution method (energy method) and since Schuff & Chenaux had not yet published their findings at the time, it was decided that there was no need for a full aeroelastic eigensolution in an early design phase. However, if reasonably fast unsteady aerodynamic solutions become

available, the extension of the energy method to the full aeroelastic eigensolution method is straight forward.

3.1.5. State-Space Representation

The state-space representation is a method originally used in control theory. It was originally adapted to aircraft aeroelasticity by Karpel [92] who intended to model the aeroelastic behavior of an aircraft over the complete flight envelope.

Since then, his method of defining the aeroelastic behavior in the complete design space via state-space representation based on a representative number of computations has been used abundantly and also adapted to turbomachines by Korte & Peitsch [101]. While Karpel used Theodorsen's theory and tabulated values by other researchers (all in 2D) as a basis for his state-space approach, the computation of aerodynamic influence coefficients has evolved since then, leading to the use of time-linearized 3D RANS solutions by Korte & Peitsch.

The state-space representation offers particular advantages when nonlinear effects are to be modeled (Korte & Peitsch [101]). If there are no prominent nonlinearities in the system, the aeroelastic eigensolution method and the state-space representation produce similar results. Based on these findings, it was concluded that the state-space method may be used beneficially in preliminary design to reduce the number of necessary unsteady aerodynamic computations to predict the aeroelastic stability in the complete compressor map. This will have to be explored in the future.

3.1.6. Energy Method

The energy method has been derived in chapter 2.3.5. Its basic assumption is that the aerodynamic damping, mass and stiffness are so small that there is virtually no change in eigenmode shape and eigenfrequency from the eigenmode shapes and eigenfrequencies of the turbomachinery stage alone. Then, the energy transfer from fluid to structure over one vibration cycle is an indication whether the vibration is damped or excited.

The energy method does not make any assumptions about flow state or inter-blade phase angle. This means that for each flow state of interest and each eigenmode shape of interest a separate unsteady aerodynamic solution is necessary. Depending on the used fluid flow model, this can result in a substantial need for computational resources.

Nevertheless, the energy method was considered an ideal tool to estimate aeroelastic stability in preliminary design, since there are no additional computations necessary except the structural modal analysis and the unsteady forced motion aerodynamics computations.

3.1.7. Panovsky-Kielb Method / Tie Dye Method

Panovsky & Kielb [133] investigated the aeroelastic properties of turbine blades with the energy method. During their research and from previous experience (see Hanamura et al. [75], influence coefficient theory) they concluded that the influence of the blade on itself and the influence of the vibration of the two neighboring blades is sufficient to determine the main unsteady aerodynamic properties of a blade vibration with a given inter-blade phase angle σ_n.

They concluded from this that it is sufficient to compute the unsteady aeroelastic properties of only three inter-blade phase angles σ_n or a case with three blade passages and only the middle one vibrating to determine the minimum aerodynamic damping of the complete stage.

Panovsky & Kielb then deduced that if the contributions of different blade passages can be superposed, so can the contributions from different eigenmode shapes. They therefore computed the aerodynamic damping for three two dimensional eigenmode shapes in one representative section of a blade passage at different reduced frequencies. Once the blade mode shapes were superposed, the critical reduced frequency for the respective eigenmode

shape could be interpolated. With this approach, it is possible to compile a "map" of eigenmode shapes and their respective critical reduced frequencies below which they are expected to become unstable.

The results of Panovsky & Kielb were obtained using a 2D time-linearized Euler code. Since then, this method has been successfully used for the design of mostly turbine blades (Kielb et al. [98], Kielb et al. [99], Meingast et al. [120]).

The Panovsky-Kielb method was developed specifically for low pressure turbine blades which (according to them) operate almost exclusively at their design conditions. However, e.g. compressor stages operate sometimes at substantial off-design conditions and still need to perform maintaining aeroelastic stability. Another disadvantage of the method is the reduction of the blade deformation to rigid body motion in two dimensions. Modern fan or compressor blade row designs may exhibit three dimensional mode shapes which cannot be approximated in 2D. There is also the potential for eigenmodes where the blade is no longer moving in a rigid body motion, but where the profile itself deforms. Both the change in operating condition as well as potential 3D or profile deformation eigenmode shapes cannot be captured by the stability diagram proposed by Panovsky & Kielb. Since the current research focuses on compressors, this method was not considered a possibility for rapid aeroelastic stability estimation.

3.1.8. Reduced Order Modeling via Proper Orthogonal Decomposition

While not being an aeroelastic method itself, reduced order modeling has to be mentioned here to give a complete account of aeroelastic methods. Clark et al. [37] have presented a method to predict the unsteady aerodynamics of a cascade of two dimensional compressor airfoils via proper orthogonal decomposition.

To create a reduced order model, Clark et al. computed a number of unsteady harmonic balance RANS solutions for a compressor blade with a forced torsion motion. These computations all had the same structural motion frequency but different "steady state" parameters (inlet and outlet conditions). A proper orthogonal decomposition method was used on a number of these harmonic balance unsteady results, identifying a number of "fluid flow eigenmode shapes" which could then be used to identify dominant flow features and even made the identification of non-synchronous vibrations possible.

This kind of fluid flow eigenvalue analysis has received increasing attention in the past years and is thought to have a number of beneficial uses in aerodynamics and aeroelasticity (see the overview articles of Taira et al. [170] and [171]).

Modeling the aeroelastic behavior of a turbomachinery stage based on a reduced order model would increase the speed of a design process significantly. The method of proper orthogonal decomposition might consequently seem to be a valuable method for aeroelastic stability estimation in preliminary design. However, there are two conditions which make it unsuitable for preliminary design. The first are the large parameter spaces explored during early design phases. The ROM based on a certain design might not correctly predict the conditions for another design which deviates substantially from it. This immediately leads to the second problem: The creation of a reduced order model via POD is based on a substantial number of unsteady computations to identify the fluid eigenmode shapes. The necessity to create new POD ROMs for different designs due to the uncertainty if the old ones still apply, leads the complete approach ad absurdum for preliminary design.

3.2. Selection of Promising Rapid Unsteady Aerodynamic Methods

In the previous chapter, different aeroelastic methods for turbomachinery aeroelastic stability estimation were listed. The most promising method for turbomachinery aeroelastic stability estimation in preliminary design was deemed to be the energy method. This is on the one hand due to its simplicity of implementation and on the other hand due to previous experiences showing the method to predict instability reliably. Most of the aeroelastic methods given in the previous chapter heavily depend on unsteady aerodynamic methods which compute unsteady pressure forces acting on deforming bodies.

To increase the speed of aeroelastic stability estimates, fast yet reliable unsteady aerodynamic methods need to be found which predict the flow around an oscillating blade in a turbomachinery stage. Therefore, a short overview of available unsteady aerodynamic methods is given in chapter 3.2.1. Then, criteria for the selection of a promising unsteady aerodynamic method are identified in chapter 3.2.2 and a selection is made in chapter 3.2.3.

3.2.1. Investigation of Available Unsteady Aerodynamic Methods

Marshall & Imregun [114] give a comprehensive overview of the available aerodynamic methods for turbomachinery in 1996. Since then, additional methods have become available. Therefore, an attempt is made to list the available unsteady aerodynamic methods in descending order of complexity.

Direct Numerical Simulation (DNS): Chapter 2.1.1 introduced DNS and explained its basic approach. This method is the most accurate and reliable method to simulate fluid flow, to date. Additionally, it is three dimensional and unsteady nonlinear by design and the implementation is straight forward. The main problem are its prohibitive numerical requirements for time and mesh resolution (only one research group seems to publish results in this area for turbomachines).

Large Eddy Simulation (LES): Chapter 2.1.2 presented LES and introduced the concept of filter functions for the purely dissipating scales which do not influence the larger scale turbulence. LES shares the advantages of DNS for being able to simulate fluid flow very accurately with the additional advantage of using a coarser mesh and being less hardware demanding. Like DNS, it is three dimensional and nonlinear unsteady by design. While being numerically less demanding than DNS, LES still requires a mesh resolution which is so fine that it is currently restricted to research applications. Additionally, the required sub-scale modeling and the filter functions are an ongoing topic of research.

Detached Eddy Simulation (DES): DES is a hybrid method combining LES in the far field with RANS (see the following point) in the boundary layer and was mentioned briefly in chapter 2.1.3. The main concern of DES is to resolve turbulence and its eddies/vortices where they are important for the physical or engineering aspects of the problem while modeling them in areas where a resolution is undesirable and would only use numerical resources without contributing to the solution of the problem. As with the above two approaches, DES is nonlinear unsteady and its sensible use is in three dimensional space (at least for turbomachines). While providing a better insight into the mechanics of the unsteady fluid flow than simpler methods, the numerical requirements are above the currently used methods for design proof purposes. Further drawbacks include its need for intelligent algorithm switching and the expert knowledge required to successfully obtain accurate results.

Reynolds Averaged Navier Stokes (RANS): In chapter 2.1.3, the basic assumptions leading to RANS solvers were introduced. For the unsteady computations required for turbomachine design proof, these methods are the current state of the art and multiple

academical and commercial codes are available. Unsteady RANS solvers can be used in two or three dimensions, depending on the main flow direction. There exist three approaches to model the unsteadiness of the flow in RANS solvers: Nonlinear unsteady methods use a time-marching algorithm to compute snapshots of the evolving unsteady flow at set time step intervals. Harmonic balance methods postulate that periodically occurring events (blade vibration, gusts from neighboring blade rows etc.) can be Fourier transformed into the frequency domain, resulting in the assumption that only the Fourier coefficients of the periodic frequency and a limited number of harmonics are sufficient to describe the periodic unsteadiness of the flow. This limited number of Fourier coefficients of the flow is then computed. The time-linearized method postulates that a harmonic excitation results in a harmonic response of the flow and consequently only computes the first harmonic response due to a harmonic excitation.

Euler: The Euler equations are the Navier Stokes equations with zero viscosity. Then, there is no need for turbulence modeling and the numerical solution is simpler. Therefore, Euler solvers were the predecessors of RANS solvers in computational fluid dynamics. Euler solvers require less computational resources (coarser mesh, less variables to be computed) than RANS or other more accurate descriptions of fluid dynamics. Still, they provide solutions with engineering accuracy for cases where viscosity can be neglected. However, for flows with viscosity dependent effects like e.g. shocks or shock boundary interaction, their results become less reliable [114]. Like the RANS equations, cases with mainly two dimensional flow can be solved in 2D. The unsteady Euler equations can be solved with nonlinear, harmonic balance and time-linearized methods like the RANS equations. At the time of Marshall & Imregun [114], 2D and 3D time-linearized Euler computations were the emerging state of the art in turbomachinery aeroelasticity.

Potential: While assuming zero viscosity led from the Navier Stokes equations to the Euler equations, additionally assuming zero vorticity leads to the potential equations, where the velocity of the fluid is the second derivative in space of a "velocity potential". With the additional assumption of incompressibility, the potential equations can be transformed into a boundary value problem where the values at the problem boundaries fully describe the flow. The potential flow equations can be solved in two or three dimensions and nonlinear and time-linearized methods exist for unsteady problems [114]. The solution of the potential equations as a boundary value problem with sufficient discretization is possible in a fast and efficient way with today's computational resources. However, already at the time when Marshall & Imregun wrote their article it was well known that potential flow solutions do not represent the flow in turbomachines very well.

3.2.2. Selection Criteria

When evaluating unsteady aerodynamic methods for preliminary design, there are boundary constraints which need to be fulfilled in order to be able to successfully determine the aerodynamic response to a harmonic surface perturbation in a specified eigenmode shape.

Comparatively fast results: The first and foremost criterion is naturally speed. In order to assess the aeroelastic stability of many potential blade shapes, the unsteady aerodynamic method needs to be able to return unsteady aerodynamic pressures resulting from a surface deformation in a comparatively short time.

Three dimensional: Another criterion defined in this research effort was the ability of the method to treat three dimensional flow. Rendu et al. [146], Weaver et al. [190] and Vogt [184] stress that there are flow phenomena important for aeroelasticity in turbomachines which cannot be captured with two dimensional methods.

Accurate: Naturally, the obtained numerical results of an unsteady aerodynamic code need to fulfill the minimum reliability requirements for preliminary design.

Well documented and available: Many research codes are either company property and therefore unavailable to other researchers or the result of short term research activities. While performing their respective tasks, obtaining them or find documentation for them often proofs challenging.

Needs to be manageable in the given time frame: Some research codes are available and documented but are so professional that implementing changes is very challenging for scientists without a degree in information technology.

Simple to automate: While the goal of virtually any computer program is the simplification of repetitive tasks, interfaces for interaction with other programs are not implemented into every program available. Since preliminary design is mostly performed with automated optimizers, interfaces for automated interaction with other programs are an indispensable condition.

Represent a wide range of possible approaches: The goal of this research was an investigation of the current options for aeroelasticity in preliminary design and the probable development in the foreseeable future. Therefore, methods needed to be evaluated which are available now without further effort, and methods which are possible to implement in the near future.

3.2.3. Selection

The available unsteady aerodynamic methods together with their respective fulfillment of the desired selection criteria can best be evaluated in matrix form:

Criterion	Potential	Euler	RANS	DES	LES	DNS
Speed	:-))	:-)	:-|	:-|	:-((	:-((
3D	:-)	:-)	:-)	:-)	:-)	:-)
Accuracy	:-|	:-|	:-)	:-)	:-))	:-))
Available and Documented	:-|	:-|	:-)	:-(	:-|	:-(
Manageability	:-)	:-)	:-)	:-(	:-(	:-(
Automatability	:-)	:-)	:-)	:-(	?	?

Table 3.1.: Applicability matrix of different unsteady aerodynamics approaches for preliminary design estimates [:-)) = very good, :-) = good, :-| = mediocre, :-(= poor, :-((= very poor].

Since LES and DNS solutions are only reported for large scale research applications, at the moment, these two approaches for unsteady aerodynamics can be disregarded immediately. DES requires still a lot of time to compute and the use requires expert knowledge. Consequently it is not considered further on.

This leaves unsteady Potential, Euler and RANS flow solvers with their three potential methods of solution: time-linearized, harmonic balance and nonlinear unsteady, respectively.

In table 3.2, the subjective applicability of the different unsteady methods is displayed.

Marshall & Imregun [114] listed a number of time-linearized 3D potential codes (LTRAN2, Guruswamy & Goorjian [72]; CAP/TSD, Batina [10] and an AIRBUS inhouse code published by Henke et al. [78]). All these codes solve the transonic small disturbance equations to determine the response of a flow to a vibratory motion. While

	Potential	Euler	RANS
Time-linearized	:-|	:-|	:-)
Harmonic balance	–	:-|	:-|
Nonlinear	:-)	:-)	:-)

Table 3.2.: Subjective applicability of unsteady Potential, Euler and RANS solvers for preliminary design estimates [:-) = good, :-| = mediocre, :-(= poor, – = not found].

this seems to be a fast and moderately accurate way of determining the unsteady response, these codes do not seem to be in use any more or are not easily available.

Time-linearized Euler solvers are available and produce fast and reasonably reliable results. The examples mentioned by Marshall & Imregun are by Hall & Lorence [73] and Giles [62], but there are also proprietary codes (Lin3D by MTU AeroEngines). While these codes are being used, and are theoretically obtainable, they were not considered, since they offer less theoretical accuracy than time-linearized RANS solvers and are slower than time-linearized potential solvers.

Time-linearized RANS solvers have become available over the past decades. Examples include Chassaing & Gerolymos [33], Ning et al. [130] or Petrie-Repar [135]. There exist varying approaches to treat the unsteady viscosity. Some solvers consider the influence of the unsteadiness of the flow on the viscosity negligible (constant-eddy-viscosity or frozen-μ approach, DLR TRACE, Kersken et al. [96]), others linearize the turbulence model as well (DLR TAU, Thormann & Widhalm [174]). The time-linearized RANS method was considered a beneficial trade-off between prediction accuracy and computation speed. While the method is currently being used for design validation purposes, it may well be used for preliminary aeroelastic design studies in a few years time.

While being theoretically possible, the author is not aware of any unsteady potential solver incorporating higher harmonics of the base frequency.

The code by Hall et al. [74] was the first harmonic balance Euler solver explicitly developed for turbomachines. Since most academic or commercial RANS solvers offer the option of switching off viscosity, most solvers mentioned for harmonic balance RANS should also have harmonic balance Euler capabilities. However, harmonic balance introduces additional computational steps and since time-linearized Euler was not considered an option, neither was harmonic balance Euler.

Harmonic balance RANS is becoming more and more a standard tool to treat periodic unsteadiness in fluid flows. Examples include Bakhle & Reddy [8], Sicot et al. [159], Frey et al. [58] but also commercial solvers feature unsteady harmonic balance RANS (an example using STAR CCM+ was published by Grigoriev et al. [69], ANSYS flow solvers also include this feature according to their website). Computing additional harmonics requires numerical resources. This includes increased memory consumption and longer computing times compared to time-linearized solvers. Consequently, harmonic balance was not considered in this study.

A number of nonlinear unsteady potential solvers have been developed over the years. Marshall & Imregun only mention an article by Tatum & Giles [172], but the mentioned code (SIMP by Rockwell International Science Center) does not seem to be available any longer. Additionally, Tatum & Giles are concerned with preliminary design of supersonic aircraft, which is not related to transonic turbomachinery applications. However, NASA developed a full potential code (PMARC, Ashby et al. [5]) around the same time which is still being used. An adapted commercial version of this code was obtained by DLR a few years back, and therefore code base and documentation are available. Considering the matrix in table 3.2, a nonlinear unsteady potential solver is diagonally opposite of time-linearized RANS solutions and was therefore considered for investigation.

There exist a number of nonlinear unsteady Euler codes for turbomachinery applications. Most of them are nowadays in combination with nonlinear unsteady RANS solvers. While Marshall & Imregun dismissed time-linearized potential codes as inaccurate, the diagonally opposite (in table 3.2) nonlinear methods suffer from a different problem. Especially the nonlinear unsteady RANS equations need a relatively small time step resolution to deliver reliable results. Additionally, (see chapter 2.1.6) nonlinear unsteady RANS solutions depend on their steady state initialization. These two reasons may lead to the necessity to compute multiple oscillation cycles until an unsteady "converged" solution for an oscillation cycle is reached. This led to the disregard of nonlinear unsteady Euler as well as nonlinear unsteady RANS solutions as options for rapid aerodynamics in preliminary design.

The remaining options from table 3.2 are consequently the diagonally opposite approaches "**time-linearized RANS**" as most most physically accurate description with the assumption of purely harmonic flow response and "**nonlinear potential flow**" as physically most reduced description of the flow without assumptions about the nature of the flow response. It was stated numerous times here, that many researchers regard the potential flow equations as unsuitable for turbomachinery flow, still they are being used with success for aircraft design and preliminary aerodynamic turbomachinery design. Additionally considering that the actuator disk theory (which is based on 2D potential flow) is being used with success in predicting stability in turbomachines, another investigation into the viability of unsteady nonlinear potential methods for turbomachines seemed justifiable.

The Reduced Frequency

Having established two aerodynamic methods which are worth investigating, there remains the question of the reduced frequency. Panovsky & Kielb [133] designed their method for aeroelastic investigation of a low pressure turbine blade to result in boundary values for the reduced frequency to indicate stability depending on the eigenmode shapes. Since its first publication, multiple articles were written with the basis of the Tie Dye method and its critical reduced frequency map (Kielb et al. [98], Kielb et al. [99], Meingast et al. [120]). Preliminary design rules stated that the reduced frequency needed to be above certain boundary values (Sisto [161]). Belz & Hennings [14] specifically designed an experiment to investigate the influence of the reduced frequency on the aeroelastic stability. Later, May [115] investigated the impact of the reduced frequency on the aeroelastic stability of a compressor blade row. Corral & Vega [42] investigated the influence of the reduced frequency on the stability of a low pressure turbine. Many more examples can be found in the literature.

Since the importance of the reduced frequency as a parameter in aeroelastic analysis of turbomachinery stages has been well proven, it was concluded that the investigation of the reduced frequency as a possible design criterion for aeroelastic stability in preliminary design needed to be included in this research, as well.

3.3. Time-Linearized, Forced Motion, RANS CFD

In the previous chapter, various aeroelastic methods were presented and the energy method was selected as most simple approach for aeroelasticity in preliminary design. Then, the available unsteady aerodynamic methods were compared against desirable characteristics for preliminary design and two unsteady aerodynamic methods were selected. Additionally, it was concluded that the parameter of reduced frequency needs special attention when investigating methods for rapid aeroelasticity in preliminary design.

The theory regarding the time-linearized module of the flow solver TRACE of DLR (linear TRACE) is given in Kersken et al. [96]. More information on the DLR flow solver TRACE can be found in the appendix B. As already mentioned, only the constant-eddy-viscosity approach (frozen-μ) is implemented into linear TRACE. According to Kersken et al., this is justifiable for attached flow, but not for complex flows with separation. This has been

verified for the DLR TAU code by Thormann & Widhalm [174], who concluded that for accurate predictions of the unsteady flow a time-linearization of the turbulence model is necessary. Still, the implemented constant-eddy-viscosity approach in linear TRACE was considered justifiable since only preliminary design computations were intended. Nevertheless, this needs to be kept in mind when considering solutions at the stall boundary of the compressor map, since the flow there is influenced by separation phenomena.

Another effect not included in a time-linearized solution are the influences of higher harmonics or neighboring blade row frequency effects. To calculate these effects simultaneously, a nonlinear unsteady computation is necessary, since blade vibration frequency and neighboring blade row effects generally do not occur at frequencies which can be introduced as base frequency and higher harmonics into a harmonic balance solver. However, since only the effects of a vibrating turbomachinery stage on itself are considered in this study, these effects can be neglected and the time-linearized module of TRACE was used as benchmark.

Numerical Setup

The required steps to obtain an assessment of the aeroelastic stability with the energy method and linear TRACE (Kersken et al. [96], 2.1.6.3 and B) are as follows:

Geometry definition: For the cases considered in this study, the geometries were already predefined. For a preliminary design study, suitable blade and casing geometries need to be defined in order to evaluate their fitness for the defined use case. This will most often be performed by an automated optimization algorithm. This includes the fluid flow volume as well as the structural properties of the stage (bladed disk, blisk...). Depending on the scope of the preliminary design, the properties of the disk may be subject to change or considered fixed.

Mesh generation: Once the geometry is defined, a suitable fluid flow mesh as well as a suitable structural mesh need to be created. In preliminary design, this is generally done via automated programs which receive the geometry definition and return a suitable mesh representation in the required format for CFD and FE solver. In the examples used for this study, these were an in-house tool at the Institute of Propulsion Technology for the fluid domain and a suite of Python programs for the structural domain.

Steady state fluid flow computation: Based on the defined use case, a steady state CFD computation for the aerodynamic design point (ADP) is performed with the appropriate boundary conditions (RPM, steady state inlet and outlet values).

Hot-to-cold transformation: Modern turbomachine stages' blades deform during operation. This needs to be considered when designing an aerodynamically optimized blade. To determine the geometry which is manufactured, based on the optimal aerodynamic geometry, a so-called "hot-to-cold" transformation is computed. To do so, the steady state aerodynamic pressures on the blade surface at the ADP in the fluid flow domain are interpolated onto the blade surface of the FE mesh. Steady state structural load computations including surface pressure and rotation are then performed and the blade's geometry is adjusted until the result of a steady state load computation with the surface pressure at the ADP result in the optimal aerodynamic geometry. For this study, the necessary computations were performed with the commercial FE solver MSC NASTRAN in combination with a suite of Python programs.

Numerical modal analysis of the structure: To determine the eigenmode shapes of the turbomachinery stage, a numerical modal analysis is performed. To include the influence of blade surface pressure and rotation on the blades' stiffness (chapter 2.2.3.3), the

modal analysis' stiffness matrix is always based on a previous steady state load computation with inertia and blade surface pressure load. As for the previous step, the necessary computations for this study were performed with MSC NASTRAN.

Eigenmode shape mapping and deformation: To determine the aerodynamic response to a surface deformation in an eigenmode shape, the eigenmode shape needs to be mapped onto the CFD mesh's surface(s) and the deformations need to be propagated into the volume mesh. For the purpose of this study, these tasks were performed with tools belonging to the DLR TRACE suite.

Unsteady time-linear RANS computation: Based on the blade surface deformation in the eigenmode shape with the respective eigenfrequency and desired inter-blade phase angle σ_n, the time-linearized unsteady flow solution is computed.

Post-processing: The result of the time-linearized unsteady fluid flow computations are the unsteady pressures on the blade surface in relation to the blade deformation. These can be extracted and the aerodynamic work can be computed according to equation (2.42). For the cases of this study, this was again performed with a suite of Python programs.

Two important notes need to be made on the "steady state fluid flow computation" part and the "numerical modal analysis of the structure" part of the aeroelastic stability assessment with the time-linearized RANS model:

The first is that steady state computations need to be performed for each operating point at which unsteady computations are desired. Depending on the structural properties of the blades, it might become necessary to include the deformation of the blade at the specified operating point into the steady state computation (static aeroelasticity, see Schuff et al. [156]).

The second is that the steady state aerodynamics influence the stiffness of the blades at each operating point and that the Campbell diagram consequently is not a two-dimensional diagram of eigenfrequencies over RPM any more, but that it gains a third dimension representing the pressure ratio at a given RPM. As a result, since the steady state computation needs to be performed anyway and FE solutions are comparatively cheap, it is advisable to perform a numerical modal analysis for every investigated operating point.

3.4. Reduced Frequency

The Strouhal number is used as a dimensionless number characterizing the relation between periodic events and the flow velocity and it is defined as:

$$Sr = \frac{f \cdot L_c}{|\vec{v}|} \tag{3.1}$$

In equation (3.1), L_c defines a characteristic length and f and $\vec{v}$ are the already known frequency and fluid flow velocity. The characteristic length is often the diameter of the body, for airfoils the airfoil thickness, the frequency is most often the frequency of the vortex shedding of the body, but differently defined Strouhal numbers exist for various use cases. Measured values for the Strouhal number relating fluid flow and vortex shedding range from 0.12 to 0.3 depending on the Reynolds number (and therefore on the viscosity of the fluid) for a long cylinder.

The reduced frequency on the other hand, is defined as:

$$\omega_{red} = \frac{\omega \cdot L_c}{|\vec{v}|} \tag{3.2}$$

The definitions of the Strouhal number (equation (3.1)) and the reduced frequency (equation (3.2)), are remarkably similar and the reduced frequency can be seen as one of the adapted Strouhal numbers. The main difference is that the Strouhal number uses the frequency and the reduced frequency uses the angular frequency. For the reduced frequency in turbomachines, the used properties are generally taken at 80% blade / channel height. The velocity is the relative velocity experienced by the blade (not only the axial component, but also the rotational component). The definition of the characteristic length is not unique in the community. Some researchers use the blade semi-chord, some use the chord length of the blade. In this research, the complete chord length was used in the definition of the reduced frequency due to historical reasons.

The important aspect of the reduced frequency is, that it is a "similarity parameter" that makes it possible to compare different blade designs. This is one of the main reasons why it became so popular in aeroelastic research. Khalak [97] investigated the comparability of different engine designs and influences on flutter stability. He concluded that one similarity parameter is by no means representative for the aeroelastic stability of a design. Khalak proposed a framework of four similarity parameters consisting of corrected mass flow $\dot{m}_c$, corrected speed N_c, compressible reduced frequency K^* and reduced (structural) damping g/ρ^*. However, he does not provide a relation between these parameters indicating aeroelastic stability. Khalak states that the first two "alone account for the corrected performance and the latter two alone account for the flight condition". The first half of this sentence implies that each point in the performance map needs to be treated separately. The second half of the sentence implies that the reduced frequency may be subject to the flight altitude, as well. The reduced structural damping introduced by Khalak does not seem to be relevant for preliminary design purposes, where the structural damping is assumed to be negligible, anyway. As a consequence, Khalak's findings help to compare different designs, but they do not contribute to finding better design parameters.

Another similarity parameter used in aeroelastic design is the mass ratio between vibrating blade and fluid mass. That the combination of "reduced frequency and mass ratio are not sufficient measures of aeroelastic similarity" was concluded by Stapelfeldt & Vahdati [166].

Corral & Vega [43] and Vega & Corral [182] investigated the influence of the reduced frequency on the aeroelastic stability at length and derived the implications of changes in reduced frequency on the stability. They are again mainly concerned with turbine applications and cannot provide a boundary value independent of the flow case which indicates aeroelastic stability.

Even though Sisto [160] dismisses methods that determine the flutter susceptibility of rotors purely via the reduced frequency as "empirical" and therefore not capable of capturing the complex relations responsible for aeroelasticity in his introduction to the *AGARD Manual on Aeroelasticity in Axial-Flow Turbomachines*, a relation between aeroelastic stability and reduced frequency is postulated by many researchers.

Therefore, it was decided to investigate the impact of the reduced frequency on the aerodynamic damping based on the boundary values for the reduced frequency for bending and torsional eigenmode shapes presented by Sisto [161].

Eigenmode shape	Design rule
First bending	$\omega_{red} > 0.4$
(relaxed form)	$\omega_{red} > \frac{1}{3}$
First torsion	$\omega_{red} > 1.6$

Table 3.3.: Reduced frequency design rules to prevent aerodynamic excitation of turbomachinery parts used during the middle of the 20$^{\text{th}}$ century (Sisto [161]).

It is worth noting that these correlations were applied at the aerodynamic design point

(ADP) and were supposed to indicate the flutter susceptibility of a rotor design in the complete operating range (Sisto [161]).

The reduced frequencies for a range of aerodynamic designs of a research fan demonstrator were computed with a suite of Python programs and compared to the minimal aerodynamic damping computed for the respective design. Results and discussion of this analysis are presented in chapter 4.2.

3.5. Nonlinear Potential Aerodynamics

Before the large scale use of RANS or even Euler CFD methods, potential flow solvers were used to determine the flow around objects. At the DLR Institute of Aeroelasticity, potential methods are frequently used to determine the aeroelastic stability of airplane configurations (Voss et al. [187], Hebler & Thormann [76], Friedewald et al. [59]). The method used in these articles is a frequency domain doublet lattice method (DLM). This has the advantage that aerodynamic responses to harmonic deformations of the structure can be solved directly. However, the used doublet lattice methods are only valid for thin planar wings.

Since potential flow methods are being used successfully to accelerate the aeroelastic stability assessment of aircraft wings in the design phase, this might be an option for turbomachinery as well. Potential flow methods result in a linear equation system which can be solved very efficiently, ergo fast. Their main disadvantage is that they become incorrect for higher Mach numbers when compressibility and shocks cannot be neglected any longer. Since Hebler & Thormann [76] and Friedewald et al. [59] showed that DLM methods can be corrected with a very limited number of unsteady RANS calculations, this problem might be solved for turbomachines as well.

When choosing a suitable potential flow method, there are certain aspects that need to be considered:

Vortex Lattice Method	**Doublet Lattice Method**
• Inviscid	• Inviscid
• Irrotational	• Irrotational
• Incompressible with extensions for compressibility correction	• Incompressible with extensions for compressibility correction
• 3D method based on surface panels	• Only planar wings
• Steady state with extensions for unsteady time stepping	• Steady state with extensions for time-linearized unsteady harmonic deformations
• Panels are independent of each other. Triangular panels are permissible.	• The panels need to be rectangular and in direction of the main flow

Since turbomachinery parts often possess a non-negligible curvature and hub and shroud influence often cannot be neglected, DLM was not considered an option. Therefore it was decided to examine the possibility to incorporate methods for fast turbomachinery aeroelasticity (cyclic symmetry, rotating wakes etc.) into the vortex lattice code CMARC.

3.5.1. CMARC

In the 1980s, NASA had need of a "well-documented code, suitable for powered-lift aerodynamic predictions, with an open architecture which would facilitate making modifications or new features" (PMARC Manual [5]). It was based largely on a version of VSAERO,

written in FORTRAN and became very popular in the scientific community due to its open architecture which allowed for modifications of the program. Still, it is not open-source and therefore not publicly available.

There exists however a fork of PMARC-12 called "CMARC" which was converted to C and can be purchased with sources. The theory of the potential flow solver CMARC is given in appendix C. DLR Institute of Aeroelasticity obtained this code and its applicability to turbomachinery problems, especially unsteady forced motion calculations, were explored.

To accomplish this, a few obstacles needed to be overcome:

- The code was capable of treating vertical (influence of second half of the airplane) and horizontal (ground effects) symmetry. Cyclic symmetry was not available, and since the size of the linear equation systems of potential methods increases quadratically with the number of panels and blade numbers can be quite substantial, this needed to be incorporated.

- In the original design, body surface velocities could be described to simulate the motion of a part of the model, but no harmonic oscillation of the surface velocities was implemented. Consequently, a surface deformation algorithm needed to be written.

- Even though designed as an "open architecture" code, the conversion to C and the age of the program introduced some dependencies which needed to be addressed before changes in the code could be implemented.

3.5.1.1. Cyclic Symmetry Implemented into CMARC

CMARC computes the dependency of the aerodynamics at one specific surface panel on the body's surface depending on the properties of all other surface panels via aerodynamic influence coefficients according to an equation presented in appendix C (equation (C.13)). The algorithm implemented to compute these for symmetry cases, is straight forward: Simply mirror each panel on the specified symmetry plane and calculate the additional influence. Then, the influence of the complete geometry on the panel is considered.

Likewise, for wake panels, the influence of wake panels for each time step is computed by mirroring the wake panels on the symmetry planes and calculate the influence of the additional wake.

This approach has been kept and has been extended to cyclic symmetry about the global x-axis of the model (which is supposed to be the main flow direction) for the computations of this thesis.

1. The implemented algorithm is only called if a cyclic symmetry is demanded by the input.

2. Depending on the number of cyclic sectors N, the sector angle is computed ($\frac{2\pi}{N}$).

3. When computing the influence coefficient matrices for surfaces and wakes, the regarded panel is rotated additional $N-1$ times and the influences on the regarded panel are summed up.

The consequence of this approach is an increased influence coefficient matrix creation time (also in each virtual time step to consider the wakes), while the influence coefficient matrix is only as large as the number of panels squared of the specified rotor section. Still, due to a fast implementation in C, the overall matrix generation time is small compared to the linear equation solution time.

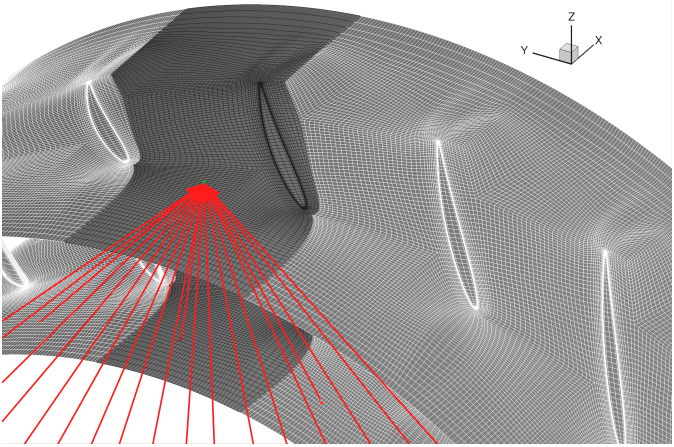

Figure 3.1.: Implemented cyclic symmetry approach. For each panel (example panel green, at the tip of the arrows), the influence of all other panels and itself is calculated and results in one row of the influence coefficient matrix. Since it is assumed that the velocity potential at each cyclic symmetric panel (red, at the base of the arrows) has the same magnitude, the influence of these panels is summed up and results in the influence coefficient of the respective panel.

3.5.1.2. Harmonic Surface Oscillation Implemented into CMARC

Surface deformations can be prescribed via surface normal velocities in CMARC. In equation (C.13), the source term is normally zero since the surfaces are considered impermeable. To prescribe a surface motion, the surface normal velocity at the panel is explicitly given and the panel source term is set to the appropriate value.

Since there was no routine which implemented a harmonically oscillating surface normal velocity, the possibility to prescribe a surface deformation at the corner points of the panels was created for this work.

$$\begin{aligned} \vec{\boldsymbol{x}}(t) &= a \cdot \sin(\omega t) \\ \dot{\vec{\boldsymbol{x}}}(t) &= \omega \cdot a \cdot \cos(\omega t) \qquad \text{with} \quad \omega = 2 \cdot \pi \cdot f \end{aligned} \tag{3.3}$$

Now, it is possible to give a maximum surface deformation vector at each panel corner point (see figure 3.2 for the surface deformation of the NACA3506 profile used in the RPG experiments). This maximum surface deformation vector at the corner points is then averaged over the panel to result in the maximum surface deformation vector at the panel control point. Together with an oscillation frequency which has to be prescribed as well, equation 3.3 can be used to compute the panel control point velocity at each point in time for an unsteady time stepping simulation. Computing the scalar product of this panel control point velocity and the panel normal vector results in the panel control point normal velocity at the respective point in time.

This then results in a source term which is harmonically oscillating. For every time step, this source term is calculated again and represents the right hand side of the equation, since the source is known. Only IBPA 0° has been implemented, yet. For time-resolved potential flow simulations with IBPAs different from 0°, the source influence coefficient matrix would have to be updated at runtime. The results given in chapter 4.3 show, that the neglected

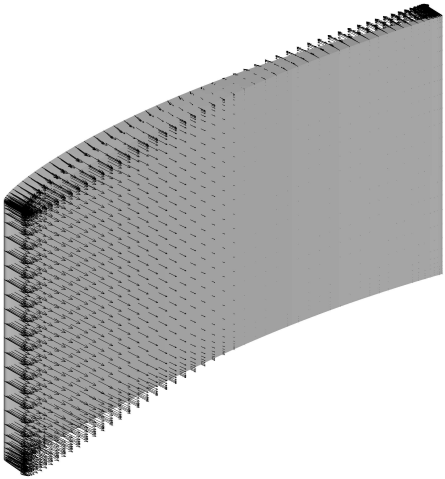

Figure 3.2.: Implemented surface deformation of a NACA3506 prismatic profile (example).

compressibility and viscosity lead to very large differences between theoretical solution and experiment. Consequently, the research was stopped at this stage for this thesis.

4. Explored Approaches for Rapid Flutter Estimation for Turbomachinery in Preliminary Design

In chapter 2, the theoretical background of turbomachinery aeroelasticity has been established. Chapter 3 then introduced the different available unsteady aerodynamic methods which might be used to rapidly assess the aeroelastic stability in an early design phase. Important aspects of the selected methods were introduced, as well.

In this chapter, the results obtained during the exploration of the three selected concepts (chapter 3.2.3) which can be used to obtain a single value describing the flutter susceptibility of a given rotor setup are presented. Also, the selected example use cases for each concept taken from DLR projects are introduced.

The first method presented (chapter 4.1) is the base line approach which resembles the final aeroelastic stability proof of a turbomachinery stage as it is performed traditionally, at the Institute of Aeroelasticity. The flutter proof for a complete demonstrator rotor with the energy method and unsteady time-linearized RANS CFD is presented. Subsequently, methods are introduced which reduce the numerical effort while trying to maintain a similar flutter assurance as a complete computation. The numerical effort is evaluated and estimations are made, when a flutter assessment in preliminary design with a time-linear RANS method becomes feasible.

The second investigation presented (chapter 4.2) is an investigation into the relation between reduced frequency and flutter susceptibility to determine if the reduced frequency might be used as a design criterion in preliminary turbomachinery design.

The third part of this chapter (chapter 4.3) presents the research conducted to assess the viability of unsteady potential fluid flow methods for use in the standard approach instead of 3D RANS methods.

Finally, in chapter 4.4 the obtained results are summarized for each investigated approach.

4.1. Perspective Application of Time-Linearized RANS Aerodynamics in Preliminary Design

It has been demonstrated that time-linearized unsteady CFD methods are capable of predicting the unsteady aerodynamic response to a harmonic excitation correctly (see e.g. Widhalm & Thormann [193]). At DLR, the time-linearized module of the TRACE CFD solver is used to determine the flutter susceptibility of turbomachinery rotors. In this chapter, the full numerical flutter susceptibility computations for one evolution step of a counter rotating demonstrator rotor are presented, followed by investigated approaches to reduce the numerical cost for a flutter susceptibility estimation via time-linearized methods.

4.1.1. DLR CRISPmulti Counter Rotating CFRP Fan Demonstrator as Test Object

Already in 1996 - 1999, DLR and MTU investigated the possible uses and advantages of a counter rotating fan manufactured from carbon fiber material in a joint project called CRISP (Schimming et al. [152]). At that time, a demonstrator (called CRISP-1m) was

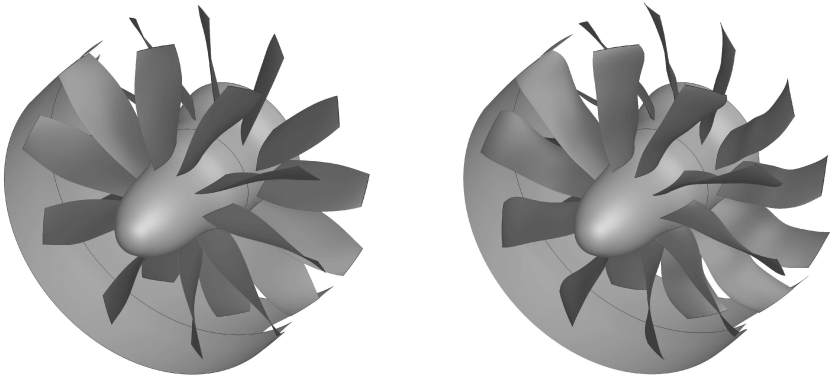

(a) CRISP-1m rotor.

(b) CRISPmulti (evolution stage 1633).

Figure 4.1.: DLR CRISP rotors.

manufactured and tested in the M2VP wind tunnel of the DLR Institute of Propulsion Technology (see figure 4.1a).

By 2010, substantial progress had been made in the development of automated optimization design procedures for turbomachinery bladings. Since counter rotating fans promise efficiency advantages and therefore fuel savings, a new project called CRISP2 (later renamed CRISPmulti) was launched to exploit the advancements made in turbomachinery design and demonstrate the uses of a counter rotating fan arrangement. To demonstrate the advanced design abilities, the geometry of the CRISP-1m demonstrator was to be improved with automated optimization design methods (see appendix D for information on the automated design process Auto-Opti of the DLR Institute of Propulsion Technology). The main goals were a 2% increase in efficiency compared to a single rotating fan and 30% weight savings due to modern carbon fiber blades as well as the demonstration of a novel manufacturing technique for carbon fiber fan blades. The intended final result of the project was a demonstrator to be tested in the modernized M2VP wind tunnel using the existing shaft and bearing systems of the CRISP-1m test rotor. Reusing the shaft and bearing system fixed the number of blades for rotor 1 to 10 and rotor 2 to 12. Similarly, the axial distance between the two rotors and the diameter of the test rotor were to be equal to the CRISP-1m rotor ($\varnothing = 1m$).

The novel manufacturing technique for carbon fiber fan blades consists in an approach that permits a higher degree of automation of the manufacturing process. Flat plates with the desired carbon fiber layup and a thermoplastic resin are pre-manufactured (or ordered). These plates are then deformed in a hot press, liquefying the resin and molding the plate into the shape of the desired fan blades. As a final manufacturing step, the blade geometry is milled from the re-solidified deformed plate (see Forsthofer & Reiber [53]). With this approach, the main advantage of CFC materials (fiber orientation along the main load direction in 3D) is preserved while trading off a small reduction in material strength (thermoplastic resin instead of thermosetting resin) for a higher degree of automation.

Once the aerodynamic and structural design phase was concluded, a full aeroelastic stability proof was conducted with the energy method and the time-linear RANS method integrated in TRACE.

The CRISPmulti demonstrator will also be used as a test case for the investigation of the reduced frequency. However, the focus between the two investigations is different. While the focus of chapter 4.1 is on the in-depth investigation of **one** design step and methods to

decrease the amount of computational resources necessary, chapter 4.2 is concerned with the aeroelastic similarity of **many** different design steps and the conclusions which might be drawn concerning the aeroelastic stability from the reduced frequency. Still, the different design geometries will be used in in chapter 4.1 as well to demonstrate possible similarities.

4.1.1.1. Finite Element Model of CRISPmulti

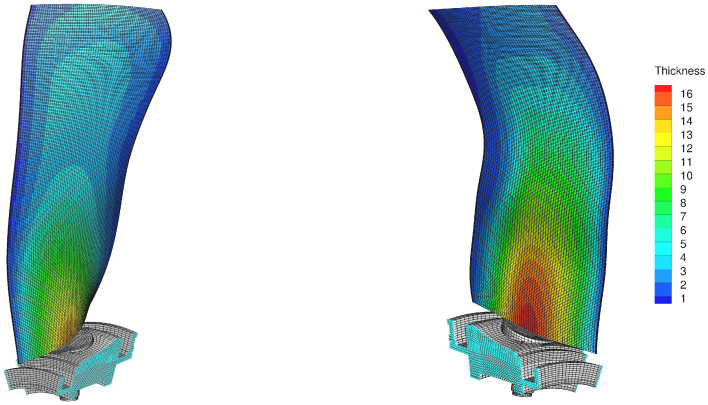

(a) CRISPmulti rotor 1 blade FE model. **(b)** CRISPmulti rotor 2 blade FE model.

Figure 4.2.: CRISPmulti FE models for rotor 1 and rotor 2, one blade each, blade thickness in mm, cyan bullets indicate cyclic symmetry nodes.

To determine the eigenmode shapes and eigenfrequencies of the manufactured blades, an FE model of the two rotors of the CRISPmulti demonstrator was created based on the optimal aerodynamic geometry found during the design phase (see figure 4.2). The models consisted of 16560 quadrilateral shell elements and 19310 volume elements for rotor 1 and 14640 quadrilateral shell elements and 19298 volume elements for rotor 2. The reason for the hybrid flat shell / volume element approach was the considerable steady state deformation of the blades under inertial and surface pressure loads. This is elaborated in appendix E.1, where the FE model is presented in detail.

The bases of the two models were created once with "traditional" FE meshing tools. The shell element meshes of the blades were created automatically with Python programs specifically written for this purpose based on the aerodynamic geometries. Consequently, it was proven that the automated FE computation in the preliminary design process performs reliably. Additionally, accurate FE models (and therefore also numerical modal analyses) were available for each investigated geometry.

Then a "hot-to-cold" (or "unrunning") computation was performed (see appendix E.2 for details), resulting in the final discretized representation of the two demonstrator rotors for finite element computations.

4.1.1.2. CFD Setup of CRISPmulti

For the final aeroelastic stability design proof of the CRISPmulti demonstrator, a CFD mesh with an intermediate mesh resolution was used. It was found in the project (see

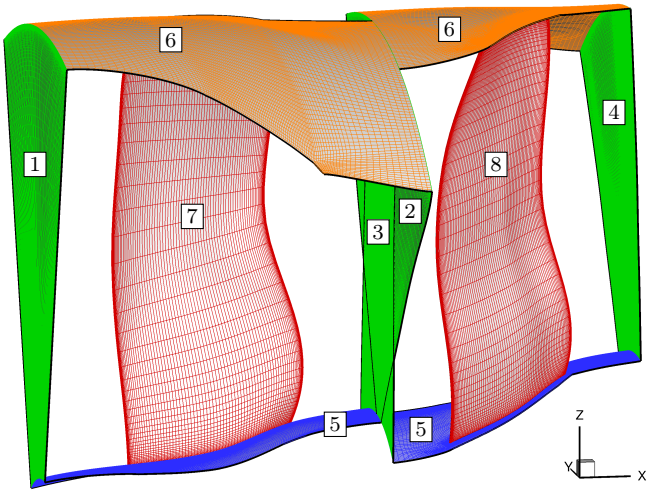

Figure 4.3.: CFD mesh of the CRISPmulti rotors used for the CFD computations with TRACE. Inlet (green, 1), outlet of the rotor 1 passage (green, 2), inlet of the rotor 2 passage (green, 3), outlet (green, 4), hub (blue, 5), shroud (orange, 6), blade rotor 1 (red, 7), blade rotor 2 (red, 8), bold black lines - cyclic symmetry boundaries.

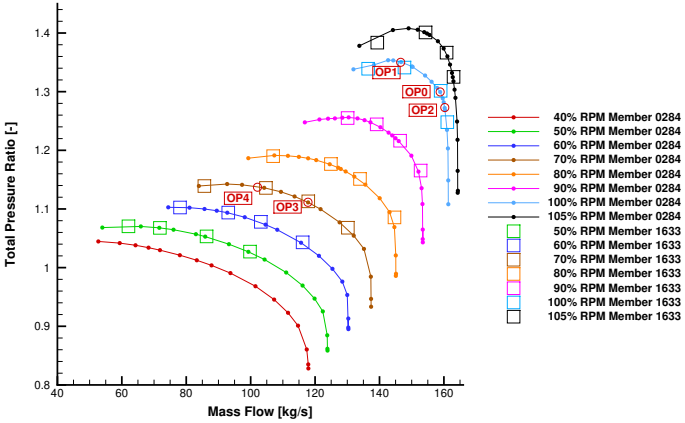

Figure 4.4.: Compressor Map of CRISPmulti evolution step 0284 (member = evolution step). OP0 - OP4 denote the operating points calculated during the automated optimization process.

appendix E.4) that the global unsteady aerodynamic properties are predicted by linear TRACE almost independently of mesh resolution. The used mesh had 803680 cells for the rotor 1 passage and 821600 cells for the rotor 2 passage. For different evolution steps of the CRISPmulti rotor, compressor maps were calculated in order to assess the aeroelastic stability for the whole operating range of the fan based on these steady state results.

The compressor map in figure 4.4 compares two evolution stages (called "Member" in Auto-Opti) investigated towards the end of the optimization process of CRISPmulti. The first one (0284) was computed with the coarser optimization mesh (see appendix E.4), the second one (1633) was computed with the final mesh presented in figure 4.3. It is obvious that the steady state aerodynamic changes between different evolution steps and for different mesh resolutions are minute. This is often the case in late stages of an automated optimization process since a very good value for most target functions has been found and the margins for improvement decrease. The additionally indicated operating points (OP0 - OP4) in figure 4.4 are the steady state aerodynamic solutions which were calculated in the automated optimization to determine the suitability of this particular geometry for the given aerodynamic requirements. Not all five indicated operating points were calculated in each optimization. For these two particular evolution steps, OP4 (70% RPM, close to the surge boundary) was not calculated, therefore there is no dot indicating a steady state solution in figure 4.4.

Comparison of Unsteady Aerodynamic Computations on Coarse and Fine Mesh

For all evolutionary steps of the CRISPmulti rotors, the CFD mesh from the automated optimization was used for the subsequent aerodynamic and aeroelastic analyses. This is in many ways not optimal, since the mesh resolution is coarse and the mesh quality is often not very good (element warp etc.), but the sheer number of different geometries did not permit a time-consuming individual mesh generation process for the aeroelastic computations. Additionally, for a fast flutter estimation process to be usable in an preliminary design, it needs to work on the meshes generated by the optimization tools.

Therefore, a mesh comparison study was conducted for the time-linearized unsteady computations with a very fine mesh created by hand specifically for the respective geometry and the optimization mesh. It was found that the unsteady time-linear RANS computations of linear TRACE result in very similar unsteady flow, independently of the mesh resolution. See appendix E.4 for details. Since the main goal of the investigations were qualitative results in a preliminary design cycle, these minute differences were deemed acceptable.

4.1.1.3. Preliminary Design Geometries of CRISPmulti

Besides the already mentioned aspects, another goal of the CRISPmulti project was the integration of as many design aspects as possible into an automated optimization tool chain to obtain the most suitable blade geometry for a given task with as little human work as possible. Since aeroelastic investigations are only possible late in the design phase, one major goal was to integrate aeroelastic design parameters already into the automated design algorithms. As a result, already in the early design stages, flutter estimations were performed parallel to the optimization procedure in order to identify such an aeroelastic design parameter. As a consequence, a large database of different configurations and aerodynamic damping values at various operating points has been generated.

Table 4.1 presents a short overview of the design geometries obtained over the different preliminary demonstrator design cycles. The different blade and eigenmode shapes of the investigated geometries are presented in figures E.8 - E.37 in the appendix. Figure E.8 and figure E.11 highlight the fact presented by Schuff & Chenaux [155] that the CRISPmulti demonstrator is prone to mode coupling, since the aerodynamic load on the blade surface (OP0 and OP1 have the same RPM) leads to a substantial change in eigenmode shape for the earlier design evolution steps.

	Design Designations	Operating Points
Design cycle 8:	0944, 1175, 1221, 1240, 1428, 1663, 1682, 1685, 1710, 1822, 1898, 1981, 2001, 2016, 2033, 2036, 2077, 2088, 2221, 2248	OP0, OP1, OP3, OP4
Design cycle 11:	4455, 5290, 5616, 5642	OP0, OP1, (OP3, OP4)
Design cycle 12:	5380, 5471, 5489	OP0, OP1, OP2, OP3
Design cycle 14:	2549, 2559, 2661	OP0, OP1, OP2, OP3
Design cycle 15:	5696, 5696_A1, 5696_A2, 5696_A4, 5696_nurCFK	OP0, OP1, OP2, OP3
Design cycle 16:	0284, 1176	OP0, OP1, OP2, OP3
Design cycle 17:	1633	OP0 (Compressor map derived)

Table 4.1.: Available design evolution stages of the CRISPmulti demonstrator fan.

4.1.2. Full Aerodynamic Stability Analysis of a given Evolution Step of an Automated Optimization

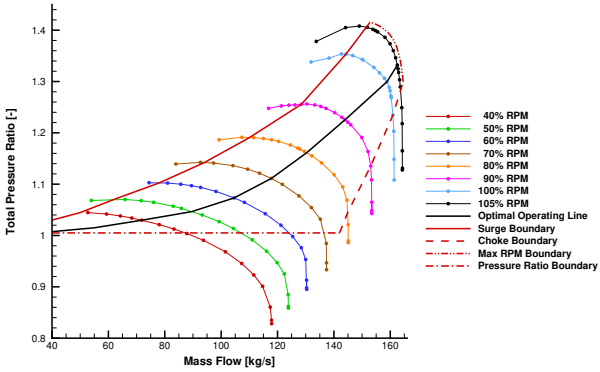

Figure 4.5.: Compressor map of the CRISPmulti rotors with estimated operating boundaries.

The operating conditions of turbomachines and especially aeroengines are variable. Therefore, turbomachines have a certain operating range in which they need to perform acceptably. For a fan or compressor this operating range is visualized in a compressor map depicting the total pressure ratio over the air mass flow through the stage. To be able to also describe a compressor's performance at different operating conditions, generally the corrected mass flow is used as x-axis of the compressor map. There are two ways of computing the corrected mass flow (see Bräunling [26]), one correcting the mass flow only with the total pressure and total temperature, and one correcting the mass flow to a reference total pressure and reference total temperature. For all compressor maps of CRISPmulti, the total inlet pressures and temperatures were the reference pressure and temperature at sea level, therefore the mass flow axis is implicitly the "corrected" mass flow axis according to the second mentioned correction formula.

In figure 4.5, the operating conditions of the CRISPmulti fan are limited by the maximum RPM, the surge boundary, the choke boundary and the pressure ratio boundary. To

determine the flutter susceptibility of a given rotor, the eigenmode shapes with the lowest frequencies need to be tested for aeroelastic instability. As already found by Fottner [54] (see figure 1.3), it is undetermined, where flutter will occur in the compressor map. It is therefore customary to cover the full operating range of the rotor with a sufficient number of steady state calculations and then perform unsteady forced motion (not to be confused with forced response) for each IBPA of each eigenmode shape.

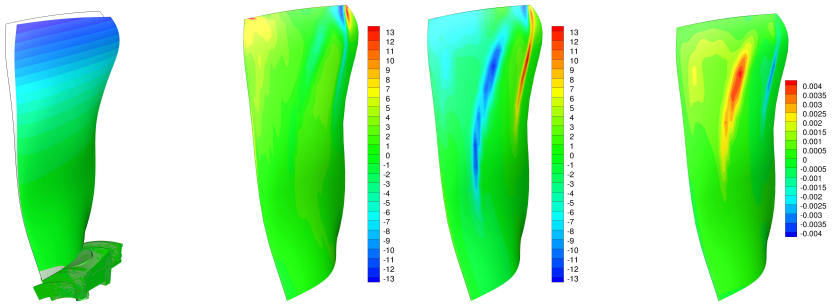

(a) Blade deformation which is mapped on the blade surfaces of the CFD mesh.

(b) Resulting complex unsteady pressure on the blade surface (real part on the left, imaginary part on the right, the indicated values are in $[Pa]$).

(c) Local aerodynamic damping resulting from blade deformation and unsteady surface pressure ($\left[\frac{1}{m^2}\right]$).

Figure 4.6.: Illustration of the results on the blade surface of a forced motion CFD simulation of eigenmode shape 1 computed with modal mass 1 at 0° IBPA and scaled with 0.0001 at the aerodynamic design point.

Generally, the operating range is covered in steps of 10% RPM starting at 50% RPM, reducing the RPM steps towards 100% RPM and beyond. The pressure ratio range is also covered by about 8 to 10 operating points per RPM line. This covers the operating range sufficiently to identify areas with aeroelastic stability problems.

In general, this amounts to the following tasks necessary to assess the aeroelastic stability of a rotor in it's operating range:

- Generate a compressor map of the turbomachinery stage at hand.
  - Perform steady state CFD calculations for 6 - 8 RPM lines with 8 - 10 pressure ratios each (dots on the RPM lines in figure 4.5) in order to resolve the compressor map to an engineering degree of accuracy.
  - Depending on the amount of blade distortion due to inertia and blade surface pressure, the steady state deformation needs to be considered (Schuff et al. [156]).
- Calculate the eigenmode shapes and eigenfrequencies at each operating point depending on inertia load and blade surface pressure load (see figure E.4 in the appendix for a summary of the numerical modal analyses carried out for the design proof geometry of CRISPmulti).
- Perform an aeroelastic stability analysis for each operating point.

- Run an unsteady forced motion CFD simulation for each IBPA of the first three eigenmode families. The results on the blade surfaces for the aerodynamic design point with a blade deformation in the first bending eigenmode shape with IBPA 0° as shown in figure 4.6.
- Determine the aeroelastic stability based on blade deformation and unsteady pressure on the blade surface. Based on equation (2.42), the local aerodynamic work is calculated from blade deformation (figure 4.6a) and complex unsteady pressure on the blade surface (figure 4.6b). The negative real part of the local aerodynamic work is the local aerodynamic damping (figure 4.6c, see chapter 2.3.5).
- The overall result for each operating point is the global aerodynamic damping Λ (local aerodynamic damping summed up for the blade) in an "aerodynamic damping diagram" (figure 4.7a). In this thesis, it depicts the logarithmic decrement of the global aerodynamic damping Λ for each IBPA σ_n for the eigenmode shape families taken into account.

- To assess the flutter susceptibility of a turbomachinery stage over the whole operating range, the minimum values for each mode shape family of each aerodynamic damping diagram are extracted. Then, a compressor map depicting the minimum aerodynamic damping Λ for each eigenmode shape family (figures 4.7b - 4.7d) and for all mode shape families combined (figure 4.7e) can be compiled.

If such an aeroelastic stability analysis was to be implemented into an automated optimization design program, the cost would be immense: Steady state CFD calculations would increase from 3 - 5 to 30 - 50. Additionally, numerous unsteady aerodynamic forced motion simulations would have to be performed. If three eigenmode shape families are considered (which is an engineering standard for aeroelastic stability computations for the design proof), and 10 blades are assumed for the rotor (which is a very low estimate originating from the CRISPmulti fan, any number below might be considered a propeller), 30 unsteady CFD simulations are necessary per operating point.

Even if time-linearized methods are used, where one unsteady solution uses the same order of magnitude of computational resources as a steady state solution, the numerical cost to check one evolution step would increase by about three orders of magnitude. If one assumes that preliminary design is performed using an automated optimization method and a normal automated optimization to take a few days, this would increase the time necessary to a few years.

Consequently, the remainder of chapter 4.1 is devoted to the investigation of methods which promise a reduction of computational effort without compromising the validity of the results.

4.1.3. Reduction of Operating Points

To reduce the amount of necessary calculations, a close look at Fottner [54] (figure 1.3) readily results in a rough estimate where flutter might occur in the operating range. Keep in mind that the goal of these investigations is a fundamental indicator in preliminary design if any given rotor structure will be susceptible to flutter, not a full flutter analysis. This full flutter analysis has to be performed in detail for the final design proof later on in the design process.

If only operating points at the compressor map boundaries are tested for aeroelastic stability, the amount of calculations necessary can be reduced substantially (figure 4.8). One approach would be to perform time-linearized CFD simulations for each RPM step just at the surge and choke boundary. The maximum RPM line would still have to be calculated completely. If these operating points show stable behavior, this is an indicator for aeroelastically stable behavior in the whole operating range.

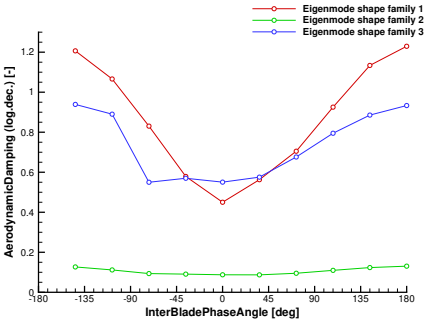

(a) Aerodynamic damping diagram for one operating point depicting the overall damping values of the blade for each IBPA.

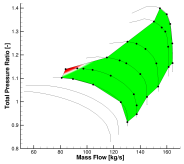

(b) Minimum damping values of eigenmode family 1 in the compressor map.

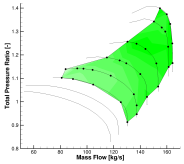

(c) Minimum damping values of eigenmode family 2 in the compressor map.

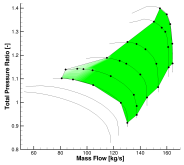

(d) Minimum damping values of eigenmode family 3 in the compressor map.

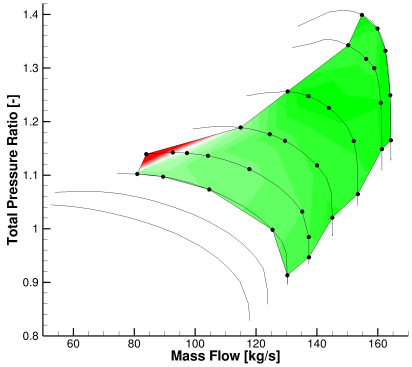

(e) Minimum damping values of all 3 eigenmode families in the compressor map.

Figure 4.7.: Illustration of the results of multiple forced motion CFD simulations in the compressor map. Shades of green indicate positive minimum damping values, shades of red indicate negative minimum damping values.

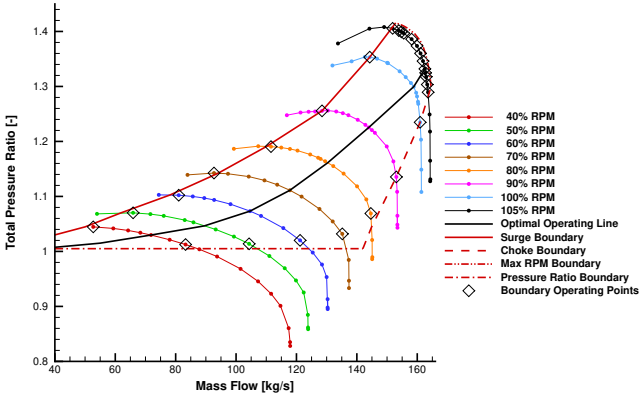

Figure 4.8.: Compressor map with highlighted operating points at the operating boundaries.

Another estimation of the number of necessary computations would then result in the reduced numbers of 15 - 20 steady state CFD calculations (operating points) per design. The number of unsteady forced motion computations per operating point would not be affected by this reduction.

A simple comparison shows that the implementation of this approach still would increase the computational resources necessary for an optimization step by two orders of magnitude (present approach 3 - 5 steady state computations vs. 15 - 20 steady state computations plus at least 450 unsteady forced motion CFD simulations).

4.1.4. Sine Approximation of the IBPA with the Lowest Aerodynamic Damping

From the last two chapters, it became apparent that the main increase in numerical effort to determine the aeroelastic stability at an operating point originates from the number of unsteady forced motion CFD simulations necessary to obtain the aerodynamic damping diagram (figure 4.7a).

Panovsky & Kielb [133] investigated the stability of a low pressure turbine with a quasi 3D Euler code. They surmised that it is sufficient to compute as little as three influence coefficients to determine the minimum aerodynamic damping at a certain aerodynamic design point. Based on three fundamental rigid body mode shapes, Panovsky & Kielb then deduce the aeroelastic stability of all other possible rigid body mode shapes.

It has been established in chapter 3.1.7, that the superposition of 2D mode shapes is not readily feasible for modern compressor blade shapes with eigenmode shapes not adhering to classical rigid body motion.

However, experience at the Institute of Aeroelasticity concurs with the observation of Panovsky & Kielb that the aerodynamic damping diagram exhibits a roughly sinusoidal shape (figure 4.9). This can be explained via the theory of influence coefficients (see Hanamura et al. [75] or May [116]) which states that the result of a blade's influence on itself is almost always positive damping and independent of the IBPA (might be interpreted as the horizontal mean in figure 4.9). The influence of the neighboring blades results in additional damping or excitation depending on the phase shift (IBPA) of the oscillation of the blades, resulting in a nice sinusoidal shape of the aerodynamic damping diagram. The blades fur-

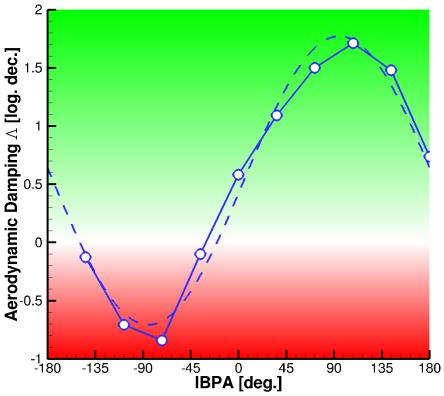

Figure 4.9.: Comparison of an aerodynamic damping diagram to a fitted sine curve.

ther away introduce higher harmonics into the aerodynamic damping diagram, but their contribution is negligible in most cases.

There are cases where the aerodynamic damping diagram does not exhibit a sinusoidal behavior (this is often observed for turbine blades with shrouds or at operating points close to the surge line) or where there are individual IBPAs substantially deviating from the sine curve in positive or negative damping direction (this is often attributed to acoustic resonance). However, for an automated optimization algorithm where predominantly a trend for the development of the aerodynamic damping Λ is desired, approximating the 'aerodynamic damping' vs. 'IBPA' curve with a sine wave might lead to acceptable results (Blocher & Aulich [19]).

If a sine wave with wavelength 2π, arbitrary phase shift and y-axis shift $\overline{x}$ is assumed for the global aerodynamic damping Λ, one can write:

$$\Lambda(\sigma) = \overline{x} + x_1 \cdot \sin(\sigma) + x_2 \cdot \cos(\sigma) \tag{4.1}$$

In equation (4.1), $\overline{x}$, x_1 and x_2 are the unknown factors describing the sine wave. If three global aerodynamic damping values Λ for three IBPA values of the sine curve are known, a linear equation system arises which can be solved for the unknowns $\overline{x}$, x_1 and x_2.

$$\begin{bmatrix} 1 & \sin(\sigma_1) & \cos(\sigma_1) \\ 1 & \sin(\sigma_2) & \cos(\sigma_2) \\ 1 & \sin(\sigma_3) & \cos(\sigma_3) \end{bmatrix} \cdot \begin{bmatrix} \overline{x} \\ x_1 \\ x_2 \end{bmatrix} = \begin{bmatrix} \Lambda(\sigma_1) \\ \Lambda(\sigma_2) \\ \Lambda(\sigma_3) \end{bmatrix} \tag{4.2}$$

In equation (4.2), the subscripts $_1$, $_2$ and $_3$ of the IBPA σ do not refer to nodal diameters but only refer to three distinct IBPAs. Pre-multiplying with the inverse of the coefficient matrix solves this linear equation system.

$$\begin{bmatrix} \overline{x} \\ x_1 \\ x_2 \end{bmatrix} = \begin{bmatrix} 1 & \sin(\sigma_1) & \cos(\sigma_1) \\ 1 & \sin(\sigma_2) & \cos(\sigma_2) \\ 1 & \sin(\sigma_3) & \cos(\sigma_3) \end{bmatrix}^{-1} \cdot \begin{bmatrix} \Lambda(\sigma_1) \\ \Lambda(\sigma_2) \\ \Lambda(\sigma_3) \end{bmatrix} \tag{4.3}$$

Consequently, the least aerodynamic damping over the IBPA range can be derived from the sine curve computed with equation (4.3) based on three computed IBPAs. Solving such a linear equation system is largely done with pre-implemented numerical solution algorithms, but investigating the definition of the inverse of a matrix shows that there are IBPA combinations resulting in more reliable sine wave approximations than others.

The optimal distribution of these three sample IBPAs in order to obtain a reliable sine curve estimation were determined to be 0° and the two IBPAs closest to ±120° (see appendix F). Based on these findings a substantial number of computed aerodynamic damping diagrams were evaluated.

4.1.4.1. Test of the Sine Curve Hypothesis on CRISPmulti Evolution Steps

To test the validity of a sine curve approximation for the global aerodynamic damping Λ over IBPA, all the calculated full aeroelastic stability analyses from the CRISPmulti project were subjected to a sine curve evaluation. For rotor 1, the initial IBPAs evaluated were 0°, 108° and −108°, for rotor 2 0°, 120° and −120°. Then, the IBPA with the predicted smallest global aerodynamic damping Λ and its two neighbors were checked. If one of the two neighbor's aerodynamic damping was smaller than the predicted IBPA's aerodynamic damping, the IBPA curve was evaluated further in the direction of smaller aerodynamic damping.

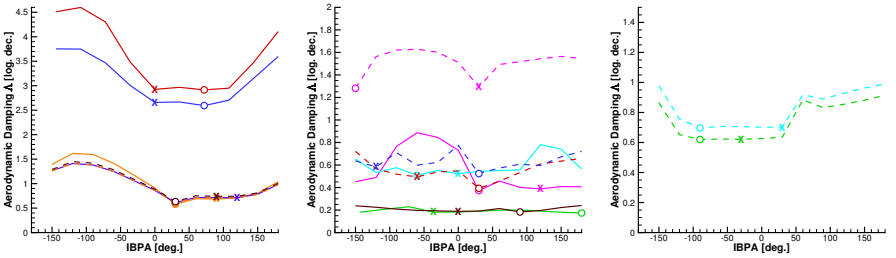

(a) Aerodynamic damping diagrams of the failed cases at OP0.

(b) Aerodynamic damping diagrams of the failed cases at OP1.

(c) Aerodynamic damping diagrams of the failed cases at OP3.

Figure 4.10.: Aerodynamic damping diagrams of cases tested during the CRISPmulti optimization where a sine approximation failed to predict the correct IBPA with the smallest global aerodynamic damping Λ (circles = global minimum, x = predicted minimum, normal lines and dashed lines as well as different colors only serve to differentiate the design geometries). The line colors only serve to differentiate between the failed cases.

Overall, this approach yielded a very high success rate (∼ 96%) whilst predicting a reduction of computational resources by about 50% for these rotors with a very small number of blades. The failed cases are depicted in figure 4.10 and show a relation between the shape of the aerodynamic damping diagram and the operating point for which they were calculated. The operating points on the working line of the fan (OP0 and OP3) show a roughly sinusoidal behavior even though the global minimum was not found. The cases where the minimum aerodynamic damping could not be predicted at OP1 (100% RPM, close to the surge boundary, see figure 4.4) do not show a sinusoidal behavior. Even though the correct IBPA with the smallest global aerodynamic damping Λ was not identified correctly, the magnitude of the smallest global aerodynamic damping was predicted with a very small error. However, while this is true for the tested cases, this cannot be assumed for different turbomachinery designs.

4.1.4.2. Results of the Tests for a Sine Curve Approximation

The tests performed on the already simulated cases of the CRISPmulti optimization showed that a sine curve approximation with testing for success results in a correct prediction in the majority of cases. However, a pure sine approximation with only three points and

prediction of the minimum global aerodynamic damping will result in unreliable results (Blocher & Aulich [19]). Therefore, the sine curve approximation might be used in an automated optimization algorithm, but at least 5 - 6 IBPAs will still need to be calculated for each case.

Following the reasoning already used for the previous numerical load estimations, the number of necessary steady state computations at the selected operating points would be in the range of 15 - 20 (if only the operating boundaries are taken into consideration based on chapter 4.1.3). The number of unsteady forced motion computations per operating point would reduce to ~ 6.

A simple comparison shows that the implementation of this still would increase the computational resources necessary for the overall optimization by almost two orders of magnitude (present approach 3 - 5 steady state computations vs. 15 - 20 steady state computations plus at least 270 unsteady forced motion CFD simulations [3 eigenmode shape families, 6 IBPAs each, per steady state operating point]).

4.1.5. Similarity Methods

During the optimization of the CRISPmulti rotors, it became apparent that some evolution steps showed a very similar aeroelastic behavior to others. Especially, the aerodynamic damping diagrams of some cases were almost identical. It was also observed that the changes in blade geometry tested by the automated optimization algorithm to achieve an improvement in aerodynamic efficiency often were minute in later stages of the optimization.

Since the blade material was not part of the optimization, it was concluded that very small changes in geometry lead to very small changes in eigenbehavior and aerodynamics. Very small changes in eigenbehavior and aerodynamics in turn lead to similar aeroelastic stability.

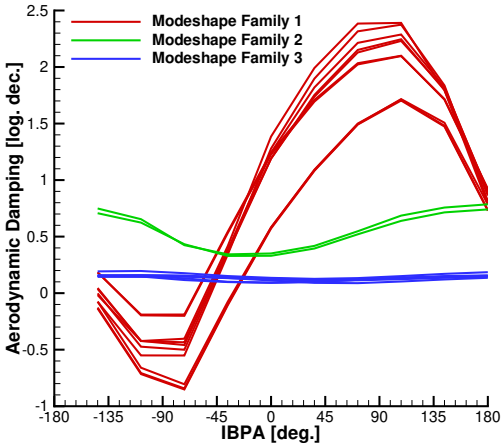

Figure 4.11.: Aerodynamic damping diagrams for cases with similar MAC values. The curves were computed at the same aerodynamic operating point for 10 different blade geometries and their respective eigenmode shapes.

Figure 4.11 illustrates this correlation. The different red, green and blue lines are aerody-

namic damping Λ values at the same operating point for different design stages of CRISPmulti with very similar geometries and very similar eigenbehavior. Even though the aerodynamic damping vs. IBPA curves vary (especially for mode shape family 1), the general shape is similar and the location of the general minimum is similar, as well.

Mayorca et al. [117] used the MAC (modal assurance criterion) to successfully determine the similarity of eigenmode shapes in aeroelastic investigations. Based on this, an even more radical reduction approach was investigated (see Blocher & Aulich [19]): If the MAC values of different optimization evolution steps are sufficiently similar, it might be permissible to predict the IBPA with the smallest aerodynamic damping from previous aeroelastic stability analyses.

The MAC value is defined as:

$$MAC = \frac{\left|\vec{\phi}_1^T \cdot \vec{\phi}_2\right|^2}{\left|\vec{\phi}_1^T \cdot \vec{\phi}_1\right| \cdot \left|\vec{\phi}_2^T \cdot \vec{\phi}_2\right|} \tag{4.4}$$

The ten very similar 'global aerodynamic damping' vs. 'IBPA' curves for eigenmode shape family 1 in figure 4.11 have the following MAC values when compared to the eigenmode shape with the smallest evolution step number:

Config. 1 vs.	MAC value
Config. 1	1.000000
Config. 2	0.996718
Config. 3	0.994406
Config. 4	0.994207
Config. 5	0.992253

Config. 1 vs.	MAC value
Config. 6	0.999995
Config. 7	0.995618
Config. 8	0.999968
Config. 9	0.998231
Config. 10	0.998605

Table 4.2.: MAC values of the ten configurations of eigenmode shape family 1 shown in figure 4.11.

To test the hypothesis that a sufficiently similar eigenmode shape will result in a similar least global aerodynamic damping value for a new evolution step's geometry and aerodynamics, the cases which were calculated for the CRISPmulti project were revisited and compared.

The different available geometries were checked in the order in which they were created during the optimization runs. For the first case, a "full" aeroelastic stability analysis was performed and the results of the already performed stability analysis were stored in a database, together with the number of unsteady CFD computations necessary. For all subsequent cases, a "full" aeroelastic stability analysis was performed if the MAC value was below a certain threshold value, otherwise the result of just one unsteady CFD simulation (at the appropriate IBPA) was stored. After this analysis, it was possible to determine how many unsteady forced motion CFD simulations could have been omitted and also how well this algorithm predicted the smallest global aerodynamic damping. Only two outcomes were permitted: "success" (the IBPA with the smallest global aerodynamic damping was identical to the one of the similar MAC eigenvalue) and "failure" (the smallest global aerodynamic damping occurred at another IBPA). Different operating points were treated separately.

The results of the two most meaningful tests are presented in table 4.3. Different conclusions can be drawn:

- The similarity of the aerodynamic damping does not only depend on the eigenmode shape, but also on the flow. The two columns indicating the "success rate" clearly differ between the operating points. At 100% RPM on the operating line and closer to the surge line (OP0, OP1) the success rate is smaller than at 70% RPM at the operating line and closer to the surge line (OP3, OP4). At 100% RPM with a smaller pressure ratio (OP2) however, the success rate is 100% if a MAC similarity is found.

Operating Point	Number of Cases	MAC Threshold Value = 0.995		MAC Threshold Value = 0.999	
		Success Rate	Computational Time Saved	Success Rate	Computational Time Saved
OP0	120	74.16%	70.35%	81.66%	61.39%
OP1	120	78.44%	64.96%	86.66%	57.42%
OP2	30	100%	66.05%	-	-
OP3	102	94.11%	72.53%	96.07%	61.41%
OP4	66	87.87%	74.77%	94.54%	61.37%

Table 4.3.: Comparison of the possible time gains when basing the aeroelastic stability analysis on an eigenmode shape MAC comparison (operating points as indicated in figure 4.4).

- Constraining the MAC threshold to a higher value will increase the rate of success at the expense of more computational time.
- Ideally, the success rate would approach 100% for all cases at some threshold value with computational resource savings still being substantial, but there seems to be no clear boundary, especially considering the flow dependency.

The conclusion from these results is that there seems to be no single simple MAC boundary value at which the aeroelastic stability for one case is similar to another. Also, the steady state flow which is the basis for the unsteady CFD simulation will have to be accounted for as well.

In addition to the issues identifiable from table 4.3, it is immediately obvious that this approach would generate a very high computational load in the beginning of a preliminary design process where the changes in geometry and the gains in aerodynamic efficiency are still large. This means, the computational load appears where it is most undesirable.

Summary for Similarity Methods

If the same assumptions are made as for the previous simplification methods, one could approximate the number of necessary computations as follows:

MAC Similarity Method Only: For the present automated optimization approach, 3 - 5 steady state RANS CFD computations plus some FEM computations which do not require much time are performed. If only the boundaries of the compressor map would be tested, the computational load would increase with the MAC similarity method to about 15 - 20 steady state computations plus about 60% of the original 450 unsteady forced motion CFD simulations (which is a similar number as the sine approximation approach).

MAC Similarity Method Combined with a Sine Approximation Approach: If one assumes a most favorable combination of these two methods, the total number of necessary unsteady forced motion CFD simulations would drop to $(60\%)^2$ of the original assumed 450 ($\Rightarrow$ 162) unsteady CFD simulations per evolution step. This is a large reduction from the originally assumed >1000 necessary simulations. However, this reduction comes at the price of reduced reliability of the aeroelastic stability prediction.

4.1.6. Reduction of Numerical Effort by Calculating only a 2D slice of the Flow Channel

Since 3D RANS methods and their respective reduced methods did not result in a large enough time saving to satisfy the needs of the presently used automated optimization

algorithm for preliminary design at DLR, less computationally time-consuming methods needed to be found. As already mentioned (section 1.5, Bräunling [26] and Crouse [45]), turbomachinery blades were/are created from profiles exhibiting desirable properties.

Therefore, it might be possible to approximate the aeroelastic stability of a turbomachinery part by its aeroelastic stability properties at one specific span section (as it is done by Panovsky & Kielb [133] and many other researchers using their method, mainly for LPT design). To test this hypothesis, one of CRISPmulti's evolution step's geometries was investigated with a quasi-2D unsteady time-linearized RANS method.

Since a full compressor map had already been calculated and the Campbell diagram was also available, slices of 1 volume cell were extracted from the 3D steady state CFD solution. Then, the blade deformation was mapped onto the left over part of the blade surface and the new "hub" and "shroud" surfaces were declared as inviscid walls. This was followed by the previously introduced time-linearized forced motion solution.

While performing these tests, it turned out that the time-linearized solution of one quasi-2D slice of a turbomachinery rotor indeed performs very fast. The solution times were at about 2 CPUmins per eigenmode shape and IBPA. However, it was discovered that the method did not perform reliably. It seems that setting the inviscid walls together with a previous 3D flow solution (with non-negligible radial flow properties) will in some cases result in an unsolvable equation system. This is another proof for the already mentioned phenomenon that the flow in turbomachines cannot be approximated to be purely two-dimensional.

It was additionally concluded that 3D steady state CFD simulations would be necessary in order to obtain the appropriate surface pressure distributions for the necessary numerical modal analysis with surface pressure and inertia loading. This would result in the 10 - 15 steady state CFD solutions based on the simplification proposed in chapter 4.1.3. Then, either a method would have to be found to make the flow acceptable for a quasi 2D time-linearized solution or steady state quasi-2D simulations with inviscid walls at "hub" and "shroud" would have to be performed to precondition the solution for quasi-2D time-linearized solutions with blade deformation. Overall, this would still increase the time necessary for an analysis of an evolution step in an automated optimization process by a factor of about 6 - 10. Since it was shown that the flow in turbomachinery rotors is often dominated by 3D phenomena which cannot be captured in a 2D flow, the validity of these investigations would be debatable. Therefore, this investigation was aborted.

4.2. Reduced Frequency to Determine the Flutter Susceptibility

In chapters 3.2.3 and 3.4, the reduced frequency ω_{red} was introduced and its significance for aeroelastic stability estimations in the past and present was stated. It was also stressed that Sisto [160] outright dismissed the concept of using the reduced frequency as a design rule already in 1987. Despite that, it is well proven (e.g. Belz & Hennings [14]) that reducing the reduced frequency of an eigenmode shape at a certain flow condition will in effect increase its flutter susceptibility.

Therefore, it was investigated if an adaptation of the reduced frequency criterion might be a first indicator of the flutter susceptibility of a certain rotor structure. An additional advantage of using the reduced frequency ω_{red} is that it can be calculated with values which are generated in a preliminary design cycle anyway.

Already in chapter 4.1.1, the counter rotating fan demonstrator CRISPmulti of DLR was introduced. In chapter 4.1, the focus was on an in-depth investigation of one design step's blade geometry. Now, the same demonstrator rotor will be used again, but the focus shifts towards the many different design steps' geometries and their inter-dependencies (see chapter 4.1.1.3 for the different design geometries).

Based on the design evolution stages given in table 4.1, the relation between the minimal aerodynamic damping Λ and the reduced frequency ω_{red} was investigated.

4.2.1. Comparison of Reduced Frequency and Least Aerodynamic Damping for an Example Use Case

As a first investigation step, the correlation between reduced frequency and minimal aerodynamic damping for each eigenmode shape found at each operating point was plotted. The eigenmode shapes were sorted by their eigenfrequencies. These results can be found in figures E.38 - E.42 in the appendix. The additional subscript for global aerodynamic damping Λ and reduced frequency ω_{red} denotes the operating point at which the values were computed. OP0 denotes the aerodynamic design point, OP1 a point at 100% RPM close to the surge margin, OP2 a point at 100% RPM close to the choke margin and OP3 and OP4 represent a point on the operating line and one close to the surge margin at 70% RPM, respectively. No apparent trend for a correlation between minimum aerodynamic damping Λ_{min} and reduced frequency ω_{red} is discernible in any of the figures E.38 - E.42 in the appendix.

Still, the main goal of the investigation was a single coefficient for each preliminary design denoting the flutter susceptibility over the complete operating range of the stage. Therefore, it was concluded that the prescribed approach from chapter 3.4 using the reduced frequency at the ADP as a measure might represent the influence of the reduced frequency ω_{red} better. Figure 4.12 consequently shows the minimal aerodynamic damping Λ_{min} for each design over the reduced frequency $\omega_{red,\,OP0}$ for each eigenmode shape family (grouped purely by their frequencies) and each rotor. While figure 4.12a, does not seem to show any trend, figures 4.12b and 4.12c seem to indicate a weak correlation between smallest computed aerodynamic damping $\Lambda_{min,\,global}$ and reduced frequency $\omega_{red,\,OP0}$ at the ADP.

One important lesson from the figures E.8 - E.37 in the appendix is that the eigenmode shapes between the different operating points and between the different design evolution steps differ. The design rules introduced in chapter 3.4 were specifically for certain eigenmode shapes. Therefore, the eigenmode shapes and their respective smallest aerodynamic dampings Λ_{min} and reduced frequencies ω_{red} were grouped according to the identified four major mode shapes (first bending, corner flap, torsion, second bending).

In figure E.43 in the appendix, the computed smallest aerodynamic damping values Λ_{min} are visualized over the reduced frequency ω_{red} and grouped by the eigenmode shapes identified from figures E.8 - E.37.

Since figure E.43 in the appendix compares the values at each operating point only, figure 4.13 establishes a relation between the reduced frequency at the aerodynamic design

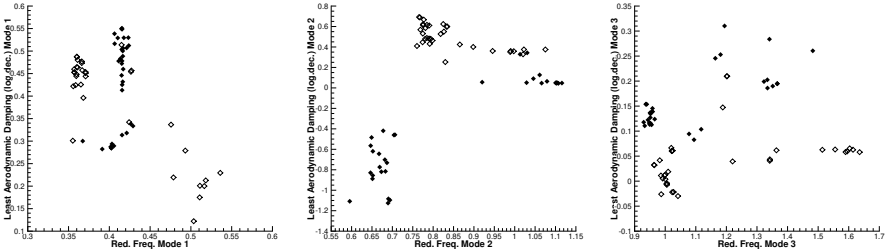

(a) Smallest aerodynamic damping of all computed operating points $\Lambda_{min,\,global}$ over reduced frequency computed at OP0 $\omega_{red,\,OP0}$, eigenmode family 1

(b) Smallest aerodynamic damping of all computed operating points $\Lambda_{min,\,global}$ over reduced frequency computed at OP0 $\omega_{red,\,OP0}$, eigenmode family 2

(c) Smallest aerodynamic damping of all computed operating points $\Lambda_{min,\,global}$ over reduced frequency computed at OP0 $\omega_{red,\,OP0}$, eigenmode family 3

Figure 4.12.: Global smallest aerodynamic damping $\Lambda_{min,\,global}$ over reduced frequency $\omega_{red,\,OP0}$ found for different rotor evolution steps (grouped by eigenmode number, full diamonds denote rotor 1 of CRISPmulti, empty diamonds denote rotor 2 of CRISPmulti).

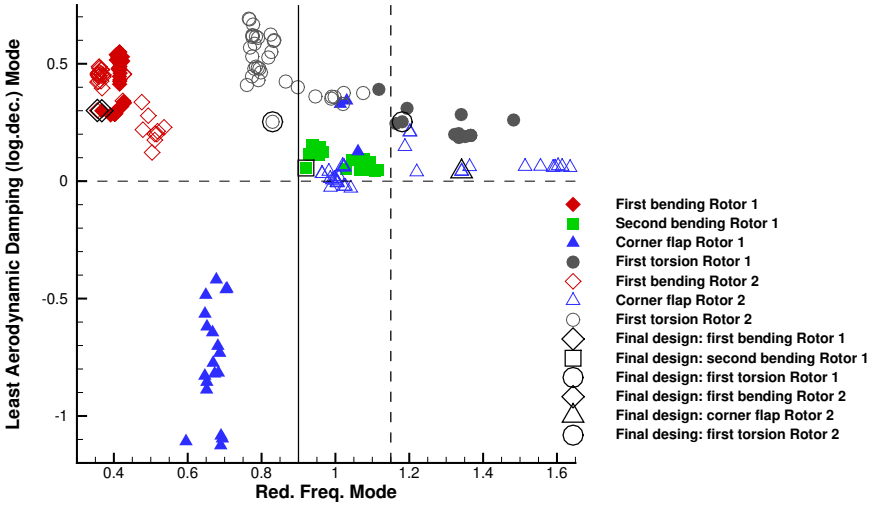

Figure 4.13.: Global smallest aerodynamic damping $\Lambda_{min,\,global}$ over reduced frequency $\omega_{red,\,OP0}$ found for different rotor evolution steps (grouped by eigenmode shape).

point $\omega_{red,\,OP0}$ and the smallest global aerodynamic damping value $\Lambda_{min,\,global}$ found for the respective design evolution step based on the eigenmode shape (analogously to figure 4.12). In figure 4.13, the second bending eigenmode shape only appears for rotor 1 and only positive global aerodynamic damping values were found. Likewise, the corner flap eigenmode shape (see e.g. first row of figure E.9) appears only in earlier design stages for rotor 1 and consequently has no "final design" representation. From this figure, a clear trend is discernible: The reduced frequency design criterion given in Sisto [161] and table 3.3, would definitely have led to stable geometries for the CRISPmulti project. However, especially the torsional eigenmode shapes violated the design criterion while still exhibiting stable behavior. Also, some eigenmode shapes appearing are not first bending or torsion but a corner flap eigenmode shape, and this is the most critical eigenmode shape for the CRISPmulti evolution steps.

An interesting observation is the higher stability of the rotor 2 torsion eigenmode shape compared to the rotor 1 torsion eigenmode shape while having lower reduced frequencies. This is attributed to the swept form of the rotor 2 blades which introduces additional aeroelastic stability in analogy to swept aircraft wings.

The reduced frequency and smallest global aerodynamic damping for the final design in the optimization cycle are highlighted in figure 4.13. The "traditional" sequence of first bending eigenmode shape, then first torsion, then some other mode shape (which was the base for the design criterion of chapter 3.4) is observed for rotor 2. For rotor 1 on the other hand, the second bending appears before the first torsion, which is not unusual but is not captured by the design rule. It is noteworthy that this design did not indicate aeroelastic stability problems for the computed operating points during the preliminary design cycle. Still, potential aeroelastic stability issues were detected at part speed approaching the surge boundary when the complete compressor map was investigated (compare to figure 4.7).

One can therefore conclude from the observations that:

- The mode shape is indeed a crucial factor for the aeroelastic stability.
- The reduced frequency criterion of 0.333 for the first bending eigenmode shape from table 3.3 would have permitted the designs created in the preliminary design of CRISPmulti. Still, the aeroelastic stability especially at part speed close to the surge boundary might not have been guaranteed (see figure 4.7 and Schuff & Chenaux [155]).
- In the case of the CRISPmulti rotor, the design criterion for the first torsional eigenmode shape could have been relaxed to a substantially lower value than the 1.6 given in table 3.3. Still, no globally valid argument can be made for this, since the observed sweep of the blade might stabilize the torsion. This may not be the case for other designs.
- Corner flap eigenmode shapes seem to be very aeroelastically unstable. They were the only eigenmode shapes which exhibited a clear boundary for stable or unstable behavior in the CRISPmulti preliminary design evolution (vertical lines in figure 4.13). Still, the stability boundary would have been different for rotor 1 (~ 0.9) and rotor 2 (~ 1.15). This is most probably due to the different corner that flaps (rotor 1 $\rightarrow$ trailing edge corner, rotor 2 $\rightarrow$ leading edge corner).

One important thing to be stressed here is: These conclusions can be drawn now that the preliminary design of the CRISPmulti rotor is finished from a relatively large number of computed cases. These results were not available at the beginning of the design cycle of the CRISPmulti case. Similarly, these results can only be used for the design of a future compressor operating in the same conditions as the CRISPmulti fan (relatively similar compressor map). For a different compressor, these values would need to be re-derived.

4.3. Vortex Lattice Forced Motion

In chapter 3.2.3, a nonlinear unsteady potential flow solution was proposed as an alternative to time-linearized RANS solutions in preliminary design, since it uses a simpler model for the aerodynamics part but makes no harmonic assumptions for the unsteady response of a flow to a vibratory deformation of a surface. Then, the selection of vortex lattice over doublet lattice as well as the used vortex lattice method (CMARC) were presented in chapter 3.5. This chapter now presents the selected use case from an experiment previously carried out, the results of the implemented changes to the vortex lattice method and the results of the computations.

The example use case is an annular cascade experiment for which steady and unsteady pressure coefficient values were available for two flow cases. These cascade flow cases were chosen because they resulted in very detailed and accurate experimental results for the steady and unsteady pressures on the blade profiles which can be used to validate numerical flow solvers. The cascade and its blade geometry are presented in chapter 4.3.1. Chapter 4.3.2 presents the two investigated flow cases and chapters 4.3.3 and 4.3.4 present the computations with the vortex lattice code CMARC for the steady and unsteady case, respectively.

4.3.1. NACA3506 Cascade Experiment as Example Use Case

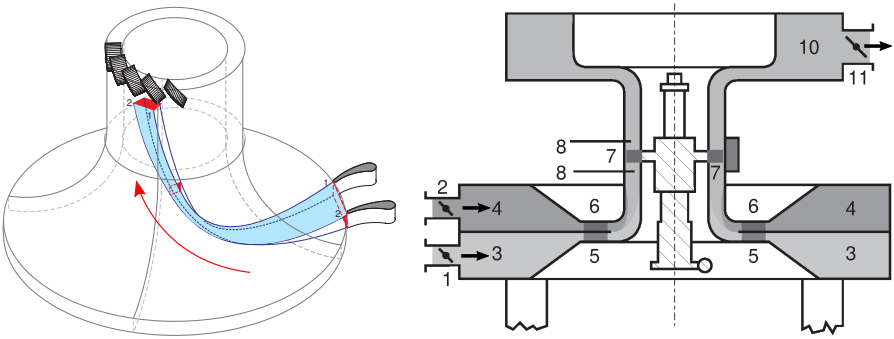

(a) Flow through an annular wind tunnel with preswirl vanes.

(b) Schematic cross section of the RPG wind tunnel (Bölcs [22]).

Figure 4.14.: Schematic flow and cross section of the RPG wind tunnel.

One of the main challenges investigating compressor or turbine blades for aeroelastic effects experimentally is the rotation of the blades themselves. Once the blades are fitted with unsteady pressure transducers and position measurement, the resulting signals need to be transmitted to a data acquisition unit. Due to the frequency of the blades' vibrations and the desire for reliable data, the amount of data transmitted from the rotating system to the data acquisition unit is quite substantial. Similarly, the blade deformation needs to be excited. This consumes considerable energy, which needs to be transported into the rotating system. The bandwidth of data which can be sampled via slip rings is limited as well as the energy that can be conducted by slip rings. One approach to remedy the limited bandwidth are telemetries that send the sampled data via radio frequencies from the rotating system to a data acquisition unit. Still, these telemetries need to be mounted very close to the axis of revolution of the rotor lest the centrifugal forces destroy the delicate electronics. Telemetries however, cannot solve the problem of transmitting large amounts of energy into a rotating system. Therefore, different excitation systems (oscillating guide

vanes, air jets, acoustic excitation, magnetic excitation, ...) have been developed which all considerably increase the complexity of the experimental setup.

To overcome these challenges, Bölcs [22] invented an annular cascade wind tunnel. This wind tunnel (originally located at the Laboratoire de Thermique Appliquée et de Turbomachines of the École Polytéchnique Fédérale de Lausanne, now Institute of Aeroelasticity, German Aerospace Center, Göttingen) uses a set of guide vanes to rotate the inlet flow (see figure 4.14a). The stationary blades of the cascade thus experience a flow almost identical to the one through a rotating rotor.

Figure 4.14b shows a cross section of the RPG wind tunnel. Air is compressed by an industrial compressor and enters the annular wind tunnel via valves (1, 2). After passing the settling chambers (3, 4) the flow passes the preswirl vanes (5, 6) and then the test cascade (7). At the positions numbered (8), there are windows for probes to measure the onflow and the flow leaving the cascade. Then, the flow enters another settling chamber (10) and leaves the wind tunnel via another valve (11).

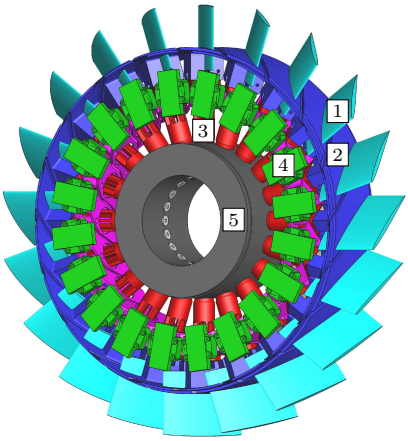

(a) Annular cascade assembly with the prismatic NACA3506 blades (cyan, 1), the blade mounting (blue, 2), the torsional spring (red, 3), the magnet arrangement (green, 4) and the base ring (gray, 5).

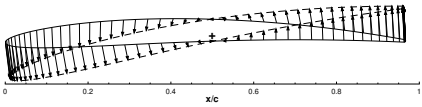

(b) Blade deformation due to electromagnetic excitation with the cross denoting the center of rotation.

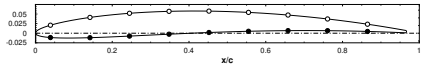

(c) Distribution of steady pressure probes at 20%, 50% and 80% channel height for three channels respectively (pressure side and suction side on adjacent blades).

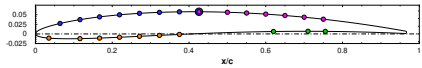

(d) Distribution of unsteady pressure transducers at 50% channel height for two channels on 4 adjacent blades (blades in clockwise order as depicted in figure 4.15a, pressure transducer colors for blades in ascending order: green, blue, orange, purple).

Figure 4.15.: The NACA3506 cascade assembly as well as blade deformation and location of pressure transducers.

Belz and Hennings ([79], [13], [14], [15]) conducted a number of experimental campaigns in this wind tunnel. One of the test cascades investigated consisted of 20 NACA3506 profiles mounted on a spring system (see figure 4.15a item 3) favoring an excitation in the first torsional rigid body mode of the blade (see figure 4.15b). To excite a blade motion in this first torsional mode, permanent magnets were mounted to the blade base (figure 4.15a item 4) which were attracted or repulsed via electromagnets facing them once the ring was mounted in the wind tunnel. Supplying a suitable electrical current (frequency and energy), resulted in an excitation of the first torsional eigenmode of the blades (the experiment setup and results are described in Belz [11] and [12]). One of the goals of the experiments was the determination of the influence of the reduced frequency on the aeroelastic stability of

the blades (see chapters 3.2.3, 3.4 and 4.2).

For several operating points, steady state and unsteady pressure measurements were performed. For the steady state pressure measurements, 3 blade channels were fitted with steady state pressure probes at 20%, 50% and 80% channel height. The steady state pressure probes were distributed on 6 blades, with the pressure and suction side probes for one channel height on adjacent blades of one blade passage (empty and filled bullets in figure 4.15c). The unsteady pressure transducers were distributed at 50% channel height over 4 blades (see figure 4.15d). The unsteady pressure distribution around one blade resulting from a specific excitation pattern was then extracted via superposition and phase shift during post-processing.

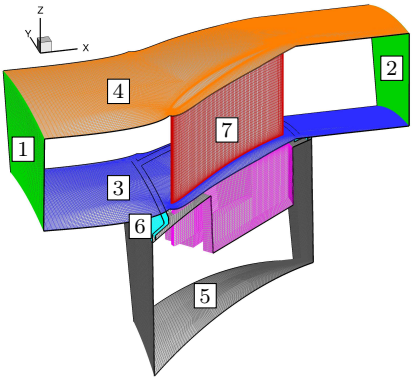

(a) CFD mesh of the annular cascade used for the CFD computations with TRACE. Inlet (green, 1), outlet (green, 2), hub (blue, 3), shroud (orange, 4), cavity (gray and purple, 5), labyrinth connection between main flow and cavity region (cyan, 6), blade (red, 7), bold black lines - cyclic symmetry boundaries and interface areas between non-matching meshes.

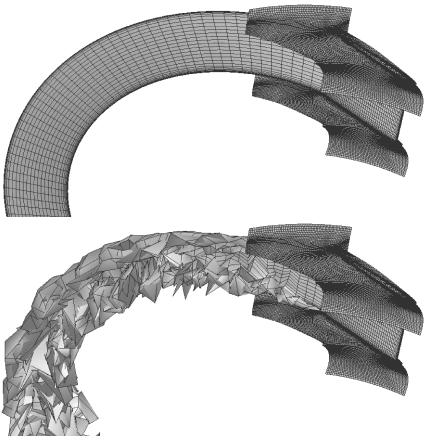

(b) Potential flow mesh based on the CFD mesh for the computations with CMARC. Computations for the flow of case s043 from table 4.4; wake convection with free stream velocity only (top) and local velocity (bottom).

Figure 4.16.: 3D finite volume CFD mesh and surface potential flow mesh for the NACA3506 annular cascade.

To double-check the blade deformation, a 3D volume FE model was created which confirmed the first eigenmode shape to be exactly as intended and shown in figure 4.15b.

For the CFD calculations a pre-existing mesh (figure 4.16a) was used. This mesh resolved not only the main flow channel of the cascade but also the cavity below the blade, since it had been shown earlier that the leakage flow through the cavity influenced the steady state results (Kahl & Hennings [90]). In figure 4.16a, only the surfaces of the volume mesh are depicted with even the cyclic symmetry surfaces omitted to visualize only the inlet, outlet and wall areas. The labyrinth connection was connected to the main flow area and the cavity area via non-matching interfaces. Since it was known from previous investigations that a leakage mass flow entering through the cavity was present in the experiments, a leak inlet was placed in the cavity, improving the agreement between experimental and numerical results greatly. The comparison and discussion of the unsteady 3D linear RANS results with the experimental data and their dependence on the accuracy of the steady state RANS solution has been discussed in Blocher et al. [21].

In figure 4.16b, the used mesh for the potential flow computations with CMARC is presented. To implement a solution which might be used in a preliminary design method, the potential flow surface mesh was based on the finite volume mesh of the 3D RANS computations. The surfaces of the volume meshes were extracted and every second mesh line was deleted in both surface coordinate directions. Due to the reported speed of 3D potential flow solvers, this was deemed sufficient.

In order to represent the influence of the full annulus on the passage mesh, cyclic symmetry expansion was implemented into the potential code CMARC (see chapter 3.5.1.1). The implemented wake convection method in CMARC was relying on the wake emanating from an airplane wing trailing edge and the airplane body from mesh lines reaching to the center symmetry line (for symmetric cases) or merging at the trailing edge of the airplane body with the wing from the symmetric other half. Only a very rudimentary wake surface intersection checking routine was implemented. For turbomachinery applications with known vortex development, this was not sufficient. Therefore, a wake surface intersection check routine was implemented which shifted intersecting points of the wakes to a small margin "outside" the hub and tip surfaces. No velocity adjustment was implemented. This resulted in the somewhat ragged wake rollup depicted in figure 4.16b (bottom half). This might be remedied by smaller wake time stepping or a more sophisticated wake smoothing routine. However a smooth wake rollup was not the goal of the investigations.

4.3.2. Investigated Flow Cases

Two test cases (one subsonic, one transonic) with the NACA3506 geometry of the RPG experiments introduced in chapter 4.3.1 were performed with the implemented changes to the CMARC program. The two cases are summarized in table 4.4.

	Subsonic Case **s043 / z043**	Transonic Case **s014 / z014**
Average onflow Mach number	0.76	0.86
Average onflow angle of attack	48.7°	49.6°
Sound velocity	333.4 $\frac{m}{s}$	326.1 $\frac{m}{s}$
Reduced frequency	0.411	0.359

Table 4.4.: Two flow cases for which steady state and unsteady blade oscillation experiments were performed in the RPG. The 's' in the description indicates the steady state flow case, the 'z' indicates an unsteady blade vibration experiment with the same steady state base flow.

The reduced frequencies of the blade eigenfrequencies excited with the magnet system were in the range of the reduced frequencies investigated for the CRISPmulti test cases. For global comparability, the global aerodynamic damping Λ over the blade surface would have to be computed, since it is the measure for the aeroelastic stability of the blade.

In light of the main goal of this investigation which was only the determination if the results of unsteady potential flow solutions are a lot faster than unsteady 3D time-linear RANS solutions while maintaining a similar accuracy, this has been omitted. Instead, the unsteady pressure prediction results of the two methods were compared directly to each other and to the results of the experiment.

4.3.3. Steady State Results with CMARC for the RPG NACA3506 Geometry

Once the adjustments to the potential flow panel code CMARC for steady state turbomachinery applications were implemented, a series of tests were performed. The first comparison was the reproduction of the steady state experimental results.

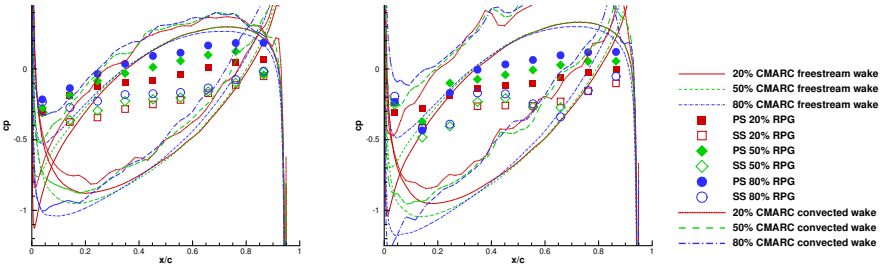

(a) Subsonic case s043. **(b)** Transonic case s014.

Figure 4.17.: Influence of wake convection scheme on the steady state solution with CMARC.

As a first numerical test, the influence of the wake on the steady state potential solution was investigated. Figure 4.17 shows the influence of the wake convection scheme (see figure 4.16b) on the steady state solution. In figure 4.17a, the influence of the wake rollup on the subsonic case is highlighted. Figure 4.17b shows the analogous results for the transonic case. In both graphs, the ragged wake rollup has two effects. The first is a change of the global shape of the surface pressure over the profile. This is desired and can be important for the accuracy of the flow solution. However, potential flow solutions are often dependent on manual tuning, therefore most potential flow solvers offer the possibility to (a) convect the wake with the local velocity, (b) convect the wake with the free stream velocity or (c) use a previously computed wake without readjustment (CMARC manual [2]).

The second effect is a ragged form of the pressure distribution on the blade surface. This is due to the ragged form of the wake and the influence of the cyclic symmetry which accounts for the influence of the neighboring wakes as well. Consequently, the unsteadiness of all circumferential wakes amplifies the influence of the wakes. This might be remedied with a computation with very small time steps and a very rigorous wake smoothing algorithm. This in turn would influence the steady state solution. The main goal of the investigation into this potential method was not an accurate steady state solution, but the determination of the effect of an unsteady blade vibration on the flow. In light of this, it was decided that a simple wake convection with the free stream velocity would be sufficient as a preliminary solution to this particular problem.

The second steady state applicability test was the comparison of the steady state surface pressures predicted by the potential flow solver CMARC with the experimental results and the steady state 3D RANS results from TRACE. Figure 4.18 shows the obtained steady state results for the comparison calculations to the experiments. In figures 4.18a and 4.18b, the steady state simulations performed with TRACE are presented. These results were not obtained in "one shot" but the leakage mass flow in the cavity (see chapter 4.3.1) was adjusted to obtain the most fitting results (see Blocher et al. [21]). The potential flow results from CMARC (figures 4.18c and 4.18d) show large differences to the experimental results in comparison to the 3D steady state RANS solutions with TRACE. There is the possibility to do a Prandtl-Glauert compressibility correction in CMARC. The results of this are presented in figures 4.18e and 4.18f. It is obvious that a compressibility correction routine improves the accuracy of the steady state results. However, they do not approach the accuracy of the 3D RANS solution and do not show the influence of the shock on the suction side of the airfoil. This shows once again that the use of steady state potential flow solutions is quite limited for flows with $\mathrm{Ma} > 0.7$.

Yet again, the results of these computations were intended as a fast alternative to obtain results which might be corrected with steady state CFD data to obtain a compressor map

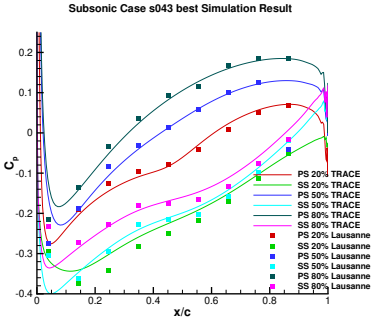

(a) Measured pressure values (s043) compared to steady state 3D RANS solution with TRACE.

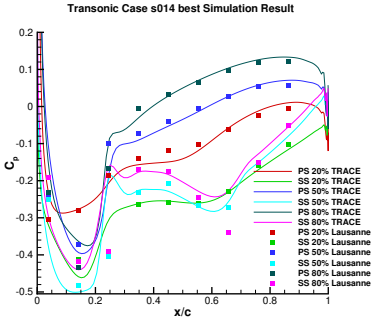

(b) Measured pressure values (s014) compared to steady state 3D RANS solution with TRACE.

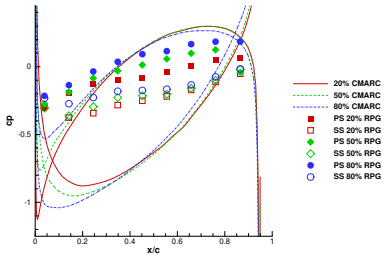

(c) Measured pressure values (s043) compared to vortex lattice solution with CMARC.

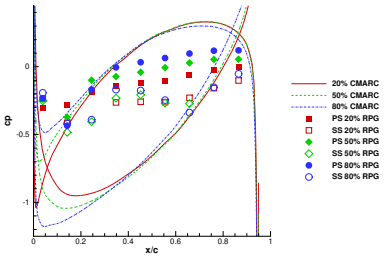

(d) Measured pressure values (s014) compared to vortex lattice solution with CMARC.

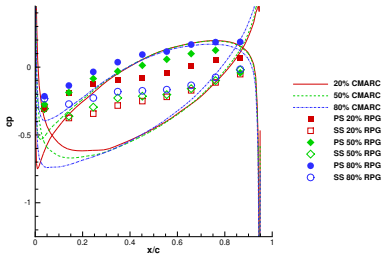

(e) Measured pressure values (s043) compared to vortex lattice solution including compressibility correction with CMARC.

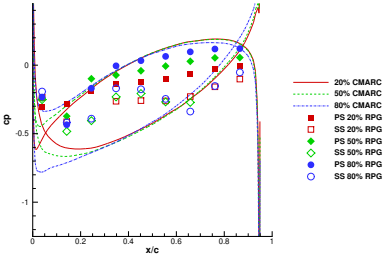

(f) Measured pressure values (s014) compared to vortex lattice solution including compressibility correction with CMARC.

Figure 4.18.: Comparison of 3D RANS, vortex lattice, vortex lattice with compressibility correction and experimental results for two flow cases measured in the RPG.

with less numerical effort than steady state 3D RANS computations. However, the observed increase in numerical efficiency was not as large as hoped for. The observed computation times were 30 min for a solution with free stream convected wake (independently of compressibility correction) and 1 h for local velocity convected wake, for cases where a complete wake development was desired. The steady state 3D RANS computations for this case on the same computer using eight CPU cores instead of one took ∼4-6 hours. This was on the one hand due to the usage of the surface mesh from the 3D RANS solution with decreased mesh density. A coarser mesh with uniform panel sizes over the complete cascade surfaces might have provided similar results with less numerical effort. However, implementing an extra surface meshing step would increase the complexity of a preliminary design method. The other factor limiting the numerical efficiency was the implementation of CMARC as a single-thread program. No parallelization was implemented into the architecture of the program and implementing it would have exceeded the scope of the work substantially. The solution times range in the magnitude of about 2 - 5 min if only one steady state solution is computed and the wake is considered stationary. To compute a compressor map with varying angles of attack and flow velocities, a special routine would have to be designed to create an appropriate wake with free stream convection for each case before each run. This was not considered for this case, since the comparability of the unsteady results to unsteady time-linearized 3D RANS computations and unsteady experimental results were the focus of the research.

4.3.4. Unsteady Results with CMARC for the RPG NACA3506 Geometry

Like the steady state flow cases of the RPG NACA3506 blade experiment, there were measured unsteady pressure coefficient values for the oscillating blades in their first torsional eigenmode shape. These values provide an invaluable data base for validating numerical tools and were used to compare the numerical accuracy of the unsteady potential flow data and the unsteady time-linear 3D RANS solution from TRACE.

To estimate the accuracy of unsteady time stepping vortex lattice methods, two unsteady experimental cases were calculated with CMARC. One was based on the subsonic steady state case s043 and had a blade torsional vibration with 0.3° amplitude at 210 Hz. The other was based on the transonic case s014 and had the same vibration. Three main cases were calculated for each setup:

- 32 physical time steps per oscillation with a wake convection only with the free stream velocity.
- 128 physical time steps per oscillation with a wake convection only with the free stream velocity.
- 32 physical time steps per oscillation with wake rollup and convection.

The results are depicted in figures 4.19 and 4.20. The results of the unsteady computations with wake convection with local velocity showed a very big impact of the ragged wakes on the unsteady solution. The results are presented in appendix G, but do not contribute to the desired finding of fast methods for unsteady aerodynamics.

The first lesson learned from the unsteady computations with CMARC is that the oscillation resolution with 32 unsteady time steps is sufficient. The results of CMARC with 32 time steps per harmonic period and 128 time steps are virtually identical. In figure 4.19a, the magnitude of the unsteady pressure is compared. The results from TRACE and experiment are very close on the suction side of the blade. The results from CMARC on the other hand show a significant offset or scaling compared to the other two results. In the adjacent figure 4.19b, the phase shift between blade deformation and unsteady pressure response is visualized. Here, the unsteady time-linearized RANS solution only manages to capture the suction side with a high degree of accuracy. The pressure side seems to develop a divergence

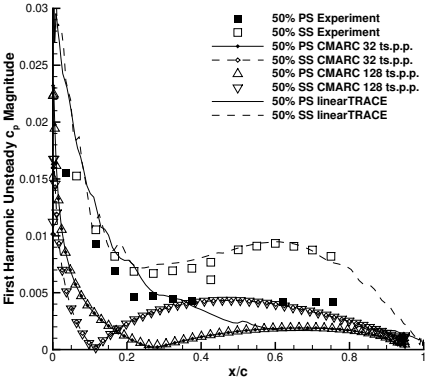

(a) Unsteady pressure coefficient c_p magnitude of the experimentally measured values compared to CMARC and TRACE results. The suffix "ts.p.p." denotes the number of time steps per harmonic period computed in the nonlinear unsteady CMARC computations.

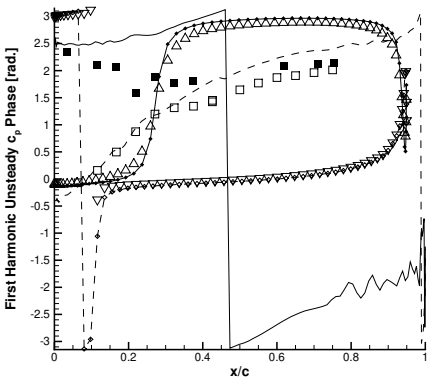

(b) Unsteady pressure coefficient c_p phase of the experimentally measured values compared to CMARC and TRACE results. The lines and symbols are identical to the ones to the left.

Figure 4.19.: Comparison of numerical and experimental results for the subsonic unsteady case z043 (0.3° blade vibration at 210 Hz, 0° IBPA).

along the blade length. This could potentially originate from the constant eddy viscosity assumption. The potential solution from CMARC does not capture the phase shift between blade surface oscillation and unsteady pressure response at all. Following the assumption that the constant viscosity already leads to errors for the time-linearized RANS solution, a completely inviscid solution will naturally not capture the phase shift very well.

The same observations with even more emphasis on the problems of potential flow solutions for transonic flows can be made for figure 4.20. The magnitude of the unsteady pressure coefficient is captured with a reasonable degree of accuracy by the time-linear RANS solution. The unsteady potential solution on the other hand does not show any shock effects and looks very similar to the solution produced for the subsonic case in figure 4.19, both for the magnitude and the phase of the unsteady pressure coefficient. This is reasonable insofar as the frequency and the amplitude of the blade oscillation in the experiments were the same and the flow angle of the mean flow was also very similar. The only major difference was the onflow velocity, which is not captured very well by a solution without compressibility correction. Consequently, the phase shift between blade surface oscillation and unsteady pressure is not captured well, either. Similar to the subsonic case, the time-linear RANS solution was able to capture the phase shift between surface motion and unsteady pressure only to a limited degree. Discrepancies can be observed on the suction side at the shock location and on the pressure side towards the trailing edge. Again, this can be attributed to the missing influence of the variation of the eddy viscosity.

The unsteady computational times for all computed CMARC comparison cases are lower than for 3D time-linearized methods, but still amount to low single digit CPUhours. As for the steady state solutions, faster computational times might be possible for surface meshes with more uniform and larger grid sizes and with increased parallelization.

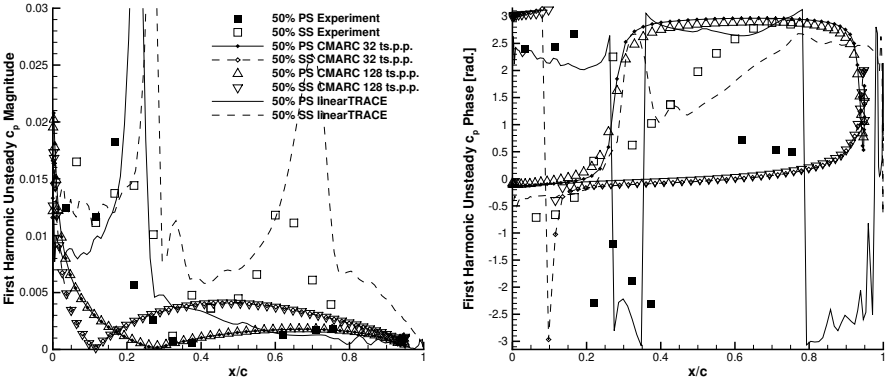

(a) Unsteady pressure coefficient c_p magnitude of the experimentally measured values compared to CMARC and TRACE results. The suffix "ts.p.p." denotes the number of time steps per harmonic period computed in the nonlinear unsteady CMARC computations.

(b) Unsteady pressure coefficient c_p phase of the experimentally measured values compared to CMARC and TRACE results. The lines and symbols are identical to the ones to the left.

Figure 4.20.: Comparison of numerical and experimental results for the transonic unsteady case z014 (0.3° blade vibration at 210 Hz, 0° IBPA).

4.4. Condensation of Results

In chapters 4.1 - 4.3, methods were investigated in order to assess the global flutter susceptibility / aeroelastic stability of a given turbomachinery stage design in a very early design phase. In this context, the term 'global' translates to "in the complete operating range" of the turbomachine. The main objective is a relatively simple to calculate value which indicates a "danger" that the optimization process will shift towards aeroelastic instability or the potential risk of flutter.

In this chapter, the results of each investigated approach are summarized and conclusions concerning their usefulness are drawn.

4.4.1. Time-Linearized Unsteady RANS for Preliminary Flutter Design

A "full" aeroelastic stability analysis for each new design proposed during a preliminary design phase of a turbomachine stage would surpass the budget of even the most ambitious design effort. Still, unsteady time-linear or harmonic balance RANS computations when performed for the correct flow case might help to identify unsuitable designs even very early on in the design process.

To reduce the numerical effort necessary for an aeroelastic stability assessment, different reduction approaches were pursued.

CFD mesh coarsening: As a first step, the mesh resolution of the steady state and unsteady RANS computations was reduced. This was done according to aerodynamic considerations for the used automated optimizer. Still, it was verified that there was negligible difference between the global damping values obtained from unsteady time-linearized computations based on a fine or a coarse mesh.

Reduction of considered operating points: Based on the results from previous investigations (e.g. Fottner [54]), it was concluded that a test for aeroelastic stability at the boundaries of the compressor map will be a sufficient criterion for aeroelastic stability in preliminary design.

Sine approximation of the 'aerodynamic damping' vs. 'IBPA' curve: Based on previous experience both at the Institute of Aeroelasticity and beyond, it was proposed and tested that the smallest global aerodynamic damping Λ of an eigenmode shape family can be approximated by a sine curve over the IBPA σ_n and the number of necessary computations can be reduced.

Similarity assumptions based on mode shape similarity: It was observed that (especially in later design stages) similar designs exhibited similar eigenmode shapes and similar 'aerodynamic damping' vs. 'IBPA' curves. The similarity of eigenmode shapes can be computed with the MAC value. Based on the MAC value, the IBPA position of the smallest aerodynamic damping was predicted in order to reduce the number of necessary unsteady time-linear computation to one per mode shape family.

Approximation of the flow channel in 2D: Based on the approaches used several years ago, which assumed the flow in turbomachines to be largely two-dimensional, a reduction of the unsteady time-linear RANS computation with forced mesh motion was investigated. It was discovered that the three-dimensionality of the flow in turbomachines leads to (a) problems setting up two-dimensional cases and (b) leads to results neglecting the acknowledged importance of the three-dimensionality of the flow, potentially invalidating the results completely.

As already stated in chapter 3.2.2, it is well known that 3D effects have a large impact on the aeroelastic stability of turbomachinery stages. This was confirmed by the investigations into 2D channel approximations.

It was confirmed that similar mode shapes in similar flow with similar eigenfrequencies result in similar aerodynamic damping diagrams. This might be useful especially in later design stages, where geometric changes leading to aerodynamic improvements are small and do not influence the eigenbehavior on a large scale. However, in preliminary design large geometric changes are expected so that this effect cannot be exploited. Also, additional investigations into methods for flow similarity comparison and similarity boundaries for flow and eigenmode shapes are necessary.

The methods of mesh coarsening, operating point reduction and sine approximation of the 'aerodynamic damping' vs. 'IBPA' curve, however result in a significant reduction of the necessary time for the aeroelastic stability assessment.

To exemplify this, a small example visualizes the potential for preliminary design:

At the time of the main preliminary design ($\sim$2014) of the CRISPmulti demonstrator, a cost of $\sim$4 steady state RANS computations on a coarse mesh was considered acceptable to assess the aerodynamic properties of a design.

Making use of the found reduction approaches, the numerical cost for a highly reliable aeroelastic stability assessment might be calculated to be:

$\sim$15 steady state RANS computations at the operating points denoting the boundaries of the compressor map

$+$ $\sim$270 unsteady time-linearized RANS computations ($\sim$15 operating points with 3 eigenmode shape families each and 6 unsteady time-linear computations each to find the smallest aerodynamic damping).

$=$ time equivalent of $\sim$285 steady state RANS computations

Together with Moore's law (introduced in chapter 1.5) and Pope's assumption that methods are scientifically "cycled down" every twenty years, it is now possible to estimate the time frame for the implementation of this method to be: $285 \div 4 = 71.25 \approx 64 = 2^6$ $\Rightarrow \sim 12$ years; assuming that the same amount of computational resources previously spent on aerodynamic computations (equivalent of 4 steady state RANS computations) will then be spent on the aeroelastic computations. The proposed approach to aeroelastic stability estimation might therefore be implemented into a preliminary design method by 2026 ($\sim$12 years after the beginning of this research in 2014).

Additionally, it was found that the flow at part speed close to the surge line exhibited the smallest aerodynamic damping and sometimes excitation for the CRISPmulti demonstrator design. This behavior is not to be mistaken for the phenomenon widely known as "flutter bite" which is in part an acoustic phenomenon as well as a flow instability phenomenon (Vahdati et al. [179]). Referring to figure 1.3, this is much rather stall flutter and often the limiting factor for compressors.

If the criterion for a highly reliable aeroelastic stability assessment is relaxed to a reasonably accurate prediction of the aeroelastic stability, only 3 - 5 operating points at the surge line need to be investigated for aeroelastic stability. The example above then changes to:

$\sim$5 steady state RANS computations at the operating points denoting the surge boundaries of the compressor map

$+$ $\sim$90 unsteady time-linearized RANS computations ($\sim$5 operating points with 3 eigenmode shape families each and 6 unsteady time-linear computations each to find the smallest aerodynamic damping).

$=$ time equivalent of $\sim$95 steady state RANS computations

$\Rightarrow$ $95 \div 4 = 23.75 \approx 22.627 = 2^{4.5} \Rightarrow \sim 9$ years

This means that within one or two years from now, a reasonably reliable aeroelastic stability assessment based on the energy method and unsteady time-linear 3D RANS computation could be implemented into a preliminary design process.

If a safeguard would be implemented into the preliminary design process which only investigates the aeroelastic stability for designs which satisfy the aerodynamic and structural criteria defined previously, this method might be used in preliminary design, starting today.

However, since the turbulence model was never time-linearized for linear TRACE and a harmonic balance module with harmonic balance turbulence model is implemented into the TRACE suite by now, the time-linear solver of TRACE is being discontinued. The harmonic balance solutions on the other hand have been observed to be much more mesh dependent than the time-linear solutions (leading to no results for unsuitable meshes, which is often the case for automatically generated meshes). Also, their perceived convergence towards an unsteady flow solution result is slower. If and when a reduced stability estimation based on harmonic balance solutions might be implemented into a preliminary design process will have to be investigated.

4.4.2. Reduced Frequency for Preliminary Flutter Design

In chapter 4.2, the investigations concerning the reduced frequency as a design criterion for aeroelastic stability in the CRISPmulti project were recounted. The results of these investigations lead to conclusions helpful in the future preliminary design of compressor stages:

- The reduced frequency cannot be used as a single global design parameter concerning aeroelastic stability, which is in accordance with Sisto [160].
- However, as observed before, (re-)derived by Khalak [97] and visualized in figure 4.13, the reduced frequency can serve as a similarity parameter to indicate similar aeroelastic behavior of similar blades with similar eigenbehavior in similar flow.
- This might be exploited in preliminary design. For a certain application, the desired flow properties are defined very early in the design process. Also, the overall properties of the blades (number of blades, approximate blade chord, flow channel height) will be defined very early on. If one early design prototype is investigated thoroughly along the lines of a reduced aeroelastic stability analysis as it is proposed in chapter 4.4.1, and frequency variations of the real mode shapes are investigated at critical operating points, lower boundaries (with a safety margin) for the reduced frequencies of different mode shapes for the specified use case might be prescribed as design criteria for the continued preliminary design process.
- Should the design undergo major alterations, or the overall form of the lowest eigenmodes change (as it was the case for CRISPmulti), this investigation would have to be repeated. Here, the MAC value might be a useful parameter to gauge the eigenmode shape similarity.

Summed up, the conclusion regarding the reduced frequency in preliminary turbomachinery design can be put as: A reduced frequency parameter cannot substitute an aeroelastic stability analysis even in preliminary design. Still, it is a similarity parameter, which might be used to gauge the aeroelastic stability of a design similar to an already investigated design.

4.4.3. Nonlinear Full Potential Aerodynamics for Preliminary Flutter Design

A nonlinear full potential method was extended to incorporate typical turbomachinery features. Cyclic symmetry, harmonic surface velocity oscillation and a safeguard against

wake-surface intersection were successfully implemented into an existing vortex lattice panel code.

Then, comparison computations were performed for a previously conducted experiment in an annular compressor cascade. The results of the nonlinear unsteady potential flow computations with simulated surface oscillation were compared to the results of the experimental campaign as well as the results of time-linearized 3D RANS computations.

There are several conclusions which can be drawn already from these preliminary tests: The results show clearly that potential flow methods do not represent fluid flows with $Ma > 0.7$ very well. But as Friedewald et al. [59] have shown this might be corrected with RANS CFD solutions. Maybe even the steady state solutions available from the optimization runs can be used for this purpose. Furthermore and as expected, potential flow methods do not predict the unsteady flow behavior in turbomachines sufficiently accurate to base an uncorrected aeroelastic stability estimator on them. Again, together with appropriate correction methods along the lines of Voss et al. [187] or Hebler & Thormann [76] and more research, they might reach this goal in the future. This was intended when the method was selected in chapter 3.2.3 and later explained in chapter 3.5.

The result of these comparisons clearly shows that time-linear RANS computations predict the measured values from the experiments better. This was expected and is even desirable if the unsteady time-linear methods are used to correct the unsteady potential results. However, the computational time needed for a nonlinear unsteady potential solution was higher than expected and while it was lower than the time needed for a 3D time-linear RANS solution, it was still in the magnitude range of an unsteady time-linear RANS run.

There are still areas of research which need to be addressed before a nonlinear unsteady potential flow solver can be used to determine the aeroelastic stability of turbomachinery stages in preliminary design. As mentioned in chapters 4.3.3 and 4.3.4, the presently implemented wake development strategy in CMARC leads to nonphysical results and needs to be improved. Furthermore, the presently implemented surface deformation routine needs to be expanded to incorporate IBPAs $\sigma_n \neq 0°$. More research is needed in the areas of parallelization and mesh representation of the computed surfaces in order to decrease the computational times. In this thesis, only unsteady potential results without compressibility correction were presented. The positive or negative influence of the compressibility correction method implemented in CMARC on the unsteady surface pressure solutions needs to be investigated.

One of the most important areas of research for the future use of unsteady potential methods in turbomachinery is the area of frequency domain potential methods which are capable to treat truly three-dimensional geometries as opposed to DLM which is only valid for flat wings. This would increase the time savings by the potential flow aerodynamics into a range that would merit a continued interest even in the light of ever increasing computational power. Then, unsteady potential correction methods along the lines of Voss et al. [187] or Hebler & Thormann [76] could be implemented for turbomachines, as well. One possible avenue investigated might be the theory presented by Williams et al. [195], but his code does not seem to be easily available and implementing his findings will require substantial efforts.

In light of the ongoing development in computational resources and the conclusions drawn in chapter 4.4.1, further investigation of nonlinear unsteady potential flow methods for turbomachines needs to be considered critically before renewed efforts in these directions are undertaken.

5. Conclusion

At the beginning of this thesis, the problem of aeroelastic instability (flutter) in turbomachines was introduced. It was stated that aeroelastic stability is currently investigated late in the design process and that the numerical proof of aeroelastic stability is costly. Redesign due to a discovered flutter problem is even more expensive. Therefore, implementing a preliminary aeroelastic stability investigation into the early design process might reduce the risk of necessary redesign due to aeroelastic stability issues. Furthermore, it was proposed that methods used for aeroelastic stability proof computations ~ 20 years ago might be suitable to be used in present day preliminary design, due to the constant development in computational resources.

Then, in chapter 2, some theoretical foundations for aerodynamics, structural dynamics and their combination to form aeroelasticity in turbomachines were introduced. The energy method was proposed as a suitable method to determine the aeroelastic stability in preliminary design.

In chapter 3, available aeroelastic and unsteady aerodynamic methods available ~ 25 years ago were reviewed on the basis of an overview article from that time. The suitability of the energy method for preliminary aeroelastic stability assessment was substantiated. Then, unsteady aerodynamic methods were reviewed to find suitable avenues of investigation. The unsteady time-linear 3D RANS method and nonlinear unsteady potential flow were chosen as possibilities. Additionally, the influence of the reduced frequency was to be investigated.

The chosen methods were applied to different test cases from DLR projects and their suitability for a rapid flutter analysis in preliminary design were evaluated in chapter 4. The results of these investigations were presented in chapter 4.4.

This chapter will now recount the findings in a more condensed form (chapter 5.1). In chapter 5.2, conclusions will be drawn from these results for aeroelastic stability estimation in turbomachines in preliminary design and the validity of the hypothesis that older and more simple methods for aeroelastic stability assessment may be used in preliminary design is evaluated. In the end, further avenues of investigation for the future are proposed (chapter 5.3).

5.1. Summary of Results

One of the main basis assumptions for the research carried out in this thesis was that the energy method is still applicable for investigating the aeroelastic stability (flutter) in turbomachines at a very early design stage, even though it has been proven that eigenmode coupling may occur for modern highly loaded slender blade designs. Consequently, the main computational load generated by aeroelastic stability assessment in a very early design stage stems from the unsteady aerodynamic computations necessary to perform a stability evaluation with the energy method.

The main goal of this thesis was the assessment if unsteady aerodynamic or other methods which were used several years ago for the final aeroelastic stability proof for turbomachines might be used nowadays as tools to gauge the aeroelastic stability of new turbomachinery designs in preliminary design phases due to the constant development in computational resources.

The investigation of three different methods was pursued and the results thereof are summarized here shortly:

Time-Linearized 3D RANS Methods

Frequency domain methods promise much faster unsteady results compared to time-resolved methods. At DLR, the flow solver TRACE incorporates a time-linearized module which can be used to determine the aerodynamic response to a forced motion of the blade surface. It was shown in chapter 4.1.2, that even though time-linearized methods are much faster than time-stepping unsteady RANS solutions, a full aeroelastic stability analysis would require about three magnitudes more computational resources than one optimization cycle only concerned with steady state aerodynamic efficiency and structural integrity.

By reducing the computational load of such a complete aeroelastic stability assessment in a suitable way, the necessary computational resources can be minimized without a large compromise on their global validity. The proposed reductions are:

- Use of a coarser finite volume mesh representation of the flow volume. The mesh needs to fulfill minimum aerodynamic requirements and still be able to deliver reliable steady state results. This is mostly done for preliminary design, anyway. It was found (see appendix E.4) that the mesh size reduction almost has a quadratical effect on the reduction of the computational times.

- Reduction of the number of investigated operating points to points most likely to exhibit aeroelastic instability. The operating points forming the boundaries of the compressor map were found to be most suitable (section 4.1.3).

- The number of IBPAs σ_n investigated per eigenmode shape at each operating point can be reduced to about 6 by assuming a sinusoidal curve of the global aerodynamic damping over the IBPAs (section 4.1.4).

- The similarity of flow cases, blade forms and eigenmode shapes might be used to reduce the number of necessary unsteady RANS calculations further (section 4.1.5).

- Based on the state of the art 30 years ago, the possibility of investigating only one representative radial slice of the flow channel with unsteady time-linearized RANS methods was investigated.

During the investigation of these reduction approaches the following results were obtained:

Even though the solution of the quasi 2D time-linearized RANS equations with forced motion can be performed very fast, two problems arise: Two-dimensional steady state solutions differ substantially from full 3D steady state solutions of the flow in turbomachinery flow channels. These three-dimensional effects have an impact on the unsteady flow and consequently introduce an error into the solution. Additionally, the question arises how representative a 2D slice of the flow will be for increasingly complex blades and their eigenmode shapes. Another problem encountered was the instability of the numerical setup when basing the unsteady 2D flow solution on a steady state 3D flow solution.

The investigated approach for reducing the number of unsteady fluid flow computations based on the similarity of the eigenmode shapes (MAC) was difficult to evaluate. On the one hand, it was obvious that similar eigenmode shapes with similar frequencies in similar flow show comparable aeroelastic stability properties. On the other hand, the definition of a globally meaningful eigenmode shape similarity threshold was not possible and might even depend on the eigenmode shape resolution. Also, the similarity of the fluid flow was not taken into account. More severely restricting is the fact that large changes in eigenmode shape and frequency behavior occur in the earliest stages of the design and consequently would shift the main computational load there.

One minor reason for concern with the sine curve approximation approach for global aerodynamic damping Λ vs. IBPA σ_n is the potential occurrence of flow states where high pressure ratios or acoustic resonance lead to cases which cannot be approximated as sine

curve, any more. Experience for the investigated rotor showed that this risk was very small for the rotor at hand. However, this risk needs to be re-investigated for each new blade design task.

The mesh coarsening and boundary operating point reduction approaches were deemed to be without negative impact on the validity of the aeroelastic stability assessment of a turbomachine stage.

Reduced Frequency as an Indicator for Aerodynamic Stability

The reduced frequency ω_{red} of turbomachinery blade vibrations was used in the mid 20th century as a design criterion to prevent stall flutter in turbomachines. Since then, the negative impact of reducing the reduced frequency ω_{red} of an eigenmode shape on the aeroelastic stability has been proven multiple times.

Therefore, the reduced frequencies ω_{red} of multiple available geometries and flow cases with their respective eigenmode shapes were compared and possible relationships between reduced frequencies and smallest global aerodynamic damping Λ_{min} were sought for.

One key result was the importance of the reduced frequency as a similarity parameter, when it is evaluated in conjunction with the eigenmode shape and the respective flow case. Previous research (Khalak [97]) indicates that four parameters including the reduced frequency influence the aeroelastic similarity of a given eigenmode shape. Since the other three parameters (inlet Mach number, "reduced damping" and inflow angle) are often predefined in a preliminary design effort, the aeroelastic stability might be approximated by using a reduced frequency parameter in conjunction with the MAC value.

However, to do so, the aeroelastic properties of the most likely outcomes as well as the sensitivity of the likely eigenmode shapes to frequency changes at critical operating points would have to be investigated before starting a preliminary design effort.

Unsteady Potential Flow Methods

Potential flow methods promise a compromise between one-equation methods and full RANS unsteady solutions. They are based on flow equations which result in accurate results for low speed aerodynamics, can be corrected to yield sufficiently reliable results even for Mach numbers between 0.5 and 0.8 and promise very efficient computational solution techniques. DLM is used for airplane preliminary aeroelastic stability estimation at the DLR Institute of Aeroelasticity. Due to the simplifications used to derive the DLM equations, they are not suitable for turbomachinery applications.

Therefore, a vortex lattice potential method was investigated for its suitability for turbomachinery unsteady aerodynamic applications. Necessary features (cyclic symmetry, blade surface deformation via normal velocities and harmonic oscillation, as well as wake surface intersection checking routines) were implemented into a nonlinear semi-commercial vortex lattice potential code.

Preliminary tests show that the steady state pressure distributions do not indicate pressure peaks but rather smooth pressure distributions over the investigated NACA3506 annular cascade profile. Similarly, the unsteady pressure results do not represent the experimental results accurately. This was expected and might be treated by correction methods already used at the Institute of Aeroelasticity (Friedewald et al. [59], Voss et al. [187], Hebler & Thormann [76]).

The main problem was the time consumption of the time accurate harmonic blade oscillation simulations. Even though efficient linear equation solution techniques were used, the required solution time for one harmonic oscillation of the blade surface was in the range of 1 - 2 CPUhours. Performing steady state wake development computations for the compressor map boundaries plus at least 6 IBPA unsteady blade surface motion computations per eigenmode shape will not result in a significant reduction of numerical resource consumption compared to unsteady time-linear RANS methods.

5.2. Conclusions Drawn from the Results

The results highlighted in the previous chapter have consequences for the future considering preliminary design of turbomachinery stages. The different conclusions will be grouped again by the investigation they were derived from, followed by a section containing the subjective obstacles which need to be addressed in order to continue successful development of turbomachines.

Time-Linearized 3D RANS Methods

In chapter 4.4.1, the implementation of the successfully tested reduction approaches into a preliminary design routine were compared to the numerical resources spent on a purely aerodynamic and structural preliminary design about 7 years ago. Then the numerical capabilities were extrapolated by Moore's law. It was concluded that a "full" reduced aeroelastic stability analysis for every tested geometry with coarse RANS mesh, checking only the compressor map boundaries for aeroelastic stability and approximating the global aerodynamic damping diagram for each eigenmode shape family by a sine wave might be implemented into a preliminary turbomachinery design method within 5 years.

Relaxing the condition of almost perfect capture of all aeroelastic instabilities and only investigating the operating points at the surge boundary for aeroelastic stability with the proposed reductions and the time-linear 3D RANS method puts the availability of an aeroelastic stability estimation in a preliminary design routine to within about 2 years.

If the numerical cost of the aeroelastic computations is kept at a minimum, only checking designs which fulfill the aerodynamic and structural requirements, or only checking every second or third design geometry, the proposed method for using 3D time-linear RANS methods together with the energy method could be implemented into a preliminary design method, starting today.

Reduced Frequency as an Indicator for Aerodynamic Stability

The conclusions which can be drawn from the investigations into the reduced frequency ω_{red} as an indicator for aeroelastic stability are twofold:

On the one hand, it was established that the reduced frequency ω_{red} as a stability indicating similarity parameter is highly dependent on the flow case and the eigenmode shape of the investigated blade design.

On the other hand, it is apparent from the results of the investigation that the reduced frequency ω_{red} is indeed a similarity parameter if the flow case and the eigenmode shape are sufficiently similar.

This can be exploited immediately in preliminary design. However, to do so an aeroelastic stability investigation of the initial design for the complete desired operating range needs to be performed. In this analysis, not only the expected stability of the most likely appearing eigenmode shapes and their frequencies need to be investigated. The frequencies of the base eigenmode shapes need to be varied in order to determine the reduced frequencies where instability will occur. Then, reduced frequency boundaries (including a sufficient safety margin, maybe even at the aerodynamic design point) could be prescribed as boundary values for the preliminary design method.

Unsteady Potential Flow Methods

When choosing non-linear potential flow methods as a test case, this was done deliberately to maintain temporal nonlinearity while sacrificing flow solution accuracy. The diagonally opposite time-linearized RANS methods (see table 3.2) use a more complex flow solution model while proposing a completely harmonic temporal model.

The reduced accuracy of the flow solutions was therefore expected and might be taken into account by suitable correction methods. The unexpected result was the necessary

time for the nonlinear time development of the unsteady flow. The time gains of the investigated unsteady nonlinear potential method compared to the investigated time-linear RANS method was about one order of magnitude. In terms of Moore's law, this is about six years.

Considering that time-linear 3D RANS methods might be implemented into a preliminary design method right now, if certain limitations are accepted, the additional effort necessary to fully implement (IBPAs $\sigma_n \neq 0$, parallelization, re-meshing) a nonlinear unsteady potential flow solver with turbomachinery capabilities seems very high.

One possible area of research might be frequency domain potential methods, but most of these solutions are highly restricted in their applicability which does not include turbomachinery flows.

Global Assessment of the Potential of Traditional Methods for Preliminary Design

Summarizing the three previous chapters and evaluating the thesis' hypothesis one can conclude that it is possible and desirable to use true and tried traditional methods for turbomachinery aeroelastic stability from ~ 20 years ago to improve the preliminary design of present day turbomachines. The most promising method to do so found in this thesis would be the use of time-linear unsteady 3D RANS methods which were used in scientific applications ~ 10 - 15 years ago in combination with the energy method.

There are a few things which need to be considered when doing so. The first is a general adherence to the scientific progress of the time which has since passed. One main example for this is, that the flow in fans and compressors cannot be approximated to be purely two-dimensional. Ergo, only three-dimensional traditional methods can be used.

Another, and much more concerning development is the availability of traditional methods from the computational past. 20 or 30 years ago, it might have still been possible to implement a published aeroelastic approach from a paper and base the current research on it. But with the appearance of Euler and later RANS codes, the possibility to do so is very limited. By now, most current research is based on numerical codes which were developed over years by teams of scientist. This means, that new developments are mostly based on (and only possible with) the numerical work done by others.

However, as scientific progress is made, older and more limited tools are discontinued and the scientists developing or maintaining them change to different areas of research or make a career change altogether. As a consequence, older codes are very hard to obtain in order to base rapid methods for preliminary design on them. This was discovered when researching panel methods capable of treating three-dimensional geometries. There are some which are being maintained and have commercial application. Their code base is naturally not available. Then, there are freely obtainable research codes which are often very limited in their applicability, or have disappeared once the scientific progress continued.

The same is true for methods implemented into research 3D RANS codes. 19 years ago, Carstens et al. [31] implemented an explicit time-marching aeroelastic method (partially integrated method) into the RANS CFD code used in this research. This particular development was not maintained once the authors of the aforementioned paper had left DLR and was inaccessible 6 years after that publication. A similar development is taking place right now with the time-linear 3D RANS method in TRACE. The turbulence model was never time-linearized and therefore the results never matched nonlinear unsteady RANS computations completely. The time-variable turbulence model was then derived and implemented into the harmonic balance module of TRACE and consequently, linear TRACE is discontinued. This means, that by the time it might be used productively, the time-linear module of the DLR 3D RANS turbomachinery solver will not be available any longer.

5.3. Proposed Future Investigations

Having determined that unsteady aerodynamic methods from the scientific past still might be used in preliminary design for aeroelastic stability estimation, it is important to maintain and conserve these methods until they might be used again.

To do so, the scientific codes developed need to be archived and made available to future scientist in order to improve on them and benefit from them.

In the area of aeroelastic stability assessment in preliminary design, there are two main areas of research which need to be treated in the future:

1. For one, the applicability of a harmonic balance 3D RANS method instead of a time-linear method in the recommended preliminary design approach needs to be investigated. Special consideration should be given to stability issues related to optimization meshes and the convergence speed of the solution.

2. An unsteady time-linear or harmonic balance potential flow solver capable of treating turbomachinery flows needs to be investigated in order to determine the usefulness of its corrected results in preliminary aeroelastic stability assessment.

References

[1] J. J. Adamczyk:
Analysis of Supersonic Stall Bending Flutter in Axial-Flow Compressor by Actuator Disk Theory, NASA Technical Paper 1345, National Aeronautics and Space Administration (NASA), Nov. 1978.

[2] AeroLogic:
Digital Wind Tunnel / CMARC, Three-Dimensional Low Order Panel Codes, 2009.

[3] R. Antona, R. Corral & J. M. Gallardo:
"Effect of the Structural Coupling on the Flutter Onset of a Sector of Low-Pressure Turbine Vanes", in: *Journal of Turbomachinery* 134.5, 051007 (Sept. 2012), issn: 0889-504X,
doi: 10.1115/1.4003837.

[4] A. Arnone, F. Poli & C. Schipani:
"A Method to Assess Flutter Stability of Complex Modes", in: *Unsteady Aerodynamics, Aeroacoustics and Aeroelasticity of Turbomachines - Proceedings of the 10th International symposium on unsteady aerodynamics, aeroacoustics and aeroelasticity of turbomachines, 2003, Durham NC, USA*, ed. by K. C. Hall, R. E. Kielb & J. P. Thomas, Springer Netherlands, Dordrecht, 2006, pp. 31–40, isbn: 978-1-4020-4605-6,
doi: 10.1007/1-4020-4605-7_3.

[5] D. L. Ashby, M. R. Dudley, S. K. Iguchi, L. Browne & J. Katz:
Potential Flow Theory and Operation Guide for the Panel Code PMARC, tech. rep., NASA Technical Memorandum 102851, National Aeronautics and Space Administration (NASA), Jan. 1991.

[6] G. Ashcroft, C. Frey & H.-P. Kersken:
"On the Development of a Harmonic Balance Method for Aeroelastic Analysis", in: *11th World Congress on Computational Mechanics (WCCM XI) / 5th European Conference on Computational Mechanics (ECCM V) / 6th European Conference on Computational Fluid Dynamics (ECFD VI)*, ed. by E. Onate, X. Oliver & A. Huerta, Barcelona, Spain, July 20–25, 2014, pp. 5885–5896.

[7] M. Aulich & U. Siller:
"High-Dimensional Constrained Multiobjective Optimization of a Fan Stage", in: *ASME 2011 Turbo Expo: Turbine Technical Conference and Exposition*, vol. 7: Turbomachinery, Parts A, B, and C, GT2011-45618, Vancouver, British Columbia, Canada, June 6–10, 2011, pp. 1185–1196, isbn: 978-0-7918-5467-9,
doi: 10.1115/GT2011-45618.

[8] M. A. Bakhle & T. S. R. Reddy:
"Harmonic Balance Computations of Fan Aeroelastic Stability", in: *International Forum on Aeroelasticity and Structural Dynamics (IFASD)*, IFASD-2009-101, Seattle, Washington, USA, June 21–25, 2009.

[9] R. E. Bartels & A. I. Sayma:
"Computational Aeroelastic Modelling of Airframes and Turbomachinery: Progress and Challenges", in: *Philosophical Transactions of the Royal Society A: Mathematical, Physical and Engineering Sciences* 365.1859 (2007), pp. 2469–2499, issn: 1364-503X,
doi: 10.1098/rsta.2007.2018.

[10] J. T. Batina:
"Efficient Algorithm for Solution of the Unsteady Transonic Small-Disturbance Equation", in: *Journal of Aircraft* 25.7 (July 1988), pp. 598–605,
doi: 10.2514/3.45629.

[11] J. Belz:
Aerodynamische und aeroelastische Untersuchungen von Triebwerksbeschaufelungen im Windkanal; Teil 1: Versuchstand, Versuchsdurchführung und Datenaufbereitung, tech. rep., IB 232-2003 C 02 (confidential), Deutsches Zentrum für Luft- und Raumfahrt e.V. - Institut für Aeroelastik, Dec. 2003.

[12] J. Belz:
Aerodynamische und aeroelastische Untersuchungen von Triebwerksbeschaufelungen im Windkanal; Teil 2: Messdaten für einen subsonischen und einen transsonischen Strömungszustand, tech. rep., IB 232-2003 C 03 (strictly confidential), Deutsches Zentrum für Luft- und Raumfahrt e.V. - Institut für Aeroelastik, 2003.

[13] J. Belz & H. Hennings:
"Aerodynamic Stability Investigations of an Annular Compressor Cascade Based on Unsteady Pressure Measurements", in: *Proceedings of the 9th International Symposium on Unsteady Aerodynamics, Aeroacoustics and Aeroelasticity of Turbomachines (ISUAAAT 2000)*, Lyon, France, Sept. 4–8, 2000, pp. 1–16.

[14] J. Belz & H. Hennings:
"Experimental Flutter Investigations of an Annular Compressor Cascade: Influence of Reduced Frequency on Stability", in: *Unsteady Aerodynamics, Aeroacoustics and Aeroelasticity of Turbomachines - Proceedings of the 10th International symposium on unsteady aerodynamics, aeroacoustics and aeroelasticity of turbomachines, 2003, Durham NC, USA*, ed. by K. C. Hall, R. E. Kielb & J. P. Thomas, Springer Netherlands, Dordrecht, 2006, pp. 77–91, isbn: 978-1-4020-4605-6,
doi: 10.1007/1-4020-4605-7_7.

[15] J. Belz, H. Hennings & G. Kahl:
"Experimental Investigation of the Forcing Function and Forced Pitching Blade Oscillations of an Annular Compressor Cascade in Transonic Flow", in: *ASME Turbo Expo 2010: Power for Land, Sea, and Air*, vol. 6: Structures and Dynamics, Parts A and B, GT2010-23590, Glasgow, United Kingdom, June 14–18, 2010, pp. 1277–1285, isbn: 978-0-7918-4401-4,
doi: 10.1115/GT2010-23590.

[16] O. O. Bendiksen:
"A New Approach to Computational Aeroelasticity", in: *32nd Structures, Structural Dynamics, and Materials Conference*, AIAA 1991-0939-CP, Baltimore, Maryland, USA, Apr. 8–10, 1991, pp. 1712–1727,
doi: 10.2514/6.1991-939.

[17] C. Berthold, J. Gross, C. Frey & M. Krack:
"Analysis of Friction-Saturated Flutter Vibrations With a Fully Coupled Frequency Domain Method", in: *Journal of Engineering for Gas Turbines and Power* 142.11, 111007 (Nov. 2020), issn: 0742-4795,
doi: 10.1115/1.4048650.

[18] R. L. Bisplinghoff, H. Ashley & R. L. Halfman:
Aeroelasticity, Dover Publications, 1996, isbn: 978-0-486-69189-3.

[19] M. Blocher & A.-L. Aulich:
"Flutter Susceptibility Approximation via Curve Fitting and MAC-Analysis in an Automated Optimization Design Process", in: *ASME Turbo Expo 2013: Turbine Technical Conference and Exposition*, vol. 7B: Structures and Dynamics, GT2013-94577, San Antonio, Texas, USA, June 3–7, 2013, ISBN: 978-0-7918-5527-0,
DOI: 10.1115/GT2013-94577.

[20] M. Blocher & I. E. Gómez Fernández:
"Time-Linearized Forced Response Analysis of a Counter Rotating Fan: Part I - Theoretical Concept of a Fully Time-Linear Forced Response Analysis", in: *ASME Turbo Expo 2014: Turbine Technical Conference and Exposition*, vol. 7B: Structures and Dynamics, GT2014-25833, Düsseldorf, Germany, June 16–20, 2014, ISBN: 978-0-7918-4577-6,
DOI: 10.1115/GT2014-25833.

[21] M. Blocher, M. May & H. Schoenenborn:
"Dependency of Unsteady Time-Linearized Flutter Investigations on the Steady State Flow Field", in: *ASME 2011 Turbo Expo: Turbine Technical Conference and Exposition*, vol. 6: Structures and Dynamics, Parts A and B, GT2011-46500, Vancouver, British Columbia, Canada, June 6–10, 2011, pp. 1415–1427, ISBN: 978-0-7918-5466-2,
DOI: 10.1115/GT2011-46500.

[22] A. Bölcs:
"A Test Facility for the Investigation of Steady and Unsteady Transonic Flows in Annular Cascades", in: *ASME 1983 International Gas Turbine Conference and Exhibit*, vol. 1: Turbomachinery, 83-GT-34, The American Society of Mechanical Engineers (ASME), Phoenix, Arizona, USA, Mar. 27–31, 1983, ISBN: 978-0-7918-7951-1,
DOI: 10.1115/83-GT-34.

[23] R. Bontempo & M. Manna:
"Ring-Vortex Panel Method for the Uniformly Loaded Propeller with Axisymmetric Hub", in: *AIAA Journal*, Aeronautics | Astronautics 58.1 (Jan. 2020), pp. 496–500, ISSN: 1533-385X,
DOI: 10.2514/1.J058605.

[24] C. Brandstetter, M. Jüngst & H.-P. Schiffer:
"Measurements of Radial Vortices, Spill Forward, and Vortex Breakdown in a Transonic Compressor", in: *Journal of Turbomachinery* 140.6, 061004 (June 2018), ISSN: 0889-504X,
DOI: 10.1115/1.4039053.

[25] L. O. Brase & W. Eversman:
"Application of Transient Aerodynamics to the Structural Nonlinear Flutter Problem", in: *Journal of Aircraft* 25.11 (Nov. 1988), pp. 1060–1068, ISSN: 1533-3868,
DOI: 10.2514/3.45703.

[26] W. J. G. Bräunling:
"Verdichter", in: *Flugzeugtriebwerke*, Springer-Verlag Berlin Heidelberg, 2009, chap. 10, pp. 859–972, ISBN: 978-3-540-76370-3,
DOI: 10.1007/978-3-540-76370-3.

[27] W. J. G. Bräunling:
Flugzeugtriebwerke, Springer-Verlag Berlin Heidelberg, 2009, ISBN: 978-3-540-76370-3,
DOI: 10.1007/978-3-540-76370-3.

[28] W. Campbell:
"The Protection of Steam-Turbine Disk Wheels from Axial Vibration", in: *Transactions of the ASME - Spring Meeting*, vol. 46, No. 1920, The American Society of Mechanical Engineers (ASME), Cleveland, Ohio, USA, May 26–29, 1924, pp. 31–160.

[29] B. Cao:
"Development of Reduced Unsteady Vortex Lattice Method Using Proper Orthogonal Decomposition Technique", in: *AIAA Journal*, Aeronautics | Astronautics 54.1 (Jan. 2016), pp. 366–370, ISSN: 1533-385X,
DOI: 10.2514/1.J054527.

[30] V. Carstens:
Berechnung der instationären Druckverteilung an harmonisch schwingenden Gittern in ebener Unterschallströmung, Teil 2: Ergebnisse für gestaffelte Gitter in kompressibler Strömung, tech. rep., IB-253 75 J 02, Deutsches Zentrum für Luft- und Raumfahrt e.V. - Institut für Aeroelastik, July 1975.

[31] V. Carstens, R. Kemme & S. Schmitt:
"Coupled Simulation of Flow-Structure Interaction in Turbomachinery", in: *Aerospace Science and Technology* 7.4 (June 2003), pp. 298–306, ISSN: 1270-9638,
DOI: 10.1016/S1270-9638(03)00016-6.

[32] F. O. Carta:
"Coupled Blade-Disk-Shroud Flutter Instabilities in Turbojet Engine Rotors", in: *Journal of Engineering for Power* 89.3 (July 1967), pp. 419–426, ISSN: 0022-0825,
DOI: 10.1115/1.3616708.

[33] J.-C. Chassaing & G. A. Gerolymos:
"Time-Linearized Navier-Stokes Analysis of Vibrating Compressors", in: *CEAS / AIAA / DGLR International Forum on Aeroelasticity and Structural Dynamics (IFASD)*, IFASD 2005-IF103, München, Germany: DGLR, June 28–July 1, 2005.

[34] V. A. Chenaux, H. Schönenborn & P. Ott:
"Evolution of the Aerodynamic Stability of an Oscillating Annular Compressor Cascade with Inlet Reverse Flow Condition Variations", in: *10th European Conference on Turbomachinery, Fluid Dynamics and Thermodynamics (ETC 10)*, ETC2013-136, Lappeenranta, Finland, Apr. 15–19, 2013.

[35] V. A. Chenaux:
"Experimental Investigation of the Aeroelastic Stability of an Annular Compressor Cascade at Reverse Flow Conditions", URN: urn:nbn:ch:bel-epfl-thesis5358-9, PhD thesis, École Polytechnique Fédérale de Lausanne, 2012,
DOI: 10.5075/epfl-thesis-5358.

[36] K. P. Clark & S. E. Gorrell:
"Analysis and Prediction of Shock-Induced Vortex Circulation in Transonic Compressors", in: *Journal of Turbomachinery* 137.12, 121007 (Dec. 2015), ISSN: 0889-504X,
DOI: 10.1115/1.4031424.

[37] S. T. Clark, F. M. Besem, R. E. Kielb & J. P. Thomas:
"Developing a Reduced-Order Model of Nonsynchronous Vibration in Turbomachinery Using Proper-Orthogonal Decomposition Methods", in: *Journal of Engineering for Gas Turbines and Power* 137.5, 052501 (May 2015), ISSN: 0742-4795,
DOI: 10.1115/1.4028675.

[38] A. R. Collar:
"The Expanding Domain of Aeroelasticity", in: *The Journal of the Royal Aeronautical Society* 50.428 (Aug. 1946), pp. 613–636,
DOI: 10.1017/S0368393100120358.

[39] R. Corral, J. Beloki, P. Calza & R. Elliott:
"Flutter Generation and Control Using Mistuning in a Turbine Rotating Rig", in: *AIAA Journal*, Aeronautics | Astronautics 57.2 (Feb. 2019), pp. 782–795, issn: 1533-385X,
doi: 10.2514/1.J056943.

[40] R. Corral & J. M. Gallardo:
"Verification of the Vibration Amplitude Prediction of Self-Excited LPT Rotor Blades Using a Fully Coupled Time-Domain Non-Linear Method and Experimental Data", in: *ASME Turbo Expo 2008: Power for Land, Sea, and Air*, vol. 5: Structures and Dynamics, Parts A and B, GT2008-51416, Berlin, Germany, June 9–13, 2008, pp. 835–847, isbn: 978-0-7918-4315-4,
doi: 10.1115/GT2008-51416.

[41] R. Corral, M. Greco & A. Vega:
"Tip-Shroud Labyrinth Seal Effect on the Flutter Stability of Turbine Rotor Blades", in: *Journal of Turbomachinery* 141.10, 101006 (Oct. 2019), issn: 0889-504X,
doi: 10.1115/1.4043962.

[42] R. Corral & A. Vega:
"Physics of Vibrating Low-Pressure Turbine Airfoils", in: *13th International Symposium on Unsteady Aerodynamics, Aeroacoustics and Aeroelasticity of Turbomachines (ISUAAAT 13)*, ISUAAAT13-S8-2, Tokyo, Japan: Curran Associates, Inc., Sept. 11–14, 2012.

[43] R. Corral & A. Vega:
"The Low Reduced Frequency Limit of Vibrating Airfoils - Part I: Theoretical Analysis", in: *Journal of Turbomachinery* 138.2, 021004 (Feb. 2016), issn: 0889-504X,
doi: 10.1115/1.4031776.

[44] E. F. Crawley:
"Aeroelastic Formulation for Tuned and Mistuned Rotors", in: *AGARD Manual on Aeroelasticity in Axial-Flow Turbomachines*, ed. by M. F. Platzer & F. O. Carta, vol. 2: Structural Dynamics and Aeroelasticity, AGARDograph No. 289, NATO AGARD (Advisory Group for Aerospace Research and Development), June 1988, chap. 19, isbn: 92-835-0467-4.

[45] J. E. Crouse:
Computer Program for Definition of Transonic Axial-Flow Compressor Blade Rows, NASA Technical Note - NASA TN D-7345, National Aeronautics and Space Administration (NASA), Feb. 1974.

[46] G. Daku & J. Vad:
"Experiment-Based Preliminary Design Guidelines for Consideration of Profile Vortex Shedding From Low-Speed Axial Fan Blades", in: *Journal of Turbomachinery* 143.6, 061014 (June 2021), issn: 0889-504X,
doi: 10.1115/1.4050392.

[47] P. Dhopade, A. J. Neely, J. Young & K. Shankar:
"High-Cycle Fatigue of Fan Blades Accounting for Fluid-Structure Interaction", in: *ASME Turbo Expo 2012: Turbine Technical Conference and Exposition*, vol. 7: Structures and Dynamics, Parts A and B, GT2012-68102, Copenhagen, Denmark, June 11–15, 2012, pp. 1365–1372, isbn: 978-0-7918-4473-1,
doi: 10.1115/GT2012-68102.

[48] E. Dowell, E. F. Crawley, H. C. C. Jr., D. A. Peters, R. H. Scanlan & F. Sisto:
A Modern Course in Aeroelasticity, Solid Mechanics and its Applications, Springer, Dordrecht, 1995, isbn: 978-0-7923-2789-9,
doi: 10.1007/978-94-011-0499-9.

[49] D. Espinal, H.-S. Im & G.-C. Zha:
"Full-Annulus Simulation of Nonsynchronous Blade Vibration Excitation of an Axial Compressor", in: *Journal of Turbomachinery* 140.3, 031008 (Mar. 2018), ISSN: 0889-504X,
DOI: 10.1115/1.4038337.

[50] M. Fiore & R. Biolchini:
"Numerical Simulation of a Counter-Rotative Open Rotor Using Phase-Lagged Conditions: Initial Validation on a Single Rotor Case", in: *Journal of Turbomachinery* 142.12, 121002 (Dec. 2020), ISSN: 0889-504X,
DOI: 10.1115/1.4047891.

[51] H. W. Försching:
Grundlagen der Aeroelastik, Springer-Verlag Berlin Heidelberg, 1974, ISBN: 978-3-642-48286-1,
DOI: 10.1007/978-3-642-48285-4.

[52] H. W. Försching:
"Aeroelastic Stability of Cascades in Turbomachinery", in: *Progress in Aerospace Sciences* 30.3 (1994), pp. 213–266, ISSN: 0376-0421,
DOI: 10.1016/0376-0421(94)90004-3.

[53] N. Forsthofer & C. Reiber:
"Structural Mechanic and Aeroelastic Approach for Design and Simulation of CFRP Fan Blades", in: *Luft- und Raumfahrt - Hochtechnologie aus Deutschland: Deutscher Luft- und Raumfahrtkongress 2016*, Braumschweig, Germany: Deutsche Gesellschaft für Luft- und Raumfahrt - Lilienthal-Oberth e.V., Sept. 13–15, 2016.

[54] L. Fottner:
"Review of Turbomachinery Blading Design Problems", in: *Blading-Design for Axial Turbomachines*, ed. by L. Fottner, AGARD Lecture Series No. 167, NATO AGARD (Advisory Group for Aerospace Research and Development), May 1989, chap. 1, ISBN: 92-835-0512-3.

[55] T. Fransson:
Project Final Report (FTR-5-93), Flutter-Free Turbomachinery Blades (FUTURE), tech. rep., Grant Agreement number: 213414, KTH Royal Institute of Technology, Stockholm, Sweden, 2013.

[56] Fraunhofer-Gesellschaft:
Vorhang auf: Fraunhofer und IBM weihen Quantencomputer ein, Press release, June 15, 2021,
URL: https://www.fraunhofer.de/content/dam/zv/de/presse-medien/2021/juni/pi14-zv-einweihung-quantencomputer.pdf.

[57] C. Frey:
On Unsteady CFD for Turbomachinery, tech. rep., Deutsches Zentrum für Luft- und Raumfahrt e.V. - Institut für Antriebstechnik, 2009.

[58] C. Frey, G. Ashcroft, H.-P. Kersken & C. Voigt:
"A Harmonic Balance Technique for Multistage Turbomachinery Applications", in: *ASME Turbo Expo 2014: Turbine Technical Conference and Exposition*, vol. 2B: Turbomachinery, GT2014-25230, Düsseldorf, Germany, June 16–20, 2014, ISBN: 978-0-7918-4561-5,
DOI: 10.1115/GT2014-25230.

[59] D. Friedewald, R. Thormann, C. Kaiser & J. Nitzsche:
"Quasi-Steady Doublet-Lattice Correction for Aerodynamic Gust Response Prediction in Attached and Separated Transonic Flow", in: *CEAS Aeronautical Journal* 9.1 (Mar. 2018), pp. 53–66, ISSN: 1869-5590,
DOI: 10.1007/s13272-017-0273-0.

[60] Y. C. Fung:
An Introduction to the Theory of Aeroelasticity, Dover Publications, 1993, ISBN: 978-0-486-67871-9.

[61] I. E. Garrick:
"On Some Fourier Transforms in the Theory of Nonstationary Flows", in: *Proceedings of the Fifth International Congress on Applied Mechanics*, Cambridge, Massachusetts, USA: John Wiley & Sons, Inc., Sept. 12–26, 1938, pp. 590–593.

[62] M. Giles:
"An Approach for Multi-Stage Calculations Incorporating Unsteadiness", in: *ASME 1992 International Gas Turbine and Aeroengine Congress and Exposition*, vol. Volume 1: Turbomachinery, 92-GT-282, Cologne, Germany, June 1–4, 1992,
DOI: 10.1115/92-GT-282.

[63] V. Gnesin, R. Rządkowski & L. Kolodyazhnaya:
"A Coupled Fluid-Structure Analysis for 3D Flutter in Turbomachines", in: *ASME Turbo Expo 2000: Power for Land, Sea, and Air*, vol. 4: Manufacturing Materials and Metallurgy; Ceramics; Structures and Dynamics; Controls, Diagnostics and Instrumentation; Education, 2000-GT-0380, Berlin, Germany, May 8–11, 2000, ISBN: 978-0-7918-7857-6,
DOI: 10.1115/2000-GT-0380.

[64] D. Goerke, A.-L. Le Denmat, T. Schmidt, F. Kocian & E. Nicke:
"Aerodynamic and Mechanical Optimization of CF/PEEK Blades of a Counter Rotating Fan", in: *ASME Turbo Expo 2012: Turbine Technical Conference and Exposition*, vol. 7: Structures and Dynamics, Parts A and B, GT2012-68797, Copenhagen, Denmark, June 11–15, 2012, pp. 21–33, ISBN: 978-0-7918-4473-1,
DOI: 10.1115/GT2012-68797.

[65] I. E. Gómez Fernández & M. Blocher:
"Time-Linearized Forced Response Analysis of a Counter Rotating Fan: Part II - Analysis of the DLR CRISP2 Model", in: *ASME Turbo Expo 2014: Turbine Technical Conference and Exposition*, vol. 7B: Structures and Dynamics, GT2014-25838, Düsseldorf, Germany, June 16–20, 2014, ISBN: 978-0-7918-4577-6,
DOI: 10.1115/GT2014-25838.

[66] I. Goulos & V. Pachidis:
"Real-Time Aero-elasticity Simulation of Open Rotors With Slender Blades for the Multidisciplinary Design of Rotorcraft", in: *Journal of Engineering for Gas Turbines and Power* 137.1, 012503 (Jan. 2015), ISSN: 0742-4795,
DOI: 10.1115/1.4028180.

[67] H. Grieb:
"Aeroelastik - Flattern und erzwungene Schaufelschwingungen", in: *Verdichter für Turbo-Flugtriebwerke*, Springer-Verlag Berlin Heidelberg, 2009, chap. 9, pp. 541–586, ISBN: 978-3-540-34374-5,
DOI: 10.1007/978-3-540-34374-5.

[68] H. Grieb:
Verdichter für Turbo-Flugtriebwerke, Springer-Verlag Berlin Heidelberg, 2009, ISBN: 978-3-540-34374-5,
DOI: 10.1007/978-3-540-34374-5.

[69] A. V. Grigoriev, A. I. Iakunin, N. B. Kuznechov, V. F. Kondratiev & N. N. Kortikov:
"Application of Harmonic Balance Method to the Simulation of Unsteady Rotor/Stator Interaction in the Single Stage", in: *10th European Conference on Turbomachinery, Fluid Dynamics and Thermodynamics (ETC 10)*, ETC2013-201, Lappeenranta, Finland, Apr. 15–19, 2013.

[70] J. Gross & M. Krack:
"Multiwave Vibrations in Mistuned Cascades With Tip-Shroud Friction", in: *Journal of Engineering for Gas Turbines and Power* 143.5, 051030 (May 2021), ISSN: 0742-4795,
DOI: 10.1115/1.4047889.

[71] B. Grüber & V. Carstens:
"The Impact of Viscous Effects on the Aerodynamic Damping of Vibrating Transonic Compressor Blades - A Numerical Study", in: *Journal of Turbomachinery* 123.2 (Apr. 2001), pp. 409–417, ISSN: 0889-504X,
DOI: 10.1115/1.1354139.

[72] P. Guruswamy & P. M. Goorjian:
"Effects of Viscosity on Transonic-Aerodynamic and Aeroelastic Characteristics of Oscillating Airfoils", in: *Journal of Aircraft* 21.9 (1984), pp. 700–707,
DOI: 10.2514/3.45017.

[73] K. C. Hall & C. B. Lorence:
"Calculation of Three-Dimensional Unsteady Flows in Turbomachinery Using the Linearized Harmonic Euler Equations", in: *ASME 1992 International Gas Turbine and Aeroengine Congress and Exposition*, vol. Volume 5: Manufacturing Materials and Metallurgy; Ceramics; Structures and Dynamics; Controls, Diagnostics and Instrumentation; Education, 92-GT-136, Cologne, Germany, June 1–4, 1992, ISBN: 978-0-7918-7897-2,
DOI: 10.1115/92-GT-136.

[74] K. C. Hall, J. P. Thomas & W. S. Clark:
"Computation of Unsteady Nonlinear Flows in Cascades Using a Harmonic Balance Technique", in: *AIAA Journal*, Aeronautics | Astronautics 40.5 (May 2002), pp. 879–886, ISSN: 1533-385X,
DOI: 10.2514/2.1754.

[75] Y. Hanamura, H. Tanaka & K. Yamaguchi:
"A Simplified Method to Measure Unsteady Forces Acting on the Vibrating Blades in Cascade", in: *Bulletin of JSME* 23.180 (June 1980), pp. 880–887,
DOI: 10.1299/jsme1958.23.880.

[76] A. Hebler & R. Thormann:
"Flutter Prediction of a Laminar Airfoil Using a Doublet Lattice Method Corrected by Experimental Data", in: *New Results in Numerical and Experimental Fluid Mechanics X*, ed. by A. Dillmann, G. Heller, E. Krämer, C. Wagner & C. Breitsamter, Notes on Numerical Fluid Mechanics and Multidisciplinary Design, Springer International Publishing, Cham, 2016, pp. 445–455, ISBN: 978-3-319-27279-5.

[77] J. P. Heners, D. M. Vogt, C. Frey & G. Ashcroft:
"Investigation of the Impact of Unsteady Turbulence Effects on the Aeroelastic Analysis of a Low-Pressure Turbine Rotor Blade", in: *Journal of Turbomachinery* 141.10, 100801 (Oct. 2019), ISSN: 0889-504X,
DOI: 10.1115/1.4043950.

[78] H. Henke, U. R. Müller & B. Schulze:
"A Viscous Inviscid Interaction Method for Use in Transonic Flutter Analysis", in: *Int. Forum on Aeroelasticity and Structural Dynamics 1991 Combined with a One-Day Workshop on Smart Material Systems and Structures*, 91-064, Aachen, Germany, June 3–6, 1991, pp. 66–77.

[79] H. Hennings & J. Belz:
"Experimental Investigation of the Aerodynamic Stability of an Annular Compressor Cascade Performing Tuned Pitching Oscillations in Transonic Flow", in: *ASME 1999 International Gas Turbine and Aeroengine Congress and Exhibition*, vol. 4: Manufacturing Materials and Metallurgy; Ceramics; Structures and Dynamics; Controls, Diagnostics and Instrumentation; Education; IGTI Scholar Award; General, 99-GT-407, Indianapolis, Indiana, USA, June 7–10, 1999, ISBN: 978-0-7918-7861-3,
DOI: 10.1115/99-GT-407.

[80] A. Hergt, S. Grund, J. Klinner, W. Steinert, M. Beversdorff & U. Siller:
"Some Aspects of the Transonic Compressor Tandem Design", in: *Journal of Turbomachinery* 141.9, 091003 (Sept. 2019), ISSN: 0889-504X,
DOI: 10.1115/1.4043280.

[81] A. Hergt, J. Klinner, J. Wellner, C. Willert, S. Grund, W. Steinert & M. Beversdorff:
"The Present Challenge of Transonic Compressor Blade Design", in: *Journal of Turbomachinery* 141.9, 091004 (Sept. 2019), ISSN: 0889-504X,
DOI: 10.1115/1.4043329.

[82] High-Level Group on Aviation Research:
Flightpath 2050 - Europe's Vision for Aviation, Maintaining global leadership and serving society's needs, tech. rep., Directorate-General for Research, Innovation / Directorate-General for Mobility, and Transport, Dec. 2012, p. 32,
DOI: 10.2777/15458.

[83] A. Hohl & J. Wallaschek:
"A Method to Reduce the Energy Localization in Mistuned Bladed Disks by Application-Specific Blade Pattern Arrangement", in: *Journal of Engineering for Gas Turbines and Power* 138.9, 092502 (Sept. 2016), ISSN: 0742-4795,
DOI: 10.1115/1.4032739.

[84] F. Holzinger, F. Wartzek, M. Jüngst, H.-P. Schiffer & S. Leichtfuss:
"Self-Excited Blade Vibration Experimentally Investigated in Transonic Compressors: Rotating Instabilities and Flutter", in: *Journal of Turbomachinery* 138.4, 041006 (Apr. 2016), ISSN: 0889-504X,
DOI: 10.1115/1.4032163.

[85] F. Holzinger, F. Wartzek, H.-P. Schiffer, S. Leichtfuss & M. Nestle:
"Self-Excited Blade Vibration Experimentally Investigated in Transonic Compressors: Acoustic Resonance", in: *Journal of Turbomachinery* 138.4, 041001 (Apr. 2016), ISSN: 0889-504X,
DOI: 10.1115/1.4032042.

[86] M. Hüls, L. Panning-von Scheidt & J. Wallaschek:
"Combined Airfoil and Snubber Design Optimization of Turbine Blades With Respect to Friction Damping", in: *Journal of Turbomachinery* 140.8, 081007 (Aug. 2018), ISSN: 0889-504X,
DOI: 10.1115/1.4040679.

[87] H. Im, X. Chen & G. Zha:
"Detached Eddy Simulation of Transonic Rotor Stall Flutter Using a Fully Coupled Fluid-Structure Interaction", in: *ASME 2011 Turbo Expo: Turbine Technical Conference and Exposition*, vol. 6: Structures and Dynamics, Parts A and B, GT2011-45437, Vancouver, British Columbia, Canada, June 6–10, 2011, pp. 1217–1230, ISBN: 978-0-7918-5466-2,
DOI: 10.1115/GT2011-45437.

[88] International Civil Aviation Organization (ICAO):
Forecasts of Scheduled Passenger and Freight Traffic, The United Nations (UN), June 28, 2021,
URL: https://www.icao.int/sustainability/pages/eap-fp-forecast-scheduled-passenger-traffic.aspx.

[89] J. A. Jones Jr.:
"A Multidisciplinary Algorithm for the 3-D Design Optimization of Transonic Axial Compressor Blades", URI: http://hdl.handle.net/10945/9780, PhD thesis, Naval Postgraduate School, Monterey, California, 2002.

[90] G. Kahl & H. Hennings:
"Computational Investigation of an Oscillating Compressor Cascade Experiment", in: *Proceedings of the 9th International Symposium on Unsteady Aerodynamics, Aeroacoustics and Aeroelasticity of Turbomachines (ISUAAAT 2000)*, Lyon, France, Sept. 4–8, 2000, pp. 819–829.

[91] J. Kamenik, I. Voutchkov, D. J. J. Toal, A. J. Keane, L. Högner, M. Meyer & R. Bates:
"Robust Turbine Blade Optimization in the Face of Real Geometric Variations", in: *Journal of Propulsion and Power*, Propulsion | Power 34.6 (Nov.–Dec. 2018), pp. 1479–1493, ISSN: 1533-3876,
DOI: 10.2514/1.B37091.

[92] M. Karpel:
"Design for Active Flutter Suppression and Gust Alleviation Using State-Space Aeroelastic Modeling", in: *Journal of Aircraft* 19.3 (Mar. 1982), pp. 221–227,
DOI: 10.2514/3.57379.

[93] J. Katz & A. I. Plotkin:
Low-Speed Aerodynamics, 2nd ed., Cambridge Aerospace Series, Cambridge: Cambridge University Press, 2001, ISBN: 978-0-521-66552-0,
DOI: 10.1017/CBO9780511810329.

[94] K. R. V. Kaza & R. E. Kielb:
"Flutter and Response of a Mistuned Cascade in Incompressible Flow", in: *AIAA Journal*, Aeronautics | Astronautics 20.8 (Aug. 1982), pp. 1120–1127, ISSN: 1533-385X,
DOI: 10.2514/3.51172.

[95] R. Kemme:
"Numerische Untersuchungen zum aeroelastischen Verhalten eines hochbelasteten Verdichterrotors", DLR-Forschungsbericht 2004-28, PhD thesis, Universität Hannover / Institut für Aeroelastik, Aug. 2004.

[96] H.-P. Kersken, C. Frey, C. Voigt & G. Ashcroft:
"Time-Linearized and Time-Accurate 3D RANS Methods for Aeroelastic Analysis in Turbomachinery", in: *Journal of Turbomachinery* 134.5, 051024 (May 2012), ISSN: 0889-504X,
DOI: 10.1115/1.4004749.

[97] A. Khalak:
"A Framework for Flutter Clearance of Aeroengine Blades", in: *Journal of Engineering for Gas Turbines and Power* 124.4 (Oct. 2002), pp. 1003–1010, ISSN: 0742-4795,
DOI: 10.1115/1.1492832.

[98] R. Kielb, J. Barter, O. Chernycheva & T. Fransson:
"Flutter of Low Pressure Turbine Blades With Cyclic Symmetric Modes: A Preliminary Design Method", in: *Journal of Turbomachinery* 126.2 (Apr. 2004), pp. 306–309, ISSN: 0889-504X,
DOI: 10.1115/1.1650380.

[99] R. Kielb, J. Barter, O. Chernysheva & T. Fransson:
"Flutter Design of Low Pressure Turbine Blades with Cyclic Symmetric Modes", in: *Unsteady Aerodynamics, Aeroacoustics and Aeroelasticity of Turbomachines - Proceedings of the 10th International symposium on unsteady aerodynamics, aeroacoustics and aeroelasticity of turbomachines, 2003, Durham NC, USA*, ed. by K. C. Hall, R. E. Kielb & J. P. Thomas, Springer Netherlands, Dordrecht, 2006, pp. 41–52, ISBN: 978-1-4020-4605-6,
DOI: 10.1007/1-4020-4605-7_4.

[100] R. E. Kielb, J. W. Barter, J. P. Thomas & K. C. Hall:
"Blade Excitation by Aerodynamic Instabilities: A Compressor Blade Study", in: *ASME Turbo Expo 2003, collocated with the 2003 International Joint Power Generation Conference*, vol. 4: Turbo Expo 2003, GT2003-38634, Atlanta, Georgia, USA, June 16–19, 2003, pp. 399–406, ISBN: 0-7918-3687-8,
DOI: 10.1115/GT2003-38634.

[101] D. Korte & D. Peitsch:
"An Adaption of the P-Method to Analyse the Aerodynamic Damping in Turbomachinery Considering Modal Coupling", in: *International Forum on Aeroelasticity and Structural Dynamics (IFASD 2013)*, vol. 1, Bristol, United Kingdom: Curran Associates, Inc., June 24–26, 2013, pp. 309–325, ISBN: 978-1-63439-102-3.

[102] A. Krug, P. Busse & K. Vogeler:
"Experimental Investigation Into the Effects of the Steady Wake-Tip Clearance Vortex Interaction in a Compressor Cascade", in: *Journal of Turbomachinery* 137.6, 061006 (June 2015), ISSN: 0889-504X,
DOI: 10.1115/1.4028797.

[103] F. Lane:
"System Mode Shapes in the Flutter of Compressor Blade Rows", in: *Journal of the Aeronautical Sciences* 23.1 (Jan. 1956), pp. 54–66,
DOI: 10.2514/8.3502.

[104] K.-B. Lee, M. Wilson & M. Vahdati:
"Effects of Inlet Disturbances on Fan Stability", in: *Journal of Engineering for Gas Turbines and Power* 141.5, 051014 (May 2019), ISSN: 0742-4795,
DOI: 10.1115/1.4042204.

[105] Y.-T. Lee & J. Feng:
"Potential and Viscous Interactions for a Multi-Blade-Row Compressor", in: *Journal of Turbomachinery* 126.4 (Oct. 2004), pp. 464–472, ISSN: 0889-504X,
DOI: 10.1115/1.1740778.

[106] S. Leichtfuss, F. Holzinger, C. Brandstetter, F. Wartzek, J. Ratz & H.-P. Schiffer:
"Aerodynamic and Aeroelastic Investigation of a Transonic Compressor Rig", in: *13th International Symposium on Unsteady Aerodynamics, Aeroacoustics and Aeroelasticity of Turbomachines (ISUAAAT 13)*, ISUAAAT13-S6-1, Tokyo, Japan: Curran Associates, Inc., Sept. 11–14, 2012.

[107] J. G. Leishman:
"Validation of Approximate Indicial Aerodynamic Functions for Two-Dimensional Subsonic Flow", in: *Journal of Aircraft* 25.10 (Oct. 1988), pp. 914–922, ISSN: 1533-3868,
DOI: 10.2514/3.45680.

[108] B. M. Lowe & D. W. Zingg:
"Efficient Flutter Prediction Using Reduced-Order Modeling", in: *AIAA Journal*, Aeronautics | Astronautics 59.7 (July 2021), pp. 2670–2683, ISSN: 1533-385X,
DOI: 10.2514/1.J060006.

[109] Y. Lu, J. Green, S. C. Stapelfeldt & M. Vahdati:
"Effect of Geometric Variability on Running Shape and Performance of a Transonic Fan", in: *Journal of Turbomachinery* 141.10, 101012 (Oct. 2019), issn: 0889-504X,
doi: 10.1115/1.4044676.

[110] Y. Lu, B. Lad & M. Vahdati:
"Transonic Fan Blade Redesign Approach to Attenuate Nonsynchronous Vibration", in: *Journal of Engineering for Gas Turbines and Power* 143.7, 071007 (July 2021), issn: 0742-4795,
doi: 10.1115/1.4050023.

[111] W. Mallik, J. A. Schetz & R. K. Kapania:
"Rapid Transonic Flutter Analysis for Aircraft Conceptual Design Applications", in: *AIAA Journal*, Aeronautics | Astronautics 56.6 (June 2018), pp. 2389–2402, issn: 1533-385X,
doi: 10.2514/1.J056218.

[112] L. Malzacher, C. Schwarze, V. Motta & D. Peitsch:
"Experimental Investigation of an Aerodynamically Mistuned Oscillating Compressor Cascade", in: *Journal of Turbomachinery* 141.7, 071012 (July 2019), issn: 0889-504X,
doi: 10.1115/1.4043474.

[113] A. N. Marques, M. M. J. Opgenoord, R. R. Lam, A. Chaudhuri & K. E. Willcox:
"Multifidelity Method for Locating Aeroelastic Flutter Boundaries", in: *AIAA Journal*, Aeronautics | Astronautics 58.4 (Apr. 2020), pp. 1772–1784, issn: 1533-385X,
doi: 10.2514/1.J058663.

[114] J. Marshall & M. Imregun:
"A Review of Aeroelasticity Methods with Emphasis on Turbomachinery Applications", in: *Journal of Fluids and Structures* 10.3 (Apr. 1996), pp. 237–267, issn: 0889-9746,
doi: 10.1006/jfls.1996.0015.

[115] M. May:
"Sensitivity Analysis With Respect to Flutter-Free Design of Compressor Blades", in: *ASME Turbo Expo 2010: Power for Land, Sea, and Air*, vol. 6: Structures and Dynamics, Parts A and B, GT2010-23557, Glasgow, United Kingdom, June 14–18, 2010, pp. 1263–1275, isbn: 978-0-7918-4401-4,
doi: 10.1115/GT2010-23557.

[116] M. May:
"Linearized Flutter Investigations of Mistuned Turbomachinery Blading", DLR Forschungsbericht 2011-02, PhD thesis, Technische Universität Berlin / Institut für Aeroelastik, 2012.

[117] M. A. Mayorca, D. M. Vogt, H. Mårtensson & T. H. Fransson:
"Prediction of Turbomachinery Aeroelastic Behavior From a Set of Representative Modes", in: *Journal of Turbomachinery* 135.1, 011032 (Jan. 2013), issn: 0889-504X,
doi: 10.1115/1.4006536.

[118] D. H. Meadows, D. L. Meadows, J. Randers & W. W. Behrens III:
The Limits to Growth, A Report for the Club of Rome's Project on the Predicament of Mankind, Potomac Associates - Universe Books, 1972, p. 205, isbn: 0-87663-165-0.

[119] G. Medic, V. Zhang, G. Wang, J. Joo & O. P. Sharma:
"Prediction of Transition and Losses in Compressor Cascades Using Large-Eddy Simulation", in: *Journal of Turbomachinery* 138.12, 121001 (Dec. 2016), issn: 0889-504X,
doi: 10.1115/1.4033514.

[120] M. Meingast, R. E. Kielb & J. P. Thomas:
"Preliminary Flutter Design Method for Supersonic Low Pressure Turbines", in: *ASME Turbo Expo 2009: Power for Land, Sea, and Air*, vol. 6: Structures and Dynamics, Parts A and B, GT2009-59177, Orlando, Florida, USA, June 8–12, 2009, pp. 507–515, ISBN: 978-0-7918-4887-6,
DOI: 10.1115/GT2009-59177.

[121] C. E. Meinzer & J. R. Seume:
"Experimental and Numerical Quantification of the Aerodynamic Damping of a Turbine Blisk", in: *Journal of Turbomachinery* 142.12, 121011 (Dec. 2020), ISSN: 0889-504X,
DOI: 10.1115/1.4048192.

[122] C. L. Memory, J. P. Chen & J. P. Bons:
"Implicit Large Eddy Simulation of a Stalled Low-Pressure Turbine Airfoil", in: *Journal of Turbomachinery* 138.7, 071008 (July 2016), ISSN: 0889-504X,
DOI: 10.1115/1.4032365.

[123] V. Michelassi, L. Chen, R. Pichler, R. Sandberg & R. Bhaskaran:
"High-Fidelity Simulations of Low-Pressure Turbines: Effect of Flow Coefficient and Reduced Frequency on Losses", in: *Journal of Turbomachinery* 138.11, 111006 (Nov. 2016), ISSN: 0889-504X,
DOI: 10.1115/1.4033266.

[124] V. Michelassi, L.-W. Chen, R. Pichler & R. D. Sandberg:
"Compressible Direct Numerical Simulation of Low-Pressure Turbines - Part II: Effect of Inflow Disturbances", in: *Journal of Turbomachinery* 137.7, 071005 (July 2015), ISSN: 0889-504X,
DOI: 10.1115/1.4029126.

[125] B. A. Miller & J. J. McNamara:
"Efficient Fluid-Thermal-Structural Time Marching with Computational Fluid Dynamics", in: *AIAA Journal*, Aeronautics | Astronautics 56.9 (Sept. 2018), pp. 3610–3621, ISSN: 1533-385X,
DOI: 10.2514/1.J056572.

[126] D. Möller, M. Jüngst, F. Holzinger, C. Brandstetter, H.-P. Schiffer & S. Leichtfuss:
"Mechanism of Nonsynchronous Blade Vibration in a Transonic Compressor Rig", in: *Journal of Turbomachinery* 139.1, 011002 (Jan. 2017), ISSN: 0889-504X,
DOI: 10.1115/1.4034029.

[127] G. E. Moore:
"Progress in Digital Integrated Electronics", in: *IEEE Solid-State Circuits Society Newsletter* 11.3 (Sept. 2006), [Copyright 1975 IEEE. Reprinted, with permission. Technical Digest. International Electron Devices Meeting, IEEE, 1975, pp. 11-13.], pp. 36–37, ISSN: 1098-4232,
DOI: 10.1109/N-SSC.2006.4804410.

[128] MSC Software:
MSC Nastran 2020 Reference Manual, 2020.

[129] S. W. Naung, M. Rahmati & H. Farokhi:
"Aeromechanical Analysis of a Complete Wind Turbine Using Nonlinear Frequency Domain Solution Method", in: *Journal of Engineering for Gas Turbines and Power* 143.1, 011018 (Jan. 2021), ISSN: 0742-4795,
DOI: 10.1115/1.4049206.

[130] W. Ning, Y. S. Li & R. G. Wells:
"Predicting Bladerow Interactions Using a Multistage Time-Linearized Navier-Stokes Solver", in: *Journal of Turbomachinery* 125.1 (Jan. 2003), pp. 25–32, issn: 0889-504X,
doi: 10.1115/1.1516570.

[131] H. M. B. Obaida, A. Rona & J. P. Gostelow:
"Loss Reduction in a 1.5 Stage Axial Turbine by Computer-Driven Stator Hub Contouring", in: *Journal of Turbomachinery* 141.6, 061009 (June 2019), issn: 0889-504X,
doi: 10.1115/1.4042305.

[132] J. A. Owczarek:
"On the Phenomenon of Pressure Pulses Reflecting Between Blades of Adjacent Blade Rows of Turbomachines", in: *Journal of Turbomachinery* 133.2, 021016 (Apr. 2011), issn: 0889-504X,
doi: 10.1115/1.4001185.

[133] J. Panovsky & R. E. Kielb:
"A Design Method to Prevent Low Pressure Turbine Blade Flutter", in: *Journal of Engineering for Gas Turbines and Power* 122.1 (Oct. 1999), pp. 89–98, issn: 0742-4795,
doi: 10.1115/1.483180.

[134] C. Peeren & K. Vogeler:
"Geometrical Modification of the Unsteady Pressure to Reduce Low-Pressure Turbine Flutter", in: *Journal of Turbomachinery* 139.9, 091011 (Sept. 2017), issn: 0889-504X,
doi: 10.1115/1.4036343.

[135] P. Petrie-Repar:
"Development of an Efficient and Robust Linearised Navier-Stokes Flow Solver", in: *Unsteady Aerodynamics, Aeroacoustics and Aeroelasticity of Turbomachines - Proceedings of the 10th International symposium on unsteady aerodynamics, aeroacoustics and aeroelasticity of turbomachines, 2003, Durham NC, USA*, ed. by K. C. Hall, R. E. Kielb & J. P. Thomas, Springer Netherlands, Dordrecht, 2006, pp. 437–448, isbn: 978-1-4020-4605-6,
doi: 10.1007/1-4020-4605-7_32.

[136] H. M. Phan & L. He:
"Validation Studies of Linear Oscillating Compressor Cascade and Use of Influence Coefficient Method", in: *Journal of Turbomachinery* 142.5, 051005 (May 2020), issn: 0889-504X,
doi: 10.1115/1.4045657.

[137] A. Placzek & A. Dugeai:
"Numerical Prediction of the Aeroelastic Damping Using Multi-Modal Dynamically Coupled Simulations on a 360° Fan Configuration", in: *15th International Forum on Aeroelasticity and Structural Dynamics (IFASD)*, IFASD-2011-084, Paris, France, June 26–30, 2011.

[138] S. B. Pope:
"An Introduction to Modelling and Simulation", in: *Turbulent Flows*, Cambridge: Cambridge University Press, 2000, chap. 8, isbn: 978-0-521-59886-6,
doi: 10.1017/CBO9780511840531.

[139] S. B. Pope:
"Direct Numerical Simulation", in: *Turbulent Flows*, Cambridge: Cambridge University Press, 2000, chap. 9, isbn: 978-0-521-59886-6,
doi: 10.1017/CBO9780511840531.

[140] S. B. Pope:
"Large-Eddy Simulation", in: *Turbulent Flows*, Cambridge: Cambridge University Press, 2000, chap. 13, ISBN: 978-0-521-59886-6,
DOI: 10.1017/CBO9780511840531.

[141] S. B. Pope:
"The Scales of Turbulent Motion", in: *Turbulent Flows*, Cambridge: Cambridge University Press, 2000, chap. 6, ISBN: 978-0-521-59886-6,
DOI: 10.1017/CBO9780511840531.

[142] S. B. Pope:
Turbulent Flows, Cambridge: Cambridge University Press, 2000, ISBN: 978-0-521-59886-6,
DOI: 10.1017/CBO9780511840531.

[143] Pratt & Whitney:
GP7200 Engine 02, used with kind permission by Pratt & Whitney, July 1, 2014,
URL: http://www.pw.utc.com/Content/Photos/Feed/Stories/GP7200-Engine-02/gp7000_cutaway_high.jpg.

[144] M. T. Rahmati, L. He & Y. S. Li:
"The Blade Profile Orientations Effects on the Aeromechanics of Multirow Turbomachines", in: *Journal of Engineering for Gas Turbines and Power* 138.6, 062606 (June 2016), ISSN: 0742-4795,
DOI: 10.1115/1.4030569.

[145] M. T. Rahmati, L. He, D. X. Wang, Y. S. Li, R. G. Wells & S. K. Krishnababu:
"Nonlinear Time and Frequency Domain Methods for Multirow Aeromechanical Analysis", in: *Journal of Turbomachinery* 136.4, 041010 (Apr. 2014), ISSN: 0889-504X,
DOI: 10.1115/1.4024899.

[146] Q. Rendu, M. Vahdati & L. Salles:
"Radial Decomposition of Blade Vibration to Identify a Stall Flutter Source in a Transonic Fan", in: *Journal of Turbomachinery* 141.10, 101011 (Oct. 2019), ISSN: 0889-504X,
DOI: 10.1115/1.4044484.

[147] M. Roser & H. Ritchie:
Transistor Count over Time, Data collected and visualized: 2020-11-01, July 19, 2021,
URL: https://ourworldindata.org/uploads/2020/11/Transistor-Count-over-time.png.

[148] R. Rządkowski, V. Gnesin & L. Kolodyazhnaya:
"Unsteady Forces Acting on Rotor Blades in Seven and Half Stages", in: *13th International Symposium on Unsteady Aerodynamics, Aeroacoustics and Aeroelasticity of Turbomachines (ISUAAAT 13)*, ISUAAAT13-S4-2, Tokyo, Japan: Curran Associates, Inc., Sept. 11–14, 2012.

[149] A. Sainarayan & A. Combes:
"Airline Operating Costs and Productivity", in: *ICAO Aviation Data and Analysis Seminar*, Tehran, Iran IR, Feb. 20–23, 2017,
URL: https://www.icao.int/mid/documents/2017/aviation%20data%20and%20analysis%20seminar/ppt3%20-%20airlines%20operating%20costs%20and%20productivity.pdf.

[150] R. D. Sandberg, R. Pichler & L. Chen:
"Assessing the Sensitivity of Turbine Cascade Flow to Inflow Disturbances Using Direct Numerical Simulation", in: *13th International Symposium on Unsteady Aerodynamics, Aeroacoustics and Aeroelasticity of Turbomachines (ISUAAAT 13)*, ISUAAAT13-S8-4, Tokyo, Japan: Curran Associates, Inc., Sept. 11–14, 2012.

[151] R. D. Sandberg, V. Michelassi, R. Pichler, L. Chen & R. Johnstone:
"Compressible Direct Numerical Simulation of Low-Pressure Turbines - Part I: Methodology", in: *Journal of Turbomachinery* 137.5, 051011 (May 2015), issn: 0889-504X, doi: 10.1115/1.4028731.

[152] P. Schimming, L. Enghardt, W. Neise, G. Schewe, S. Schmitt, R. Schnell, L. Wallscheid & Y. Zhang:
Experimentelle Untersuchungen zur Aeroakustik, -elastik und -dynamik am CRISP-1m-Modell, tech. rep., Förderkennzeichen LFT9601, Abschlussbericht 1996-1999, DLR e.V., 2000.

[153] S. Schmitt:
"Simulation von Flattern und aerodynamischer Zwangserregung in Turbomaschinenbeschaufelungen", DLR-FB-2003-22, PhD thesis, Ruhr-Universität Bochum / Institut für Aeroelastik, 2003.

[154] M. Schuff & V. Chenaux:
"Coupled Mode Flutter of a Linear Compressor Cascade in Subsonic and Transonic Flow Conditions", in: *18th International Symposium on Transport Phenomena and Dynamics of Rotating Machinery (ISROMAC18)*, Virtual, Online, Nov. 23–26, 2020.

[155] M. Schuff & V. A. Chenaux:
"Coupled Mode Flutter Analysis of Turbomachinery Blades Using an Adaptation of the p-k Method", in: *Journal of Engineering for Gas Turbines and Power* 143.2, 021017 (Feb. 2021), issn: 0742-4795,
doi: 10.1115/1.4048986.

[156] M. Schuff, T. Lengyel-Kampmann & N. Forsthofer:
"Influence of the Steady Deformation on Numerical Flutter Prediction for Highly Loaded and Flexible Fan Blades", in: *ASME Turbo Expo 2017: Turbomachinery Technical Conference and Exposition*, vol. 7B: Structures and Dynamics, GT2017-64027, Charlotte, North Carolina, USA, June 26–30, 2017, isbn: 978-0-7918-5093-0, doi: 10.1115/GT2017-64027.

[157] A. D. Scillitoe, P. G. Tucker & P. Adami:
"Numerical Investigation of Three-Dimensional Separation in an Axial Flow Compressor: The Influence of Freestream Turbulence Intensity and Endwall Boundary Layer State", in: *Journal of Turbomachinery* 139.2, 021011 (Feb. 2017), issn: 0889-504X,
doi: 10.1115/1.4034797.

[158] C. E. Seeley, C. Wakelam, X. Zhang, D. Hofer & W.-M. Ren:
"Investigations of Flutter and Aerodynamic Damping of a Turbine Blade: Experimental Characterization", in: *Journal of Turbomachinery* 139.8, 081011 (Aug. 2017), issn: 0889-504X,
doi: 10.1115/1.4035840.

[159] F. Sicot, G. Dufour & A. Dugeai:
"A Harmonic Balance Method for Aerodynamic Damping Prediction in Turbomachinery", in: *9th European Conference on Turbomachinery, Fluid Dynamics and Thermodynamics (ETC 9)*, Istanbul, Turkey, Mar. 21–25, 2011,
url: https://oatao.univ-toulouse.fr/8505/.

[160] F. Sisto:
"Introduction and Overview", in: *AGARD Manual on Aeroelasticity in Axial-Flow Turbomachines*, ed. by M. F. Platzer & F. O. Carta, vol. 1: Unsteady Turbomachinery Aerodynamics, AGARDograph No. 289, NATO AGARD (Advisory Group for Aerospace Research and Development), Mar. 1987, chap. 1, ISBN: 92-835-1543-9.

[161] F. Sisto:
"Stall Flutter", in: *AGARD Manual on Aeroelasticity in Axial-Flow Turbomachines*, ed. by M. F. Platzer & F. O. Carta, vol. 1: Unsteady Turbomachinery Aerodynamics, AGARDograph No. 289, NATO AGARD (Advisory Group for Aerospace Research and Development), Mar. 1987, chap. 7, ISBN: 92-835-1543-9.

[162] J. Smagorinsky:
"General Circulation Experiments with the Primitive Equations", in: *Monthly Weather Review* 91.3 (Mar. 1963), pp. 99–164, ISSN: 0027-0644,
DOI: 10.1175/1520-0493(1963)091<0099:GCEWTP>2.3.CO;2.

[163] P. R. Spalart, W.-H. Jou, M. Strelets & S. R. Allmaras:
"Comments on the Feasibility of LES for Wings, and on a Hybrid RANS/LES Approach", in: *Advances in DNS/LES, Proceedings of the First AFOSR International Conference on DNS/LES*, ed. by C. Liu & Z. Liu, Ruston, Louisiana, USA: Greyden Press, Aug. 4–8, 1997, pp. 137–148, ISBN: 1570743657.

[164] R. Srivastava & T. G. Keith Jr.:
"Shock Induced Flutter of Turbomachinery Blade Row", in: *ASME Turbo Expo 2004: Power for Land, Sea, and Air*, vol. 6: Turbo Expo 2004, GT2004-53479, Vienna, Austria, June 14–17, 2004, pp. 487–496, ISBN: 0-7918-4171-5,
DOI: 10.1115/GT2004-53479.

[165] R. Srivastava, J. Panovsky, R. Kielb, L. Virgin & K. Ekici:
"Nonlinear Flutter in Fan Stator Vanes With Time Dependent Fixity", in: *Journal of Turbomachinery* 134.2, 021009 (Mar. 2012), ISSN: 0889-504X,
DOI: 10.1115/1.4003253.

[166] S. Stapelfeldt & M. Vahdati:
"On the Importance of Engine-Representative Models for Fan Flutter Predictions", in: *Journal of Turbomachinery* 140.8, 081005 (Aug. 2018), ISSN: 0889-504X,
DOI: 10.1115/1.4040110.

[167] A. J. Strazisar, J. R. Wood, M. D. Hathaway & K. L. Suder:
Laser Anemometer Measurements in a Transonic Axial-Flow Fan Rotor, NASA Technical Paper 2879, National Aeronautics and Space Administration (NASA), Nov. 1989.

[168] T. Sun, P. Petrie-Repar, D. M. Vogt & A. Hou:
"Detached-Eddy Simulation Applied to Aeroelastic Stability Analysis in a Last-Stage Steam Turbine Blade", in: *Journal of Turbomachinery* 141.9, 091002 (Sept. 2019), ISSN: 0889-504X,
DOI: 10.1115/1.4043407.

[169] K. Suzuki, F. Zhao & M. Vahdati:
"Numerical Analysis of Flutter in Variable Geometry Compressors", in: *ASME Turbo Expo 2020: Turbomachinery Technical Conference and Exposition*, vol. 10A: Structures and Dynamics, GT2020-16093, Virtual, Online, Sept. 21–25, 2020, ISBN: 978-0-7918-8421-8,
DOI: 10.1115/GT2020-16093.

[170] K. Taira, S. L. Brunton, S. T. M. Dawson, C. W. Rowley, T. Colonius, B. J. McKeon, O. T. Schmidt, S. Gordeyev, V. Theofilis & L. S. Ukeiley:
"Modal Analysis of Fluid Flows: An Overview", in: *AIAA Journal*, Aeronautics | Astronautics 55.12 (Dec. 2017), pp. 4013–4041, ISSN: 1533-385X,
DOI: 10.2514/1.J056060.

[171] K. Taira, M. S. Hemati, S. L. Brunton, Y. Sun, K. Duraisamy, S. Bagheri, S. T. M. Dawson & C.-A. Yeh:
"Modal Analysis of Fluid Flows: Applications and Outlook", in: *AIAA Journal*, Aeronautics | Astronautics 58.3 (Mar. 2020), pp. 998–1022, ISSN: 1533-385X,
DOI: 10.2514/1.J058462.

[172] K. E. Tatum & G. L. Giles:
"Integrating Nonlinear Aerodynamic and Structural Analysis for a Complete Fighter Configuration", in: *Journal of Aircraft* 25.12 (Dec. 1988), pp. 1150–1156,
DOI: 10.2514/3.45715.

[173] M. Terstegen, C. Sanders, P. Jeschke & H. Schönenborn:
"Rotor-Stator Interactions in a 2.5-Stage Axial Compressor - Part I: Experimental Analysis of Tyler-Sofrin Modes", in: *Journal of Turbomachinery* 141.10, 101002 (Oct. 2019), ISSN: 0889-504X,
DOI: 10.1115/1.4043961.

[174] R. Thormann & M. Widhalm:
"Linear-Frequency-Domain Predictions of Dynamic-Response Data for Viscous Transonic Flows", in: *AIAA Journal*, Aeronautics | Astronautics 51.11 (Nov. 2013), pp. 2540–2557, ISSN: 1533-385X,
DOI: 10.2514/1.J051896.

[175] M. G. Turner, K. Park, K. Siddappaji, S. Dey, D. P. Gutzwiller, A. Merchant & D. Bruna:
"Framework for Multidisciplinary Optimization of Turbomachinery", in: *ASME Turbo Expo 2010: Power for Land, Sea, and Air*, vol. 7: Turbomachinery, Parts A, B, and C, GT2010-22228, Glasgow, United Kingdom, June 14–18, 2010, pp. 623–631, ISBN: 978-0-7918-4402-1,
DOI: 10.1115/GT2010-22228.

[176] J. C. Tyacke & P. G. Tucker:
"Future Use of Large Eddy Simulation in Aero-engines", in: *Journal of Turbomachinery* 137.8, 081005 (Aug. 2015), ISSN: 0889-504X,
DOI: 10.1115/1.4029363.

[177] I. Ulbricht:
"Stabilität des stehenden Ringgitters", PhD thesis, Technische Universität Berlin, 2002,
DOI: 10.14279/depositonce-412.

[178] M. Vahdati, K.-B. Lee & P. Sureshkumar:
"A Review of Computational Aeroelasticity Of Civil Fan Blades", in: *International Journal of Gas Turbine, Propulsion and Power Systems* 11.4 (Oct. 2020), pp. 22–35,
DOI: 10.38036/jgpp.11.4_22.

[179] M. Vahdati, G. Simpson & M. Imregun:
"Mechanisms for Wide-Chord Fan Blade Flutter", in: *Journal of Turbomachinery* 133.4, 041029 (Oct. 2011), ISSN: 0889-504X,
DOI: 10.1115/1.4001233.

[180] A. C. L. M. van Rooij, J. Nitzsche & R. P. Dwight:
"Prediction of Aeroelastic Limit-Cycle Oscillations Based on Harmonic Forced-Motion Oscillations", in: *AIAA Journal*, Aeronautics | Astronautics 55.10 (Oct. 2017), pp. 3517–3529, ISSN: 1533-385X,
DOI: 10.2514/1.J055852.

[181] V. V. Vedeneev, M. Kolotnikov & P. Makarov:
"Experimental Validation of Numerical Blade Flutter Prediction", in: *Journal of Propulsion and Power*, Propulsion | Power 31.5 (Sept.–Oct. 2015), pp. 1281–1291, ISSN: 1533-3876,
DOI: 10.2514/1.B35419.

[182] A. Vega & R. Corral:
"The Low Reduced Frequency Limit of Vibrating Airfoils - Part II: Numerical Experiments", in: *Journal of Turbomachinery* 138.2, 021005 (Feb. 2016), ISSN: 0889-504X,
DOI: 10.1115/1.4031777.

[183] H. K. Versteeg & W. Malalasekera:
An introduction to Computational Fluid Dynamics, Pearson Education Limited, 1995, ISBN: 978-0-582-21884-0.

[184] D. Vogt:
"Experimental Investigation of Three-Dimensional Mechanisms in Low-Pressure Turbine Flutter", URN: urn:nbn:se:kth:diva-205, PhD thesis, Kungliga Tekniska Högskolan, Stockholm, May 2005, p. 189, ISBN: 91-7178-034-3.

[185] D. M. Vogt & T. H. Fransson:
"Towards Flutter-Free Turbomachinery Blades", in: *Innovation for Sustainable Aviation in a Global Environment, Proceedings of the Sixth European Aeronautics Days*, ed. by D. Knörzer & J. Szodruch, Madrid, Spain: IOS Press, Mar. 30–Apr. 1, 2011, pp. 161–167, ISBN: 978-1-61499-062-8,
DOI: 10.3233/978-1-61499-063-5-161.

[186] A. Voss:
"Comparison between VLM and CFD Maneuver Loads Calculation at the Example of a Flying Wing Configuration", in: *Journal of Aeroelasticity and Structural Dynamics* (Dec. 2019), pp. 19–37, ISSN: 1974-5117,
DOI: 10.3293/asdj.2019.52.

[187] R. Voss, L. Tichy & R. Thormann:
"A ROM Based Flutter Prediction Process and its Validation with a New Reference Model", in: *15th International Forum on Aeroelasticity and Structural Dynamics (IFASD)*, Paris, France, June 26–30, 2011.

[188] M. M. Waldrop:
"The chips are down for Moore's law", in: *Nature* 530 (Feb. 11, 2016), pp. 144–147, ISSN: 0028-0836,
DOI: 10.1038/530144a.

[189] T. Watanabe, T. Azuma, S. Uzawa, T. Himeno & C. Inoue:
"Unsteady Pressure Measurement on Oscillating Blade in Transonic Flow Using Fast-Response Pressure-Sensitive Paint", in: *Journal of Turbomachinery* 140.6, 061003 (June 2018), ISSN: 0889-504X,
DOI: 10.1115/1.4039180.

[190] M. M. Weaver, S. R. Manwaring, R. S. Abhari, M. G. Dunn, M. J. Salay, K. K. Frey & N. Heidegger:
"Forcing Function Measurements and Predictions of a Transonic Vaneless Counter Rotating Turbine", in: *ASME Turbo Expo 2000: Power for Land, Sea, and Air*, vol. 4: Manufacturing Materials and Metallurgy; Ceramics; Structures and Dynamics; Controls, Diagnostics and Instrumentation; Education, 2000-GT-0375, Berlin, Germany, May 8–11, 2000, ISBN: 978-0-7918-7857-6,
DOI: 10.1115/2000-GT-0375.

[191] A. P. S. Wheeler, R. D. Sandberg, N. D. Sandham, R. Pichler, V. Michelassi & G. Laskowski:
"Direct Numerical Simulations of a High-Pressure Turbine Vane", in: *Journal of Turbomachinery* 138.7, 071003 (July 2016), ISSN: 0889-504X,
DOI: 10.1115/1.4032435.

[192] D. S. Whitehead:
Vibration and Sound Generation in a Cascade of Flat Plates in Subsonic Flow, R. & M. No. 3685, Ministry of Defence (Procurement Executive) - Aeronautical Research Council Reports and Memoranda, Feb. 1970.

[193] M. Widhalm & R. Thormann:
"Efficient Evaluation of Dynamic Response Data with a Linearized Frequency Domain Solver at Transonic Separated Flow Condition", in: *35th AIAA Applied Aerodynamics Conference*, AIAA 2017-3905, Denver, Colorado, USA, June 5–9, 2017,
DOI: 10.2514/6.2017-3905.

[194] S. Willeke, L. Schwerdt, L. Panning-von Scheidt & J. Wallaschek:
"Intentional Response Reduction by Harmonic Mistuning of Bladed Disks With Aerodynamic Damping", in: *Journal of Engineering for Gas Turbines and Power* 140.12, 121010 (Dec. 2018), ISSN: 0742-4795,
DOI: 10.1115/1.4040898.

[195] M. H. Williams, J. Cho & W. N. Dalton:
"Unsteady Aerodynamic Analysis of Ducted Fans", in: *Journal of Propulsion and Power*, Propulsion | Power 7.5 (Sept.–Oct. 1991), pp. 800–804, ISSN: 1533-3876,
DOI: 10.2514/3.23394.

[196] Y. Wu & X.-C. Cai:
"A Fully Implicit Domain Decomposition Based ALE Framework for Three-Dimensional Fluid-Structure Interaction with Application in Blood Flow Computation", in: *Journal of Computational Physics* 258 (Feb. 2014), pp. 524–537, ISSN: 0021-9991,
DOI: 10.1016/j.jcp.2013.10.046.

[197] K. Yamada, M. Furukawa, Y. Tamura, S. Saito, A. Matsuoka & K. Nakayama:
"Large-Scale Detached-Eddy Simulation Analysis of Stall Inception Process in a Multistage Axial Flow Compressor", in: *Journal of Turbomachinery* 139.7, 071002 (July 2017), ISSN: 0889-504X,
DOI: 10.1115/1.4035519.

[198] M. Zhang & L. He:
"Efficient Large-Eddy Simulation Method for Blade Trailing-Edge Cooling Optimization", in: *Journal of Propulsion and Power*, Propulsion | Power 34.4 (July–Aug. 2018), pp. 854–863, ISSN: 1533-3876,
DOI: 10.2514/1.B36501.

[199] W. Zhang, M. Vahdati & F. Zhao:
"Impact of Exit Duct Dynamic Response on Compressor Stability", in: *Journal of Turbomachinery* 142.11, 111006 (Nov. 2020), ISSN: 0889-504X,
DOI: 10.1115/1.4048153.

A. Conventions

A.1. Blade numbering and IBPA definition at DLR

At DLR, the CFD code used for turbomachinery computations is TRACE. The convention for blade numbering in TRACE is in a mathematically positive way around the axis of rotation (Frey [57]). See figure A.1 for an illustration.

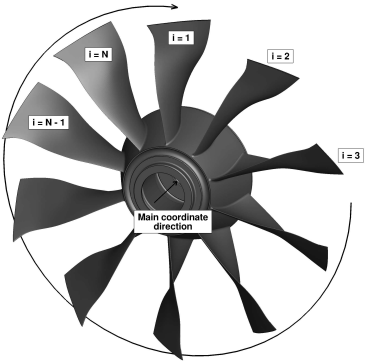

Figure A.1.: Blade numbering convention for TRACE.

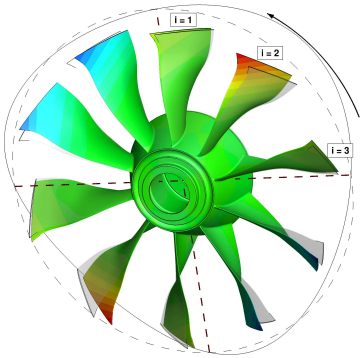

Figure A.2.: Positive inter-blade phase angle convention for TRACE, illustrated for a traveling wave of order 2 on a 10 blade blisk.

Likewise, the convention in TRACE is that a positive IBPA is for the blade with the larger number to be further along in its oscillation cycle. In figure A.2, the traveling wave deformation of order 2 for a blisk rotor with 10 blades is shown. The bold brown dashed lines indicate the rotating lines of zero deformation. The black line indicates the sine waves of the deformation around the circumference of the rotor with the dashed line indicating the position of the blades at rest. Blade number 1 is moving away from the reader, while blade number 2 is at its maximum deformation away from the reader and blade number 3 is moving towards the reader. If a sinusoidal oscillation is presumed, blade number 1 is at an angle of 0.1π, blade number 2 is at an angle of 0.5π and blade number 3 is at an angle of 0.9π in their 2π oscillation cycle ($\rightarrow$ the IBPA is $+0.4\pi$ or $+72°$).

When this oscillation is animated, the deformation pattern travels in a mathematically negative direction around the axis of cyclic symmetry. This is indicated by the arrow in figure A.2.

A.2. Nodal Diameters and Traveling Waves

In chapter 2.2.4, the implications of cyclic symmetry on a turbomachinery stage was introduced. Especially the nodal diameters and traveling waves due to superposition of nodal diameters were introduced. In figure A.3, all nodal diameters and traveling waves of the first blade bending eigenmode shape family are visualized for completeness.

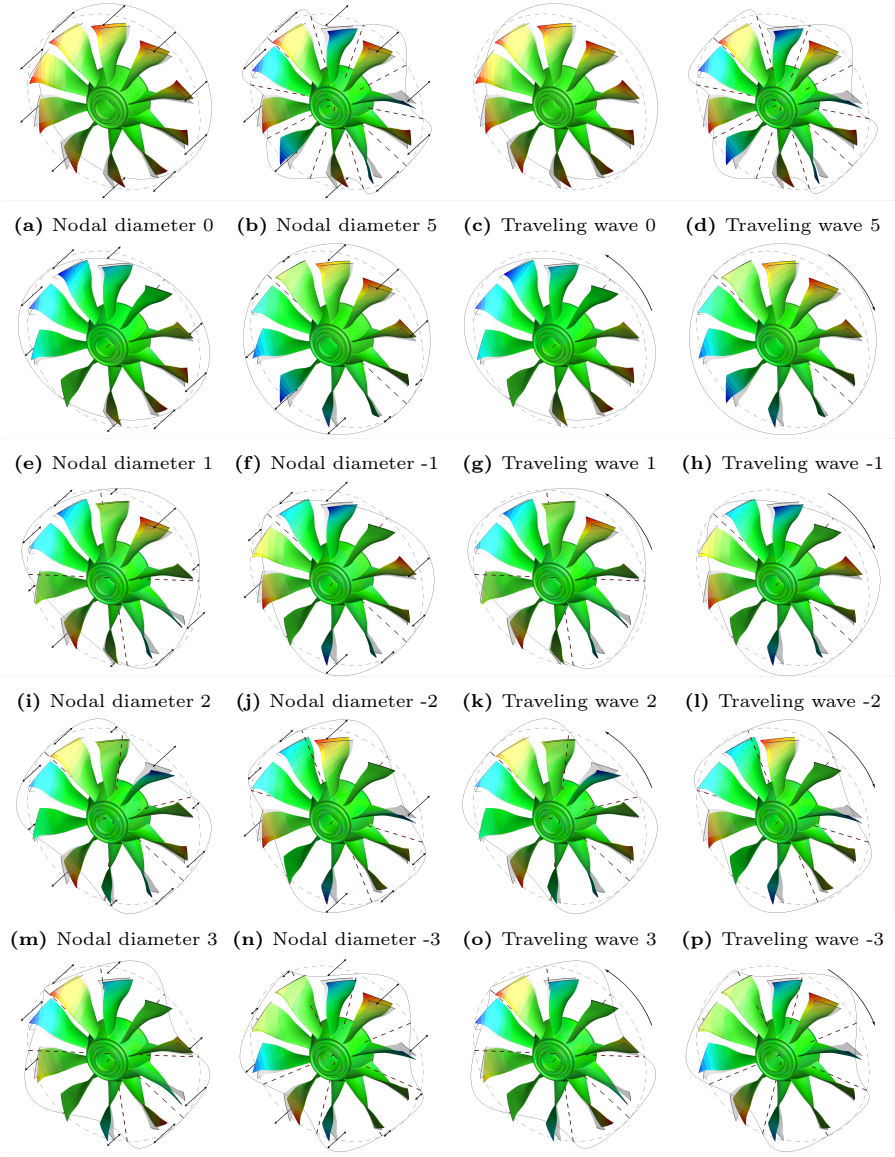

(a) Nodal diameter 0 **(b)** Nodal diameter 5 **(c)** Traveling wave 0 **(d)** Traveling wave 5

(e) Nodal diameter 1 **(f)** Nodal diameter -1 **(g)** Traveling wave 1 **(h)** Traveling wave -1

(i) Nodal diameter 2 **(j)** Nodal diameter -2 **(k)** Traveling wave 2 **(l)** Traveling wave -2

(m) Nodal diameter 3 **(n)** Nodal diameter -3 **(o)** Traveling wave 3 **(p)** Traveling wave -3

(q) Nodal diameter 4 **(r)** Nodal diameter -4 **(s)** Traveling wave 4 **(t)** Traveling wave -4

Figure A.3.: Nodal diameter and traveling wave eigenmode shapes of the first blade bending eigenmode shape family of a 10 blade blisk.

B. DLR Flow Solver TRACE

At DLR the flow solver TRACE is used for computational simulations of fluid flows in turbomachines. TRACE has five main flow solution approaches:

1. A steady state module allows for the solution of the time-average mean flow through a turbomachine part.

2. An adjoint module allows for the determination of the gradient of a specific flow variable or the sensitivity of a flow variable to mesh deformations. This module is used in automated optimization tool chains to not only obtain result values for the design variables but also a gradient, which improves the quality of interpolation between different data samples (already calculated design variations).

3. A time-linearized module allows for the simulation of the response of a fluid flow to a small-scale harmonic disturbance. If this disturbance is the deformation of a surface, this time-linearized module of TRACE allows for the solution of the unsteady aerodynamic pressure arising due to that deformation and subsequently to the energy transferred between fluid and structure. The solution of the time-linearized module is always based on a steady state solution of the flow and returns only the harmonic oscillations of the flow variables about this mean steady state solution.

4. A harmonic balance module allows for the solution of the Fourier coefficients of the flow properties in time up to a certain number of harmonics. Basically, the flow is not only split into the steady state mean flow and one harmonic oscillation but the steady mean flow and a user-specified number of higher harmonics. This equation system is not solved in the frequency domain in TRACE, but by a time-marching method. Therefore, an advantage is that the solution is not dependent on the initialization like in the time-linear module, but a disadvantage is that it takes often considerably longer to converge to a solution. Like in the time-linear module, boundary perturbations for the first harmonic can be prescribed.

5. A nonlinear unsteady time-marching module solves the time-dependent RANS equations. Like the harmonic balance method, the solution is theoretically independent of the initialization but shows much better convergence for a realistic initialization with a previously calculated steady state case. As for the other unsteady modules, it is possible to prescribe a surface deformation.

In theory, all three of the time-unsteady modules of TRACE can be used to determine the unsteady pressure on a turbomachinery part due to a surface deformation. All three of them have advantages and disadvantages which can be listed as follows:

Time-linearized module

Advantages Reasonably fast and fairly robust

Disadvantages The turbulence model has never been linearized even though Widhalm & Thormann [193] showed that this is vital for accurate results.

Harmonic balance module

Advantages Contains a harmonic decomposition of the turbulence model and returns faster results than the nonlinear unsteady module.

Disadvantages Considerably slower than the time-linearized module and at times numerically unstable.

Nonlinear unsteady module

Advantages Most accurate RANS representation of the unsteady flow in a turbomachine.

Disadvantages Very long computation times due to the fact that even the unsteady solution needs to develop over time (several harmonic oscillations need to be calculated for a final result).

Due to the severe time limitations on the aeroelastic calculations for an automated optimization tool chain, only the time-linearized module was considered for the cases presented in this thesis.

C. Potential Flow Aerodynamics

A thorough introduction to the theory of potential flow dynamics can be found in Katz & Plotkin [93]. Here, only the main outline leading to the formulations used in the applied panel code CMARC are given.

As already mentioned in chapter 2.1.5, the continuity equation for an inviscid, irrotational and incompressible fluid can be derived to be the second derivative in space of a velocity potential.

$$\nabla\Phi = \vec{\boldsymbol{v}} \tag{2.1 (repeated)}$$

$$\begin{aligned} \frac{\cancel{\partial \boldsymbol{\rho}}}{\cancel{\partial t}} + \frac{\partial \boldsymbol{\rho}\vec{\boldsymbol{v}}_x}{\partial x} + \frac{\partial \boldsymbol{\rho}\vec{\boldsymbol{v}}_y}{\partial y} + \frac{\partial \boldsymbol{\rho}\vec{\boldsymbol{v}}_z}{\partial z} &= 0 \\ \Rightarrow \frac{\partial \vec{\boldsymbol{v}}_x}{\partial x} + \frac{\partial \vec{\boldsymbol{v}}_y}{\partial y} + \frac{\partial \vec{\boldsymbol{v}}_z}{\partial z} &= 0 \\ \Rightarrow \nabla^2\Phi &= 0 \end{aligned} \tag{2.2 (repeated)}$$

That said, the solution of equation (2.2) can only be accomplished if two assumptions are made. The first assumption is that the body for which a flow solution is desired, is impermeable. That means no fluid enters or leaves the body, which immediately leads to the conclusion that the flow in normal direction of the body boundary always needs to be zero.

$$\nabla\Phi \cdot \vec{\boldsymbol{n}} = 0 \tag{C.1}$$

The second assumption is that the influence of the body on the flow is negligible very far away from the body.

$$\lim_{\vec{\boldsymbol{r}}\to\infty} (\nabla\Phi - \vec{\boldsymbol{v}}_\infty) = 0 \tag{C.2}$$

In equation (C.2), $\vec{\boldsymbol{r}}$ is the vector from the body to an arbitrary point in the surrounding flow and $\vec{\boldsymbol{v}}_\infty$ is the fluid flow velocity in undisturbed flow.

If the region of fluid flow is divided into two regions (region of interest with potential Φ and region of no interest with potential Φ_i, where the region of interest is the fluid flow and the region of no interest is inside the body **and** beyond the far field boundary). With the help of Green's second identity the problem defined on a volume can be reduced to a problem just defined by the volume surfaces. The velocity potential Φ_P at any given point can then be given as the sum of the influence of the volume boundaries on this point. It has been proven useful to model a wake as additional surface leaving the body in flow direction to capture aerodynamic effects correctly. The volume surfaces are then the surface at the far field boundary S_∞, the surface of the body itself S_B and the surface around the wake S_W (see figure C.1).

$$\Phi_P = \frac{1}{4\pi} \iint_{S_B+S_W+S_\infty} (\Phi - \Phi_i)\, \vec{\boldsymbol{n}} \cdot \nabla \left(\frac{1}{\vec{\boldsymbol{r}}}\right) dS - \frac{1}{4\pi} \iint_{S_B+S_W+S_\infty} \left(\frac{1}{\vec{\boldsymbol{r}}}\right) \vec{\boldsymbol{n}} \cdot (\nabla\Phi - \nabla\Phi_i)\, dS \tag{C.3}$$

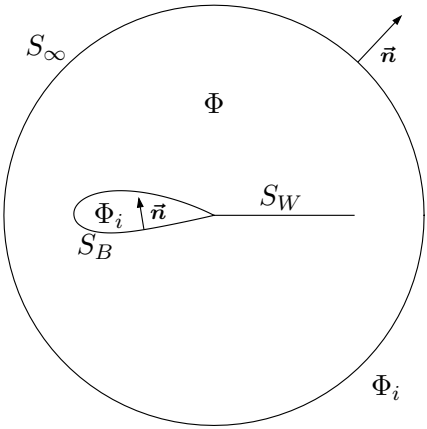

Figure C.1.: Visualization of the potential flow around a body (adapted from Katz & Plotkin [93]).

In equation (C.3), the term $\Phi - \Phi_i$ is the difference of the velocity potential of the flow interior and exterior of the surface at each point on the surfaces and called a doublet. The term $-\vec{n}\,(\nabla\Phi - \nabla\Phi_i)$ is the difference in normal velocity interior and exterior of the surface at each point on the surfaces and called a source. When the influence of each surface point's source and doublet value is summed up, the velocity potential at any given point of interest can be calculated.

Taking into consideration equation (C.2), which states that the velocity potential at the far field boundary is equal on both sides of the boundary, and postulating that there cannot be a velocity source in a wake, equation (C.3) reduces to:

$$\begin{aligned}\Phi_P =& \frac{1}{4\pi} \iint_{S_B} (\Phi - \Phi_i)\, \vec{n} \cdot \nabla \left(\frac{1}{\vec{r}}\right) dS - \frac{1}{4\pi} \iint_{S_B} \left(\frac{1}{\vec{r}}\right) \vec{n} \cdot (\nabla\Phi - \nabla\Phi_i)\, dS \\ &+ \frac{1}{4\pi} \iint_{S_W} (\Phi_u - \Phi_l)\, \vec{n} \cdot \nabla \left(\frac{1}{\vec{r}}\right) dS + \phi_{\infty P}\end{aligned} \tag{C.4}$$

In equation (C.4), the influence of the far field flow on point P is the potential $\phi_{\infty P}$, and the source term of the wake has been eliminated. The velocity potential difference is calculated directly over the wake, where Φ_u is the velocity potential above the wake and Φ_l is the velocity potential below the wake.

If the point P is located on the surface of the body S_B, the first term in equation (C.4) will diverge to infinity. Via a mathematical trick (let the surface have a hemispherical indentation so point P does not touch it, and then reduce the radius of that hemispherical indentation to zero), it is possible to calculate the contribution of the surface doublet at point P on itself to be $\frac{1}{2}(\Phi - \Phi_i)_P$ if point P is outside of the surface and $-\frac{1}{2}(\Phi - \Phi_i)_P$ if point P is interior to the surface.

If point P is an interior point, equation (C.4) can be transformed to be:

$$\begin{aligned}\Phi_P =& \frac{1}{4\pi} \iint\limits_{S_B - P} (\Phi - \Phi_i)\, \vec{\boldsymbol{n}} \cdot \nabla \left(\frac{1}{\vec{\boldsymbol{r}}}\right) dS - \frac{1}{4\pi} \iint\limits_{S_B} \left(\frac{1}{\vec{\boldsymbol{r}}}\right) \vec{\boldsymbol{n}} \cdot (\nabla\Phi - \nabla\Phi_i)\, dS \\ &+ \frac{1}{4\pi} \iint\limits_{S_W} (\Phi_u - \Phi_l)\, \vec{\boldsymbol{n}} \cdot \nabla \left(\frac{1}{\vec{\boldsymbol{r}}}\right) dS + \phi_{\infty_P} - \frac{1}{2}(\Phi - \Phi_i)_P\end{aligned} \tag{C.5}$$

The integration range $(S_B - P)$ translates to "the body's surface without the point P". Introducing a perturbation potential ϕ as the difference between total potential at a point Φ and the far field potential ϕ_∞

$$\Phi = \phi_\infty + \phi, \tag{C.6}$$

equation (C.5) can be written as:

$$\begin{aligned}0 =& \frac{1}{4\pi} \iint\limits_{S_B - P} \phi \vec{\boldsymbol{n}} \cdot \nabla \left(\frac{1}{\vec{\boldsymbol{r}}}\right) dS - \frac{1}{4\pi} \iint\limits_{S_B} \left(\frac{1}{\vec{\boldsymbol{r}}}\right) \vec{\boldsymbol{n}} \cdot (\nabla\Phi - \nabla\phi_\infty)\, dS \\ &+ \frac{1}{4\pi} \iint\limits_{S_W} (\Phi_u - \Phi_l)\, \vec{\boldsymbol{n}} \cdot \nabla \left(\frac{1}{\vec{\boldsymbol{r}}}\right) dS - \frac{1}{2}\phi_P\end{aligned} \tag{C.7}$$

The doublet and source strengths are defined as:

$$4\pi\mu = \phi = (\Phi - \phi_\infty) \tag{C.8}$$

$$4\pi\sigma = -\vec{\boldsymbol{n}} \cdot (\nabla\Phi - \nabla\phi_\infty) \tag{C.9}$$

Since the gradient of the velocity potential is the velocity and the surface normal velocity $\vec{\boldsymbol{n}} \cdot \vec{\boldsymbol{v}}_P$ is either zero or known and the far field velocity $\vec{\boldsymbol{v}}_\infty$ is known as well, the source value can be calculated for every case directly (relaxing the restrictions given in equation (C.1) again).

$$\sigma = \frac{1}{4\pi} (\vec{\boldsymbol{n}} \cdot \vec{\boldsymbol{v}}_P - \vec{\boldsymbol{n}} \cdot \vec{\boldsymbol{v}}_\infty) \tag{C.10}$$

If equations (C.8) and (C.9) are introduced into equation (C.7), an equation for the doublet strengths μ at each point on the inside of the body surface arises:

$$0 = \iint\limits_{S_B - P} \mu \vec{\boldsymbol{n}} \cdot \nabla \left(\frac{1}{\vec{\boldsymbol{r}}}\right) dS - 2\pi\,\mu_P + \iint\limits_{S_B} \left(\frac{\sigma}{\vec{\boldsymbol{r}}}\right) dS + \iint\limits_{S_W} \mu_{S_W}\, \vec{\boldsymbol{n}} \cdot \nabla \left(\frac{1}{\vec{\boldsymbol{r}}}\right) dS \tag{C.11}$$

Likewise, the velocity potential at any point P in the fluid region can be calculated if the sources σ and doublets μ at the surfaces are known:

$$\Phi_P = \iint\limits_{S_B - P} \mu \vec{\boldsymbol{n}} \cdot \nabla \left(\frac{1}{\vec{\boldsymbol{r}}}\right) dS + K\,\mu_P + \iint\limits_{S_B} \left(\frac{\sigma}{\vec{\boldsymbol{r}}}\right) dS + \iint\limits_{S_W} \mu_{S_W}\, \vec{\boldsymbol{n}} \cdot \nabla \left(\frac{1}{\vec{\boldsymbol{r}}}\right) dS + \phi_{\infty_P} \tag{C.12}$$

Here, K is an operator taking different values for different cases of point P. For points in the fluid flow region (not on a surface) $K = 0$, for points on the inner side of a plane surface $K = -2\pi$ and for points on the outer side of a plane surface $K = 2\pi$.

To solve equation (C.12) numerically, the surface is discretized into smaller surface panels. It is assumed that the doublet μ and source σ strengths are constant over a panel. Then, surface integrals can be calculated for each panel following equation (C.12), where only the geometry and position of the surface need to be considered since μ and σ are considered constant.

To determine the doublet strengths μ on each surface panel, control points are distributed in the center of each panel on the interior side of the panel. Then, the influence of all other surface panels and the panel itself on the control points are summed up, leading to N_B interdependent linear equations for N_B surface panels with N_B control points.

$$\sum_{K=1}^{N_B} (\mu_K \cdot C_{JK}) + \sum_{K=1}^{N_B} (\sigma_K \cdot B_{JK}) + \sum_{L=1}^{N_W} (\mu_L \cdot C_{JL}) = 0 \Bigg|_{J=1,N_B} \tag{C.13}$$

The influence coefficients of each panel on another are:

$$B_{JK} = \iint_K \frac{1}{\vec{r}} dS \tag{C.14}$$

and

$$C_{JK} = \iint_K \vec{n} \cdot \nabla \frac{1}{\vec{r}} dS \tag{C.15}$$

$$C_{JJ} = -2\pi \tag{C.16}$$

Here, the terms arising from equation (C.15) represent the influence of the body surface on the control point (first term on the right hand side of equation (C.7)) and equation (C.16) represents the influence of the panel on itself (last term in equation (C.7)).

Equation (C.15) is naturally used for the wake as well. It is assumed that the strength of the wake doublets is the difference between the doublet strengths of the two panels between which the wake starts. If a wake time stepping algorithm is used, the doublet strength of the wake panels is convected downstream with the panels (see Ashby et al. [5]). Once the system of linear equations with the influence coefficients has been found, it can be solved with any numerical linear equation solver for the doublet strengths of each panel.

From the doublet strengths, the velocity potential Φ is known via equation (C.8). Since the normal velocity at the body surface is known, only the tangential velocity needs to be calculated. This is done via differentiation with the velocity potentials of the neighboring panels. Once the velocity is known, the pressure coefficient at each surface point can be calculated.

$$C_{p\,K} = 1 - \frac{v_K^2}{v_\infty^2} + \left(\frac{2 \cdot 4\pi}{v_\infty^2}\right) \left(\frac{\mu\,(t) - \mu\,(t-1)}{\Delta t}\right) \tag{C.17}$$

The last term in equation (C.17) represents the unsteady term $\frac{d\Phi}{dt}$.

D. Automated Optimization in Turbomachinery Design

As already mentioned in chapter 1.5, the design of turbomachinery parts is done more and more by automated optimization tool chains. The automated optimizer used at DLR Institute of Propulsion Technology is called Auto-Opti. It can serve as an example for the general approach to optimization problems in engineering. A more in-depth introduction to Auto-Opti can be found in Aulich & Siller [7].

Before starting a multi-parameter optimization, the scope of the optimization needs to be expressed in a mathematical way:

1. Free design parameters need to be specified. In turbomachinery design, these free parameters are a parametric description of the geometry of the part. In Auto-Opti, these parameters are variables describing the hub and shroud contour of a stage and variables describing the blade profiles at different flow channel cross sections. To ensure manufacturability, the admissible range of values for some of these variables can be specified. The terminology in automated optimization is not consistent. Different terms are used for the same things by different people. The free design parameters are sometimes called "parameter space", sometimes "design space", sometimes "free variables" depending on the background of the people describing an optimization.

2. One or more design variables need to be designated as targets of the optimization. The goal of the optimization is a minimization or a maximization of these values. These variables mostly are scalar values which generally would result from a "full" analysis cycle of a given rotor geometry. E.g. the isentropic efficiency η_{is}, the stall margin, the surge margin or the maximum total pressure ratio Π_t for a given stage. These results to be optimized are sometimes called "fitness functions", at other times "target functions" or "objective functions".

3. Additionally, design penalties can be prescribed. E.g. in turbomachinery design it is often inadmissible for the first eigenfrequency to be lower than the revolutions per second, the maximum blade deformation due to aerodynamic loading is not allowed to surpass a certain value or the outflow properties (swirl / angle) should have specific properties. Also a maximum or minimum mass flow might be a criterion. These design penalties are called "restrictions" or "constraints".

It is immediately obvious that it would most certainly be impossible for a design engineer to understand the impact of changing any given design parameter on the aerodynamic, structural or aeroelastic properties of a turbomachine part. Therefore, mathematical models for multidimensional data are used in an automated optimization process to interpolate between or extrapolate from already tested design points and to find even more optimal design points.

Figure D.1 visualizes an exemplary approach for an automated optimization of a turbomachinery part with the DLR tool Auto-Opti. On the right hand side of figure D.1, the "full" design tool chain is started by a main process (Gru) for a chosen rotor or stator geometry in a child process (minion number k). This child process performs an automated set of simulation instructions (called "tool chain") which contain most design operations which are necessary to determine the mechanical and aerodynamic properties of a design variation. As key parts of this tool chain, the solid parts of the geometry are discretized

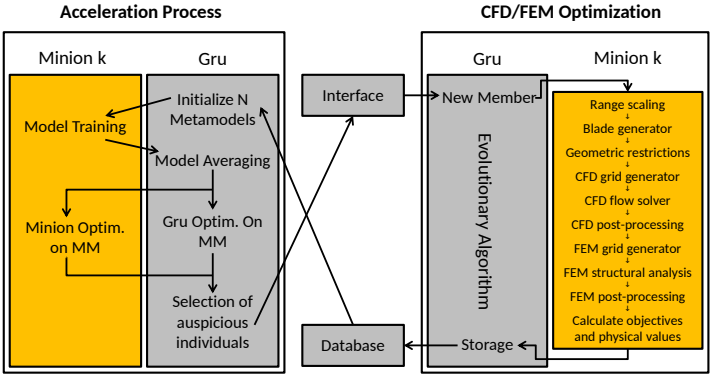

Figure D.1.: Flowchart of an automated optimization with Auto-Opti (from Goerke et al. [64]).

with a finite element mesh and the fluid flow path is discretized with a CFD mesh. These meshes are not necessarily as dense as they would have to be for a final design proof, but they are accurate enough to capture the main characteristics of a given design.

With these FE and CFD discretizations, critical operating points are simulated (mostly between 3 and 5 steady state flow cases and at least one structural load simulation taking into account the rotation and the aerodynamic loading at the aerodynamic design point plus at least a numerical modal analysis at the aerodynamic design point). Exemplary, these operating points are visualized in figure 4.4 as OP0 - OP4. In the visualized case, OP0 is the aerodynamic design point (100% RPM, maximum isentropic efficiency), OP1 is a point with a higher pressure ratio (closer to the surge boundary) at 100% RPM, OP2 is a point with a lower pressure ratio than OP0 (closer to the choke boundary) at 100% RPM, OP3 is at 70% RPM on the working line of the compressor and OP4 is again a point closer to the surge boundary at 70% RPM.

At any given point in this process, if a failed restriction is encountered, the design variation is returned to the main Gru process with an appropriate error designator (namely "Geometry restrictions", "CFD post-processing", "FEM post-processing" and "Calculate objectives and physical values" are the points in figure D.1 where this can happen). All successful and failed design variations are then stored in a data base together with their respective result values.

This data base of "fully" analyzed design variations is then used by a second design process to intelligently determine design parameter combinations which might lead to similar or even better target results (**only** based on the parameter values and the target and restriction results). These meta models ("MM" in figure D.1) are based on Kriging approaches or neural networks. Once these meta models have determined promising design parameter combinations, these are returned to the main Gru process on the right hand side for evaluation. This quickly leads to a large database of design parameter combinations and their applicability for a given use case.

As already mentioned in chapter 1.5, it would be very convenient to be able to include a design penalty for aeroelastic instability or even to formulate a design variable for aeroelastic stability for an automated optimization process. This has been one of the research efforts at DLR Institute of Aeroelasticity for the past years and some of the solution strategies explored were presented in this thesis.

E. Additional Information on CRISPmulti

In chapter 4.1.1, the DLR CRISPmulti counter rotating fan demonstrator was introduced. This chapter of the appendix will present additional information on the used models and results.

E.1. CRISPmulti Finite Element Model

Structural analysis of the CRISPmulti rotors was performed with a hybrid flat element / volume element mesh. The rotor disk and blade mounting are volume elements, the blade itself is made up of shell elements. The reason for this is twofold: For one, the material properties of CFC materials are highly anisotropic. Shell elements posses a distinct element coordinate system and it is very convenient to define the main fiber direction parallel to the shell surface. Since the fiber orientation is along the blade skeletal surface due to the manufacturing technique, the fiber content and direction is known for each blade thickness and can be specified easily. Another reason for using shell elements is the included capability in MSC Nastran to update shell element stiffnesses in non-linear load simulations. The blade deformation of CFC blades under inertial and surface pressure load can be quite substantial. Updated stiffness matrices for volume elements with a defined material coordinate system which does not follow the blade deformation will become nonphysical. Since MSC Nastran shell elements possess their own shell coordinate system which rotates with a shell element deformation (and in which the material properties of the composite material are specified), this problem can be circumvented elegantly. Deformation comparisons with other FE solvers at different Institutes of DLR showed very good agreement with sometimes substantially reduced numerical effort.

To generate the shell FE mesh the skeletal surface of the blades was interpolated from the CFD blade surface meshes and re-discretized. Figure E.1 shows the CFD surface meshes of both rotor blades of evolution stage 1633 of CRISPmulti and the respective resulting skeletal FE mesh together with the surface pressures projected onto the skeletal surfaces.

Figure E.2 visualizes the blade mounting of the CFC blades for rotor 1 of CRISPmulti exemplary. Rotor 2 follows the same approach. In figure E.2a, the hybrid CFC blade is shown. The translational degrees of freedom between shell and volume elements were treated with a matching mesh approach. The rotational degrees of freedom between the shell elements and the volume elements were connected via multi-point constraints. Figures E.2b and E.2c show the titanium blade foot which is connected with glue and safety pins to the lower end of the blade. CRISP-1m had adjustable blades, therefore the blade mounting contains a friction bearing depicted in figures E.2d, E.2e and E.2f, even though no blade adjustment was considered in the design process of CRISPmulti. The fully mounted blade in one section of the disk is shown in figure E.2g.

The final FE models of one blade section for each rotor are depicted in figure 4.2. The cyan bullets indicate the cyclic symmetry nodes. Since it was assumed that there would be a lot of friction damping in the blade mounting itself, and therefore no blade coupling around the rotor, the cyclic symmetry nodes were used as fixed boundary conditions for all FE calculations performed. The final blade meshes had 16560 (rotor 1) and 14640 (rotor 2) quadrilateral shell elements and 19310 / 19298 volume elements (bricks, prisms or tetrahedrons).

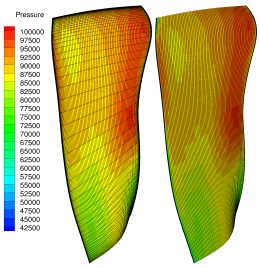

(a) Surface pressure on the pressure side of the rotor 1 blade (left) and interpolated pressure on the FE skeletal mesh (right).

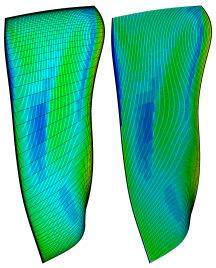

(b) Surface pressure on the suction side of the rotor 1 blade (left) and interpolated pressure on the FE skeletal mesh (right).

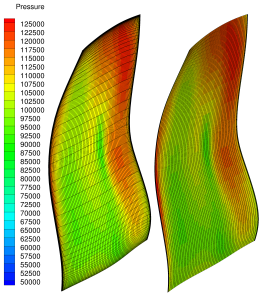

(c) Surface pressure on the pressure side of the rotor 2 blade (left) and interpolated pressure on the FE skeletal mesh (right).

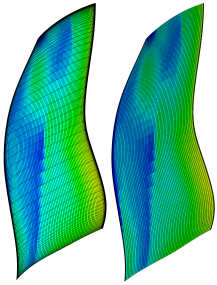

(d) Surface pressure on the suction side of the rotor 2 blade (left) and interpolated pressure on the FE skeletal mesh (right).

Figure E.1.: CRISPmulti shell FE mesh based on the automated optimization CFD mesh and surface pressure interpolation.

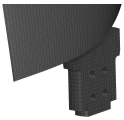

(a) CFC hybrid blade (dark gray).

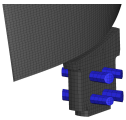

(b) Blade and safety pins (blue).

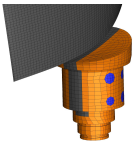

(c) Blade secured in titanium foot (orange) with safety pins.

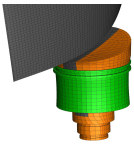

(d) Blade foot in inner half of friction bearing (green).

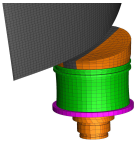

(e) Inner half of friction bearing on blade foot with washer (purple).

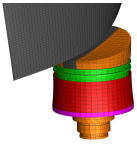

(f) Added outer half of friction bearing (red).

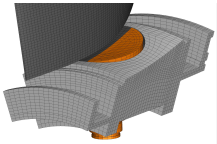

(g) Blade mounted in disk (light gray).

Figure E.2.: CRISPmulti rotor 1 blade mounting.

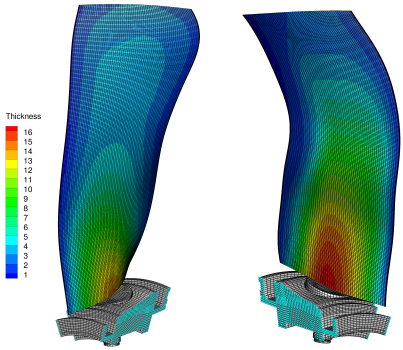

(a) CRISPmulti rotor 1 blade FE model. **(b)** CRISPmulti rotor 2 blade FE model.

Figure 4.2.: CRISPmulti FE models for rotor 1 and rotor 2, one blade each, blade thickness in *mm*, cyan bullets indicate cyclic symmetry nodes (repeated).

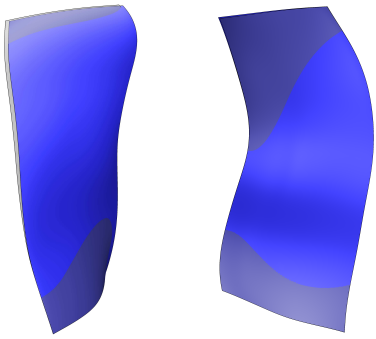

(a) Blade on rotor 1. **(b)** Blade on rotor 2.

Figure E.3.: CRISPmulti original aerodynamically optimal (hot, light gray) geometry and manufacturing (cold, blue) geometry of the blades of evolution step 1633.

E.2. Hot-to-Cold Transformation

The blade shapes of the different CRISPmulti evolution stages were found in an automated optimization algorithm. This means that an optimal blade geometry at the optimization design point was returned. The problem with this is that the inertial load and the blade surface pressure under operating conditions will lead to a deformation of the blade. Should the design geometry be manufactured directly and without adjustments, the blade shape at operating conditions would not be the aerodynamically optimal blade geometry.

Consequently, the geometry to be manufactured needs to be deduced from the optimized geometry at operating conditions. This is called a "hot-to-cold" transformation and is described in Forsthofer & Reiber [53]. Basically, the inertial load and the surface pressure loads are applied to the optimized geometry. The difference between the resulting blade shape and the optimized geometry is subtracted from the optimized geometry to form the first "cold" geometry shape. This is continued until the final "cold" geometry's blade shape under inertial and pressure load matches the optimized geometry to a certain degree of accuracy (see figure E.3 for an impression of the "hot" and "cold" shapes of the blades on the two CRISPmulti rotors).

Obtaining the pressure load acting on the FE model has already been visualized in figure E.1. Once the contributions from pressure and suction side of the blades are known, the suction side's pressure is subtracted from the pressure side's pressure to obtain the resulting pressure acting on the shell element surface.

E.3. Standard FE Calculations

For each evolution step of CRISPmulti, a Campbell diagram was calculated in order to determine the risk for forced response events. To determine the frequency ranges of the different blade eigenmode shapes at different inertia and pressure load states, the surface pressures from the different operating points in the compressor map (figure 4.4 in chapter 4.1.1.2) were interpolated as shown in chapter E.1, visualized in figure E.1. The

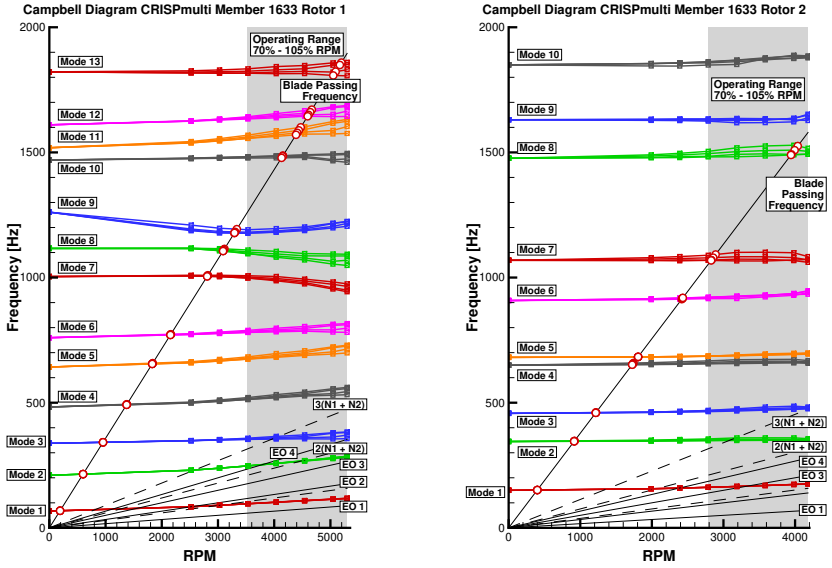

(a) Rotor 1. **(b)** Rotor 2.

Figure E.4.: CRISPmulti Campbell diagrams of the blades of evolution step 1633.

resulting Campbell diagrams show that the influence of the steady state surface pressure has a significant influence on the eigenfrequencies (figure E.4).

A byproduct of the computation of the Campbell diagrams were the eigenmode shapes and eigenfrequencies at all aerodynamic operating points. Since it is customary to check the first three eigenmode shape families for aeroelastic stability, figure E.5 shows the eigenmode shapes of the CRISPmulti rotor blades at 0 RPM. The blades on rotor 1 (figure E.5a - E.5c) show a classical eigenmode shape pattern (first bending, second bending, first torsion), while the blades of rotor 2 (figure E.5d - E.5f) show a less obvious eigenmode shape distribution (first bending, flapping of the upper end of the trailing edge, torsion of the upper half of the blade). The eigenmode shapes with inertial and surface pressure load on the other hand show at times a substantially different behavior. This will be visualized in appendix E.5.

E.4. CFD Mesh Studies

The CRISPmulti demonstrator was aerodynamically and structurally optimized with the DLR in-house tool Auto-Opti. For the aerodynamic optimization, a coarse CFD mesh was used. This mesh was designed to capture the main characteristics of the flow while permitting very rapid 3D RANS computations with TRACE. Experience from previous optimizations had shown that using a very coarse mesh (especially in radial direction) permitted much faster computation times while leading to a minor error in aerodynamic efficiency. Since the main objective of an automated optimization is the determination of global trends in aerodynamic efficiency and not the final computation of absolutely reliable values, this was deemed an acceptable practice. The final design and some intermediate designs were verified with finer CFD meshes.

This approach could not be taken for granted for the unsteady linearized RANS compu-

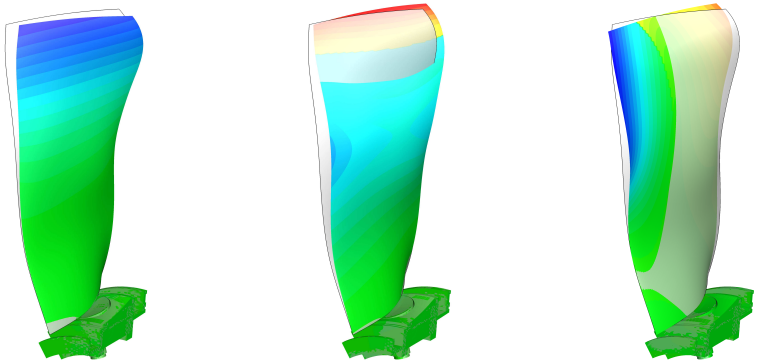

(a) Eigenmode shape 1, Rotor 1 **(b)** Eigenmode shape 2, Rotor 1 **(c)** Eigenmode shape 3, Rotor 1

(d) Eigenmode shape 1, Rotor 2 **(e)** Eigenmode shape 2, Rotor 2 **(f)** Eigenmode shape 3, Rotor 2

Figure E.5.: CRISPmulti eigenmode shapes of the blades of evolution step 1633 at 0 RPM.

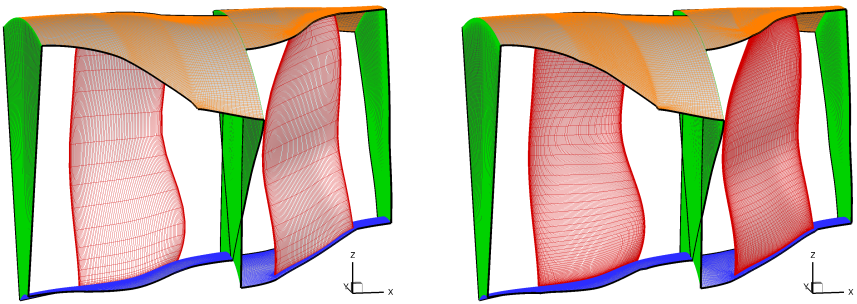

(a) Optimization CFD mesh of evolution step 5696 with 34 cells in radial direction.

(b) Verification CFD mesh of evolution step 5696 with 128 cells in radial direction.

Figure E.6.: Optimization and verification CFD mesh of evolution step 5696 of the CRISPmulti demonstrator. Compare to figure 4.3 for the description of the different surfaces.

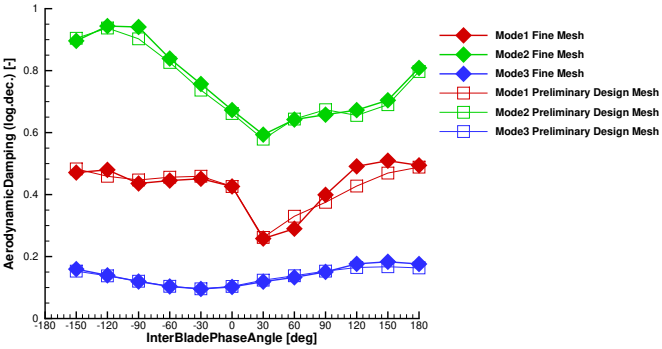

Figure E.7.: Global aerodynamic damping diagram of one operating point for the optimization mesh and the verification mesh of evolution step 5696 of the CRISPmulti demonstrator.

tations. Therefore, comparison computations were performed on a preliminary design stage for the similarity of the unsteady aerodynamics on coarse and fine meshes. The overall optimization mesh was compared to a mesh with the resolutions generally used for final design proof computations. The optimization mesh had 34 cells in radial direction and in total 340 184 cells for the rotor 1 passage and 347 800 cells in total for the rotor 2 passage. The fine mesh had 128 cells in radial direction and 2 890 308 / 2 872 388 cells for rotor 1 and rotor 2 passage, respectively (figure E.6).

The aerodynamic damping of the different meshes for the same flow case differed only marginally (see figure E.7). The computation times on the other hand differed substantially: The fine mesh used 24 CPUs for approx. 7.5 h while the coarse mesh used 8 CPUs for approx. 0.5 h. Therefore, it was decided that using a relatively coarse mesh still resulted in accurate time-linearized unsteady results.

For the final design proof computations it was decided, that an intermediate mesh would result in the best trade-off between computational efficiency and aerodynamic accuracy. The results of the computations presented in chapter 4.1 were therefore computed with a computational mesh with 80 cells in radial direction resulting in 803 680 / 821 600 cells for the rotor 1 and rotor 2 passage, respectively.

E.5. Blade Eigenmode Shapes of Different Evolution Steps of the CRISPmulti Project

In chapter 4.1.4, 4.1.5 and 4.2, a database of preliminary designs and their eigenbehavior under different load cases as well as the resulting global aerodynamic damping Λ values is referred to. Here, the different geometries and their eigenmode shapes at various operating points are given for completeness. The location of the operating points in the compressor map is given in figure 4.4. The origin of the different evolution steps numbered with four digits is given in table 4.1.

In the following figures of this chapter, the gray shaded geometry indicates the optimal aerodynamic form of the blade tested in the preliminary design routine. The shape with the color contour represents the maximum deformation in the respective eigenmode shape. Keep in mind that eigendeformations can be scaled arbitrarily and still represent the same eigendeformation. If mode shapes are deformed in the opposite direction (scaled with -1.0), then this is no mistake but the result of an automated printing routine which was applied

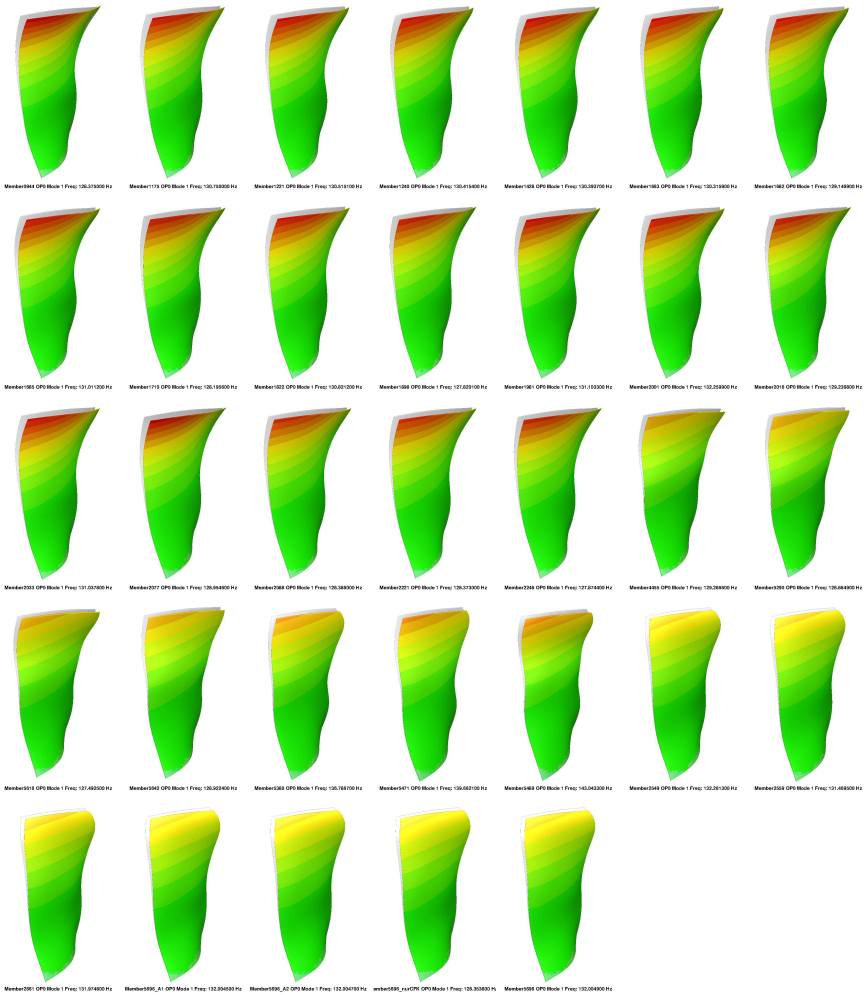

Figure E.8.: 1st eigenmode shapes of Rotor 1 at OP0 for various evolution steps of the CRISPmulti project (0944, 1175, 1221, 1240, 1428, 1663, 1682, 1685, 1710, 1822, 1898, 1981, 2001, 2016, 2033, 2077, 2088, 2221, 2248, 4455, 5290, 5616, 5642, 5380, 5471, 5489, 2549, 2559, 2661, 5696_A1, 5696_A2, 5696_-nurCFK, 5696).

to the FE results which do not have a preferred deformation direction (± 1.0, the scale itself is defined via the generalized mass or stiffness).

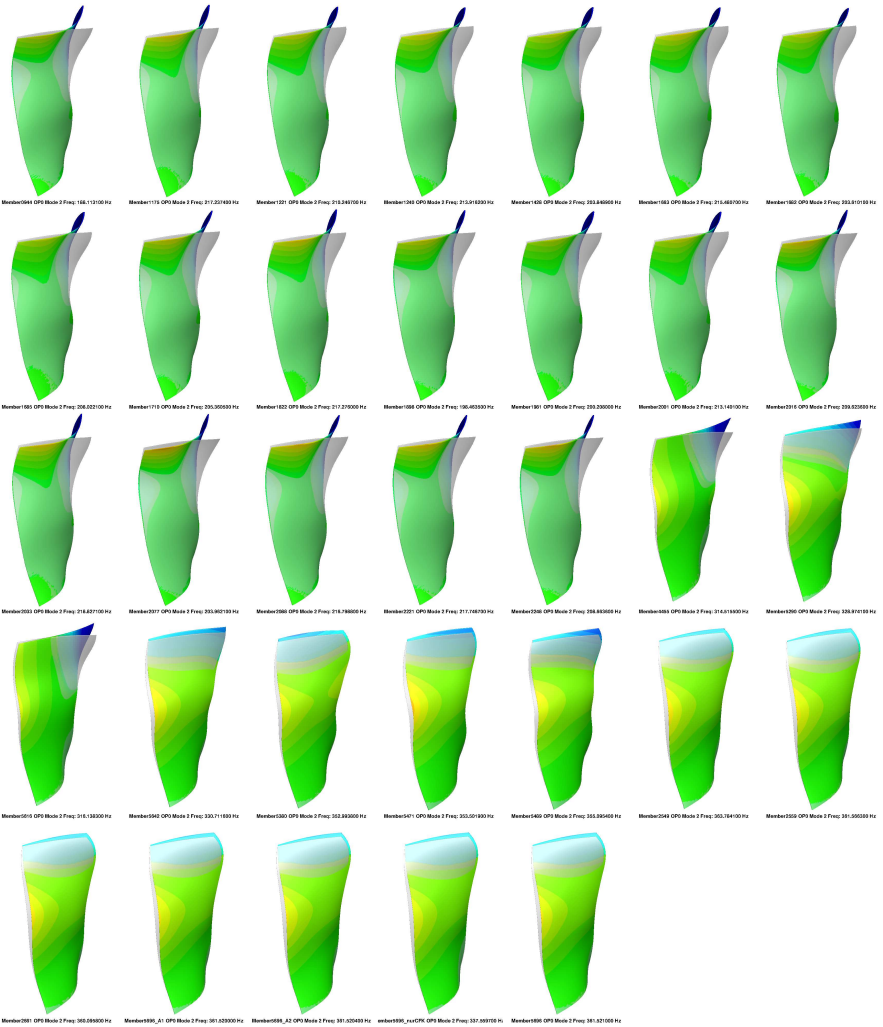

Figure E.9.: 2nd eigenmode shapes of Rotor 1 at OP0 for various evolution steps of the CRISPmulti project (0944, 1175, 1221, 1240, 1428, 1663, 1682, 1685, 1710, 1822, 1898, 1981, 2001, 2016, 2033, 2077, 2088, 2221, 2248, 4455, 5290, 5616, 5642, 5380, 5471, 5489, 2549, 2559, 2661, 5696_A1, 5696_A2, 5696_-nurCFK, 5696).

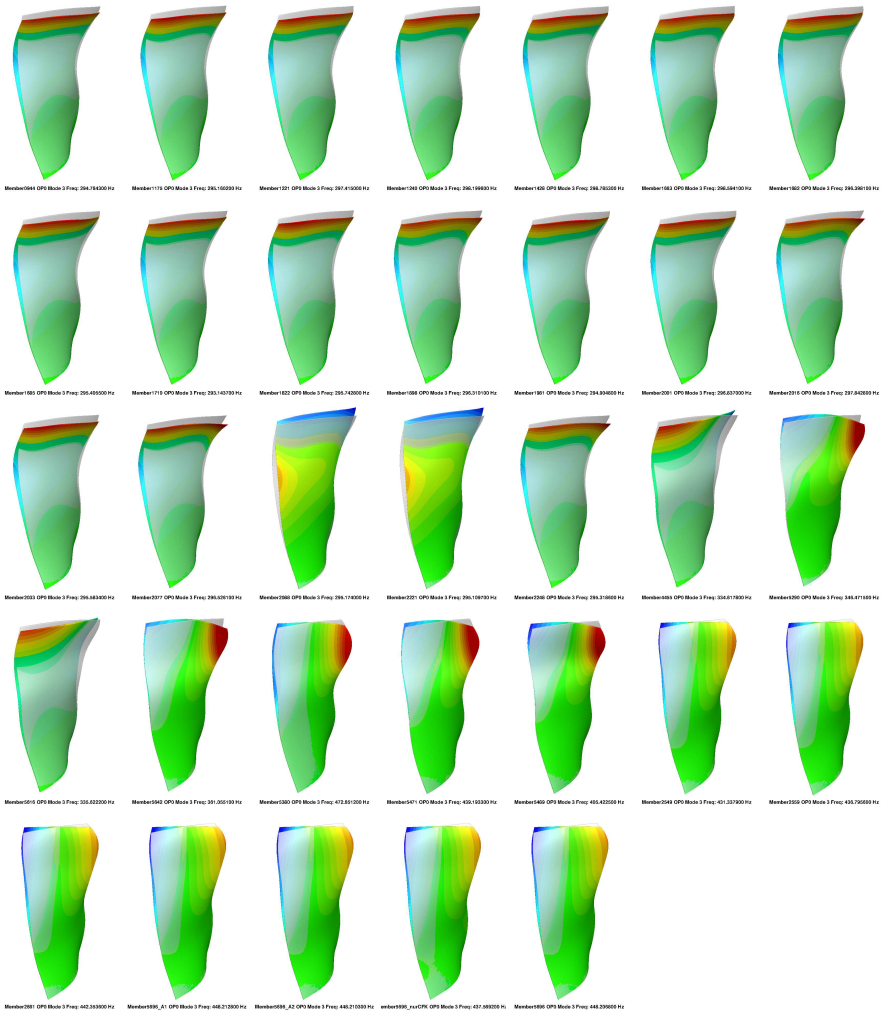

Figure E.10.: 3rd eigenmode shapes of Rotor 1 at OP0 for various evolution steps of the CRISPmulti project (0944, 1175, 1221, 1240, 1428, 1663, 1682, 1685, 1710, 1822, 1898, 1981, 2001, 2016, 2033, 2077, 2088, 2221, 2248, 4455, 5290, 5616, 5642, 5380, 5471, 5489, 2549, 2559, 2661, 5696_A1, 5696_A2, 5696_-nurCFK, 5696).

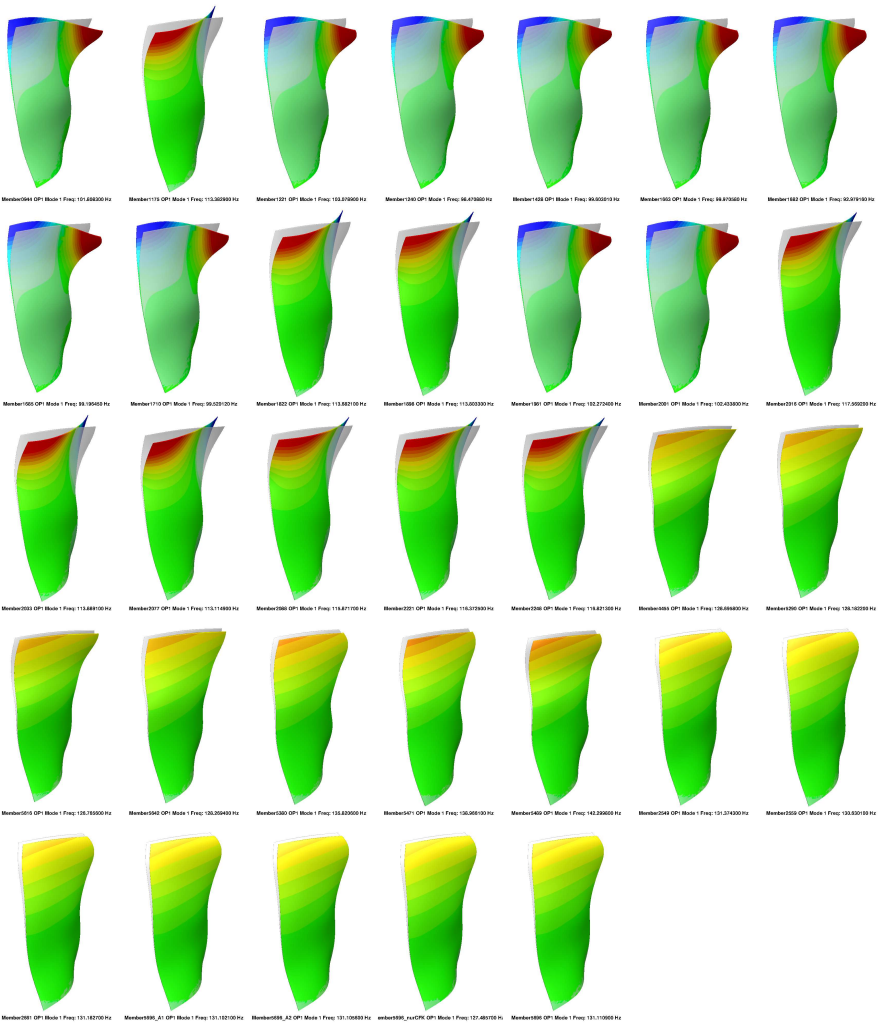

Figure E.11.: 1st eigenmode shapes of Rotor 1 at OP1 for various evolution steps of the CRISPmulti project (0944, 1175, 1221, 1240, 1428, 1663, 1682, 1685, 1710, 1822, 1898, 1981, 2001, 2016, 2033, 2077, 2088, 2221, 2248, 4455, 5290, 5616, 5642, 5380, 5471, 5489, 2549, 2559, 2661, 5696_A1, 5696_A2, 5696_-nurCFK, 5696).

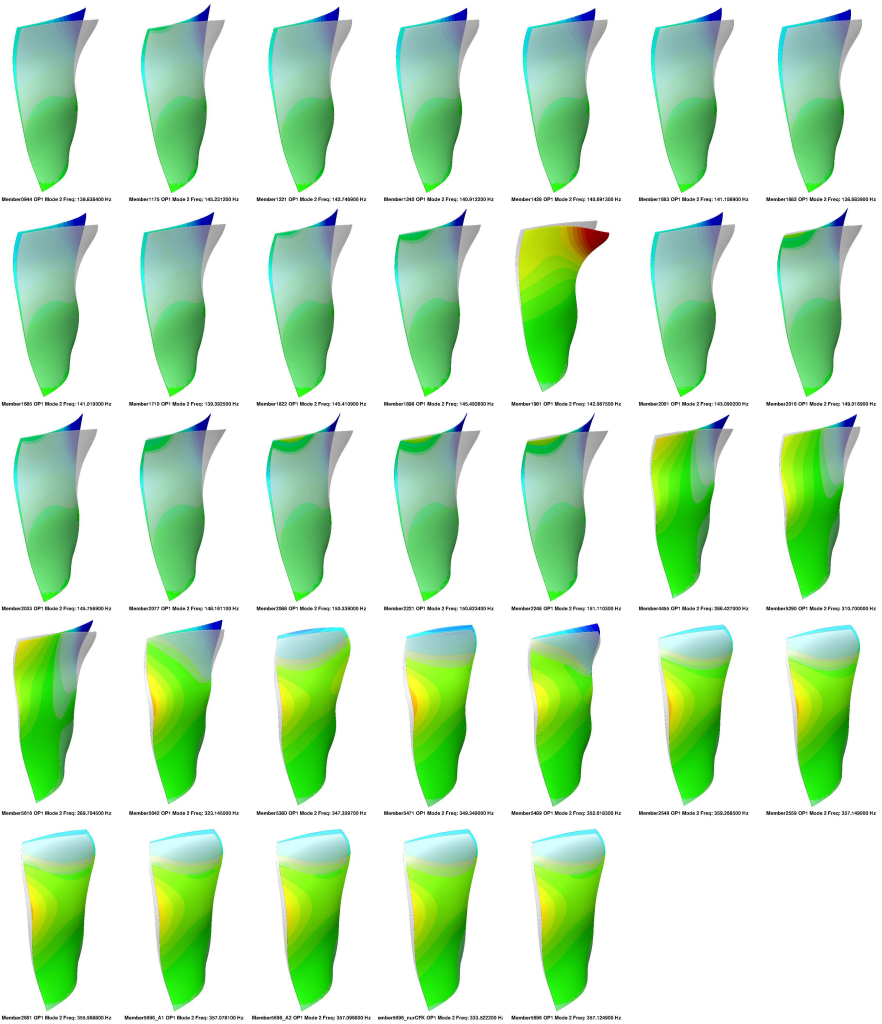

Figure E.12.: 2nd eigenmode shapes of Rotor 1 at OP1 for various evolution steps of the CRISPmulti project (0944, 1175, 1221, 1240, 1428, 1663, 1682, 1685, 1710, 1822, 1898, 1981, 2001, 2016, 2033, 2077, 2088, 2221, 2248, 4455, 5290, 5616, 5642, 5380, 5471, 5489, 2549, 2559, 2661, 5696_A1, 5696_A2, 5696_-nurCFK, 5696).

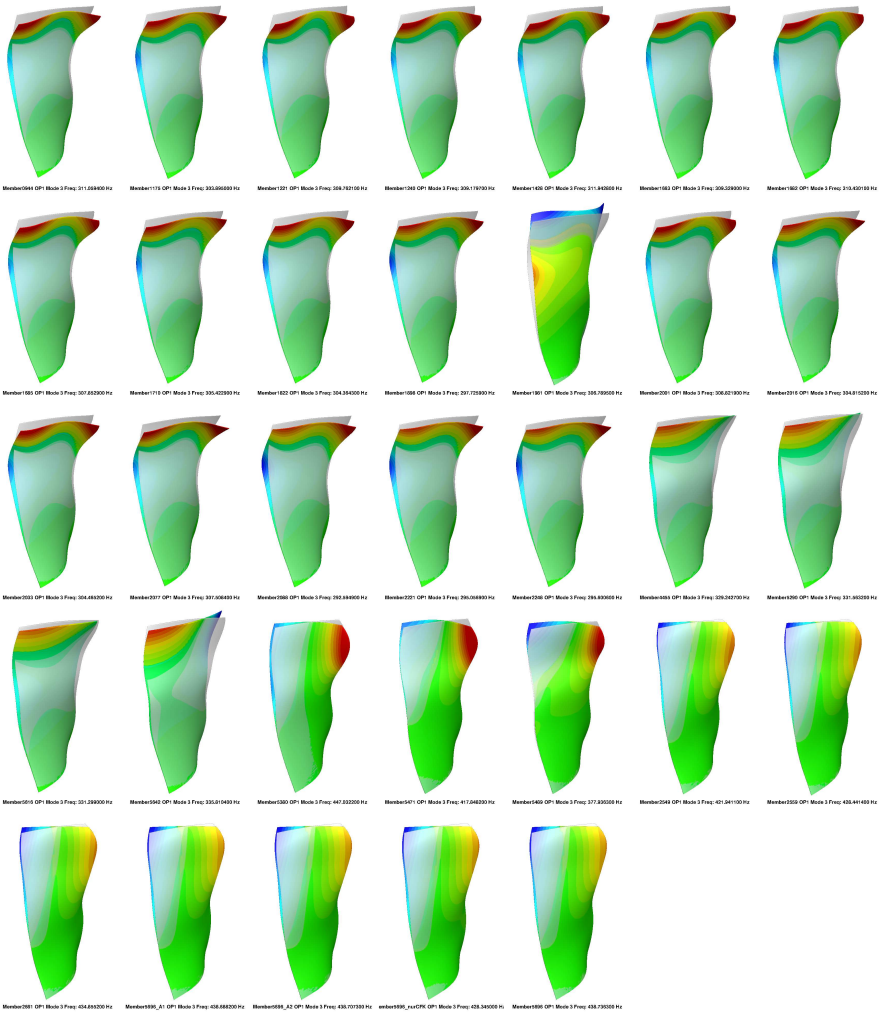

Figure E.13.: 3rd eigenmode shapes of Rotor 1 at OP1 for various evolution steps of the CRISPmulti project (0944, 1175, 1221, 1240, 1428, 1663, 1682, 1685, 1710, 1822, 1898, 1981, 2001, 2016, 2033, 2077, 2088, 2221, 2248, 4455, 5290, 5616, 5642, 5380, 5471, 5489, 2549, 2559, 2661, 5696_A1, 5696_A2, 5696_-nurCFK, 5696).

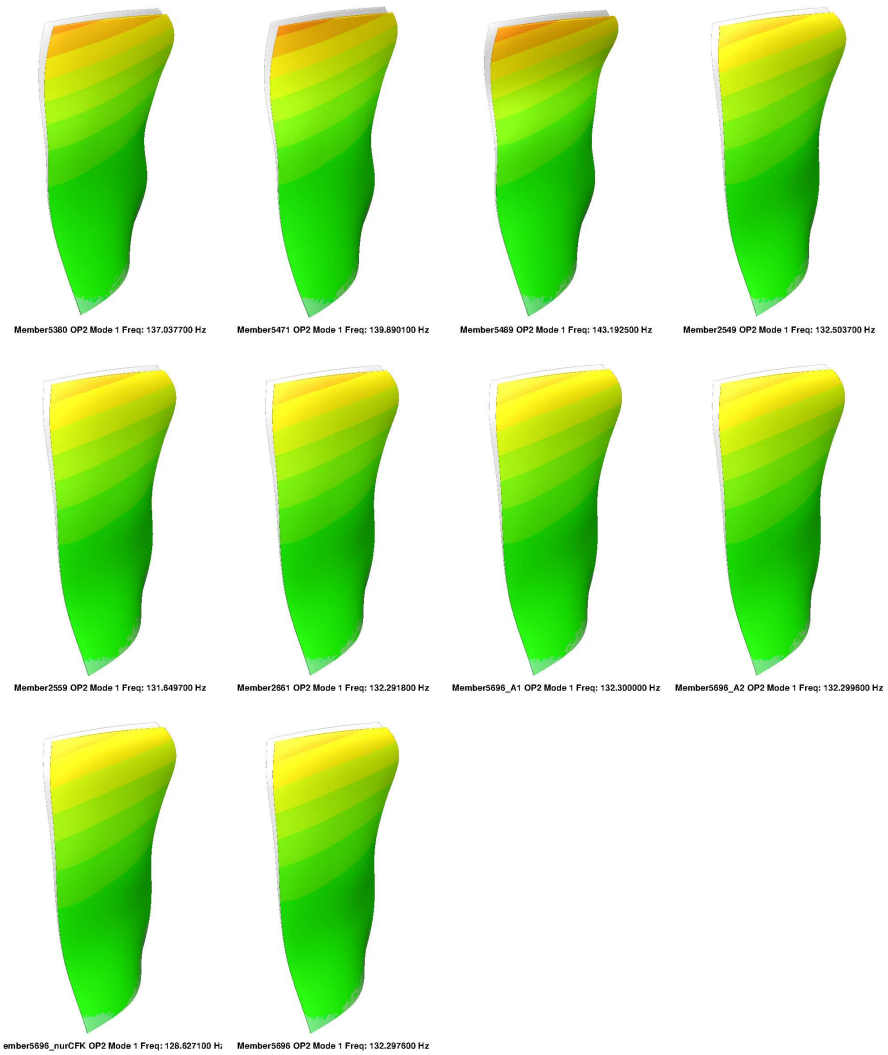

Figure E.14.: 1st eigenmode shapes of Rotor 1 at OP2 for various evolution steps of the CRISPmulti project (5380, 5471, 5489, 2549, 2559, 2661, 5696_A1, 5696_A2, 5696_nurCFK, 5696).

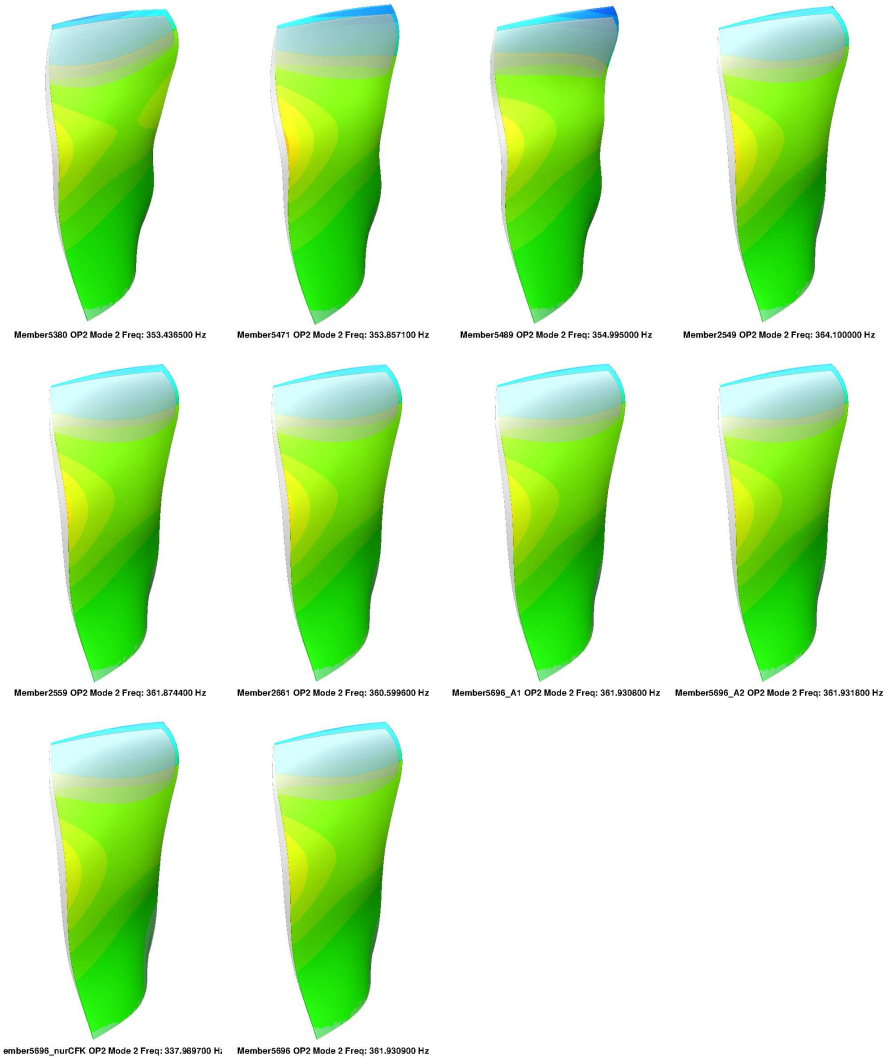

Figure E.15.: 2nd eigenmode shapes of Rotor 1 at OP2 for various evolution steps of the CRISPmulti project (5380, 5471, 5489, 2549, 2559, 2661, 5696_A1, 5696_A2, 5696_nurCFK, 5696).

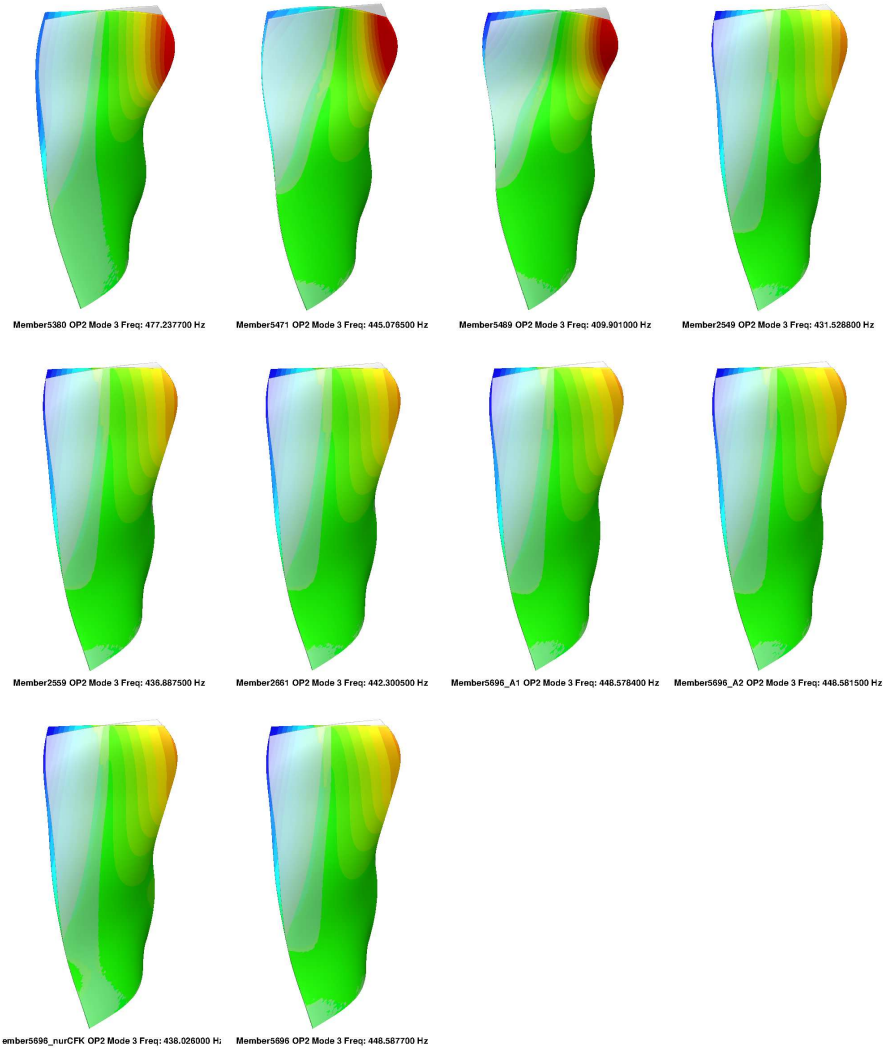

Figure E.16.: 3rd eigenmode shapes of Rotor 1 at OP2 for various evolution steps of the CRISPmulti project (5380, 5471, 5489, 2549, 2559, 2661, 5696_A1, 5696_A2, 5696_nurCFK, 5696).

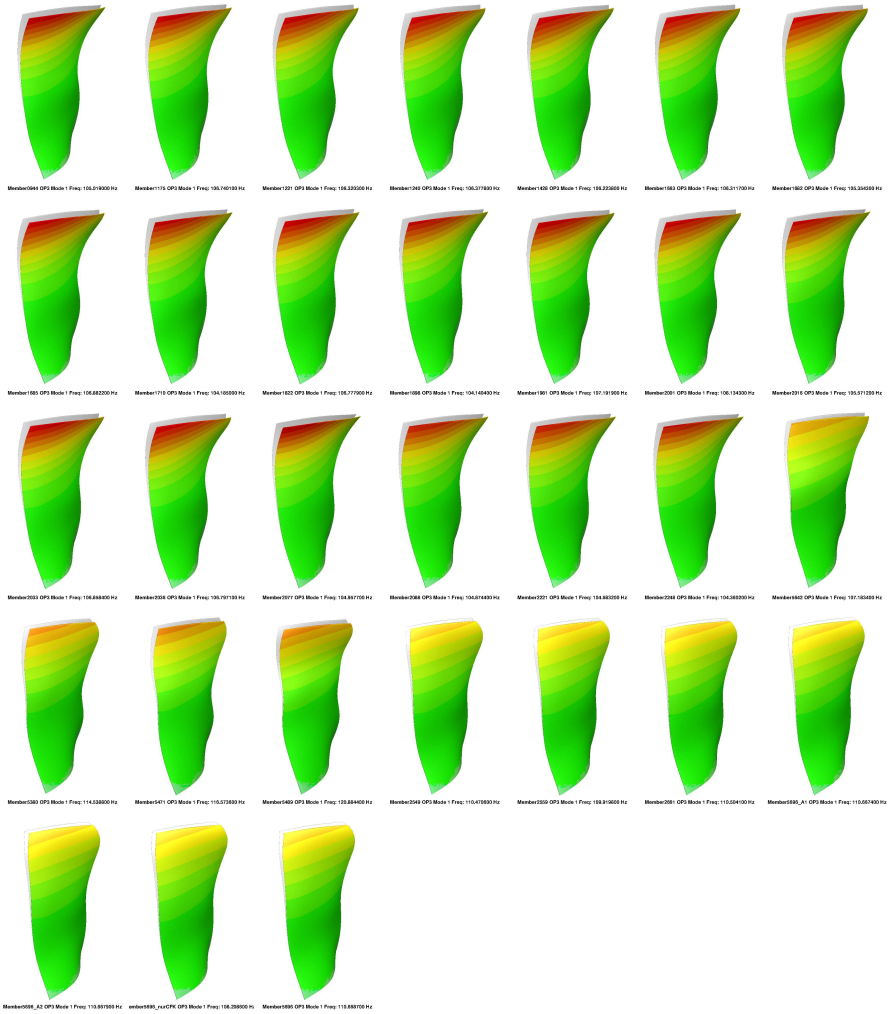

Figure E.17.: 1st eigenmode shapes of Rotor 1 at OP3 for various evolution steps of the CRISPmulti project (0944, 1175, 1221, 1240, 1428, 1663, 1682, 1685, 1710, 1822, 1898, 1981, 2001, 2016, 2033, 2036, 2077, 2088, 2221, 2248, 5642, 5380, 5471, 5489, 2549, 2559, 2661, 5696_A1, 5696_A2, 5696_nurCFK, 5696).

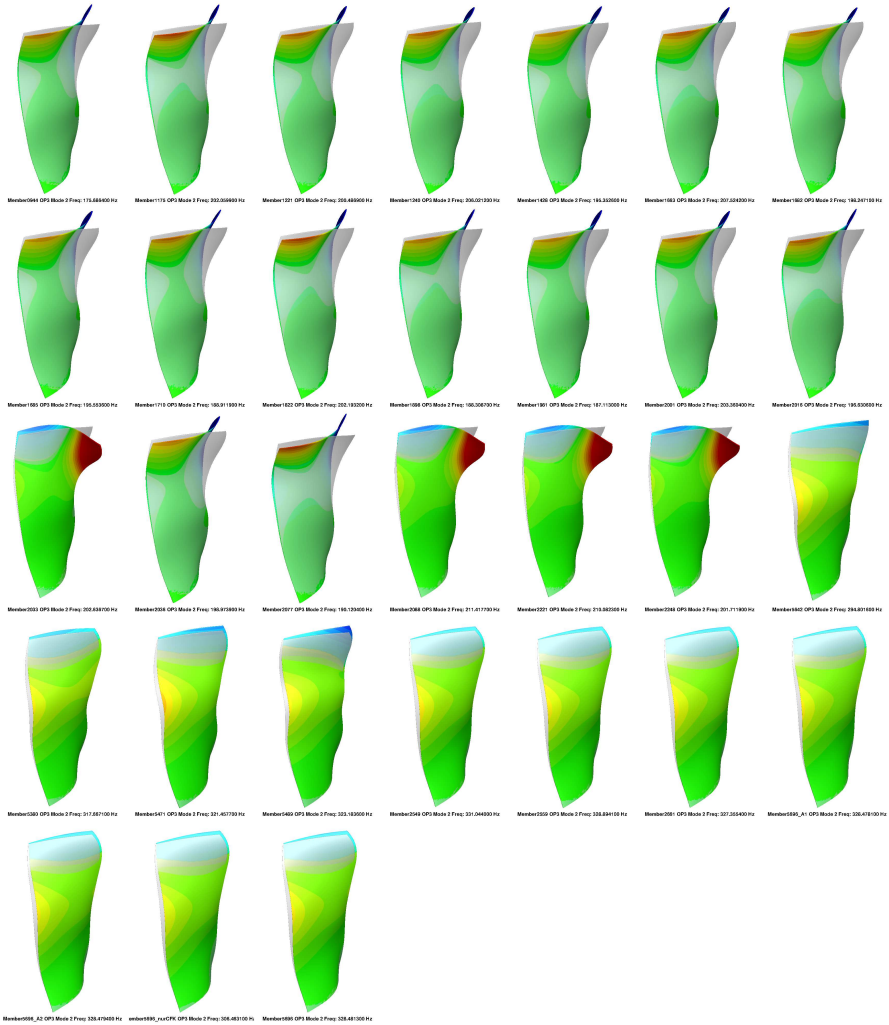

Figure E.18.: 2nd eigenmode shapes of Rotor 1 at OP3 for various evolution steps of the CRISPmulti project (0944, 1175, 1221, 1240, 1428, 1663, 1682, 1685, 1710, 1822, 1898, 1981, 2001, 2016, 2033, 2036, 2077, 2088, 2221, 2248, 5642, 5380, 5471, 5489, 2549, 2559, 2661, 5696_A1, 5696_A2, 5696_nurCFK, 5696).

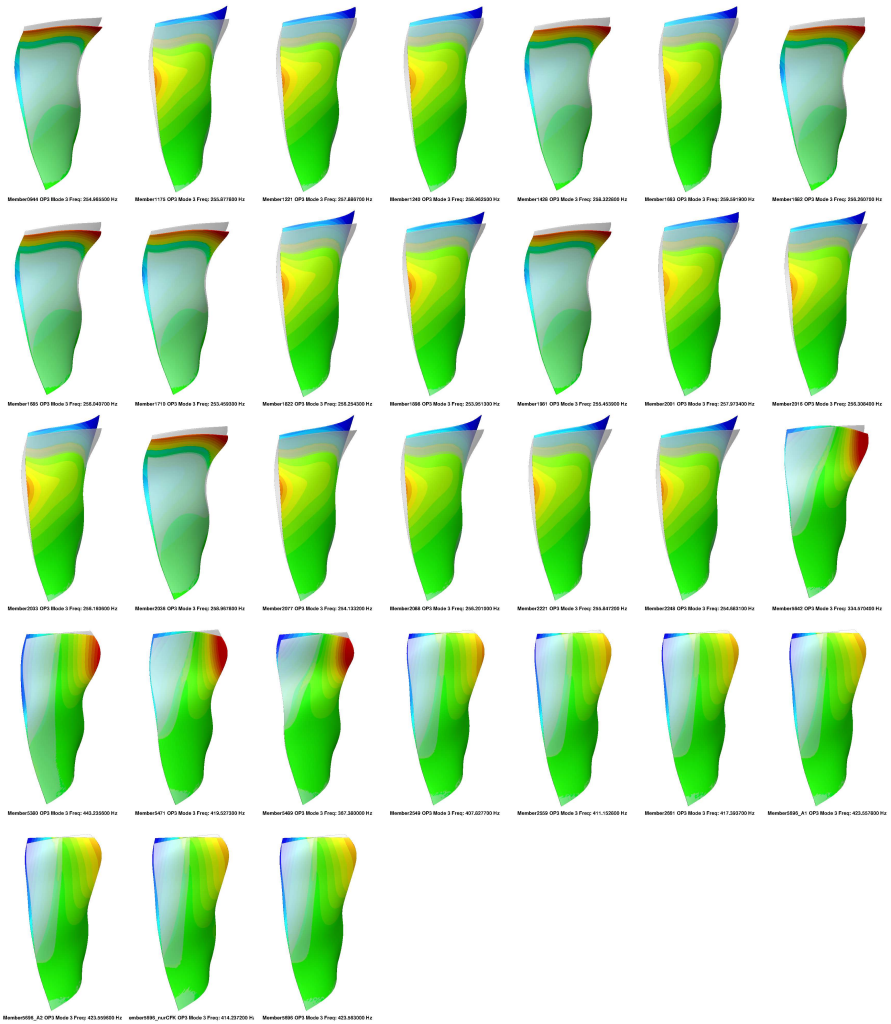

Figure E.19.: 3rd eigenmode shapes of Rotor 1 at OP3 for various evolution steps of the CRISPmulti project (0944, 1175, 1221, 1240, 1428, 1663, 1682, 1685, 1710, 1822, 1898, 1981, 2001, 2016, 2033, 2036, 2077, 2088, 2221, 2248, 5642, 5380, 5471, 5489, 2549, 2559, 2661, 5696_A1, 5696_A2, 5696_nurCFK, 5696).

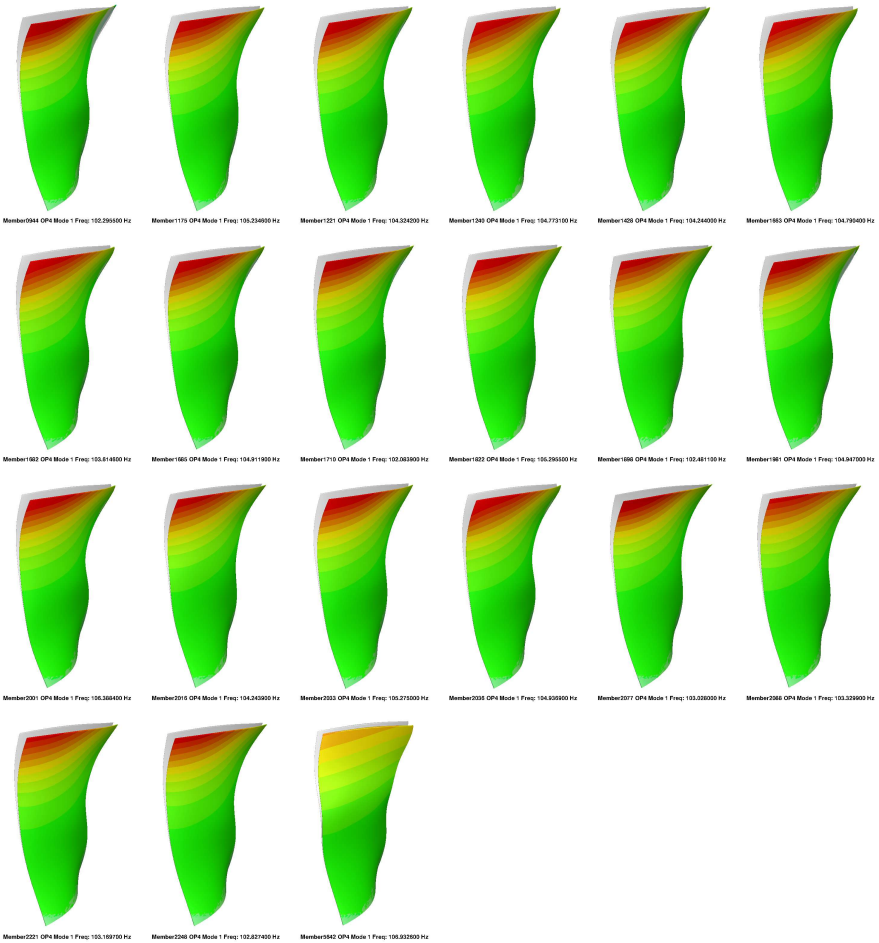

Figure E.20.: 1st eigenmode shapes of Rotor 1 at OP4 for various evolution steps of the CRISPmulti project (0944, 1175, 1221, 1240, 1428, 1663, 1682, 1685, 1710, 1822, 1898, 1981, 2001, 2016, 2033, 2036, 2077, 2088, 2221, 2248, 5642).

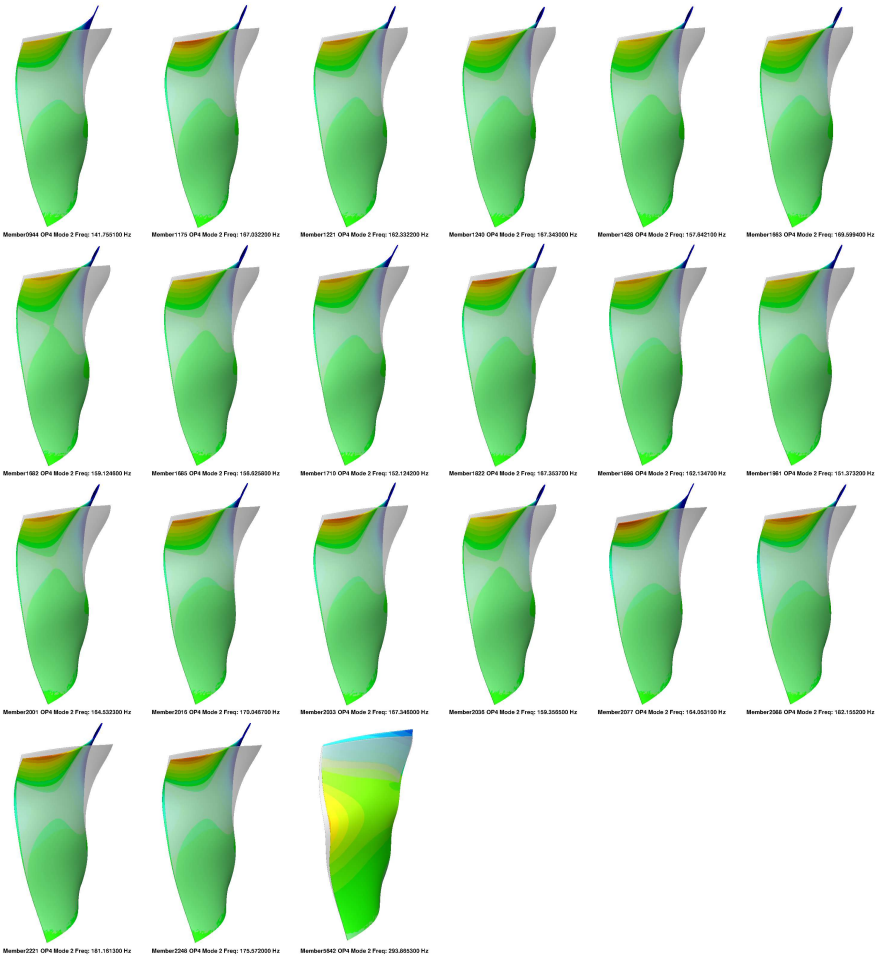

Figure E.21.: 2nd eigenmode shapes of Rotor 1 at OP4 for various evolution steps of the CRISPmulti project (0944, 1175, 1221, 1240, 1428, 1663, 1682, 1685, 1710, 1822, 1898, 1981, 2001, 2016, 2033, 2036, 2077, 2088, 2221, 2248, 5642).

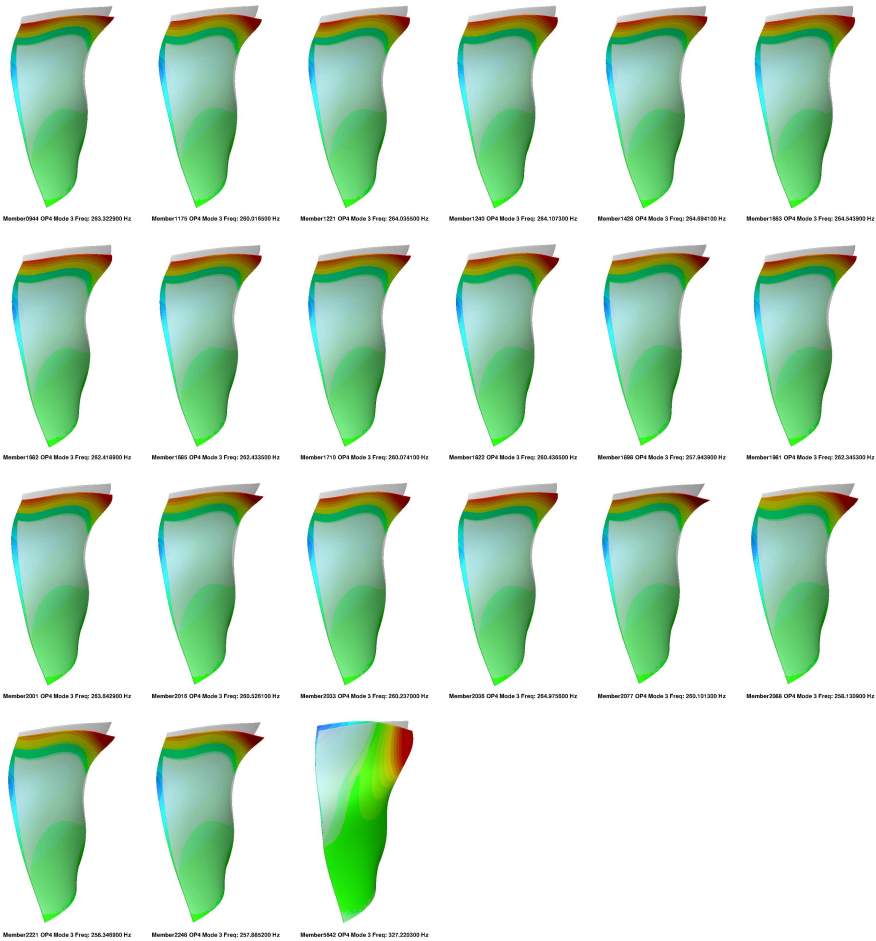

Figure E.22.: 3$^{\text{rd}}$ eigenmode shapes of Rotor 1 at OP4 for various evolution steps of the CRISPmulti project (0944, 1175, 1221, 1240, 1428, 1663, 1682, 1685, 1710, 1822, 1898, 1981, 2001, 2016, 2033, 2036, 2077, 2088, 2221, 2248, 5642).

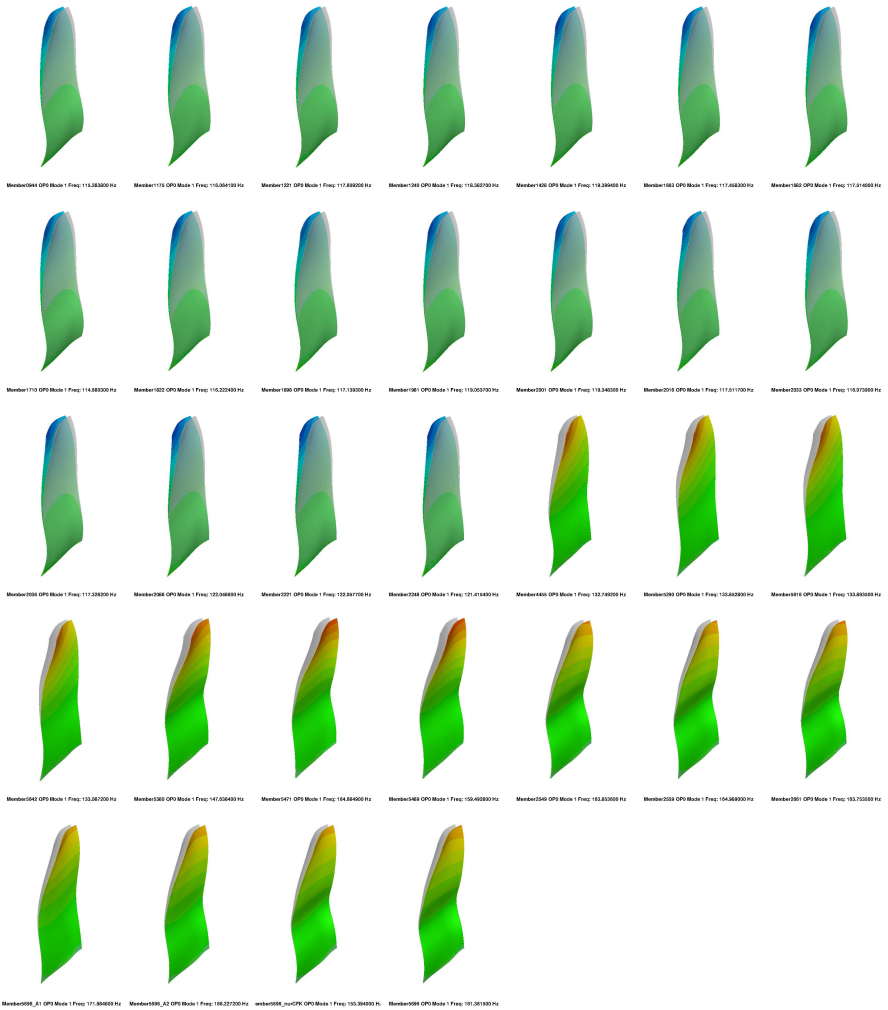

Figure E.23.: 1st eigenmode shapes of Rotor 2 at OP0 for various evolution steps of the CRISPmulti project (0944, 1175, 1221, 1240, 1428, 1663, 1682, 1710, 1822, 1898, 1981, 2001, 2016, 2033, 2036, 2088, 2221, 2248, 4455, 5290, 5616, 5642, 5380, 5471, 5489, 2549, 2559, 2661, 5696_A1, 5696_A2, 5696_nurCFK, 5696).

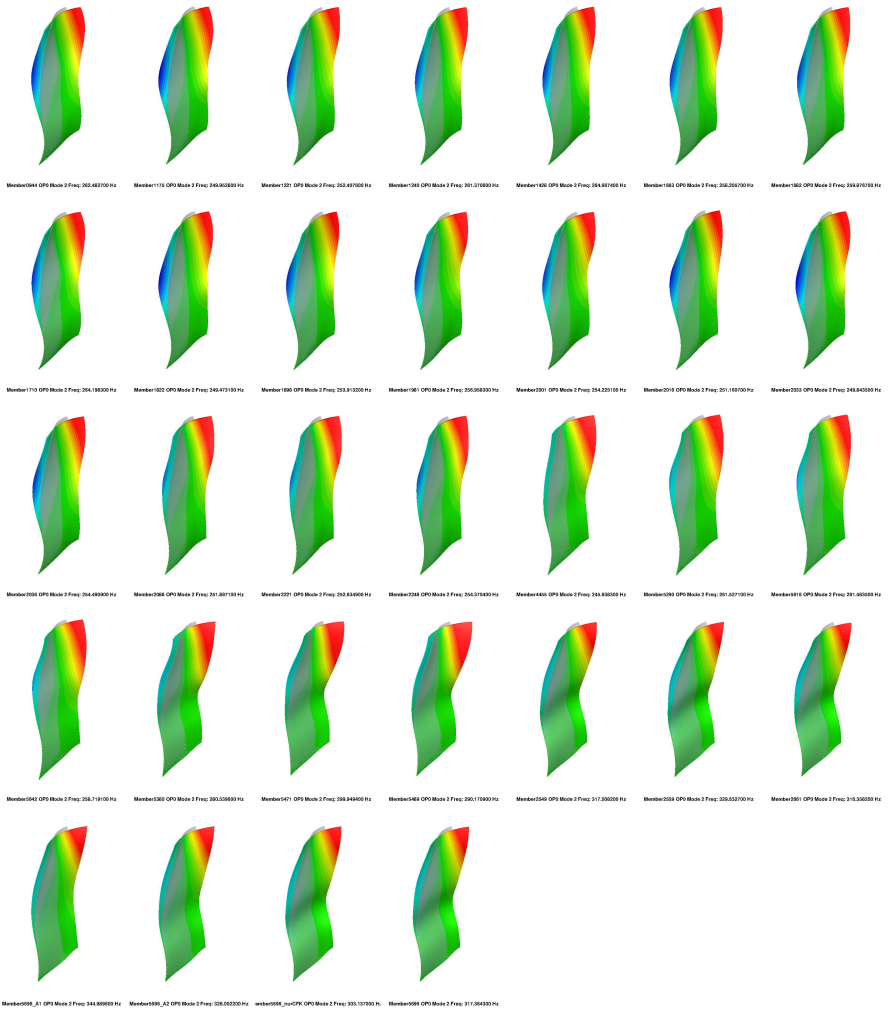

Figure E.24.: 2nd eigenmode shapes of Rotor 2 at OP0 for various evolution steps of the CRISPmulti project (0944, 1175, 1221, 1240, 1428, 1663, 1682, 1710, 1822, 1898, 1981, 2001, 2016, 2033, 2036, 2088, 2221, 2248, 4455, 5290, 5616, 5642, 5380, 5471, 5489, 2549, 2559, 2661, 5696_A1, 5696_A2, 5696_nurCFK, 5696).

Figure E.25.: 3rd eigenmode shapes of Rotor 2 at OP0 for various evolution steps of the CRISPmulti project (0944, 1175, 1221, 1240, 1428, 1663, 1682, 1710, 1822, 1898, 1981, 2001, 2016, 2033, 2036, 2088, 2221, 2248, 4455, 5290, 5616, 5642, 5380, 5471, 5489, 2549, 2559, 2661, 5696_A1, 5696_A2, 5696_nurCFK, 5696).

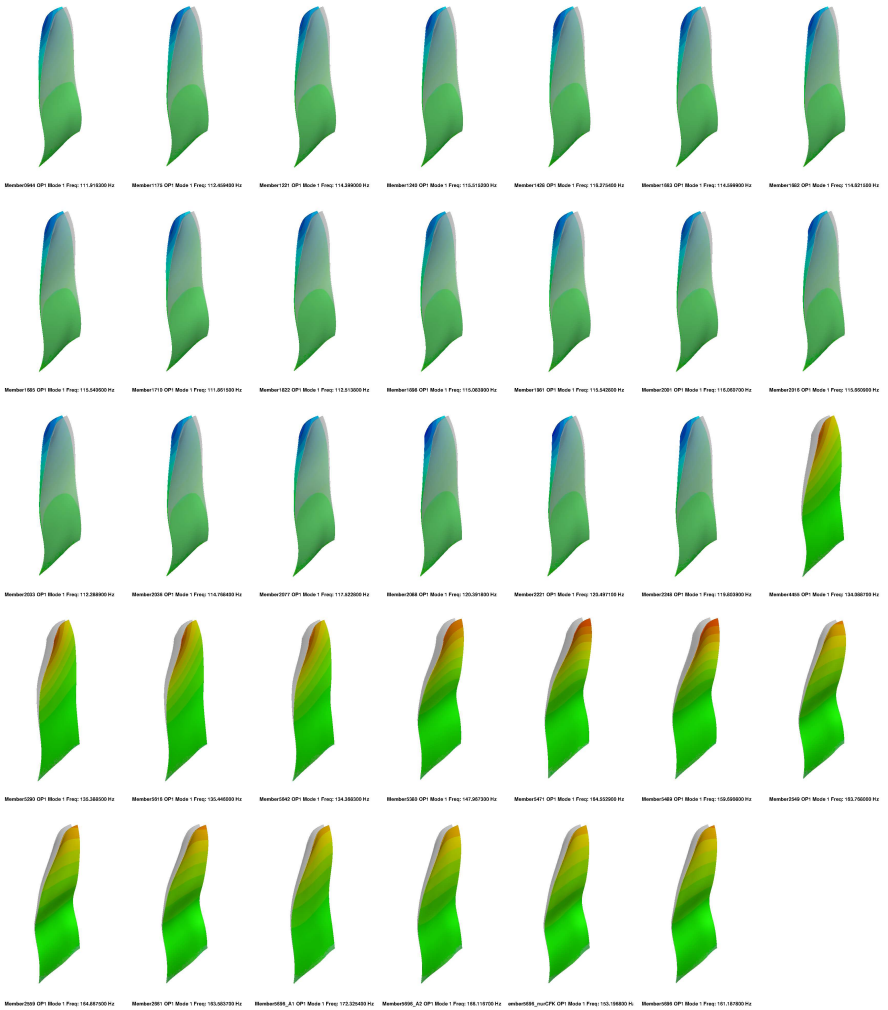

Figure E.26.: 1st eigenmode shapes of Rotor 2 at OP1 for various evolution steps of the CRISPmulti project (0944, 1175, 1221, 1240, 1428, 1663, 1682, 1685, 1710, 1822, 1898, 1981, 2001, 2016, 2033, 2036, 2077, 2088, 2221, 2248, 4455, 5290, 5616, 5642, 5380, 5471, 5489, 2549, 2559, 2661, 5696_A1, 5696_A2, 5696_nurCFK, 5696).

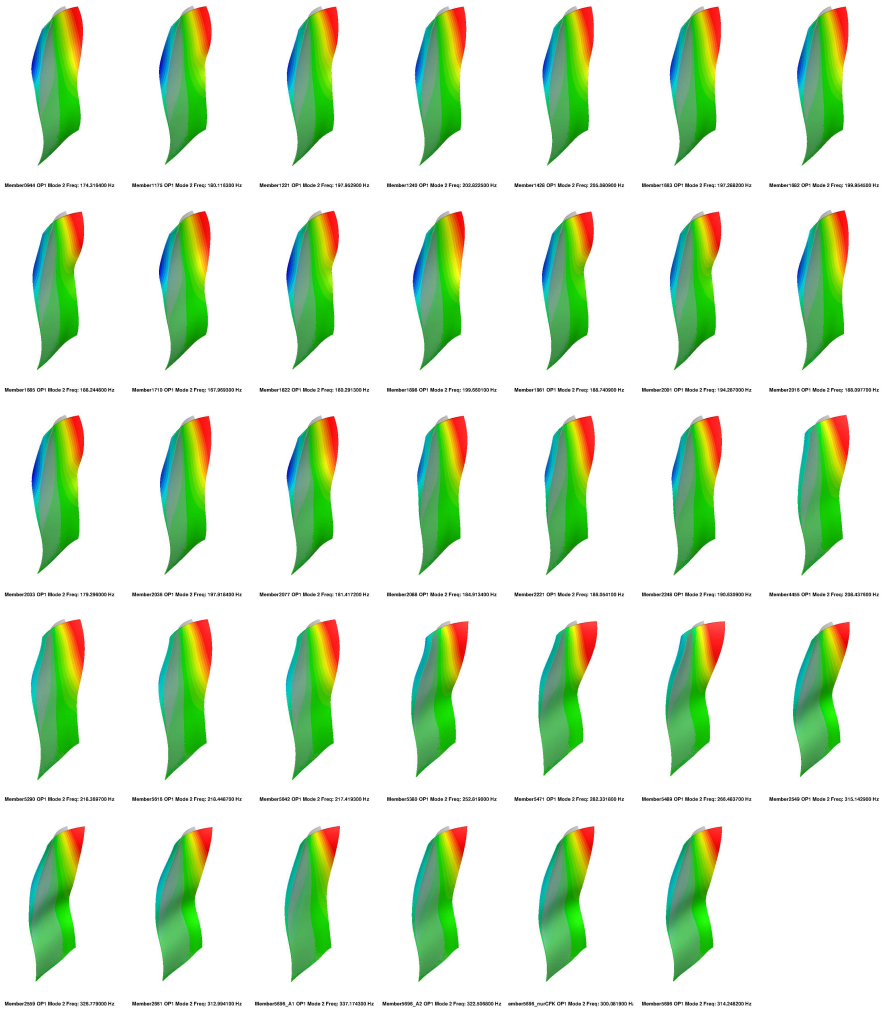

Figure E.27.: 2nd eigenmode shapes of Rotor 2 at OP1 for various evolution steps of the CRISPmulti project (0944, 1175, 1221, 1240, 1428, 1663, 1682, 1685, 1710, 1822, 1898, 1981, 2001, 2016, 2033, 2036, 2077, 2088, 2221, 2248, 4455, 5290, 5616, 5642, 5380, 5471, 5489, 2549, 2559, 2661, 5696_A1, 5696_A2, 5696_nurCFK, 5696).

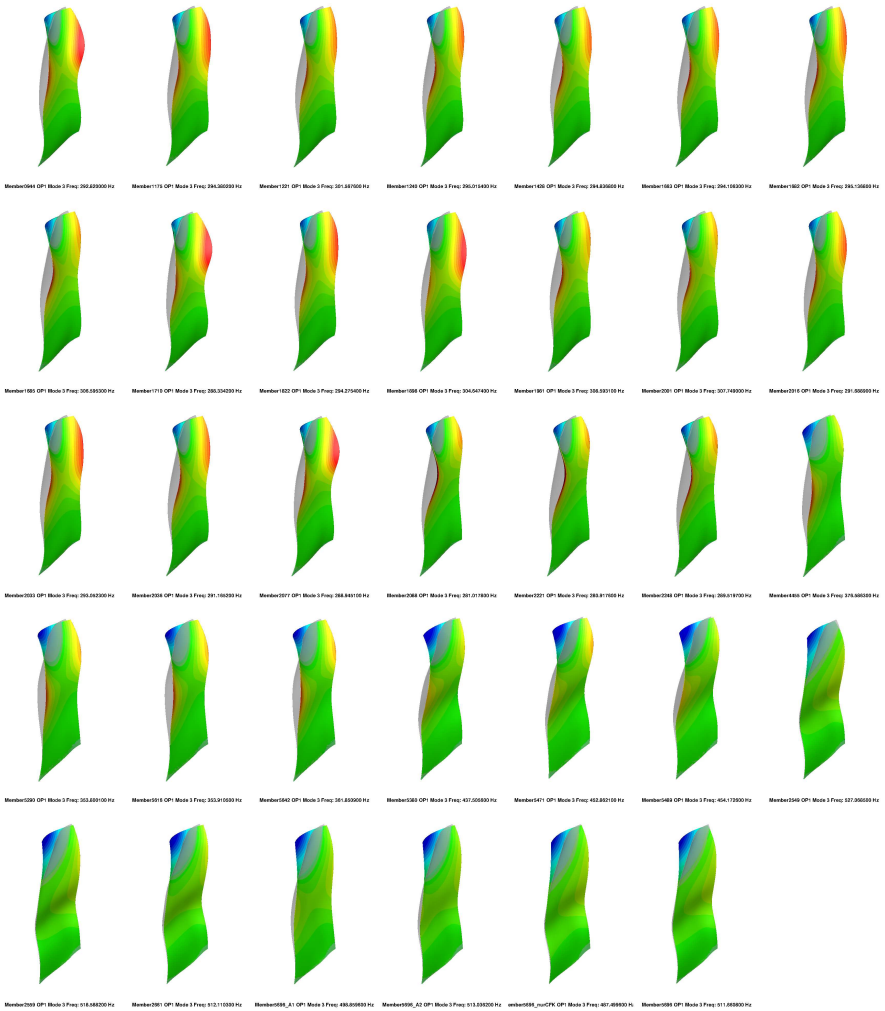

Figure E.28.: 3rd eigenmode shapes of Rotor 2 at OP1 for various evolution steps of the CRISPmulti project (0944, 1175, 1221, 1240, 1428, 1663, 1682, 1685, 1710, 1822, 1898, 1981, 2001, 2016, 2033, 2036, 2077, 2088, 2221, 2248, 4455, 5290, 5616, 5642, 5380, 5471, 5489, 2549, 2559, 2661, 5696_A1, 5696_A2, 5696_nurCFK, 5696).

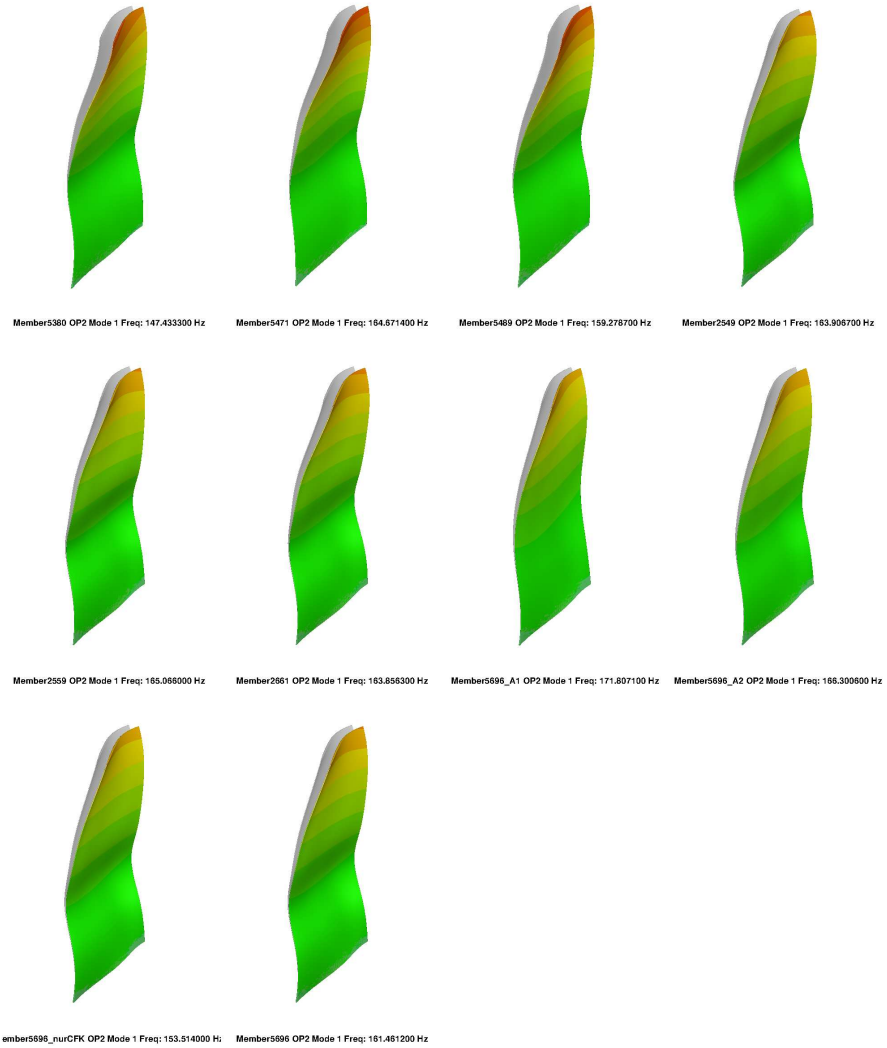

Figure E.29.: 1st eigenmode shapes of Rotor 2 at OP2 for various evolution steps of the CRISPmulti project (5380, 5471, 5489, 2549, 2559, 2661, 5696_A1, 5696_A2, 5696_nurCFK, 5696).

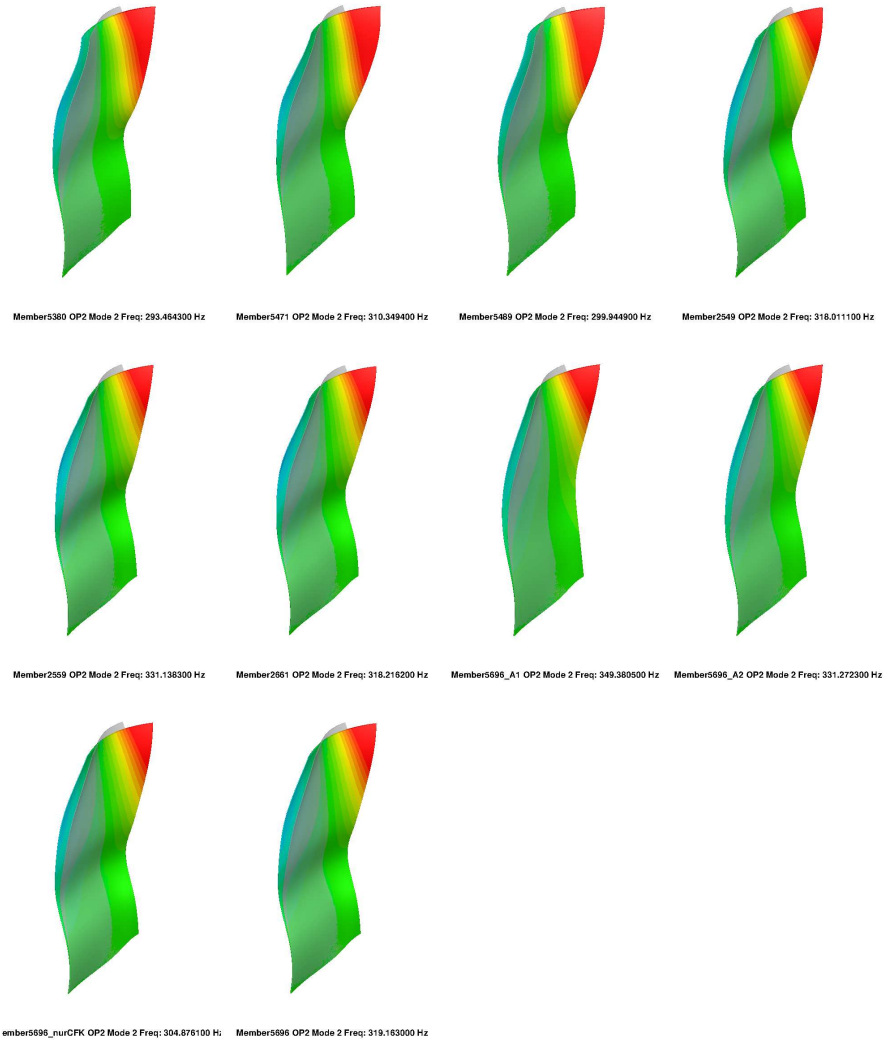

Figure E.30.: 2nd eigenmode shapes of Rotor 2 at OP2 for various evolution steps of the CRISPmulti project (5380, 5471, 5489, 2549, 2559, 2661, 5696_A1, 5696_A2, 5696_nurCFK, 5696).

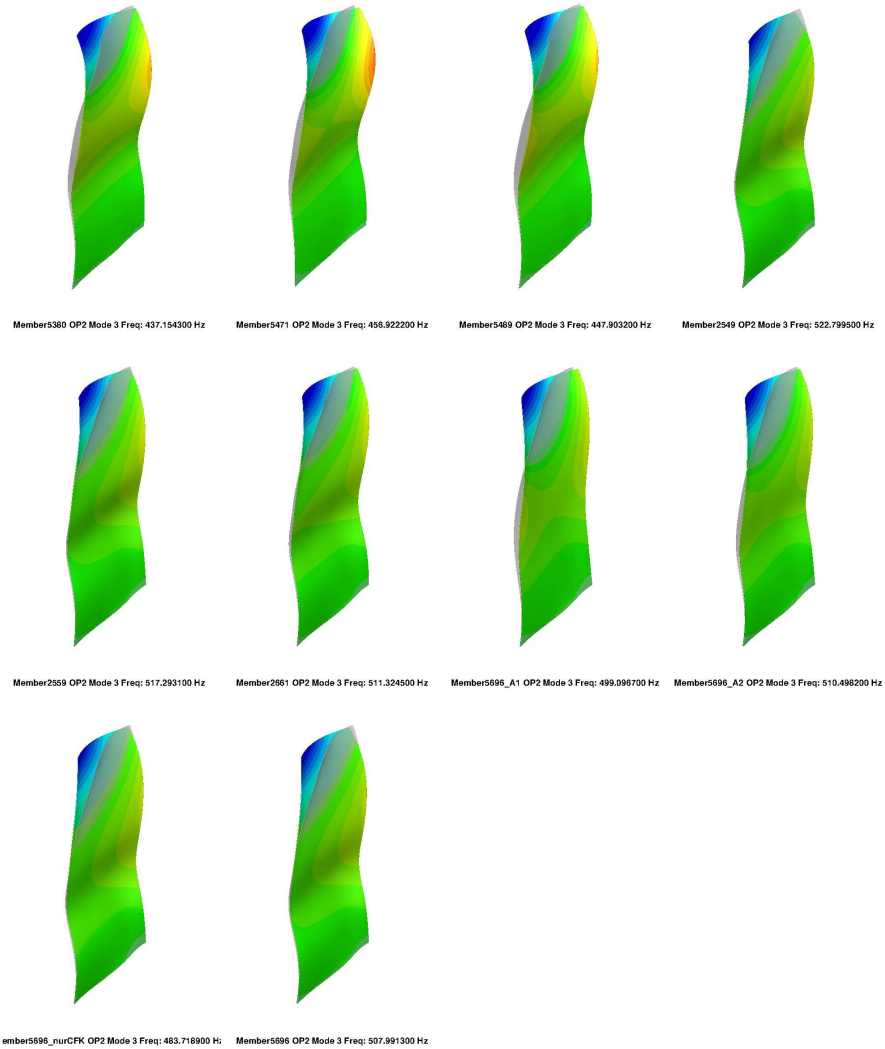

Figure E.31.: 3rd eigenmode shapes of Rotor 2 at OP2 for various evolution steps of the CRISPmulti project (5380, 5471, 5489, 2549, 2559, 2661, 5696_A1, 5696_A2, 5696_nurCFK, 5696).

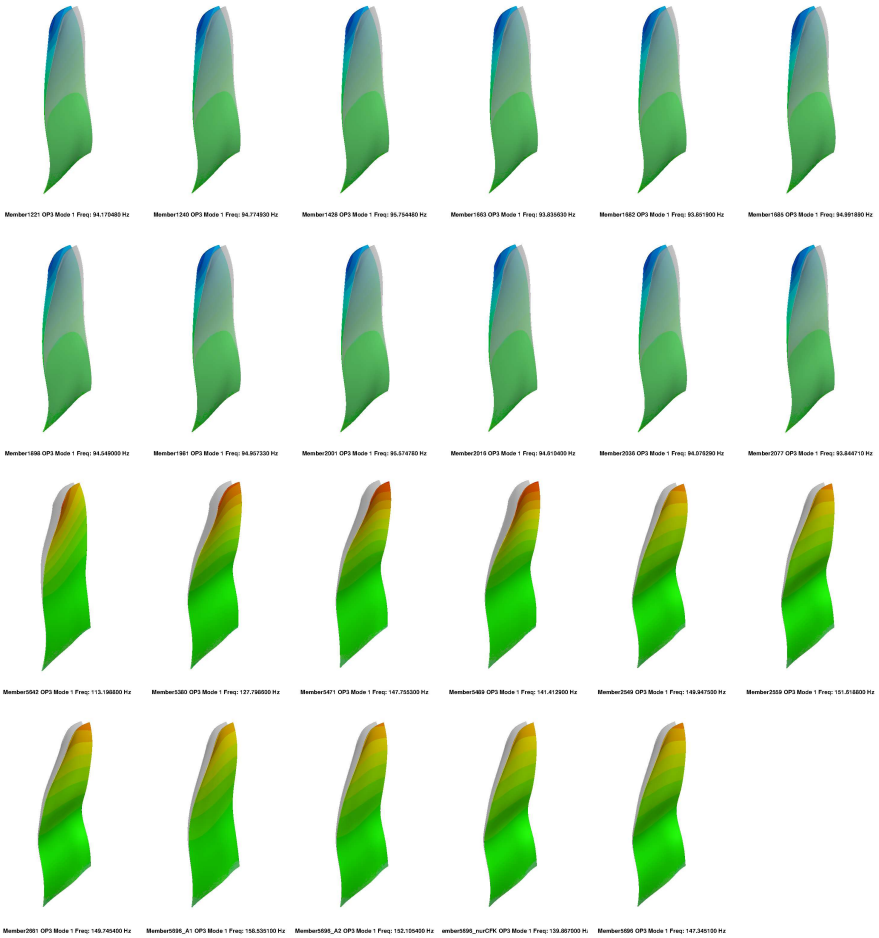

Figure E.32.: 1st eigenmode shapes of Rotor 2 at OP3 for various evolution steps of the CRISPmulti project (1221, 1240, 1428, 1663, 1682, 1685, 1898, 1981, 2001, 2016, 2036, 2077, 5642, 5380, 5471, 5489, 2549, 2559, 2661, 5696_A1, 5696_A2, 5696_nurCFK, 5696).

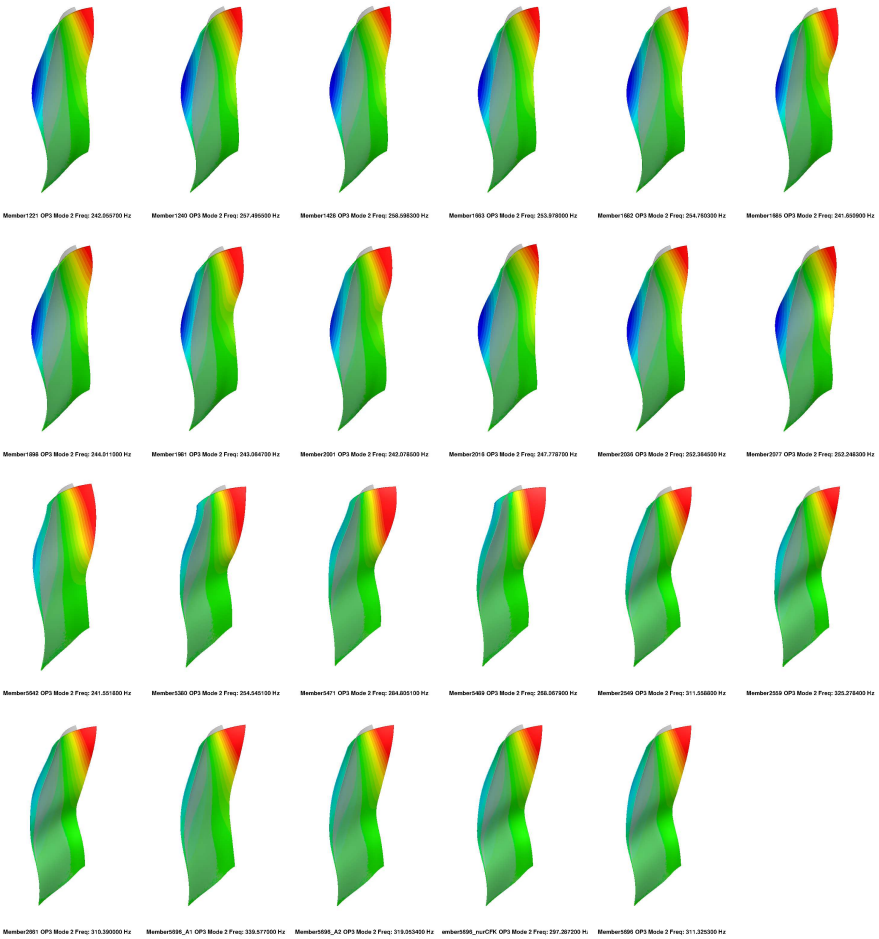

Figure E.33.: 2nd eigenmode shapes of Rotor 2 at OP3 for various evolution steps of the CRISPmulti project (1221, 1240, 1428, 1663, 1682, 1685, 1898, 1981, 2001, 2016, 2036, 2077, 5642, 5380, 5471, 5489, 2549, 2559, 2661, 5696_A1, 5696_A2, 5696_nurCFK, 5696).

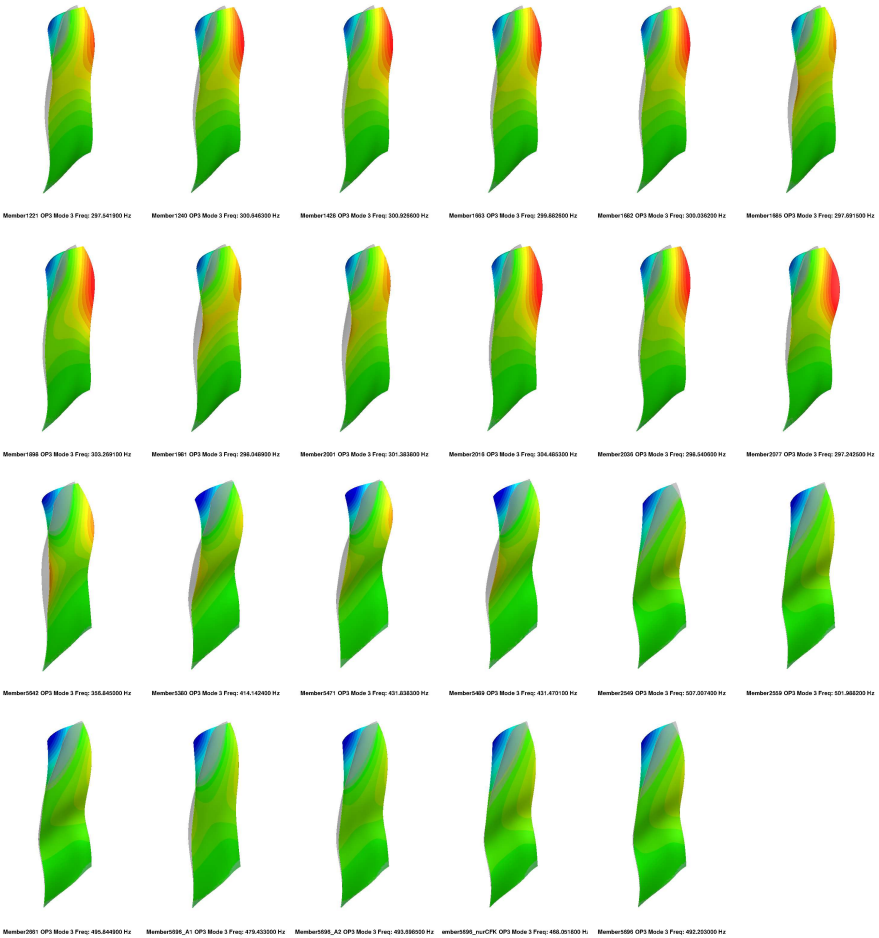

Figure E.34.: 3rd eigenmode shapes of Rotor 2 at OP3 for various evolution steps of the CRISPmulti project (1221, 1240, 1428, 1663, 1682, 1685, 1898, 1981, 2001, 2016, 2036, 2077, 5642, 5380, 5471, 5489, 2549, 2559, 2661, 5696_A1, 5696_A2, 5696_nurCFK, 5696).

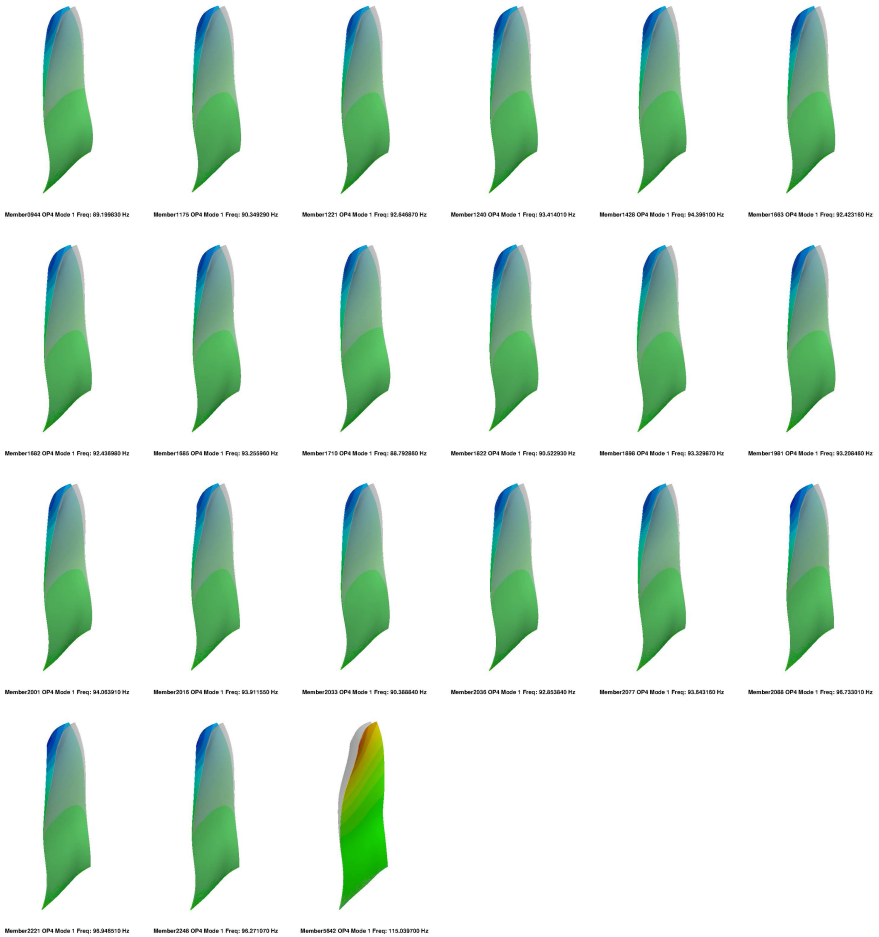

Figure E.35.: 1st eigenmode shapes of Rotor 2 at OP4 for various evolution steps of the CRISPmulti project (0944, 1175, 1221, 1240, 1428, 1663, 1682, 1685, 1710, 1822, 1898, 1981, 2001, 2016, 2033, 2036, 2077, 2088, 2221, 2248, 5642).

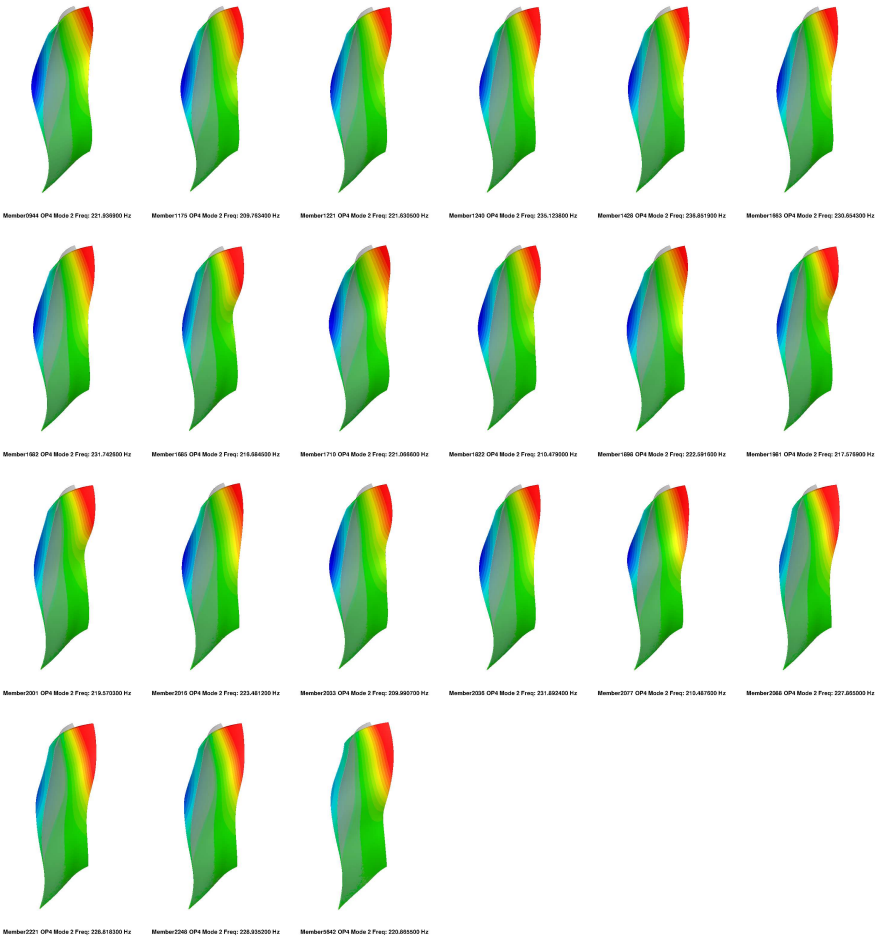

Figure E.36.: 2nd eigenmode shapes of Rotor 2 at OP4 for various evolution steps of the CRISPmulti project (0944, 1175, 1221, 1240, 1428, 1663, 1682, 1685, 1710, 1822, 1898, 1981, 2001, 2016, 2033, 2036, 2077, 2088, 2221, 2248, 5642).

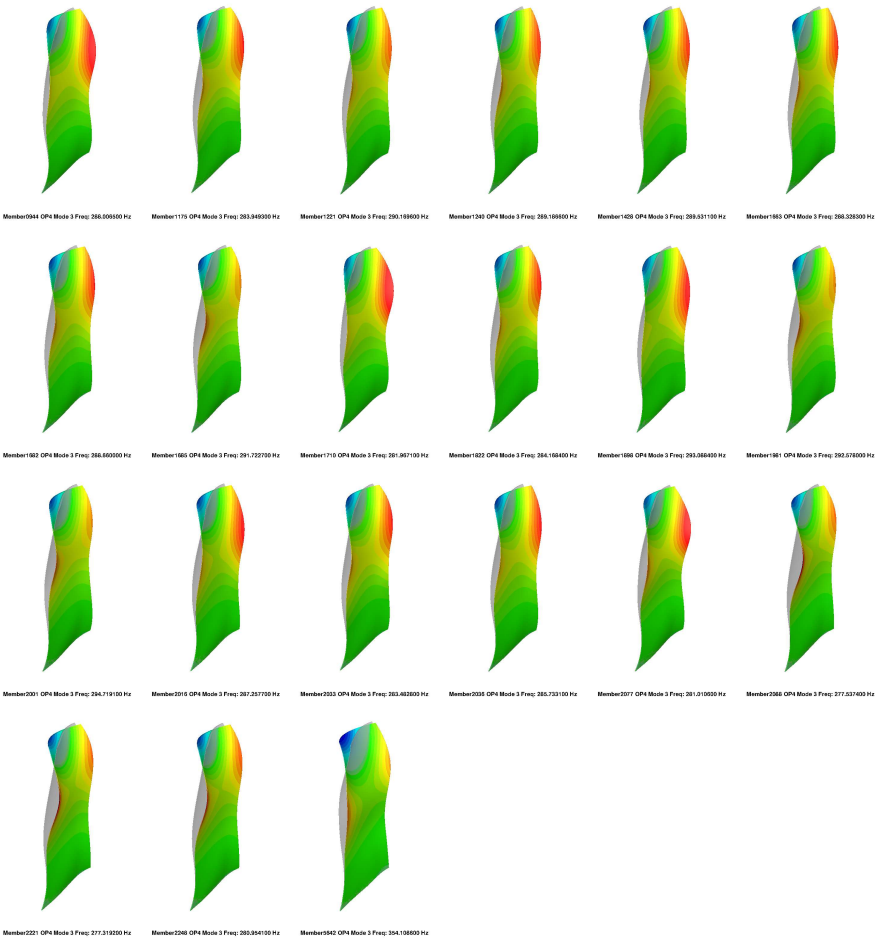

Figure E.37.: 3rd eigenmode shapes of Rotor 2 at OP4 for various evolution steps of the CRISPmulti project (0944, 1175, 1221, 1240, 1428, 1663, 1682, 1685, 1710, 1822, 1898, 1981, 2001, 2016, 2033, 2036, 2077, 2088, 2221, 2248, 5642).

E.6. Smallest Aerodynamic Damping over Reduced Frequency

In chapter 4.2.1, the combined least aerodynamic damping over reduced frequency diagrams were given for different evaluation approaches. As a supplement, the least aerodynamic damping over the reduced frequency is given for each computed operating point, here.

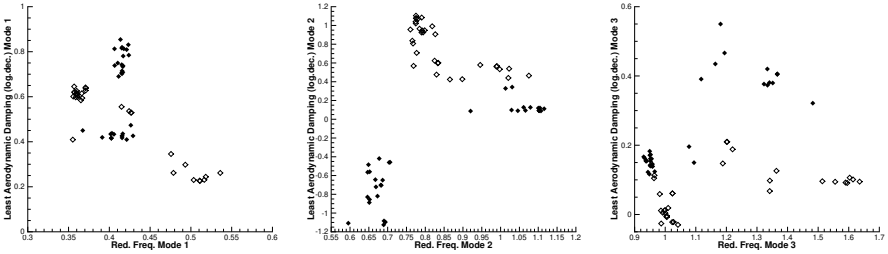

(a) Operating point OP0, eigenmode family 1 **(b)** Operating point OP0, eigenmode family 2 **(c)** Operating point OP0, eigenmode family 3

Figure E.38.: Smallest aerodynamic damping $\Lambda_{min,\,OP0}$ over reduced frequency $\omega_{red,\,OP0}$ found for different rotor evolution steps (full diamonds denote rotor 1 of CRISPmulti, empty diamonds denote rotor 2 of CRISPmulti).

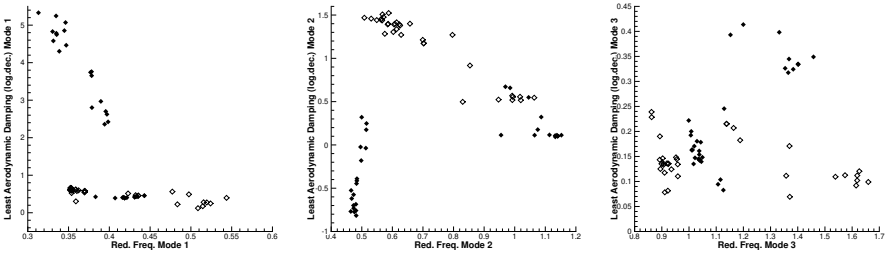

(a) Operating point OP1, eigenmode family 1 **(b)** Operating point OP1, eigenmode family 2 **(c)** Operating point OP1, eigenmode family 3

Figure E.39.: Smallest aerodynamic damping $\Lambda_{min,\,OP1}$ over reduced frequency $\omega_{red,\,OP1}$ found for different rotor evolution steps (full diamonds denote rotor 1 of CRISPmulti, empty diamonds denote rotor 2 of CRISPmulti).

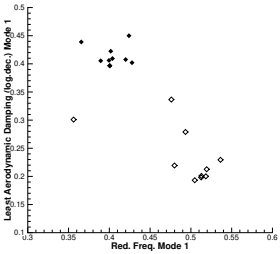

(a) Operating point OP2, eigenmode family 1

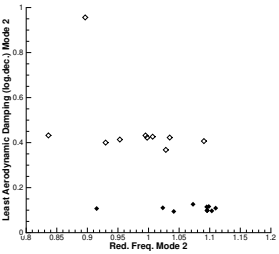

(b) Operating point OP2, eigenmode family 2

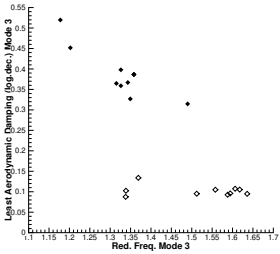

(c) Operating point OP2, eigenmode family 3

Figure E.40.: Smallest aerodynamic damping $\Lambda_{min,\,OP2}$ over reduced frequency $\omega_{red,\,OP2}$ found for different rotor evolution steps (full diamonds denote rotor 1 of CRISPmulti, empty diamonds denote rotor 2 of CRISPmulti).

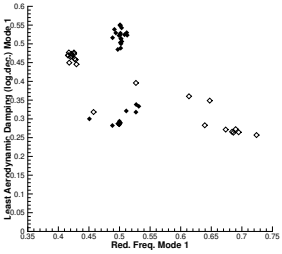

(a) Operating point OP3, eigenmode family 1

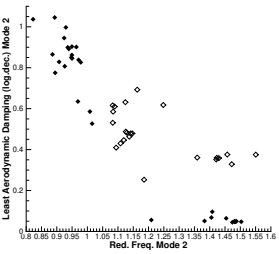

(b) Operating point OP3, eigenmode family 2

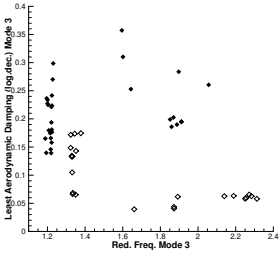

(c) Operating point OP3, eigenmode family 3

Figure E.41.: Smallest aerodynamic damping $\Lambda_{min,\,OP3}$ over reduced frequency $\omega_{red,\,OP3}$ found for different rotor evolution steps (full diamonds denote rotor 1 of CRISPmulti, empty diamonds denote rotor 2 of CRISPmulti).

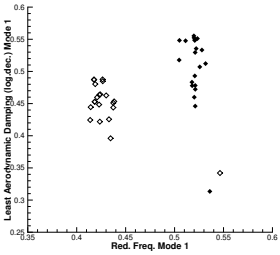

(a) Operating point OP4, eigenmode family 1

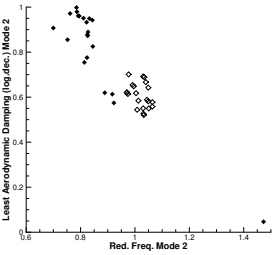

(b) Operating point OP4, eigenmode family 2

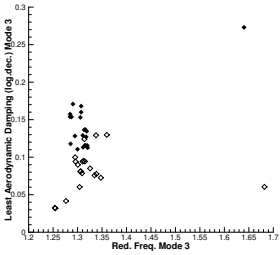

(c) Operating point OP4, eigenmode family 3

Figure E.42.: Smallest aerodynamic damping $\Lambda_{min,\,OP4}$ over reduced frequency $\omega_{red,\,OP4}$ found for different rotor evolution steps (full diamonds denote rotor 1 of CRISPmulti, empty diamonds denote rotor 2 of CRISPmulti).

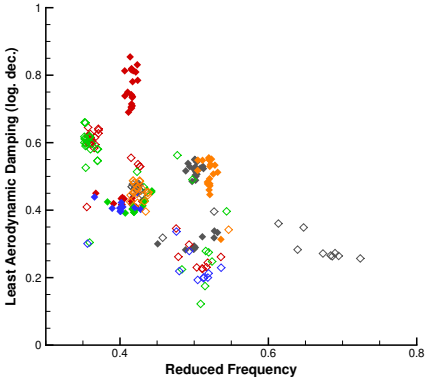

(a) Smallest aerodynamic damping Λ_{min} over reduced frequency ω_{red} of all computed operating points, first bending eigenmode shape

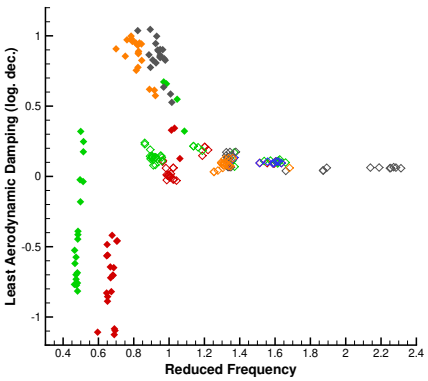

(b) Smallest aerodynamic damping Λ_{min} over reduced frequency ω_{red} of all computed operating points, corner flap eigenmode shape

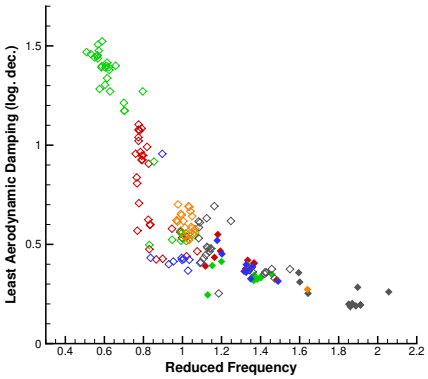

(c) Smallest aerodynamic damping Λ_{min} over reduced frequency ω_{red} of all computed operating points, torsion eigenmode shape

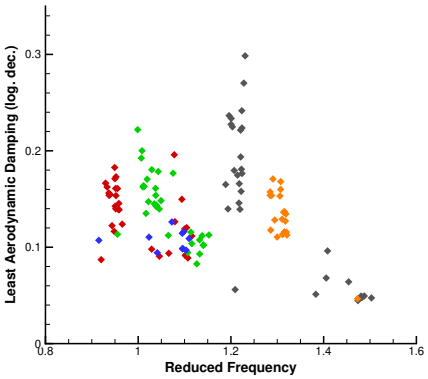

(d) Smallest aerodynamic damping Λ_{min} over reduced frequency ω_{red} of all computed operating points, second bending eigenmode shape

Figure E.43.: Smallest aerodynamic damping Λ_{min} over reduced frequency ω_{red} found for different rotor evolution steps at different operating points (grouped by eigenmode shape, full diamonds denote rotor 1 of CRISPmulti, empty diamonds denote rotor 2 of CRISPmulti, red denotes OP0, green denotes OP1, blue denotes OP2, gray denotes OP3, orange denotes OP4).

F. Optimal Distribution of Sample Points on a 360° Circle

In chapter 4.1.4, it was shown that three sample points on a 360° wave length are necessary to define a sine wave. Then, it was shown in equation (4.3) that the inverse of a coefficient matrix needs to be computed to derive the defining parameters of the sine wave. The inverse of a matrix can be obtained as:

$$\left[\boldsymbol{A}\right]^{-1} = \frac{\text{adj}\left[\boldsymbol{A}\right]}{\det\left[\boldsymbol{A}\right]} \tag{F.1}$$

In Equation (F.1), adj $\left[\boldsymbol{A}\right]$ is not the adjoint of $\left[\boldsymbol{A}\right]$ but the less well known adjugate. In this chapter the the derivation of the optimal distribution of the three points on the wave defining the sine curve is highlighted.

The Determinant

The determinant of a 3x3 matrix $\left[\boldsymbol{A}\right]$ is defined as:

$$\begin{aligned}\det\left[\boldsymbol{A}\right] = \quad & (A_{11}\cdot A_{22}\cdot A_{33}) + (A_{12}\cdot A_{23}\cdot A_{31}) + (A_{13}\cdot A_{21}\cdot A_{32}) \\ & - (A_{13}\cdot A_{22}\cdot A_{31}) - (A_{12}\cdot A_{21}\cdot A_{33}) - (A_{11}\cdot A_{23}\cdot A_{32})\end{aligned} \tag{F.2}$$

Since the determinant is in the denominator of equation (F.1), it is important that $\det\left[\boldsymbol{A}\right] \neq 0$.

Also, the relation between σ_1, σ_2 and σ_3 can be used when calculating the determinant:

$$\begin{aligned}\sigma_2 &= \sigma_1 + \varphi \\ \sigma_3 &= \sigma_1 + \theta\end{aligned} \tag{F.3}$$

The determinant of the coefficient matrix can then be shown to be:

$$
\begin{aligned}
&\det\begin{bmatrix} 1 & \sin(\sigma_1) & \cos(\sigma_1) \\ 1 & \sin(\sigma_1+\varphi) & \cos(\sigma_1+\varphi) \\ 1 & \sin(\sigma_1+\theta) & \cos(\sigma_1+\theta) \end{bmatrix} \\
= \;& \sin(\sigma_1+\varphi)\cdot\cos(\sigma_1+\theta) + \sin(\sigma_1)\cdot\cos(\sigma_1+\varphi) + \cos(\sigma_1)\cdot\sin(\sigma_1+\theta) \\
& - \cos(\sigma_1)\cdot\sin(\sigma_1+\varphi) - \sin(\sigma_1)\cdot\cos(\sigma_1+\theta) - \cos(\sigma_1+\varphi)\cdot\sin(\sigma_1+\theta) \\
= \;& (\sin(\sigma_1)\cdot\cos(\varphi) + \cos(\sigma_1)\cdot\sin(\varphi))\cdot(\cos(\sigma_1)\cdot\cos(\theta) - \sin(\sigma_1)\cdot\sin(\theta)) \\
& + \sin(\sigma_1)\cdot(\cos(\sigma_1)\cdot\cos(\varphi) - \sin(\sigma_1)\cdot\sin(\varphi)) \\
& + \cos(\sigma_1)\cdot(\sin(\sigma_1)\cdot\cos(\theta) + \cos(\sigma_1)\cdot\sin(\theta)) \\
& - \cos(\sigma_1)\cdot(\sin(\sigma_1)\cdot\cos(\varphi) + \cos(\sigma_1)\cdot\sin(\varphi)) \\
& - \sin(\sigma_1)\cdot(\cos(\sigma_1)\cdot\cos(\theta) - \sin(\sigma_1)\cdot\sin(\theta)) \\
& - (\cos(\sigma_1)\cdot\cos(\varphi) - \sin(\sigma_1)\cdot\sin(\varphi))\cdot(\sin(\sigma_1)\cdot\cos(\theta) + \cos(\sigma_1)\cdot\sin(\theta)) \\
= \;& \cancel{\sin(\sigma_1)\cdot\cos(\sigma_1)\cdot\cos(\varphi)\cdot\cos(\theta)} + \cos^2(\sigma_1)\cdot\sin(\varphi)\cdot\cos(\theta) \\
& - \sin^2(\sigma_1)\cdot\cos(\varphi)\cdot\sin(\theta) - \cancel{\sin(\sigma_1)\cdot\cos(\sigma_1)\cdot\sin(\varphi)\cdot\sin(\theta)} \\
& + \cancel{\sin(\sigma_1)\cdot\cos(\sigma_1)\cdot\cos(\varphi)} - \sin^2(\sigma_1)\cdot\sin(\varphi) \\
& + \cancel{\sin(\sigma_1)\cdot\cos(\sigma_1)\cdot\cos(\theta)} + \cos^2(\sigma_1)\cdot\sin(\theta) \\
& - \cancel{\sin(\sigma_1)\cdot\cos(\sigma_1)\cdot\cos(\varphi)} - \cos^2(\sigma_1)\cdot\sin(\varphi) \\
& - \cancel{\sin(\sigma_1)\cdot\cos(\sigma_1)\cdot\cos(\theta)} + \sin^2(\sigma_1)\cdot\sin(\theta) \\
& - \cancel{\sin(\sigma_1)\cdot\cos(\sigma_1)\cdot\cos(\varphi)\cdot\cos(\theta)} + \sin^2(\sigma_1)\cdot\sin(\varphi)\cdot\cos(\theta) \\
& - \cos^2(\sigma_1)\cdot\cos(\varphi)\cdot\sin(\theta) + \cancel{\sin(\sigma_1)\cdot\cos(\sigma_1)\cdot\sin(\varphi)\cdot\sin(\theta)} \\
= \;& (\sin^2(\sigma_1)+\cos^2(\sigma_1))\cdot[\sin(\varphi)\cdot\cos(\theta) - \cos(\varphi)\cdot\sin(\theta) + \sin(\theta) - \sin(\varphi)] \\
= \;& \sin(\theta) + \sin(\varphi-\theta) - \sin(\varphi)
\end{aligned}
\tag{F.4}
$$

In addition to being very simple to calculate, equation (F.4) shows that the determinant is not dependent of the first angle at all, but just of the difference between the three angles.

The determinant of the coefficient matrix is shown in figure F.1. The lines where the determinant is zero ($\theta = 0$, $\varphi = 0$ or $\theta = \varphi$) need to be avoided at all cost, since a division by zero is impossible. The extremal points of this function are at $(\varphi = 120°, \theta = -120°)$ and $(\varphi = -120°, \theta = 120°)$ and indicate the angle combinations where the division in the matrix inversion is most robust.

The Adjugate

The adjugate of a 3x3 matrix $[\boldsymbol{A}]$ is defined as:

$$
\operatorname{adj}[\boldsymbol{A}] = \begin{bmatrix}
\det\begin{bmatrix} A_{22} & A_{23} \\ A_{32} & A_{33} \end{bmatrix} & -\det\begin{bmatrix} A_{12} & A_{13} \\ A_{32} & A_{33} \end{bmatrix} & \det\begin{bmatrix} A_{12} & A_{13} \\ A_{22} & A_{23} \end{bmatrix} \\
-\det\begin{bmatrix} A_{21} & A_{23} \\ A_{31} & A_{33} \end{bmatrix} & \det\begin{bmatrix} A_{11} & A_{13} \\ A_{31} & A_{33} \end{bmatrix} & -\det\begin{bmatrix} A_{11} & A_{13} \\ A_{21} & A_{23} \end{bmatrix} \\
\det\begin{bmatrix} A_{21} & A_{22} \\ A_{31} & A_{32} \end{bmatrix} & -\det\begin{bmatrix} A_{11} & A_{12} \\ A_{31} & A_{32} \end{bmatrix} & \det\begin{bmatrix} A_{11} & A_{12} \\ A_{21} & A_{22} \end{bmatrix}
\end{bmatrix}
\tag{F.5}
$$

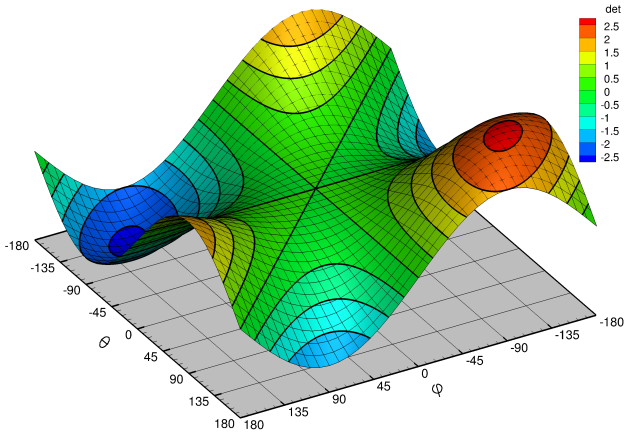

Figure F.1.: Determinant of the matrix dependent on φ and θ.

This is the transpose of the cofactor matrix. Again using the definitions of equation (F.3), the adjugate of the coefficient matrix is calculated as:

$$\begin{aligned}
&\operatorname{adj}\begin{bmatrix} 1 & \sin(\sigma_1) & \cos(\sigma_1) \\ 1 & \sin(\sigma_1+\varphi) & \cos(\sigma_1+\varphi) \\ 1 & \sin(\sigma_1+\theta) & \cos(\sigma_1+\theta) \end{bmatrix} \\
&= \begin{bmatrix} \begin{pmatrix} \sin(\sigma_1+\varphi)\cdot\cos(\sigma_1+\theta) \\ -\cos(\sigma_1+\varphi)\cdot\sin(\sigma_1+\theta) \end{pmatrix} & \begin{pmatrix} -\sin(\sigma_1)\cdot\cos(\sigma_1+\theta) \\ +\cos(\sigma_1)\cdot\sin(\sigma_1+\theta) \end{pmatrix} & \begin{pmatrix} \sin(\sigma_1)\cdot\cos(\sigma_1+\varphi) \\ -\cos(\sigma_1)\cdot\sin(\sigma_1+\varphi) \end{pmatrix} \\ -\cos(\sigma_1+\theta)+\cos(\sigma_1+\varphi) & \cos(\sigma_1+\theta)-\cos(\sigma_1) & -\cos(\sigma_1+\varphi)+\cos(\sigma_1) \\ \sin(\sigma_1+\theta)-\sin(\sigma_1+\varphi) & -\sin(\sigma_1+\theta)+\sin(\sigma_1) & \sin(\sigma_1+\varphi)-\sin(\sigma_1) \end{bmatrix}
\end{aligned} \tag{F.6}$$

One can see that the base angle σ_1 cannot be extracted from the adjugate of the coefficient matrix. Therefore, one can write it again as:

$$\begin{aligned}
&\operatorname{adj}\begin{bmatrix} 1 & \sin(\sigma_1) & \cos(\sigma_1) \\ 1 & \sin(\sigma_2) & \cos(\sigma_2) \\ 1 & \sin(\sigma_3) & \cos(\sigma_3) \end{bmatrix} \\
&= \begin{bmatrix} \begin{pmatrix} \sin(\sigma_2)\cdot\cos(\sigma_3) \\ -\sin(\sigma_3)\cdot\cos(\sigma_2) \end{pmatrix} & \begin{pmatrix} \sin(\sigma_3)\cdot\cos(\sigma_1) \\ -\sin(\sigma_1)\cdot\cos(\sigma_3) \end{pmatrix} & \begin{pmatrix} \sin(\sigma_1)\cdot\cos(\sigma_2) \\ -\sin(\sigma_2)\cdot\cos(\sigma_1) \end{pmatrix} \\ \cos(\sigma_2)-\cos(\sigma_3) & \cos(\sigma_3)-\cos(\sigma_1) & \cos(\sigma_1)-\cos(\sigma_2) \\ \sin(\sigma_3)-\sin(\sigma_2) & \sin(\sigma_1)-\sin(\sigma_3) & \sin(\sigma_2)-\sin(\sigma_1) \end{bmatrix}
\end{aligned} \tag{F.7}$$

There are two requirements for this coefficient matrix to deliver a robust solution:

- To not overemphasize the importance of one calculated damping value, the three numbers in each line of the adjugate should be as similar as possible to represent their influence on the sine curve.
- The three columns of the coefficient matrix need to be orthogonal, otherwise the determinant will be zero and the matrix cannot be inverted.

These two criteria contradict each other (the most similar values in two lines [equal values], automatically lead to a non-orthogonal matrix. Therefore it was decided to use a case where the determinant of the matrix is as large as possible. This is the case for $\varphi = 120°$ and $\theta = -120°$ or vice versa.

Since the case of $\sigma_1 = 0°$ is present in every configuration and the most simple to simulate in time-linearized and time-accurate methods, it was decided to use a setup with $\sigma_1 = 0°$ and σ_2 and σ_3 as close to $120°$ and $-120°$ as possible for the configuration at hand.

G. Vortex Lattice Unsteady Results with Local Velocity Wake Convection

In chapter 4.3.4, the unsteady fluid flow results of CMARC were compared to experiments and unsteady time-linearized 3D RANS computations. One additional experiment was conducted in order to determine the validity of the 3D panel code CMARC for turbomachinery applications. In this experiment, the unsteady computation was performed with "natural" wake development where the wake was stepped with the local velocity.

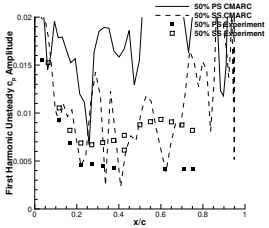

(a) Unsteady c_p amplitude CMARC results with 32 time steps per oscillation and wake convection with local velocity.

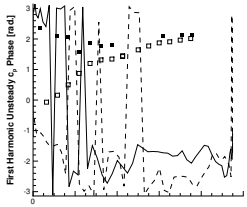

(b) Unsteady c_p phase CMARC results with 32 time steps per oscillation and wake convection with local velocity.

Figure G.1.: CMARC vs. experimental results for unsteady subsonic case z043 (0.3° blade vibration at 210 Hz, 0° IBPA).

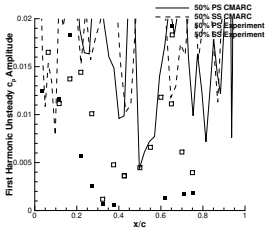

(a) Unsteady c_p amplitude CMARC results with 32 time steps per oscillation and wake convection with local velocity.

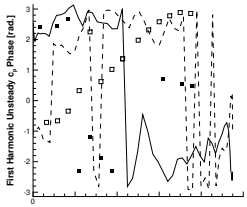

(b) Unsteady c_p phase CMARC results with 32 time steps per oscillation and wake convection with local velocity.

Figure G.2.: CMARC vs. experimental results for unsteady transonic case z014 (0.3° blade vibration at 210 Hz, 0° IBPA).

As one can see from figures G.1 and G.2, the results were heavily influenced by the ragged wake convection and consequently did not yield usable results. This is in accordance with the findings from chapter 4.3.3, where the steady state results were influenced heavily by the ragged wake convection.